



Performance increase of electron cyclotron resonance magnetic nozzle thruster via magnetically thickened resonance region

Hitchens, Oliver

<https://openresearch.surrey.ac.uk/esploro/outputs/doctoral/Performance-increase-of-electron-cyclotron-resonance/99991466602346/filesAndLinks?index=0>

Hitchens, O. (2025). Performance increase of electron cyclotron resonance magnetic nozzle thruster via magnetically thickened resonance region [University of Surrey]. <https://doi.org/10.15126/thesis.901635>



Performance Increase of Electron Cyclotron Resonance Magnetic Nozzle Thruster via Magnetically Thickened Resonance Region

Oliver Hitchens[†]

Submitted for the Degree of
Doctor of Philosophy

University of Surrey

May 4, 2025

Principal Supervisor:

Dr Andrea Lucca Fabris[†]

Co-supervisor:

Dr Nicola Baresi[†]



[†] Surrey Space Centre

School of Mathematics, Physics & Space,
University of Surrey, Guildford, GU2 7XH, United Kingdom

Declaration of Originality

This thesis and the work to which it refers are the results of my own efforts. Any ideas, data, images or text resulting from the work of others (whether published or unpublished) are fully identified as such within the work and attributed to their originator in the text, bibliography or in footnotes. This thesis has not been submitted in whole or in part for any other academic degree or professional qualification. I agree that the University has the right to submit my work to the plagiarism detection service TurnitinUK for originality checks. Whether or not drafts have been so-assessed, the University reserves the right to require an electronic version of the final document (as submitted) for assessment as above.

Signed:

Date:

Abstract

Electron Cyclotron Resonance (ECR) magnetic nozzle thrusters are a promising technology due to their electrodeless nature allowing for reduced erosion rates and extended lifetimes. Their simple design makes them relatively low-cost, however their typically low performance prevents them from becoming commercially viable. This thesis investigates multiple novel techniques to enhance the performance of ECR magnetic nozzle thrusters. Each is experimentally characterised to determine performance and the physical mechanism by which it is affected.

The primary focus of this thesis is investigating the effect of the magnetic field strength gradient at resonance on the thruster performance. It was found analytically that decreasing the magnetic field strength gradient at resonance increases the thickness of the resonance region and the energy transferred from the microwaves to the electrons. This was then investigated experimentally using two different ECR thrusters. Using an electromagnet, the magnetic field strength gradient at resonance was decreased, resulting in an increase in thrust and specific impulse of 60 %, while thruster efficiency was increased by 16 %. By using an iron ring to decrease the magnetic field strength gradient at resonance, instead of an electromagnet, thrust and specific impulse increased by 15 %, while thruster efficiency increased by 32 %.

The use of dual microwave frequencies at low-frequency separations was investigated and was found to increase thrust and specific impulse by up to 13 %. The effect of changing the resonance region location was also investigated, with the thrust found to decrease if the resonance region was located in the rear 8 mm of the thruster's 20 mm long chamber. Lastly, a magnetic mirror trap was implemented, which was found to decrease the propellant mass flow rate required for ignition and could increase the performance of miniaturised, low mass flow rate ECR thrusters.

Chaos is order yet undeciphered

JOSÉ SARAMAGO

Acknowledgements

This thesis has only been made possible by my supervisor Dr Andrea Lucca Fabris, to whom I would like to express my deepest gratitude. From entertaining some of my more crazy ideas to aiding my attendance at some incredible conferences, his support has never wavered. I could not have asked for a better mentor.

To Moe Ahmed, who has been with me from the start, with whom I have shared an office and roamed America, I could not have asked for a better colleague and friend. Special thanks to Dr James Stubbing for showing me the ropes around the lab and bearing with my many questions. Also to Dr Mansur Tisaev, Sam Lane, Dr Silvia Masillo and Sam Reeve for your selfless help and guidance, I appreciate you all and know that you will achieve incredible things. To Dave Fishlock, Alex Todd, Luca Ferrian and David Jones, your technical assistance has saved me many times over and I am truly grateful. And to Brian Eades, Jono Stacey and Rowan Lonsdale the work you do is masterful and I truly appreciate the extra time you take to answer my questions regarding manufacturing processes.

My sincere thanks to my examiners, both past and present, for volunteering their time and guidance. Your insight and feedback has contributed significantly to my research. I would also like to extend my thanks to the Doctoral College for funding my studies, as well as the Institution of Mechanical Engineers and Royal Aeronautical Society for funding me to attend some incredible conferences. To the Electric Rocket Propulsion Society for enabling the International Electric Propulsion Conference, thank you for fostering such a welcoming and vibrant community. And of course, thank you to everyone from the Surrey Space Centre for your kindness and collaboration, it has been a privilege to work alongside you all.

Finally, to my family. Words cannot express my gratitude towards my partner Freya, who has supported me every step of the way. A PhD is a daunting task, but with you I feel as though I can take on the world. To my parents who have supported me, taught me to take risks and live life to the fullest, I am forever grateful. Last but certainly not least, to my grandparents who have supported my education and encouraged my love of space, I appreciate everything you have done for me, thank you kindly.

Contents

1 INTRODUCTION	1
1.1 Spacecraft Propulsion	1
1.2 Electric Propulsion	4
1.2.1 Measuring Performance	6
1.3 ECR Magnetic Nozzle Thrusters	9
1.4 Focus of the Thesis	16
2 LITERATURE REVIEW	17
2.1 Electromagnetic Waves in Plasmas	18
2.2 Electron Cyclotron Resonance (ECR) Heating	23
2.2.1 Collisionless Heating Model	24
2.2.2 Doppler Broadened Resonance Region	26
2.3 Ion Acceleration in a Magnetic Nozzle	28
2.4 Development of the Coaxial ECR Thruster at ONERA	34
2.5 University of Michigan's ECR Thruster	38
2.6 Facility Effects	39
2.6.1 Background Pressure	40
2.6.2 Facility Size & Conductivity	41
2.7 Thesis Objectives	42
3 EXPERIMENTAL SETUP	43
3.1 Vacuum Chamber	44
3.2 Microwave Line	47
3.3 Torsional Thrust Balance	49
3.4 Langmuir Probe (Electron Measurements)	51
3.5 Faraday Probe (Ion Beam Measurements)	58
3.6 Retarding Potential Analyser (Ion Energy Measurements)	64
4 THRUSTER GEOMETRY OPTIMISATION	70
4.1 Chamber Geometry	71
4.2 Injector Position	79
4.3 Antenna Length & Shape	81
4.4 Antenna Material	84
4.5 Thruster Floating Potential	86
4.6 Conclusion	88
5 EFFECTS OF MAGNETIC FIELD GRADIENT AT RESONANCE	89
5.1 Magnetic Model	90
5.2 Magnetic Field Strength Gradient at Resonance Effects	94
5.3 Mass Flow Rate Effects	101
5.4 Thruster Power Effects	104
5.5 Background Pressure Effects	107
5.6 Conclusion	111

6 EFFECTS OF ADDING A MAGNETIC MIRROR TRAP	112
6.1 Magnetic Mirror Theory	113
6.2 Magnetic Model	116
6.3 Thruster Performance	118
6.4 Conclusion	125
7 EFFECTS OF RESONANCE REGION LOCATION	126
7.1 Displacement Mechanism	127
7.2 Thruster Performance vs Location	129
7.3 Plume Measurements vs Location	131
7.4 Conclusion	135
8 DECREASING MAGNETIC FIELD GRADIENT AT RESONANCE VIA PASSIVE COMPONENTS	136
8.1 Magnetic Model	137
8.2 Resonance Region Location Effects	142
8.3 Mass Flow Rate Effects	149
8.4 Thruster Power Effects	154
8.5 Background Pressure Effects	158
8.6 Alternative Propellants (Krypton & Argon)	166
8.7 Plasma Plume Map	171
8.8 Conclusion	174
9 EFFECTS OF ADDING A SECOND MICROWAVE FREQUENCY	175
9.1 Microwave Generator Design	176
9.2 Frequency Difference Effects	179
9.3 Discussion	182
9.4 Conclusion	184
10 CONCLUSIONS	185
10.1 Decreasing Magnetic Field Strength Gradient at Resonance	186
10.2 Dual Microwave Frequencies	188
10.3 Resonance Region Location	189
10.4 Magnetic Mirror Trap	190
10.5 Future Work: Other Ideas	191
APPENDIX	193
A List of Thrusters with a Nominal Thrust between 0.1 and 10.0 mN	193
B Test Diagram for Small ECR Thruster	194
C Sputter Deposition on Backplate	195
D Antenna Erosion	196

List of Figures

1.1	A map of the solar system in the style of a subway map. With the Δv required for each manoeuvre in m/s. Artwork by U. Carion[2].	2
1.2	Simplified electrical circuit of a Resistojet thruster.	4
1.3	Simplified electrical circuit of a GIT.	4
1.4	Simplified electrical circuit of an ECR thruster.	5
1.5	Thrust and specific impulse ranges for various forms of propulsion. Reproduced from Y. Choi[6].	5
1.6	Infographic explaining the operation of an ECR magnetic nozzle thruster. As this is intended for public dissemination, the physics has been simplified.	10
1.7	Flowchart showing the theorised sequence of events that produces thrust in an ECR thruster. Note that these events occur simultaneously, not in sequence.	11
1.8	Diagram showing how electromagnetic waves are transmitted through a coaxial cable. This field pattern, where neither the electric nor the magnetic field lines are oriented in the direction of propagation, is known as the Transverse Electromagnetic Mode (TEM). The inner and outer conductors are both grey while the insulator is yellow. Reproduced from K.J. Chung[9].	11
1.9	Diagram of a waveguide fed ECR thruster with a magnetic nozzle. Reproduced from J.C. Sercel[13].	12
1.10	An early version of the permanent magnet coaxial ECR thruster. Diagram (left), photo (right). Reproduced from F. Cannat[16].	13
1.11	Specific impulse as a function of the thrust to power ratio of low power propulsion systems for small satellites, with a nominal thrust between 0.1 and 10.0 mN. Including Field-Emission Electric Propulsion (FEEP), Hall Effect Thrusters (HET), Gridded Ion Thrusters (GIT) and Electron Cyclotron Resonance (ECR) thrusters. Performance values obtained from ENPULSION GmbH.[20][21][22] and I.S. Vavilov[23] can be found in Appendix A.	15
2.1	Photo of the plume of an ECR magnetic nozzle thruster from one of the first publications about the technology in 1965. Reproduced from D.B. Miller et al.[11]. . . .	17
2.2	The high density plasma that can form around a spaceship during atmospheric reentry can reflect incoming electromagnetic waves. Reproduced from SpaceX[30]. . .	18
2.3	Diagrams showing the direction of the wave vector, \mathbf{k} , and the electric field vector, \mathbf{E} , in relation to the magnetic field, \mathbf{B} , for the Right-hand polarised wave (R-wave), Left-hand polarised wave (L-wave), Ordinary wave (O-wave) and Extraordinary wave (X-wave). Reproduced from F.F. Chen[29].	19
2.4	Expected propagation, resonance and cutoff regions of microwaves in a cold plasma. Presented as a Clemmow-Mullaly-Allis (CMA) Diagram. Reproduced from I. Funaki[32].	21
2.5	Simplified cross-sectional diagram of a coaxial ECR magnetic nozzle thruster.	23
2.6	Vector arrows for the amplitude of the R-wave \vec{E}_R , the electrons tangential velocity \vec{v}_\perp and the force on the electron due to the R-wave \vec{F}_R at four points though the electrons rotation. Wave and electron in phase. Reproduced from M.A. Lieberman[41].	24
2.7	Vector arrows for the amplitude of the L-wave \vec{E}_L , the electrons tangential velocity \vec{v}_\perp and the force on the electron due to the L-wave \vec{F}_L at four points though the electrons rotation. Reproduced from M.A. Lieberman[41].	24
2.8	The energy gain of an electron in one pass through a resonance region. Produced using my collisionless heating model of the R-wave and L-wave with an in phase electron.	25

2.9	Diagram showing how an electron spirals around magnetic field lines. Reproduced from X. Sun[47].	28
2.10	Diagram showing how an ambipolar electric field forms in the plume of an ECR thruster and acts to accelerate the ions downstream. Reproduced from D. Packan[51].	31
2.11	Magnetic field lines showing the magnetic field in a magnetic nozzle (left) and in a magnetic nozzle containing a plasma induced diamagnetic current (right). Reproduced from F.H. Ebersohn[53].	32
2.12	Detachment of the electrons from magnetic field lines (B lines), due to the electric field produced by downstream ions. Reproduced from H.G. Kosmahl et al.[50] . . .	33
2.13	Electromagnet ECR thruster prototype. Reproduced from F. Cannat[57].	34
2.14	Permanent magnet ECR thruster prototype. Reproduced from T. Vialis[15].	35
2.15	Diagram of ONERA's latest ECR thruster with 27.5 mm outer conductor diameter. Reproduced from S. Peterschmitt[36].	36
2.16	Photo and corresponding diagram of ONERA's 70 mm outer conductor diameter ECR thruster. The geometries shown here have been altered to protect the intellectual property of ONERA. All dimensions in millimetres. Reproduced from S. Peterschmitt[36].	37
2.17	ECR thruster schematic showing the two resonance regions created by the two microwave frequencies. Reproduced from B.N. Wachs[58].	38
2.18	Thrust produced by the same ECR thruster at different background pressures and vacuum chamber sizes. Reproduced from V. Dèsangles et al.[7].	39
2.19	Percentage of plume power lost to electron collisions and ion collisions from 1.3×10^{-6} mbar to 3.5×10^{-5} mbar. Reproduced from B. Wachs[26].	40
3.1	The "Daedalus" vacuum chamber within which all test campaigns were conducted.	43
3.2	Sublimation curves of the rare gases. Reproduced from A. Ferreira[63].	44
3.3	Diagram of the test configuration and equipment for the large ECR thruster.	46
3.4	Test setup for the small ECR thruster (left) and large ECR thruster (right).	46
3.5	The replacement of the thruster with a power meter and dummy load to calculate the insertion loss, IL , of the microwave line.	47
3.6	Photo of an unmodified N-type connector with burnt PTFE dielectric and melted inner conductor.	48
3.7	Photo of a correctly modified N-type connector with 1.5 mm diameter holes, indicated with red circles.	48
3.8	Torsional thrust balance calibration. A line of best fit is applied to thirteen individual measurement points. The gradient of this line defines the relationship between force and the displacement of the thrust balance.	49
3.9	A thrust step measurement on the torsional thrust balance. Displacement before the thrust step is averaged and a line of best fit is applied. Displacement after the thrust step is also averaged and a line of best fit is applied. The displacement difference between these two lines is used to calculate thrust.	50
3.10	Langmuir probe current as a function of bias voltage with respect to the grounded vacuum chamber. Raw data in red, smoothed data in blue.	51
3.11	Langmuir probe for the small ECR thruster whose results are presented in chapters 4, 5 and 6.	52
3.12	Langmuir probe for the large ECR thruster whose results are presented in chapters 4, 7, 8 and 9.	52
3.13	Photo of the equipment used to operate the Langmuir probe.	53

3.14	Langmuir probe current as blue line. Ion current as red dashed line. The ion current is a line of best fit applied to the data that lies beneath the floating potential.	55
3.15	Electron current as a function of bias voltage. The electron current is the probe current minus the ion current.	55
3.16	Electron current derivative as a function of bias voltage. Plasma potential defined by highest point, red circle.	55
3.17	Probe current as a function of bias voltage. Comparing the original ion current approximation against the new ion current approximation.	57
3.18	Faraday probe collector and coplanar guard ring.	58
3.19	Peak normalised probe current as a function of bias voltage at different probe rotation angles. Small ECR thruster, 73 W thruster power, 0.10 mg/s xenon mass flow rate, 2 A electromagnet current.	61
3.20	Faraday probe collector current as a function of rotation angle for different bias potentials. At 0° the probe is aligned with the centreline of the thruster. Small ECR thruster, 73 W thruster power, 0.10 mg/s xenon mass flow rate, 2 A electromagnet current.	62
3.21	Faraday probe collector current as a function of rotation angle for different bias potentials. At 0° the probe is aligned with the centreline of the thruster. Large ECR thruster without iron ring, 145 W thruster power, 0.39 mg/s xenon mass flow rate.	63
3.22	Photo of the Retarding Potential Analyser (RPA) with grid visible behind grounded enclosure.	64
3.23	Cross-sectional diagram showing the distance of each grid from the collector.	65
3.24	Photo of RPA grids, spacers and collector, with grounded enclosure removed.	65
3.25	Collector current as a function of the electron repelling grid potential. Potential of the ion selection grid maintained at 0 V to allow for all ions to be collected. Large ECR thruster without iron ring, 145 W thruster power, 0.39 mg/s xenon mass flow rate.	66
3.26	Collector current and normalised ion energy distribution for the large ECR thruster without iron ring. 29 W thruster power, 0.39 mg/s xenon mass flow rate.	67
3.27	Normalised ion energy distribution for the large ECR thruster without iron ring. RPA facing the thruster and RPA facing perpendicular to the thruster. 115 W thruster power, 0.39 mg/s xenon mass flow rate.	69
4.1	Comparison of the three ECR thrusters used for this geometry study.	70
4.2	AVS-UK ECR thruster. 30.0 mm chamber diameter, 16.0 mm chamber length.	71
4.3	Thrust, specific impulse and thruster efficiency as a function of the energy absorbed per unit mass of propellant. Xenon mass flow rates between 0.10 mg/s and 0.50 mg/s were used. AVS-UK ECR thruster, 30 mm chamber diameter, linear antenna.	72
4.4	Thrust, specific impulse and thruster efficiency as a function of the energy absorbed per unit mass of propellant. Xenon mass flow rates between 0.10 mg/s and 0.50 mg/s were used. AVS-UK ECR thruster, 16 mm chamber length, linear antenna.	73
4.5	Cross-sectional view of the small thruster. 22.5 mm chamber diameter, 21.0 mm chamber length, 2.5 mm antenna diameter, 23.0 mm antenna length.	74
4.6	Cross-sectional diagram of a helicon thruster with mechanically separated back wall (yellow) and lateral wall (blue). Reproduced from K. Takahashi et al.[92].	75

4.7	The three chamber geometries tested with the small ECR thruster. Conductive material in light grey, ceramic in white and permanent magnet in dark grey. Xenon propellant injected from two 1 mm diameter injectors, 6 mm downstream of the backplate.	76
4.8	Thrust, specific impulse and thruster efficiency as a function of thruster power for three different chamber geometries. Small ECR thruster, 0.25 mg/s xenon mass flow rate. Three readings taken for each test condition, standard errors from 0.001 mN to 0.007 mN.	76
4.9	Cross-sectional view of the large ECR thruster. 74.0 mm chamber diameter, 20.0 mm chamber length, 2.5 mm antenna diameter, 20.0 mm antenna length.	77
4.10	Labeled cross-sectional view of the large thruster.	77
4.11	Thrust, specific impulse and thruster efficiency as a function of thruster power for the small and large ECR thrusters. 0.08 mg/s xenon mass flow rate for the small thruster and 0.39 mg/s for the large thruster with resonance region 10 mm from backplate. Three readings taken for each test condition, standard errors from 0.002 mN to 0.015 mN.	78
4.12	Cross-sectional diagram of the small ECR thruster with both injector displacements visible. Resonance region highlighted in red (modelled using FEMM[93]).	79
4.13	Thrust as a function of thruster power with varying injector displacement. Small ECR thruster, 0.25 mg/s xenon mass flow rate. Three readings taken for each test condition, standard errors from 0.001 mN to 0.006 mN.	80
4.14	AVS-UK ECR thruster with linear antenna (left) and helical antenna (right). During operation (top), after operation (bottom).	81
4.15	Thrust, specific impulse and thruster efficiency as a function of the energy absorbed per unit mass of propellant. Xenon mass flow rates between 0.10 mg/s and 0.50 mg/s were used. AVS-UK ECR thruster, 16 mm chamber length, 30 mm chamber diameter.	82
4.16	Thrust, specific impulse and thruster efficiency as a function of thruster power for five different lengths of antenna. Small ECR thruster, 0.10 mg/s xenon mass flow rate. Three readings taken for each test condition, standard errors from 0.003 mN to 0.036 mN.	83
4.17	Microscope images of the end of a 2.5 mm \varnothing antenna. Pure graphite with machining circles visible (left), 1 μm Diamond Like Carbon (DLC) coating (right).	84
4.18	Scanning Electron Microscope (SEM) images of the tip of the antenna. Pure graphite antenna (left). 1 μm Diamond Like Carbon (DLC) coating with graphite visible beneath the layer (right).	85
4.19	Thrust as a function of thruster power for a pure graphite antenna and Diamond Like Carbon (DLC) coated antenna. Small ECR thruster, 0.10 mg/s xenon mass flow rate. Three readings taken for each test condition, standard errors from 0.001 mN to 0.018 mN.	85
4.20	Thruster floating potential and thrust as a function of thruster power with 0.08 mg/s xenon mass flow rate. Three readings taken for each test condition, standard errors from 3 V to 4 V and 0.001 mN to 0.008 mN respectively.	86
4.21	The small ECR thruster with dielectric sheet in its exit plane.	87
4.22	Thrust as a function of thruster power for the small ECR thruster both without and with a dielectric sheet in its exit plane. 0.25 mg/s xenon mass flow rate. Three readings taken for each test condition, standard errors from 0.002 mN to 0.008 mN.	87

5.1	Sixteen photos of the small ECR thruster with electromagnetic coil removed, comparing mass flow rates and thruster powers. 1/40 s, f/6.3 and ISO 100.	89
5.2	Cross-sectional view of the small ECR thruster with electromagnetic coil.	90
5.3	Magnetic field strength plot for the small ECR thruster with varying coil currents. Each solid line shows the change in magnetic field strength with respect to displacement from the back of the thruster's chamber along its central axis. The dashed line shows the magnetic field strength at which resonance occurs, 87.5 mT. Modelled using FEMM[93].	91
5.4	Five axisymmetric magnetic field models of the small ECR thruster, with varying electromagnetic coil currents. Permanent magnet indicated by grey box, electromagnet indicated by white box, dashed lines outline the chamber. Resonance region defined as the region between B_{0U} and B_{0L} and indicated in red when inside the chamber, or grey when outside the chamber. Modelled using FEMM[93].	93
5.5	Thrust and cross-sectional resonance area (normalised) as a function of the electromagnetic coil current. Small ECR thruster, 74 W thruster power, 0.10 mg/s xenon mass flow rate. Three measurements taken for each coil current, standard errors from 0.003 mN to 0.016 mN. Cross-sectional resonance area is calculated from the red regions in figure 5.4.	94
5.6	Specific impulse as a function of the electromagnetic coil current. Small ECR thruster, 74 W thruster power, 0.10 mg/s xenon mass flow rate. Three measurements taken for each coil current, standard errors from 3 s to 16 s.	95
5.7	Efficiency as a function of the electromagnetic coil current. Thruster efficiency not accounting for coil power shown by white circles, accounting for coil power shown as dark circles. Small ECR thruster, 74 W thruster power, 0.10 mg/s xenon mass flow rate. Three measurements taken for each coil current, standard errors from 0.01 % to 0.29 %.	95
5.8	Ion current density as a function of rotation angle of the Faraday probe at five different electromagnetic coil currents. Probe swept three times for each coil current, mean value at each angle is used. Small ECR thruster, 71 W thruster power, 0.10 mg/s xenon mass flow rate.	96
5.9	Ion current density as a function of rotation angle of the Faraday probe at five different electromagnetic coil currents. Probe swept three times for each coil current, mean value at each angle is used. Small ECR thruster, 69 W thruster power, 0.10 mg/s xenon mass flow rate.	97
5.10	Thrust and ion beam current as a function of electromagnetic coil current (top), normalised cross-sectional area of the resonance region (middle) and magnetic field strength gradient at resonance on the central axis (bottom). Small ECR thruster, 71 W thruster power, 0.10 mg/s xenon mass flow rate. Three thrust measurements taken for each coil current, standard errors from 0.003 mN to 0.016 mN. Cross-sectional resonance area calculated from the red regions in figure 5.4.	98
5.11	Electron temperature as a function of electromagnetic coil current (top) and cross-sectional area of the resonance region (bottom). Cross-sectional resonance area was only calculated for integer values of coil current, hence the bottom plot only contains values for coil currents of 0 A, 1 A, 2 A, 3 A and 4 A. Small ECR thruster, 69 W thruster power, 0.10 mg/s xenon mass flow rate. Three measurements taken for each coil current, standard errors from 0.17 eV to 0.37 eV.	99

5.12 Thruster floating potential and plasma potential as a function of electromagnetic coil current. Small ECR thruster, 69 W thruster power, 0.10 mg/s xenon mass flow rate. Three measurements taken for each test condition, standard errors from 0.33 V to 1.45 V and 0.60 V to 1.21 V respectively.	100
5.13 Thrust, specific impulse and thruster efficiency as a function of xenon mass flow rate. Small ECR thruster, 78 W thruster power, 3 A coil current. Three readings taken for each mass flow rate, standard errors from 0.004 mN to 0.016 mN. Thruster efficiency does not account for electromagnetic coil power.	101
5.14 Ion current density as a function of rotation angle of the Faraday probe at three different mass flow rates. Probe swept three times for each mass flow rate, mean value at each angle is used. Small ECR thruster, 78 W thruster power, 3 A coil current.	102
5.15 Ion beam current as a function of mass flow rate. Small ECR thruster, 78 W thruster power, 3 A coil current.	102
5.16 Electron temperature, thruster floating potential and plasma potential as a function of xenon mass flow rate. Small ECR thruster, 78 W thruster power, 3 A coil current. Three readings taken for each mass flow rate, standard errors from 0.20 eV to 0.44 eV, 0.33 V to 1.53 V and 0.44 V to 1.15 V respectively.	103
5.17 Thrust, specific impulse and thruster efficiency as a function of thruster power. Small ECR thruster, 0.10 mg/s xenon mass flow rate, 3 A coil current. Three readings taken for each power level, standard errors from 0.015 mN to 0.017 mN. Thruster efficiency does not account for electromagnetic coil power.	104
5.18 Ion current density as a function of rotation angle of the probe at three different thruster powers. Probe swept three times for each power, mean value at each angle is used. Small ECR thruster, 0.10 mg/s xenon mass flow rate, 3 A coil current.	105
5.19 Ion beam current as a function of thruster power. Small ECR thruster, 0.10 mg/s xenon mass flow rate, 3 A coil current.	105
5.20 Electron temperature, thruster floating potential and plasma potential as a function of thruster power. Small ECR thruster, 0.10 mg/s xenon mass flow rate, 3 A coil current. Three readings taken for each power level, standard errors from 0.07 eV to 0.30 eV, 0.33 V to 0.58 V and 1.10 V to 1.51 V respectively.	106
5.21 Thrust as a function of background pressure. Small ECR thruster, 68 W thruster power, 0.10 mg/s xenon mass flow rate, 3 A coil current. Three readings taken for each background pressure, standard errors from 0.002 mN to 0.011 mN.	107
5.22 Ion current density as a function of rotation angle, showing the ion beam profile of the thruster at different background pressures. Small ECR thruster, 70 W thruster power, 0.10 mg/s xenon mass flow rate, 3 A coil current. 0° is when the probe is aligned with the central axis of the thruster. Probe swept three times for each background pressure, mean value at each angle is used.	108
5.23 Ion beam current and divergence efficiency as a function of background pressure. Small ECR thruster, 70 W thruster power, 0.10 mg/s xenon mass flow rate, 3 A coil current.	109
5.24 Electron temperature, thruster floating potential and plasma potential as a function of background pressure. Small ECR thruster, 68 W thruster power, 0.10 mg/s xenon mass flow rate. Three readings taken for each background pressure, standard errors from 0.15 eV to 0.49 eV, 0.33 V to 1.00 V and 0.24 V to 0.39 V respectively.	110

5.25	Flowchart showing the theorised sequence of events and the variables that are increased/decreased as a result. The method with which each variable was measured is shown in green.	111
6.1	Magnetic mirror reflection of an electron beam. The guiding centre of the reflected beam does not follow that of the incident beam due to grad-B drift and curvature drift in a non uniform field. Reproduced from R. Stenzel[103].	112
6.2	An electron that travels into a region with a stronger magnetic field will have its velocity parallel to magnetic field lines reduced. If the magnetic field is strong enough, this velocity will then reverse. Reproduced from P.P. Uroine[104].	113
6.3	Grad-B drift of an electron in a magnetic field where the magnetic field strength gradient is orthogonal to magnetic field lines. Reproduced from A. Peeters[105].	114
6.4	Curvature of a magnetic field. Reproduced from F.F. Chen[29].	115
6.5	Axisymmetric magnetic field model of the smaller ECR thruster with one permanent magnet (left) and two permanent magnets (right). Magnetic field strength shown with colours, chamber outlined with black dashed line, ring magnets shown as grey boxes with arrows showing their direction of magnetisation, resonance region shown in yellow. Modelled using FEMM[93].	116
6.6	Magnetic field strength as a function of displacement from the back of the small ECR thruster's chamber along the thruster's central axis, for the thruster with a single magnet and two magnets. Dashed line shows the magnetic field strength at resonance. Modelled using FEMM[93].	117
6.7	Thrust as a function of electromagnetic coil current in steps of 1.0 A (left) and 0.5 A (right). 74 W thruster power for the 1 magnet configuration, 124 W thruster power for the 2 magnet configuration. Small ECR thruster, 0.10 mg/s xenon mass flow rate. Three readings taken for each test condition, standard errors from 0.002 mN to 0.045 mN.	118
6.8	Axisymmetric magnetic field models of the small ECR thruster, with one ring magnet (left) and two ring magnets (right). Resonance region shown in red, chamber outlined with black dashed line, permanent ring magnets shown as grey boxes with arrows showing their direction of magnetisation, electromagnet shown as white boxes. Modelled using FEMM[93].	119
6.9	Axisymmetric magnetic field model of the smaller ECR thruster with one permanent magnet (left) and two permanent magnets (right). Magnetic field strength shown with colours, chamber outlined with black dashed line, permanent ring magnets shown as grey boxes with arrows showing their direction of magnetisation, electromagnet shown in white. Modelled using FEMM[93].	120
6.10	Ion current density as a function of rotation angle of the Faraday probe. Probe swept three times for each thruster configuration, mean value at each angle is used. Small ECR thruster, 73 W thruster power, 0.10 mg/s xenon mass flow rate, 3 A coil current.	120
6.11	Thrust and specific impulse as a function of thruster power. Small ECR thruster, 0.10 mg/s xenon mass flow rate, 3 A coil current. Three readings taken for each test condition, standard errors from 0.007 mN to 0.015 mN.	121
6.12	Thruster efficiency (not accounting for electromagnetic coil power) as a function of thruster power. Small ECR thruster, 0.10 mg/s xenon mass flow rate, 3 A coil current. Three readings taken for each test condition, standard errors from 0.06 % to 0.35 %.	122

6.13	Electron temperature as a function of thruster power. Small ECR thruster, 0.10 mg/s xenon mass flow rate, 3 A coil current. Three readings taken for each test condition, standard errors from 0.15 eV to 0.69 eV.	122
6.14	Thrust, specific impulse and thruster efficiency as a function of mass flow rate. 77 W thruster power for the 1 magnet configuration, 120 W thruster power for the 2 magnet configuration. Small ECR thruster, 3 A coil current. Three readings taken for each test condition, standard errors from 0.005 mN to 0.036 mN. Thruster efficiency does not account for electromagnetic coil power.	123
6.15	Electron temperature (top) and density (bottom) as a function of xenon mass flow rate. 77 W thruster power for the 1 magnet configuration, 120 W thruster power for the 2 magnet configuration. Small ECR thruster, 3 A coil current. Three readings taken for each test condition, standard errors from 0.12 eV to 0.36 eV and 3.7×10^{14} m ⁻³ to 3.9×10^{15} m ⁻³ respectively.	124
7.1	By varying the position of the thruster's chamber relative to the ring magnet, the position of the resonance region within the chamber can be varied. Resonance region shown in red (modelled using FEMM[93]).	126
7.2	Cross-sectional view of the large ECR thruster on top of a motorised linear rail (left), fixed ring magnet assembly shown in faded white. Photo of the large ECR thruster installed on the thrust balance (right).	127
7.3	Magnetic field plot of the large ECR thruster, showing how the back of the thrust chamber is displaced from the resonance region. Resonance region shown in red when residing within the thrust chamber, and grey when residing outside of the thrust chamber. Modelled using FEMM[93].	128
7.4	Thruster power and reverse microwave power measured at the generator as a function of the displacement of the resonance region from the backplate. Large ECR thruster, 240 W forward microwave power at the generator, 0.39 mg/s xenon mass flow rate. Three readings taken for each test condition, standard errors from 0.23 W to 1.61 W and 0.30 W to 1.00 W respectively.	129
7.5	Thrust, specific impulse and thruster efficiency as a function of the displacement of the resonance region from the backplate. Thruster powers can be found from figure 7.4. Large ECR thruster, 0.39 mg/s xenon mass flow rate. Three readings taken for each test condition, standard errors from 0.002 mN to 0.029 mN.	130
7.6	Ion current density as a function of rotation angle of the probe at nine different resonance region displacements. Probe swept three times for each displacement, mean value at each angle is used. Thruster powers can be found from figure 7.4. Large ECR thruster, 0.39 mg/s xenon mass flow rate.	131
7.7	Ion beam current as a function of displacement of the resonance region from the backplate. Thruster powers can be found from figure 7.4. Large ECR thruster, 0.39 mg/s xenon mass flow rate.	132
7.8	Electron temperature as a function of displacement of the resonance region from the backplate. Thruster powers can be found from figure 7.4. Large ECR thruster, 0.39 mg/s xenon mass flow rate. Three readings taken for each displacement, standard errors from 0.2 eV to 1.6 eV.	132
7.9	Thruster floating potential and plasma potential as a function of displacement of the resonance region from the backplate. Thruster powers can be found from figure 7.4. Large ECR thruster, 0.39 mg/s xenon mass flow rate. Three readings taken for each displacement, standard errors from 0.4 V to 0.6 V and 0.2 V to 1.5 V respectively.	133

7.10	Normalised ion energy distribution at different resonance region displacements from the backplate. Thruster powers can be found from figure 7.4. Large ECR thruster, 0.39 mg/s xenon mass flow rate.	134
7.11	Most probable ion energy as a function of the displacement of the resonance region from the backplate. Most probable ion energy is approximated using the technique outlined in section 3.6. Thruster powers can be found from figure 7.4. Large ECR thruster, 0.39 mg/s xenon mass flow rate.	134
8.1	By adding a ferromagnetic ring, the magnetic field strength gradient at resonance can be decreased, increasing the thickness of the resonance region and the energy absorbed by electrons passing through. Large ECR thruster, resonance region shown in red (modelled using FEMM[93]).	136
8.2	Magnetic field strength plot for the large ECR thruster without iron ring (thin resonance region) and with iron ring (thick resonance region). Solid lines show the change in magnetic field strength with respect to displacement from the backplate along the central axis. Dashed line shows the magnetic field strength at which resonance occurs, 87.5 mT. Data obtained from the same model shown in figure 8.3. Modelled using FEMM[93].	137
8.3	Axisymmetric magnetic field model of the large ECR thruster without the iron ring (thin resonance region) and the thruster with the ion ring (thick resonance region). The portion of the resonance region that resides inside the thrust chamber is shown in red. Resonance region that resides outside the thrust chamber shown in grey. Modelled using FEMM[93].	138
8.4	Key dimensions of the axisymmetric magnetic circuitry and thrust chamber for the large ECR thruster with the iron ring. The portion of the resonance region that resides inside the thrust chamber is shown in red. Resonance region that resides outside the thrust chamber shown in grey. Modelled using FEMM[93].	139
8.5	Magnetic field divergence angle as a function of angular location, at a radius of: a) 80 mm from the ring magnet; b) 300 mm from the ring magnet. Modelled using FEMM[93].	140
8.6	Diagram of the large ECR thruster, to show where measurements were taken for the plots in figure 8.5. The magnetic field lines that pass through the resonance region at a radius of 7 mm are shown in red. Modelled using FEMM[93].	141
8.7	Thruster power and reverse microwave power measured at the generator as a function of the displacement of the resonance region from the backplate for the large ECR thruster with iron ring. 240 W forward microwave power at the generator, 0.39 mg/s xenon mass flow rate. Three measurements taken for each displacement, standard errors from 0.23 W to 2.48 W and 0.14 W to 1.51 W respectively.	142
8.8	Thrust, specific impulse and thruster efficiency as a function of the displacement of the resonance region from the backplate both without and with the iron ring. Thruster powers can be found from figures 7.4 and 8.7 respectively. Large ECR thruster, 0.39 mg/s xenon mass flow rate. Three measurements taken for each test condition, standard errors from 0.006 mN to 0.024 mN.	143
8.9	Ion current density as a function of rotation angle of the probe at five different resonance region displacements from the backplate for the large ECR thruster both without and with the iron ring. Thruster powers can be found from figures 7.4 and 8.7 respectively, 0.39 mg/s xenon mass flow rate.	144

8.10 Ion beam current as a function of displacement of the resonance region from the backplate for the large ECR thruster both without and with the iron ring. Thruster powers can be found from figures 7.4 and 8.7 respectively, 0.39 mg/s xenon mass flow rate.	145
8.11 Electron temperature as a function of displacement of the resonance region from the backplate for the large ECR thruster both without and with the iron ring. Thruster powers can be found from figures 7.4 and 8.7 respectively, 0.39 mg/s xenon mass flow rate. Three readings taken for each test condition, standard errors from 0.1 eV to 1.6 eV.	146
8.12 Plasma potential as a function of displacement of the resonance region from the backplate for the large ECR thruster both without and with the iron ring. Thruster powers can be found from figures 7.4 and 8.7 respectively, 0.39 mg/s xenon mass flow rate. Three readings taken for each test condition, standard errors from 0.2 V to 1.3 V.	147
8.13 Thruster floating potential as a function of displacement of the resonance region from the backplate for the large ECR thruster both without and with the iron ring. Thruster powers can be found from figures 7.4 and 8.7 respectively, 0.39 mg/s xenon mass flow rate. Three readings taken for each test condition, standard errors from 0.4 V to 0.6 V.	147
8.14 Normalised ion energy distribution for the large ECR thruster both without and with the iron ring. 10 mm displacement of the resonance region from the backplate, 144 W thruster power, 0.39 mg/s xenon mass flow rate.	148
8.15 Thrust as a function of mass flow rate for the large ECR thruster both without and with the iron ring. 145 W thruster power. Three readings taken for each test condition, standard errors from 0.004 mN to 0.019 mN.	149
8.16 Specific impulse and thruster efficiency as a function of mass flow rate for the large ECR thruster both without and with the iron ring. 145 W thruster power. Three readings taken for each test condition, standard errors from 1 s to 3 s and 0.01 % to 0.05 % respectively.	150
8.17 Thruster floating potential as a function of mass flow rate for the large ECR thruster both without and with the iron ring. 145 W thruster power. Three readings taken for each test condition, standard errors from 0.33 V to 1.53 V.	151
8.18 Ion current density as a function of rotation angle of the probe at five different xenon mass flow rates, for the large ECR thruster both without and with the iron ring. 143 W thruster power.	152
8.19 Normalised ion energy distribution for the large ECR thruster without the iron ring, at varying xenon mass flow rates. 146 W thruster power.	153
8.20 Normalised ion energy distribution for the large ECR thruster with the iron ring, at varying xenon mass flow rates. 144 W thruster power.	153
8.21 Thrust and specific impulse as a function of thruster power for the large ECR thruster both without and with the iron ring. 0.39 mg/s xenon mass flow rate. Three readings taken for each test condition, standard errors from 0.002 mN to 0.015 mN.	154
8.22 Thruster efficiency as a function of thruster power for the large ECR thruster both without and with the iron ring. 0.39 mg/s xenon mass flow rate. Three readings taken for each test condition, standard errors from 0.01 % to 0.07 %.	155

8.23 Thruster floating potential as a function of thruster power for the large ECR thruster both without and with the iron ring. 0.39 mg/s xenon mass flow rate. Three readings taken for each test condition, standard errors from 0.33 V to 0.67 V	155
8.24 Ion current density as a function of rotation angle of the probe at five different thruster powers, for the large ECR thruster both without and with the iron ring. 0.39 mg/s xenon mass flow rate.	156
8.25 The effect of thruster power on the Electron Energy Distribution Function (EEDF) for the large ECR thruster both with and without the iron ring. Langmuir probe 150 mm downstream, along the thruster's central axis. 0.39 mg/s xenon mass flow rate.	157
8.26 Thrust and specific impulse as a function of background pressure for the large ECR thruster both without and with the iron ring. 145 W thruster power, 0.39 mg/s xenon mass flow rate. Three readings taken for each test condition, standard errors from 0.011 mN to 0.044 mN.	158
8.27 Thruster efficiency as a function of background pressure for the large ECR thruster both without and with the iron ring. 145 W thruster power, 0.39 mg/s xenon mass flow rate. Three readings taken for each test condition, standard errors from 0.04 % to 0.10 %.	159
8.28 Ion current density as a function of rotation angle of the probe at five different background pressures, for the large ECR thruster both without and with the iron ring. 145 W thruster power, 0.39 mg/s xenon mass flow rate.	160
8.29 Ion beam current as a function of background pressure, for the large ECR thruster both without and with the iron ring. 145 W thruster power, 0.39 mg/s xenon mass flow rate.	160
8.30 Far field beam divergence angle as a function of background pressure, for the large ECR thruster both without and with the iron ring. 145 W thruster power, 0.39 mg/s xenon mass flow rate.	161
8.31 Electron temperature as a function of background pressure for the large ECR thruster without the iron ring. 145 W thruster power, 0.39 mg/s xenon mass flow rate. Three readings taken for each test condition, standard errors from 0.07 eV to 0.51 eV.	161
8.32 Plasma potential as a function of background pressure for the large ECR thruster without the iron ring. 145 W thruster power, 0.39 mg/s xenon mass flow rate. Three readings taken for each test condition, standard errors from 0.71 V to 0.88 V	162
8.33 Thruster floating potential as a function of background pressure for the large ECR thruster both without and with the iron ring. 145 W thruster power, 0.39 mg/s xenon mass flow rate. Three readings taken for each test condition, standard errors from 0.33 V to 2.33 V	162
8.34 Normalised ion energy distribution for the large ECR thruster without the iron ring, at varying background pressures. 144 W thruster power, 0.39 mg/s xenon mass flow rate.	163
8.35 Normalised ion energy distribution for the large ECR thruster with iron ring, at varying background pressures. 144 W thruster power, 0.39 mg/s xenon mass flow rate.	164
8.36 Plasma potential at the RPA as a function of background pressure. Approximated using the technique outlined in section 3.6. Large ECR thruster both without and with the iron ring, 144 W thruster power, 0.39 mg/s xenon mass flow rate.	164

8.37	Flowchart showing the theorised sequence of events and the variables that are increased/decreased as a result. The method with which each variable was measured is shown in green.	165
8.38	Thrust, specific impulse and thruster efficiency as a function of mass flow rate for the large ECR thruster both without and with the iron ring operating with xenon, krypton and argon. 144 W thruster power. Three readings taken for each test condition, standard errors from 0.004 mN to 0.046 mN.	167
8.39	Thruster floating potential as a function of mass flow rate for the large ECR thruster both without and with the iron ring for xenon and krypton. 144 W thruster power. Three readings taken for each test condition, standard errors from 0.33 V to 1.00 V.	168
8.40	Ion current density as a function of rotation angle of the probe for the large ECR thruster both without and with the iron ring using xenon and krypton propellant. 144 W thruster power, 0.44 mg/s propellant mass flow rate.	169
8.41	Normalised ion energy distribution for the large ECR thruster with the iron ring, using both xenon and krypton propellants. 144 W thruster power, 0.44 mg/s xenon mass flow rate.	170
8.42	Points at which Langmuir probe measurements were taken to create the maps of plasma potential and electric field strength in figures 8.43 and 8.44. Radial displacement relative to the large ECR thruster's central axis, axial displacement relative to the thrust chamber's exit.	171
8.43	Plasma potential map for the large ECR thruster both without and with the iron ring. Radial displacement relative to the thruster's central axis, axial displacement relative to the thrust chambers exit. 90 W thruster power, 0.39 mg/s xenon mass flow rate.	172
8.44	Electric field strength map for the large ECR thruster both without and with the iron ring. Radial displacement relative to the thruster's central axis, axial displacement relative to the thrust chambers exit. 90 W thruster power, 0.39 mg/s xenon mass flow rate.	173
8.45	Flowchart showing the theorised sequence of events and the variables that are increased/decreased as a result. The method with which each variable was measured is shown in green. It is thought that decreasing the magnetic field strength gradient at resonance also results in increased electron temperatures in the resonance region and higher ion energies, however these were unable to be measured with the current experimental setup.	174
9.1	Photo of the large ECR thruster operating at 129 W thruster power and 0.39 mg/s xenon mass flow rate. There was no visual difference observed when switching between using single and dual microwave frequencies.	175
9.2	Diagram showing the individual components of the new Software Defined Radio (SDR) driven microwave generator in black boxes.	176
9.3	Diagram of the experimental setup for the tests in chapter 9.	177
9.4	Thrust as a function of thruster power for the large ECR thruster without the iron ring. Comparing the older generator against the newer generator. 0.39 mg/s xenon mass flow rate. Three readings taken for each test condition, standard errors from 0.002 mN to 0.046 mN.	178

9.5	Thruster power as a function of the frequency difference of the two microwave signals at three power levels. Large ECR thruster, 0.39 mg/s xenon mass flow rate, $f_1 = 2.435$ GHz. Three readings taken for each test condition, standard errors from 0.07 W to 0.48 W.	178
9.6	Thruster floating potential as a function of the frequency difference of the two microwave signals at three different thruster powers. Large ECR thruster without the iron ring, 0.39 mg/s xenon mass flow rate, $f_1 = 2.435$ GHz.	179
9.7	Thrust and thruster floating potential as a function of the frequency difference of the two microwave signals for the large ECR thruster without the iron ring. 64 W thruster power, 0.39 mg/s xenon mass flow rate, $f_1 = 2.435$ GHz. Three thrust readings taken at each frequency difference, standard errors from 0.002 mN to 0.018 mN.	180
9.8	Thrust and thruster floating potential as a function of the frequency difference of the two microwave signals for the large ECR thruster without the iron ring at thruster powers of 129 W, 64 W and 32 W. 0.39 mg/s xenon mass flow rate, $f_1 = 2.435$ GHz. Three thrust readings taken for each test condition, standard errors from 0.002 mN to 0.061 mN.	181
9.9	Power spectral density plot of the floating potential of a Langmuir probe in the plume of the smaller ONERA ECR thruster. Varying xenon mass flow rate at 30 W thruster power (left). Varying thruster power at 0.14 mg/s xenon mass flow rate (right). Arbitrary units used for the y-axis. Reproduced from D. Maddaloni et al.[116].	182
9.10	The harmonics and intermodulation products of the two microwave signals. Reproduced from [119].	183
10.1	Photo of the large ECR thruster operating at 145 W thruster power and 0.39 mg/s xenon mass flow rate.	185
10.2	Flowchart showing the theorised sequence of events that relates a decrease in magnetic field strength gradient at resonance to an increase in thruster performance.	186
10.3	Photos of the large ECR thruster with the resonance region at the front of the thruster's chamber (left), middle (middle) and rear (right). The resonance region can be seen as a faint band of light on the inner wall of the thruster's chamber.	189
10.4	Three different levels of magnetic thickening of the resonance region. With the resonance region stretched at: a) a single point, b) two points and c) three points. Modelled using FEMM[93].	191
10.5	Erosion marks on the rear of the thruster are evidence that a fraction of the plasma does not separate from magnetic field lines and impinges on the rear of the thruster.	192
B.1	Diagram of the test configuration and equipment for the small ECR thruster.	194
C.1	Photo of the large ECR thruster after testing, showing dark patches on the dielectric backplate between the injector holes. These were found to be conductive and so are thought to be carbon deposited via sputter erosion of thruster's graphite chamber wall.	195
D.1	Photo of the eroded antenna that was used with the large ECR thruster (left) and a new antenna (right). The eroded antenna's diameter at its tip reduced from 2.5 mm to 2.3 mm over the course of the test campaign.	196

List of Tables

1.1	Performance values for ONERA's small and large ECR thrusters.[7]	14
2.1	The cutoff and resonant frequencies for the four types of electromagnetic waves that can occur in a plasma.	21
2.2	The performance improvement of the coaxial ECR thruster due to its development at ONERA from 2015[16] to 2020[36].	37
3.1	Gas correction factors for a nitrogen calibrated pressure gauge.[65][66][67][68] . . .	45
3.2	Corrected background pressures at given mass flow rates for xenon, krypton and argon. Six readings were taken for each flow rate with standard errors from 2×10^{-8} mbar to 3×10^{-7} mbar. Vacuum pump maintenance between test campaigns resulted in faster pumping speeds for the large ECR thruster. The base background pressure was 4.8×10^{-6} mbar for all tests.	45
3.3	Dimensions and position of the Langmuir probe's electrode for the small ECR thruster whose results are presented in chapters 4, 5 and 6, and large ECR thruster whose results are presented in chapters 4, 7, 8 and 9.	52
3.4	The values of the probe radius to Debye length ratio that define the sheath. Different data processing methods are required for each of the three different sheaths.	56
3.5	Faraday probe dimensions.	59
3.6	Ion current fraction for an ECR thruster[76] and SEE yield of molybdenum[75]. . .	60
4.1	Maximum Secondary Electron Emission (SEE) yields for a range of antenna materials[98][99]. Note that SEE yield is dependent on the energy of the impinging electron, which is not constant for the values here.	84
4.2	Key dimensions of the final configurations of the two thrusters that are used for all following tests in this thesis, as well as their maximum performance values. Compared against the two thrusters that have been developed at ONERA[36]. * Performance values for the ONERA thrusters are those taken in the smaller B61 vacuum chamber to enable a more representative comparison[7].	88
5.1	Values that define the resonance region along the central axis of the small ECR thruster for each electromagnetic coil current.	91
6.1	The respective microwave powers of the two thruster configurations at 3 A of electromagnetic coil current. Power to the electromagnet is not included.	119
7.1	Mean measurements for the near, middle and far resonance region locations.	135
8.1	Values that define the resonance region along the central axis of the large ECR thruster without the iron ring (thin resonance region) and with the iron ring (thick resonance region).	138
8.2	Atomic mass, first ionisation energy and first ionisation cross section[112] (assuming electron temperatures of 20 eV) for xenon, krypton and argon.	166
A.1	List of thrusters with a nominal thrust between 0.1 and 10.0 mN. Including Field-Emission Electric Propulsion (FEEP), Hall Effect Thrusters (HET), Gridded Ion Thrusters (GIT) and Electron Cyclotron Resonance (ECR) thrusters. Performance values obtained from ENPULSION GmbH.[20][21][22] and I.S. Vavilov[23].	193

Abbreviations

CFDL	Current-Free Double Layer	PTFE	Polytetrafluoroethylene
DLC	Diamond Like Carbon	R-wave	Right-hand polarised wave
ECR	Electron Cyclotron Resonance	RF	Radio Frequency
EEDF	Electron Energy Distribution Function	RPA	Retarding Potential Analyser
FEEP	Field-Emission Electric Propulsion	SDR	Software Defined Radio
FEMM	Finite Element Method Magnetics	SEE	Secondary Electron Emission
GIT	Gridded Ion Thruster	SEM	Scanning Electron Microscope
HET	Hall Effect Thruster	TEM	Transverse Electromagnetic Mode
L-wave	Left-hand polarised wave	UHR	Upper Hybrid Resonance
O-wave	Ordinary wave	VSWR	Voltage Standing Wave Ratio
ONERA	Office National d'Etudes et de Recherches Aérospatiales	X-wave	Extraordinary wave

Constants

c	speed of light	$299\ 792\ 458\ \text{ms}^{-1}$	m_e	electron mass	$9.1094 \times 10^{-31}\ \text{kg}$
e	elementary charge	$1.6022 \times 10^{-19}\ \text{C}$	N_A	Avogadro's constant	$6.0221 \times 10^{23}\ \text{mol}^{-1}$
g_0	standard gravity	$9.8067\ \text{ms}^{-2}$	ϵ_0	permittivity of free space	$8.8542 \times 10^{-12}\ \text{Fm}^{-1}$
k_B	Boltzmann's constant	$1.3807 \times 10^{-23}\ \text{JK}^{-1}$	μ_0	permeability of free space	$1.2566 \times 10^{-6}\ \text{NA}^{-2}$

Nomenclature

B	magnetic field [T]	η_b	beam divergence efficiency
E	electric field [V/m]	η_e	electrical efficiency
F	Lorentz force [N]	η_m	mass utilisation efficiency
v	electron velocity [m/s]	η_t	thruster efficiency
ΔB_D	width of Doppler broadening in magnetic field strength [T]	$\frac{\partial B}{\partial x}$	magnetic field strength gradient [T/m]
ΔB_{ecr}	range of magnetic field strengths over which ECR occurs [T]	γ_e	polytropic coefficient
Δf_D	width of Doppler broadening in frequency [Hz]	γ_k	SEE yield from the k^{th} ion species
Δv	change in velocity [m/s]	κ_G	correction for ions collected in the gap between collector and guard ring [m^2]
Δx_D	resonance region thickness due to Doppler broadening [m]	κ_g	gas correction factor
Δx_{ecr}	resonance region thickness [m]	κ_{SEE}	correction factor for secondary electron emission at the collector surface
\dot{m}_i	ion mass flow rate [kg/s]	λ_D	Debye length [m]
\dot{m}_p	propellant mass flow rate [kg/s]	$(\frac{\partial B}{\partial x})_{\parallel}$	gradient of the magnetic field parallel to magnetic field lines [T/m]
\dot{v}_{\parallel}	acceleration parallel to magnetic field lines [m/s ²]	v_R	curvature drift velocity [m/s]
η_{α}	multiply charged species efficiency	v_{VB}	grad-B drift velocity [m/s]
		\mathcal{E}	electron energy [eV]

μ_e	electron magnetic moment [J/T]	I_{FP}	Faraday probe current at location (θ_{fp}, r_{fp}) [A]
Ω_k	ion current fraction of the k^{th} species	I_{sp}	specific impulse [s]
ϕ_a	ion acceleration voltage [V]	IL	insertion loss
ϕ_B	bias voltage [V]	j	ion current density [A/m^2]
ϕ_b	ion beam potential [J]	k	wave vector [m^{-1}]
ϕ_{max}	maximum potential drop in plume [V]	m_i	ion mass [kg]
ϕ_p	plasma potential [V]	m_{dry}	spacecraft dry mass [kg]
θ_b	half-angle divergence of the beam [rad]	m_{fuel}	spacecraft fuel mass [kg]
θ_{fp}	Faraday probe angle of rotation [rad]	n_e	electron density [m^{-3}]
A_c	cross-sectional area of the collector face [m^2]	n_i	ion density [m^{-3}]
A_{lp}	Langmuir probe collection area [m^2]	P_b	beam power [W]
B	magnetic field strength [T]	p_c	corrected pressure [Pa]
B_0	magnetic field strength at resonance [T]	p_i	indicated pressure [Pa]
B_{0L}	lower bound of the resonance region [T]	p_{base}	base pressure [Pa]
B_{0U}	upper bound of the resonance region [T]	P_{fwd}	forward power [W]
B_{max}	maximum magnetic field strength [T]	P_{jet}	kinetic thrust power of the beam [W]
B_{min}	minimum magnetic field strength [T]	P_{rev}	reverse power [W]
E	electric field amplitude [V/m]	$P_{thruster}$	thruster power [W]
E_i	ion energy [J]	P_T	total electrical power into the thruster [W]
E_L	L-wave amplitude [V/m]	q	ion charge [C]
E_R	R-wave amplitude [V/m]	r_c	collector radius [m]
E_{ecr}	energy gain of an electron in one pass through a resonance region [J]	r_L	Larmor radius [m]
$E_{i,max}$	maximum ion energy [J]	r_{Bc}	magnetic field radius of curvature [m]
F_L	force on an electron due to the L-wave [N]	r_{fp}	Faraday probe radius of rotation [m]
f_m	microwave frequency [Hz]	r_{gr}	guard ring inner radius [m]
F_R	force on an electron due to the R-wave [N]	r_{lp}	Langmuir probe electrode radius [m]
$f_{c,e}$	electron cyclotron frequency [Hz]	S_{ecr}	absorbed power per unit area of the resonance region [W/m^2]
$f_{p,e}$	electron plasma frequency [Hz]	T	thrust [N]
f_{UH}	upper hybrid resonant frequency [Hz]	T_{e0}	electron temperature at thruster exit [eV]
h_c	collector height [m]	T_e	electron temperature [eV]
h_{gr}	guard ring height [m]	v_{\parallel}	velocity parallel to magnetic field lines [m/s]
I^+	singly charged ion current [A]	v_{\perp}	velocity perpendicular to magnetic field lines [m/s]
I^{++}	doubly charged ion current [A]	v_{ex}	exhaust velocity [m/s]
I_e	electron current [A]	v_i	ion velocity [m/s]
I_i	ion current [A]	v_{th}	electron thermal velocity [m/s]
I_{axial}	axial ion beam current [A]	Z_k	ion charge state
I_{beam}	ion beam current [A]		
$I_{e,sat}$	electron saturation current [A]		

1 INTRODUCTION

“Why concentrate on space when there are so many problems down here on earth?”

Anyone working in space research will be familiar with this question and likely have a well-crafted response at the ready. However, this seemingly simple question is deceptively complex, often leading to answers that raise more questions and leave both parties unsatisfied. A typical answer may include how the Global Positioning System (GPS) and imaging satellites save a vast number of lives each year in disaster response, and how climate satellites are essential in telling us where and how to combat climate change. It might highlight that in 2023 NASA’s budget was just 3.1% that of the budget for America’s Department of Defence[1], or how microgravity is enabling the development of 3D-printed organs for transplant, and is accelerating the search for a cure for cancer. These facts and figures, powerful as they are, rarely satisfy the person asking the question. This is because the question is rarely formed from facts and figures, but rather from the perception of the space industry as a whole.

Space tourism for billionaires and videos of rockets billowing greenhouse gases foster feelings of dread and despair, yet those working in space could not be more optimistic and upbeat. Why is this? Their optimism rarely originates from the facts and figures above. Instead, it is something more innate, something embedded deep within our DNA. The human desire to explore the unknown. This desire drove Galileo and Newton to revolutionise our understanding of the natural world, it drove Marco Polo and Ibn Battuta to broaden our horizons, and Marie Curie and Rosalind Franklin to push the boundaries of science. To abandon exploration now would be a disservice to all those who have come before us. The greatest benefits of exploring the unknown are just that, unknown. It is only in retrospect that we see how important exploration is, and how beneficial it is to every single person on our planet.

1.1 Spacecraft Propulsion

Propulsion systems are essential in enabling our access to space. They allow for rockets to escape earth’s pull, making it possible to put spacecraft into orbit or launch them further into the solar system. Once in space, propulsion systems are essential in allowing spacecraft to get to where they want to go. Propulsion keeps the International Space Station from falling into our atmosphere, it helps point the Hubble and James Webb space telescopes, and it allows spacecraft to avoid crashing into each other.

Similar to a car, the destinations that you can reach in a spacecraft are limited by the amount of fuel that you have, as well as the total mass of the vehicle. On earth our car tells us how far it can travel in kilometres or miles, and if our destination is closer than the cars range, we know we can reach it. Conversely, due to the lack of air resistance in space, it is possible for a spacecraft in motion to stay in motion indefinitely. This gives many spacecraft an effectively infinite range, making distance a useless metric in determining which destinations you can reach in space. Instead we find that to get to a destination, a specific change in velocity, Δv , is required. This number is not influenced by the size or mass of a spacecraft, only on the route that is taken to get from origin to destination. This is illustrated in the style of a subway map by U. Carion[2] in figure 1.1.

The Solar System

A subway map

Artwork by Ulysse Carion.
Original calculations by /u/CuriousMetaphor.

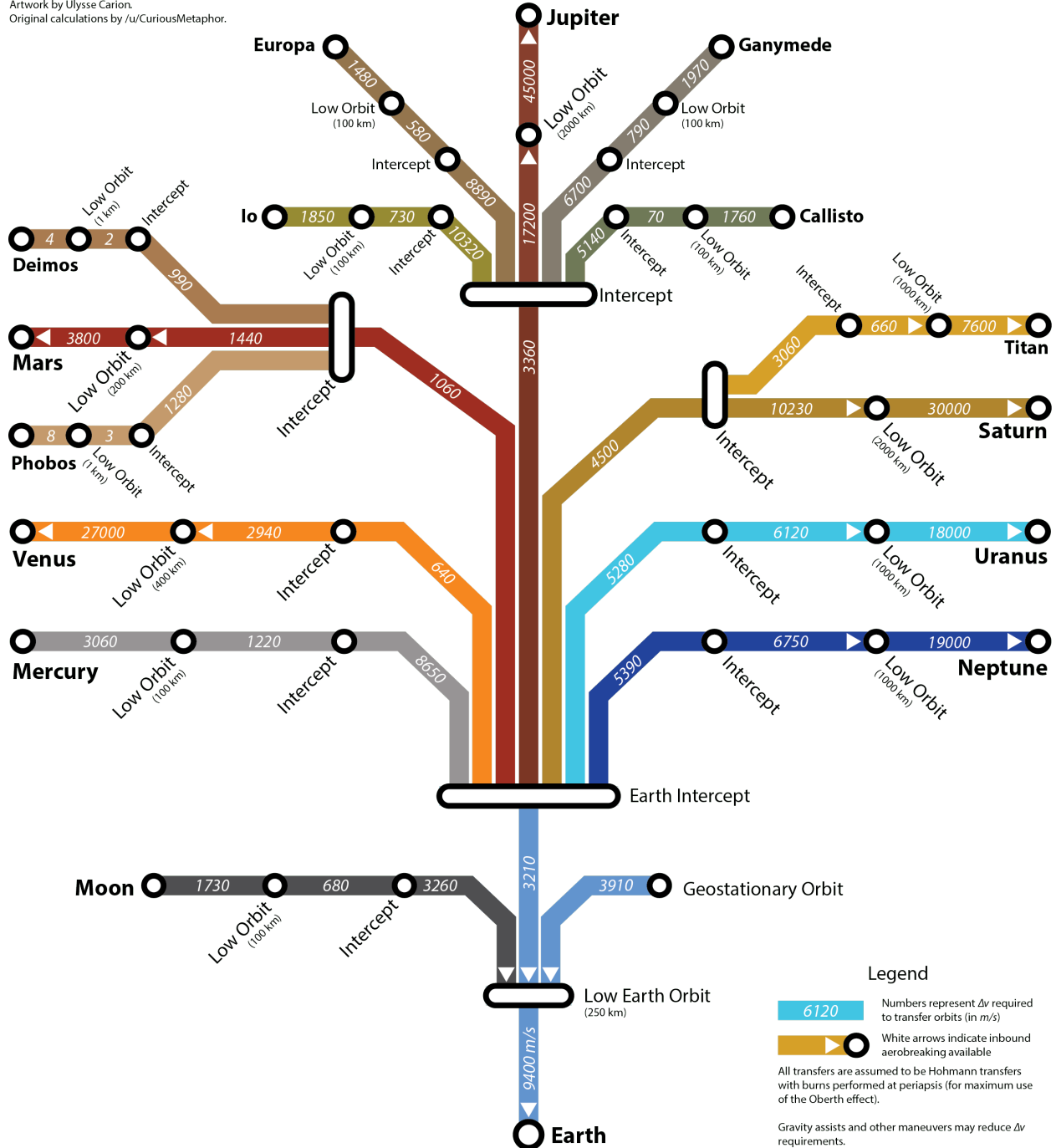


Figure 1.1: A map of the solar system in the style of a subway map. With the Δv required for each manoeuvre in m/s. Artwork by U. Carion[2].

To determine how much change in velocity, Δv , a spacecraft is capable of, the rocket equation is used, see equation 1.1, where Δv is change in velocity in m/s, v_{ex} is the velocity of the exhaust in m/s, m_{fuel} is the mass of the spacecraft's fuel in kg and m_{dry} is the spacecraft's dry mass in kg.

$$\Delta v = v_{ex} \ln \left(1 + \frac{m_{fuel}}{m_{dry}} \right) \quad (1.1)$$

To increase the Δv of a spacecraft, you can decrease the dry mass of the spacecraft, increase the mass of the fuel or increase the velocity of the exhaust. Exhaust velocity is therefore a measure of how efficiently the fuel is used and is often given in the form of specific impulse, I_{sp} , see equation 1.2, where I_{sp} is specific impulse in s and g_0 is standard gravity in m/s².

$$I_{sp} = \frac{v_{ex}}{g_0} \quad (1.2)$$

By imagining the most simple case of a system comprising a launch vehicle and a spacecraft, equation 1.1 gets split into two parts. This is shown in equation 1.3, where ₁ denotes the values for the launch vehicle and ₂ denotes the values for the spacecraft.

$$\Delta v = v_{ex,1} \ln \left(1 + \frac{m_{fuel,1}}{m_{dry,1} + m_{dry,2} + m_{fuel,2}} \right) + v_{ex,2} \ln \left(1 + \frac{m_{fuel,2}}{m_{dry,2}} \right) \quad (1.3)$$

It can be seen that the denominator in the first term includes the dry mass of the launch vehicle, $m_{dry,1}$, as well as the total mass of the spacecraft, $m_{dry,2} + m_{fuel,2}$. This means that any reduction in mass of the spacecraft has a compounding effect, increasing the Δv of the launch vehicle. By increasing the fuel efficiency of the spacecraft, $v_{ex,2}$, the required fuel mass can be reduced, $m_{fuel,2}$. This then has the knock-on effect of increasing the Δv of the launch vehicle. The more stages that a rocket has, the greater increase in Δv for a given reduction in spacecraft fuel mass. This makes it essential to increase the fuel efficiency of the spacecraft by as much as possible, optimising the spacecraft's thruster for a large I_{sp} .

A launch vehicle requires a large amount of thrust to escape Earth's gravity and attain orbit. Creating this high thrust requires large propellant mass flow rates, and a process well suited for energising these large propellant mass flow rates uses chemical energy stored in the propellant itself. This process is therefore known as chemical propulsion. While chemical propulsion can produce high thrusts, it does not produce a high v_{ex} and so limits the Δv . Once in space however, a small thrust can generate a large Δv if it is sustained for a long duration. By using a low propellant mass flow rate, and energising it with electrical energy from the spacecraft's solar panels or batteries, high propellant kinetic energies are able to be achieved. This process is aptly named electric propulsion. While the low propellant mass flow rate limits the thrust, the high propellant kinetic energy usually results in a larger v_{ex} when compared to chemical propulsion.

It should be noted that figure 1.1 assumes that a spacecraft is using a Hohmann transfer for each orbital manoeuvre. These Hohmann transfers allow for the spacecraft to take advantage of the Oberth effect, whereby the Δv required for an orbital manoeuvre can be

minimised if the Δv is delivered at periapsis (when the spacecraft is closest to the body it is orbiting). This can be achieved using chemical propulsion, where the high thrust allows for a large Δv to be achieved in minutes. The low thrust of electric propulsion however, requires a thruster to fire for months or years to achieve a similar Δv . For this reason, a spacecraft with electric propulsion cannot take as much of an advantage of the Oberth effect and will usually follow a trajectory with a larger Δv than that achievable by chemical propulsion. However, as electric propulsion has $\sim 10\times$ higher I_{sp} than chemical propulsion, it is the far better option if optimising for a large Δv or high spacecraft mass. This has resulted in electric propulsion now becoming more used than chemical propulsion on spacecraft[3], as well as being chosen to transport the new space station to the moon[4].

1.2 Electric Propulsion

There are three different mechanisms used to convert a spacecraft's stored electrical energy into the kinetic energy of the exhaust: Electrothermal, Electrostatic and Electromagnetic.

Electrothermal

Electrothermal thrusters conductively heat the propellant which is then expanded through a nozzle to accelerate it. This conductive heating can be done simply by passing a current through a resistor adjacent to the propellant, as in Resistojet thrusters. Alternatively, a plasma can be generated to heat the propellant, as in Arcjet and Microwave Electrothermal Thrusters. These systems usually have higher thrusts for a given power than Electrostatic and Electromagnetic systems, but a lower specific impulse.

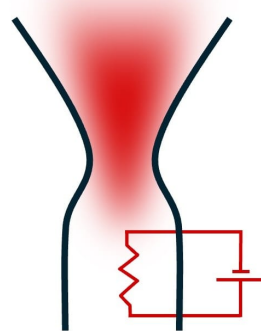


Figure 1.2: Simplified electrical circuit of a Resistojet thruster.

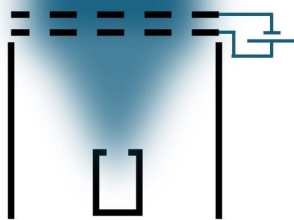


Figure 1.3: Simplified electrical circuit of a GIT.

Electrostatic

Electrostatic thrusters use a static electric field in the direction of acceleration to accelerate ions up to high velocities, as in Hall Effect Thrusters (HET) and Gridded Ion Thrusters (GIT). These are the most developed type of electric propulsion, with their operation having been demonstrated in space since 1964[5]. These thrusters typically have high specific impulse but low thrust.

Electromagnetic

Electromagnetic thrusters use an electromagnetic field, where the electric field is not in the direction of acceleration. For example, microwaves can be used to generate a plasma which is then accelerated using a strong magnetic field, as in Electron Cyclotron Resonance (ECR) thrusters. ECR thrusters show promise as a competitor to electrostatic thrusters, but they have yet to be flown in space.

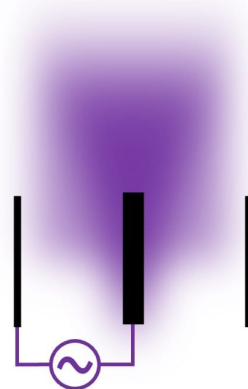


Figure 1.4: Simplified electrical circuit of an ECR thruster.

Figure 1.5 plots these different types of electric propulsion with specific impulse (fuel efficiency) on the y-axis and thrust on the x-axis. Electrostatic systems can be seen to occupy the top left corner of the plot, with chemical propulsion systems occupying the bottom right. The bottom left quadrant represents undesirable performance and so is of no interest, and the top right is limited by the high electrical power it requires.

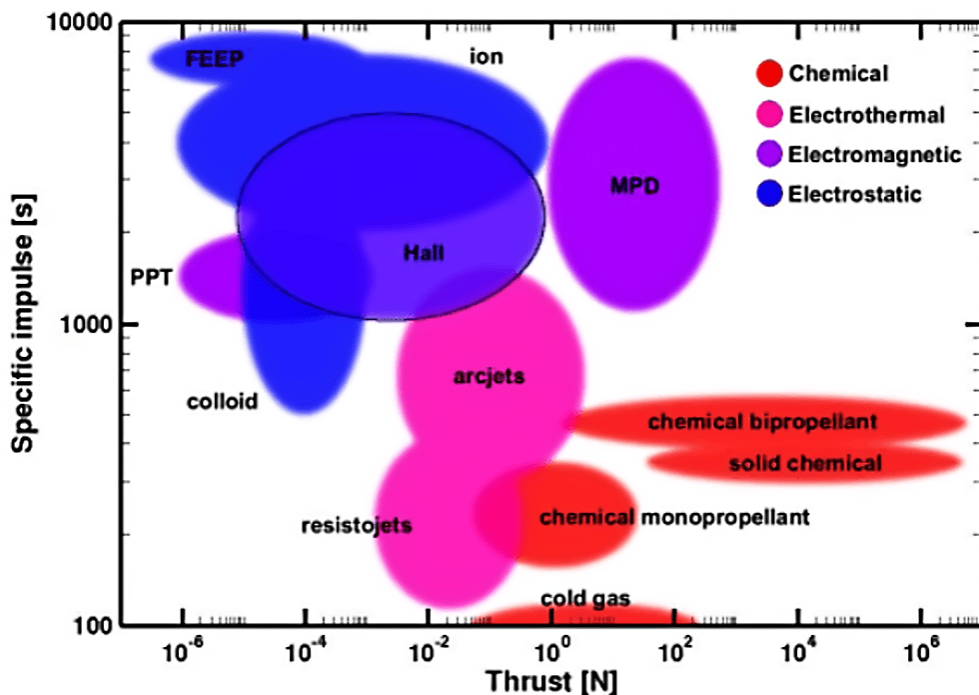


Figure 1.5: Thrust and specific impulse ranges for various forms of propulsion. Reproduced from Y. Choi[6].

MPD thrusters stand out as the highest performance electric thruster, however their power requirement exceeds that of which a spacecraft is currently capable of generating, so they are not yet viable. Electron Cyclotron Resonance (ECR) Magnetic Nozzle thrusters, the topic of this thesis, are relatively under-researched and so cannot be placed on this plot. The latest ground tests were conducted in 2023 and were able to produce a thrust of 5.6 mN at 2300 s specific impulse[7]. This roughly places ECR thruster performance in line with the Hall Effect Thruster, see figure 1.5.

1.2.1 Measuring Performance

This thesis investigates a number of mechanisms designed to increase ECR thruster performance. However, to determine if these mechanisms are successful at increasing thruster performance, a way to measure thruster performance must first be defined. Three metrics are used throughout this thesis to measure thruster performance. These metrics are thrust, specific impulse and thruster efficiency, as defined below. It should be noted that some of the following metrics assume the presence of an ionised exhaust, which is not true for all electric thrusters but does apply to the thrusters investigated in this thesis.[8]

Thrust, T

Thrust is likely the most obvious performance metric of an electric thruster. The higher the thrust the faster a spacecraft can manoeuvre and the shorter the transfer time between origin and destination. High thrust is therefore desirable when a spacecraft has a time sensitive payload. Thrust can be calculated from equation 1.4, where \dot{m}_p is the propellant mass flow rate in kg/s, v_{ex} is the exhaust velocity in m/s and v_i is the ion velocity in m/s.

$$T = \dot{m}_p v_{ex} \approx \dot{m}_p v_i \quad (1.4)$$

The approximation that $v_{ex} \approx v_i$ is often made for electrostatic/electromagnetic thrusters, as the exhaust can be assumed to consist entirely of ions. From equation 1.4 it can be seen that increasing \dot{m}_p will increase thrust. However, this also requires higher power to accelerate the increased propellant mass flow rate up to the same exhaust velocity. Increasing thrust by increasing v_{ex} likewise requires more power to accelerate the propellant up to a greater exhaust velocity. For this reason, most electric thrusters are thrust limited by the electrical power available from the spacecraft.[8]

Specific Impulse, I_{sp}

Specific impulse is a measure of the fuel efficiency of a thruster and can be found using equation 1.5, where v_{ex} is the exhaust velocity in m/s and g_0 is the standard acceleration of gravity in m/s².

$$I_{sp} = \frac{v_{ex}}{g_0} \quad (1.5)$$

Equation 1.5 shows that the only way to increase specific impulse is to increase v_{ex} . This can be achieved by increasing the power used to accelerate the propellant or by decreasing the propellant mass flow rate while keeping power constant. Both methods increase the energy given to a unit mass of propellant, increasing its acceleration and ultimately its velocity.[8]

Thruster Efficiency, η_t

Thruster efficiency (also known as total efficiency) can be simply described as a measure of how efficiently the thruster converts electrical energy into the kinetic energy of the exhaust. It is therefore defined as the kinetic thrust power of the ion beam, $P_{jet} = \frac{1}{2}\dot{m}_p v_{ex}^2$, divided by the total electric power to the thruster, P_T , see equation 1.6.

$$\eta_t = \frac{P_{jet}}{P_T} \quad (1.6)$$

As can be seen from equations 1.7 and 1.8, both thrust and specific impulse are proportional to the root of the product of thruster efficiency and total electrical power into the thruster, $\sqrt{\eta_t P_T}$. As power generation is limited on spacecraft, it is essential to have a high thruster efficiency to produce the highest thrust or specific impulse for a given power.[8]

$$T = \sqrt{\dot{m}_p 2\eta_t P_T} \quad (1.7)$$

$$I_{sp} = \sqrt{\frac{2\eta_t P_T}{\dot{m}_p g_0^2}} \quad (1.8)$$

The mechanism by which thrust is produced in an electric propulsion system is complex and differs across different types of thrusters. Each step in the mechanism generates inefficiencies that reduces the overall performance of the thruster. With ECR thrusters for example, an inefficiency is produced when energy is lost to heating the thruster instead of the propellant. Another inefficiency is produced when not all the propellant is ionised. Another when energy is used to ionise an already ionised particle and another when the ions are accelerated at an angle to one-another, so that a component of their force cancels out. Therefore, thruster efficiency can also be defined by the product of its individual efficiencies, see equation 1.9, where η_e , η_α , η_b and η_m are the electrical efficiency, multiply charged species efficiency, beam divergence efficiency and mass utilisation efficiency respectively.[8]

$$\eta_t = \eta_e \eta_\alpha \eta_b \eta_m \quad (1.9)$$

To develop a propulsion system with a high thrust and specific impulse, these efficiencies should be increased by as much as possible. But to do this, they must first be measured and understood.

Electrical Efficiency, η_e

Electrical efficiency is a measure of how well the thruster converts electrical energy into the electrical energy of the exhaust, and can be defined as the ratio of beam power, $P_b = I_b \phi_b$, to total thruster power, P_T , where I_b and ϕ_b are the beam current and voltage respectively.[8]

$$\eta_e = \frac{P_b}{P_T} \quad (1.10)$$

Multiply Charged Species Efficiency, η_α

An ideal ion beam comprises only singly charged ions, however some ions inevitably become doubly charged. This uses up energy that would otherwise be used to further accelerate the ions or generate new ions. Doubly charging ions is therefore a source of inefficiency. Assuming that the beam comprises only singly and doubly charged ions, the multiply charged species efficiency can be defined by equation 1.11, where I^+ and I^{++} are the singly charged ion current and the doubly charged ion current respectively. Such that the total ion beam current is $I_{beam} = I^+ + I^{++}$.[8]

$$\eta_\alpha = \left(\frac{I^+ + \frac{1}{\sqrt{2}}I^{++}}{I^+ + I^{++}} \right)^2 \quad (1.11)$$

Beam Divergence Efficiency, η_b

In a perfectly collimated beam, 100% of the thrust produced by the ions is used to accelerate the spacecraft. Unfortunately, every ion beam has some degree of divergence, reducing the beams effective thrust. By assuming uniform divergence of the ion beam, equation 1.12 can be used to account for the corresponding loss in efficiency, where θ_b is the average half-angle divergence of the ion beam.[8]

$$\eta_b = \cos^2(\theta_b) \quad (1.12)$$

Mass Utilisation Efficiency, η_m

The mass utilisation efficiency, η_m , accounts for the fraction of propellant that escapes the thruster without being ionised. This un-ionised propellant cannot be accelerated by magnetic or electric fields and therefore produces a negligible amount of thrust. This efficiency coefficient can be calculated using equation 1.13, where \dot{m}_i and \dot{m}_p are the ion mass flow rate and propellant mass flow rate respectively.[8]

$$\eta_m = \frac{\dot{m}_i}{\dot{m}_p} \quad (1.13)$$

1.3 ECR Magnetic Nozzle Thrusters

In order to better understand how an ECR magnetic nozzle thruster works, we can split its operation into two parts. The first part is Electron Cyclotron Resonance (ECR) Heating, which is the mechanism by which the propellant is energised. The second part is Ion Acceleration in a Magnetic Nozzle, which is how the thermal energy of the propellant is transferred into the kinetic energy of the exhaust, generating thrust. These are briefly summarised below, but are described in more detail in sections 2.2 and 2.3.

Electron Cyclotron Resonance (ECR) Heating

Electron Cyclotron Resonance (ECR) is a mechanism by which energy can be efficiently transferred from an electromagnetic wave into electrons when a magnetic field is present. Electrons in a magnetic field spin around magnetic field lines at their electron cyclotron frequency, see equation 2.6. The electric field of a right-hand polarised electromagnetic wave rotates around magnetic field lines at the wave's frequency. Therefore, when the electron's cyclotron frequency matches the wave's frequency, the electric field can align with the electron such that energy is continuously transferred into the electron. This resonant transfer of energy from the wave into an electron is a highly efficient means of electron heating and is known as Electron Cyclotron Resonance (ECR). This mechanism of ECR heating is described in more detail in section 2.2.

Ion Acceleration in a Magnetic Nozzle

A magnetic nozzle simply describes a divergent magnetic field. We know that electrons in a magnetic field spin around magnetic field lines and therefore have kinetic energy tangential to the magnetic field lines. When the magnetic field diverges, this tangential kinetic energy is converted into kinetic energy parallel to the magnetic field lines, accelerating the electrons out of the magnetic nozzle. When a plasma is exposed to a magnetic nozzle, the electrons are accelerated away from the ions, out of the magnetic nozzle. This charge separation forms an electric field that accelerates the ions towards the electrons. The acceleration of these ions generates an equal and opposite force on the magnetic nozzle that we call thrust. This mechanism of ion acceleration in a magnetic nozzle is described in more detail in section 2.3.

A thruster that uses ECR heating to energise a propellant, and a magnetic nozzle to accelerate it is known as an ECR magnetic nozzle thruster. A simplified cross-sectional diagram of an ECR magnetic nozzle thruster is shown in figure 1.6. Conductive material is shown in grey, while dielectric material is shown in yellow. Gaseous propellant is injected into the chamber from the sides, while microwaves are fed into the thruster from the bottom and are emitted by a central antenna. A ring magnet is used to generate a divergent magnetic field within the thruster. As the gaseous propellant contains a small number of free electrons, these begin to spin around magnetic field lines. When the rotational frequency of these electrons matches the frequency of the microwaves, the electrons resonantly absorb the microwave energy via ECR heating. These hot electrons collide with neutral particles, ionising them to

A BRIEF INTRODUCTION TO THE ELECTRON CYCLOTRON RESONANCE MAGNETIC NOZZLE THRUSTER

A gas propellant is fed into the thruster's central chamber. The gas consists of neutral propellant atoms as well as a small number of free electrons that are confined to the chamber by a magnetic field.

The electrons are pushed away from the magnet by its divergent magnetic field. They accelerate out of the thruster, spinning around magnetic field lines.

These free electrons absorb microwave energy emitted by the antenna in a process called Electron Cyclotron Resonance. The electrons collide with nearby propellant atoms, knocking their electrons off and turning them into positively charged ions.

The positive ions are attracted to the negative electrons and are pulled out of the thruster after them. These ions accelerate from 0 to 20,000 meters per second, pushing back on the thruster and generating thrust.

Plasma is a cloud of positive ions, negative electrons, and neutral particles, it is also known as the fourth state of matter.

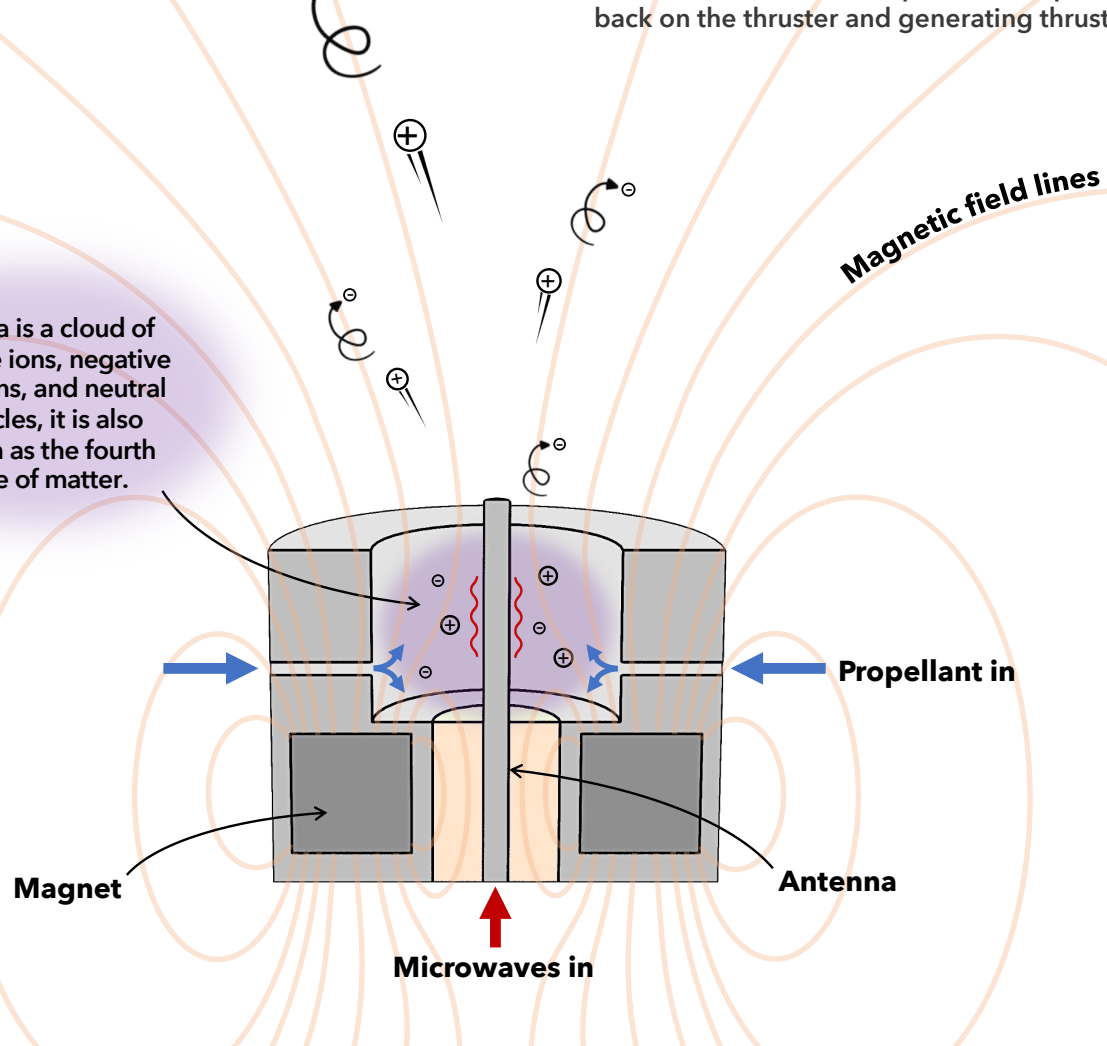


Figure 1.6: Infographic explaining the operation of an ECR magnetic nozzle thruster. As this is intended for public dissemination, the physics has been simplified.

form a plasma within the thruster's chamber.

The divergent magnetic field accelerates the electrons downstream. This mass exodus of electrons generates a negative potential downstream of the thruster. The positive ions are attracted towards this negative potential and accelerate out of the thruster towards the electrons. This is known as ambipolar acceleration. The reaction force generated by this acceleration of ions pushes back on the thruster, producing thrust.

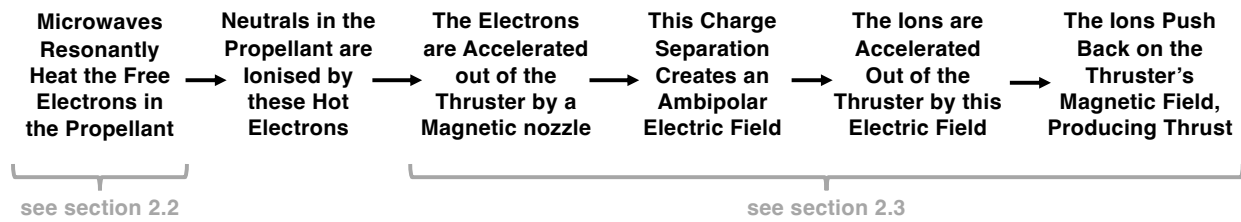


Figure 1.7: Flowchart showing the theorised sequence of events that produces thrust in an ECR thruster. Note that these events occur simultaneously, not in sequence.

The transmission of microwaves through the region between an inner and outer conductor, is known as coaxial microwave transmission. Coaxial microwave transmission is shown in more detail in figure 1.8, where the inner and outer conductors are both grey and the insulator between them is yellow. The antenna of an ECR thruster is essentially an extension of the inner conductor, and the thruster chamber walls are an extension of the outer conductor. For this reason the antenna will sometimes be referred to as the inner conductor and the chamber walls the outer conductor.

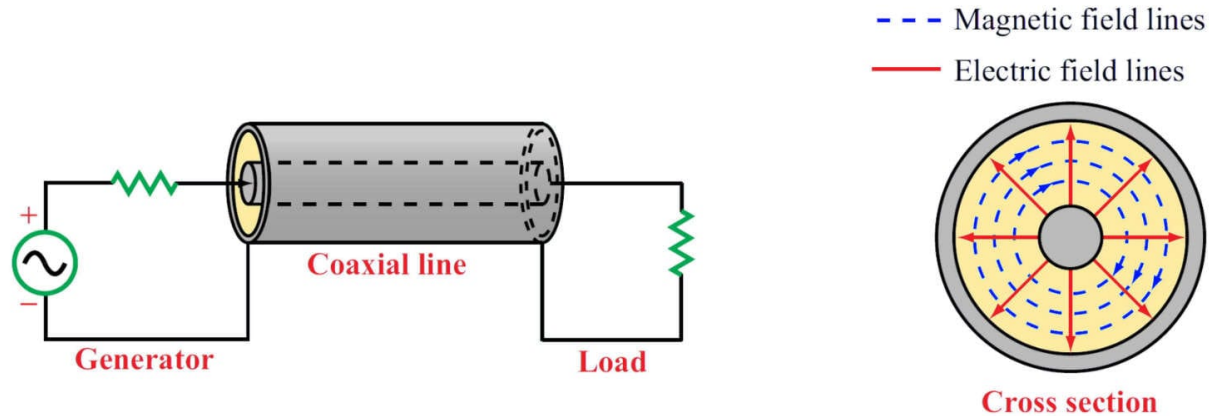


Figure 1.8: Diagram showing how electromagnetic waves are transmitted through a coaxial cable. This field pattern, where neither the electric nor the magnetic field lines are oriented in the direction of propagation, is known as the Transverse Electromagnetic Mode (TEM). The inner and outer conductors are both grey while the insulator is yellow. Reproduced from K.J. Chung[9].

Electrostatic thrusters, such as the Gridded Ion Thruster (GIT), use an electrode that forms a strong electric field to accelerate ions. This loss of ions, but not electrons, can cause

a thruster to become negatively charged which can significantly decrease its performance. This charging is negated by firing electrons out into the thruster's plume to neutralise it. The device used to do this is aptly named a neutraliser. Unfortunately these neutralisers have short lifetimes and are restricted to using less reactive gases. Electrodes for electrostatic thrusters are also a limiting factor on lifetime due to their high rate of erosion.

In ECR thrusters, electrons and ions are accelerated together, negating the need for an electrode or a neutraliser. This could make ECR thrusters inherently more reliable and should result in lower erosion rates and therefore longer lifetimes[10]. The lack of a neutraliser also allows for a wider range of propellants to be used, while the simpler design makes ECR thrusters easier to develop and cheaper to manufacture.

A Brief History of ECR Thrusters

The first publication of an ECR thruster was jointly achieved in 1965 by NASA[11] (in collaboration with General Electric) and the University of Tokyo[12]. Both studies used a waveguide, not an antenna, to transmit microwaves into the plasma, see figure 1.9. A waveguide is simply a conductive pipe that guides an electromagnetic wave by reflecting it off its internal walls. They are larger than coaxial cables, due to them using a different mode to propagate the wave.

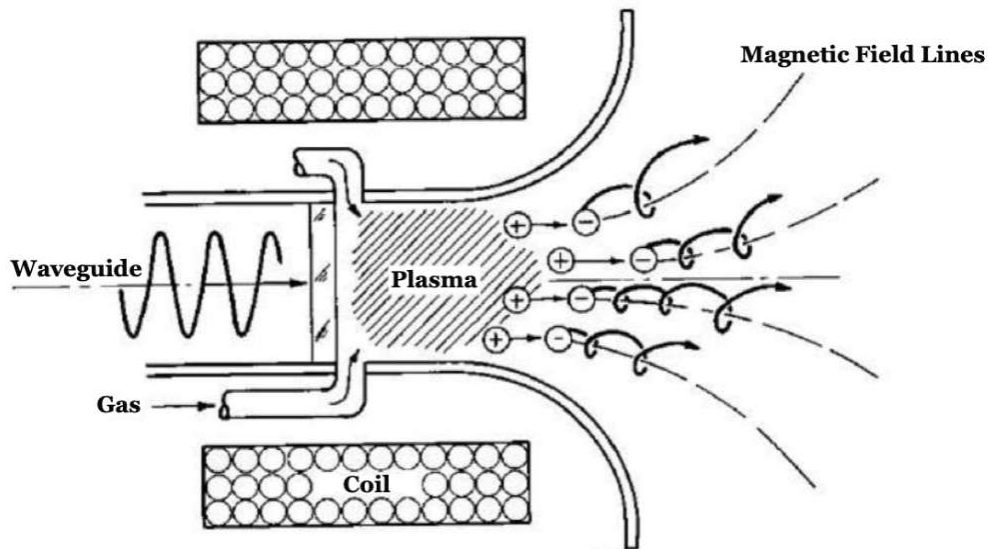


Figure 1.9: Diagram of a waveguide fed ECR thruster with a magnetic nozzle. Reproduced from J.C. Sercel[13].

Microwave generators at the time were large, heavy and inefficient, making them a poor choice for use in spacecraft. At the same time, DC electric propulsion systems were displaying adequate performance with smaller, lighter and more efficient power supplies, making them a far more attractive option. It's perhaps unsurprising then that the next study on ECR thrusters wasn't conducted until 1987, by J.C. Sercel at the California Institute of Technology[14]. This study again used a waveguide to feed microwaves into a plasma, however the thruster efficiency was only 2 %, far below the 41 % predicted by theory. By

measuring the energy loss mechanisms in the thruster, the sources of this low efficiency were found. Thruster efficiency was split into four parts, microwave coupling efficiency (30 %), mass utilisation efficiency (85 %), electrical efficiency (30 %) and divergence efficiency (24 %). Microwave coupling efficiency is defined as the ratio of the microwave power deposited into the plasma over the microwave power delivered to the thruster. It is believed that the use of a waveguide is responsible for the 30 % microwave coupling efficiency, as ECR thrusters that instead use a linear antenna to transmit microwaves have microwave coupling efficiencies of up to 98 %[7]. Electrical efficiency has since been improved via the use of permanent magnets over electromagnets. While low divergence efficiency has recently been linked to high facility background pressures and can be increased by using a higher capacity pumping system.

Variations on the ECR thruster design have been developed and tested over the years. Arguably the most significant development to the ECR thruster occurred at the ONERA French Aerospace Lab, when S. Larigaldie first tested the coaxial ECR thruster in 2010[15]. The coaxial configuration emits microwaves from a central antenna that is completely immersed within the plasma, see figure 1.10. The coaxial geometry transports microwaves using the Transverse Electromagnetic Mode (TEM) as shown in figure 1.8. TEM can be sustained at very small dimensions, but cannot be created within a waveguide, allowing for a higher degree of geometry optimisation of the coaxial ECR thruster over the waveguide ECR thruster. By 2015, the thruster efficiency of the coaxial ECR thruster had been measured at 16 %, an increase of 8× over the waveguide ECR thruster[16]. Since then, further development at ONERA has increased thruster efficiency up to 53 %, making the ECR thruster competitive with the current state of the art Hall Effect Thrusters and Gridded Ion Thrusters[7]. However, as an ECR thruster has yet to be flown in space, its real-world performance has yet to be measured.

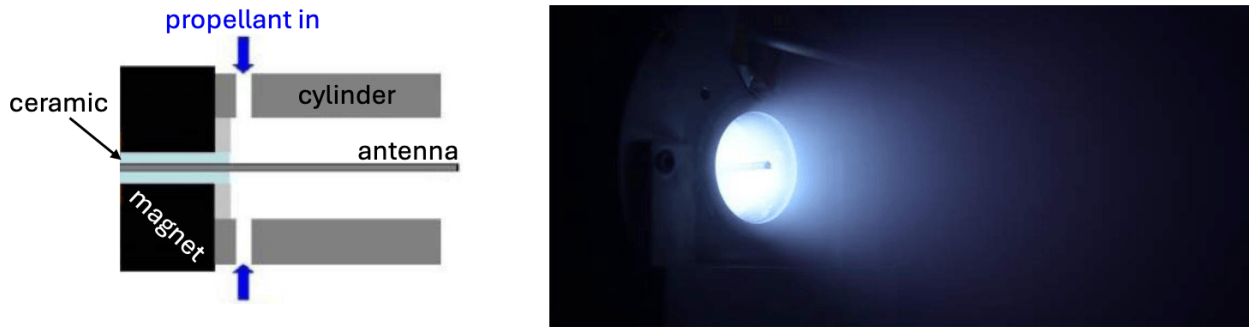


Figure 1.10: An early version of the permanent magnet coaxial ECR thruster. Diagram (left), photo (right). Reproduced from F. Cannat[16].

Relative Performance

The high ECR thruster performance obtained by ONERA has been credited to a novel development of the thruster. This novelty has yet to be shared with the wider research community and so remains the undisclosed intellectual property of ONERA. As such, no other organisation has been able to match these high performances. This analysis of ECR thruster relative performance therefore relies solely on data obtained by ONERA. Despite

this limited dataset, performance has been verified in three different vacuum facilities, using a thrust balance that was independently tested, adding credibility to the results.[7][17]

ONERA found that by increasing the diameter of the thruster's chamber, it was possible to efficiently couple more power into the plasma. Table 1.1 shows the performance of both their 27.5 mm diameter thruster, as well as their 70.0 mm diameter thruster. As can be seen from table 1.1, increasing chamber diameter allows for higher thrust and specific impulse at a sacrifice to the ratio of thrust to power. The comparable performance at these two different power levels suggests that ECR thrusters could scale to even higher powers.

Table 1.1: Performance values for ONERA's small and large ECR thrusters.[7]

	SMALL ECR THRUSTER	LARGE ECR THRUSTER
Chamber Diameter [mm]	27.5	70.0
Power [W]	25	146
Mass Flow Rate [mg/s]	0.10	0.25
Thrust [mN]	1.5	5.6
Specific Impulse [s]	1580	2310
Thruster Efficiency [%]	44	43
Thrust to Power [mN/kW]	60	38

It should be noted however that these power values are measurements of the microwave power deposited into the plasma. A complete ECR thruster propulsion system would have additional power losses related to the efficiency of the microwave generator, power deposition in the microwave line and power reflected back to the generator. To make a fair comparison with other electric propulsion types, the total propulsion system power must first be estimated, taking into account these additional power losses.

Power deposition in the microwave line can be assumed to be negligible, as the final version of an ECR thruster would likely have the generator situated adjacent to the thruster. Reflected power can also be assumed to be negligible, as the microwave line and thruster can be tuned to reduce reflected power to insignificant levels. The primary source of this additional power loss is then the microwave generator, which has historically suffered from low efficiencies of around 45 %[18]. Recently however, a 25 W, 70 % efficient microwave generator has been developed and demonstrated by Thales Microelectronics[19]. This generator was initially targeted for 100 W with >85 % efficiency. However, as this higher efficiency has not yet been demonstrated, this study shall presume a microwave generator efficiency of 70 %. Despite this generator not being powerful enough for the higher power ECR thruster, a 70 % efficiency will still be presumed so that the two ECR thrusters can be compared. The power values for ONERA's ECR thrusters are therefore adjusted to 36 W and 209 W respectively. To compare these ECR thrusters against current flight proven electric propulsion systems for small satellites, their performance is plotted in figure 1.11.

The choice of which propulsion system a spacecraft will use is highly complex and is influenced by many constraints. One such constraint is the spacecraft's mass budget which

defines the maximum mass of the propellant. The Δv required by the spacecraft then defines the minimum specific impulse (fuel efficiency) required of the thruster. All thrusters below this value on the y-axis of figure 1.11 can then be eliminated. Given that the power budget of a spacecraft is usually limited by its area of solar panels, a high thrust to power ratio is desirable, as a higher thrust will reduce the manoeuvre time of a satellite.

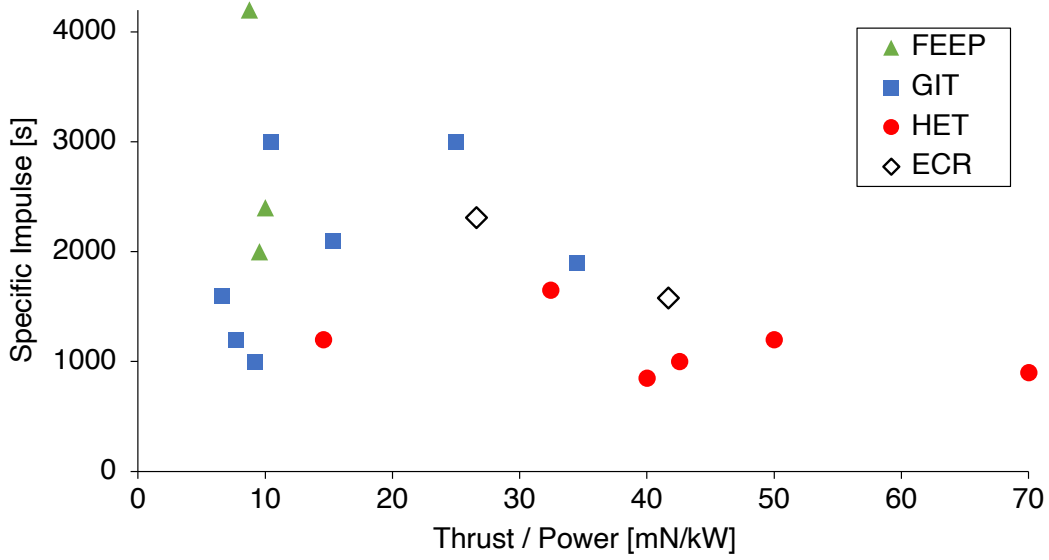


Figure 1.11: Specific impulse as a function of the thrust to power ratio of low power propulsion systems for small satellites, with a nominal thrust between 0.1 and 10.0 mN. Including Field-Emission Electric Propulsion (FEEP), Hall Effect Thrusters (HET), Gridded Ion Thrusters (GIT) and Electron Cyclotron Resonance (ECR) thrusters. Performance values obtained from ENPULSION GmbH.[20][21][22] and I.S. Vavilov[23] can be found in Appendix A.

Figure 1.11 plots the performance of propulsion systems for small satellites, with a nominal thrust between 0.1 and 10.0 mN. Field-Emission Electric Propulsion (FEEP) can be seen to only be attractive to satellites with a requirement for high fuel efficiency, although what this plot does not show is the low cost and size of FEEP that makes them a more attractive option. Hall Effect Thrusters (HETs) are by far the most attractive option when a short manoeuvre time is preferred over high fuel efficiency. This, combined with their relatively simple and cheap construction has resulted in HETs becoming the most commonly flown thruster in space. GITs can be seen to fill the gap between FEEP and HETs, where both high fuel efficiencies and high thrusts are required. However, complex construction and correspondingly high costs make GITs a less attractive option than figure 1.11 would suggest. ECR thrusters can be seen to also fill that gap in performance between FEEP and HETs. However, the lack of a neutraliser makes ECR thrusters potentially even cheaper and longer lasting than HETs, making them a highly attractive option for spacecraft manufacturers. FEEP, GITs and HETs are also relatively mature technologies, with less potential for significant future performance improvements when compared to the relatively immature ECR thruster. There is therefore the potential for ECR thrusters to become even more competitive in the coming decades.

1.4 Focus of the Thesis

Motivation

ECR magnetic nozzle thrusters have been significantly less developed than more conventional electric propulsion systems like HET's and GIT's. Despite this, they show promise as a high performing electric thruster for small satellites[7]. Their ease of scalability in both size and power suggests that the technology could be scaled up/down even further, while their simple design could allow for significant commercial success. This disparity between the lack of research and the potential impact of the technology, made ECR thrusters stand out as a field of research where I could make the most impact.

Novelty

Recent research on ECR magnetic nozzle thrusters has concentrated on increasing their power[7], implementing dual microwave frequencies[24], understanding ion acceleration[25], and investigating facility effects[26]. Relatively little research has been conducted on the transfer of energy from the microwaves to the electrons via ECR heating. This thesis looks at how this energy transfer is achieved and has established that decreasing the gradient of the magnetic field at resonance increases ECR heating, thereby increasing thruster performance. Two experimental campaigns using two different thrusters have proven that decreasing the magnetic field gradient at resonance significantly increases thruster performance. This mechanism could play a crucial role in ensuring the commercial success of ECR magnetic nozzle thrusters. Concurrent testing has also investigated the relationship between resonance region location and thruster performance, as well as performance enhancements achieved by introducing a second microwave frequency.

Primary Objective: Find Novel Techniques to Enhance ECR Thruster Performance

Since the mechanism driving the high performance of ONERA's ECR thrusters remains unknown, developing a new approach to increase thruster performance is required for these thrusters to be commercially viable. Thruster efficiencies are currently $\sim 10\%$ [27][28] and likely need increasing to above 40 % to achieve commercial success.

Sub Objectives:

1. Increase thruster performance by decreasing magnetic field strength gradient...
 - (a) using an electromagnet, see Ch. 5.
 - (b) using a ferromagnetic material, see Ch. 8.
2. Increase thruster performance by adding a magnetic mirror trap, see Ch. 6.
3. Investigate the effect of resonance region location on thruster performance, see Ch. 7.
4. Increase thruster performance by adding a second microwave frequency, see Ch. 9.

For each sub objective, direct thrust measurements are used to measure changes to thruster performance. Plasma probes are also used to measure changes to the electrons, ions and plasma potential that drive these changes in performance.

2 LITERATURE REVIEW

This literature review will first explore the fundamental physical mechanisms behind the ECR magnetic nozzle thruster. This will be split into three sections:

2.1	Electromagnetic Waves in Plasmas	18
2.2	Electron Cyclotron Resonance (ECR) Heating	23
2.3	Ion Acceleration in a Magnetic Nozzle	28

These fundamental physical mechanisms will then be used to explain how the ECR magnetic nozzle thruster has been developed in the past decade. This will also be split into three sections:

2.4	Development of the Coaxial ECR Thruster at ONERA	34
2.5	University of Michigan's ECR Thruster	38
2.6	Facility Effects	39

The one key takeaway from this literature review is that the energy/velocity of the ions in the exhaust is directly proportional to the energy of the electrons at the thruster. Electron Cyclotron Resonance (ECR) heating transfers electromagnetic energy directly to the electrons. Therefore, optimising this transfer of energy has the potential to significantly increase the energy/velocity of the ions, thereby increasing specific impulse. It is this mechanism that will be exploited to increase thruster performance in chapters 5 and 8.

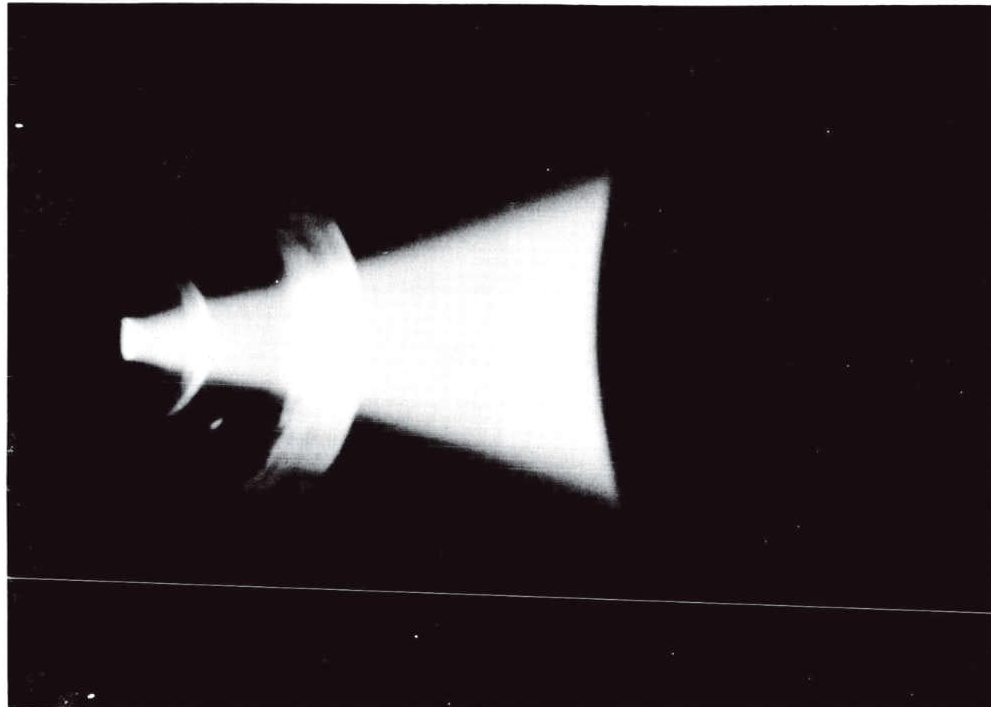


Figure 2.1: Photo of the plume of an ECR magnetic nozzle thruster from one of the first publications about the technology in 1965. Reproduced from D.B. Miller et al.[11].

2.1 Electromagnetic Waves in Plasmas

A plasma can be thought of as a mixture of negatively charged electrons, positively charged ions and neutral particles. These charges create a dynamic web of electric and magnetic fields within the plasma. Understandably then, this makes the propagation of electromagnetic waves through a plasma extremely difficult to predict. Perhaps the most famous example of this is the high density atmospheric plasma generated during spacecraft reentry, see figure 2.2. If this plasma is allowed to envelope a spacecraft it can create a Faraday cage, reflecting electromagnetic waves and causing a communication blackout for any astronauts inside. The ability of a plasma to reflect electromagnetic waves can also be useful however, as bouncing radio waves off the ionosphere allows us to significantly increase their range[29].

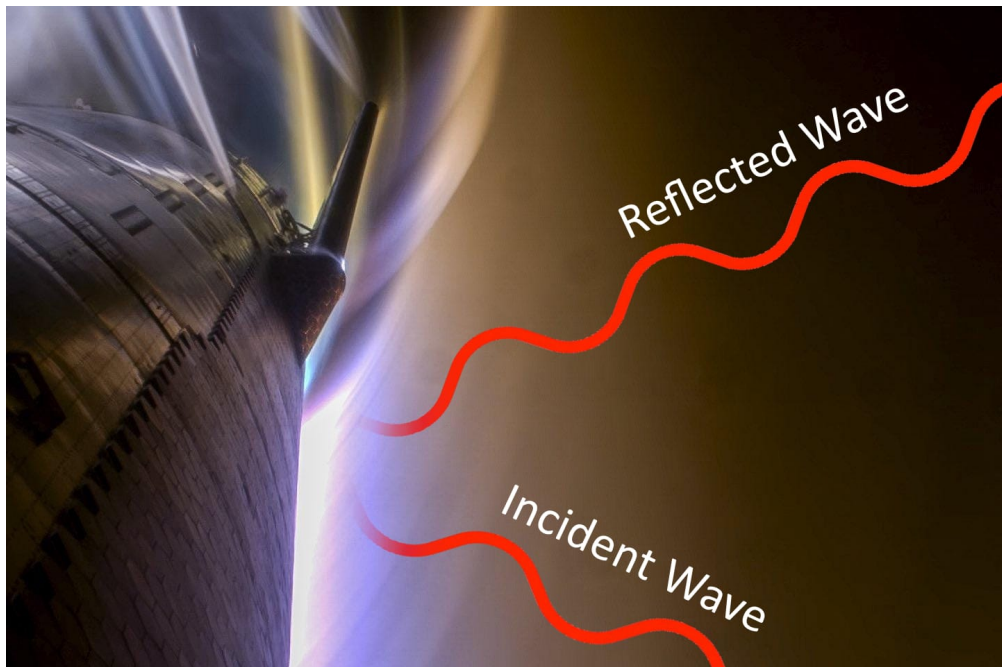


Figure 2.2: The high density plasma that can form around a spaceship during atmospheric reentry can reflect incoming electromagnetic waves. Reproduced from SpaceX[30].

It is important then to find the conditions at which electromagnetic waves are reflected by a plasma. This understanding can also be used to determine how to get a wave to be absorbed by a plasma. The two conditions that need to be found are the cutoff condition where a wave is reflected, and the resonance condition where a wave is absorbed. Since the thruster relies on heating a plasma to produce thrust, the conditions for resonance need to be achieved before the wave experiences cutoff and is reflected.

To make matters harder, when a static background magnetic field is present, electromagnetic waves in a plasma can take on four different forms. The first two forms are the Right-hand polarised wave (R-wave) and Left-hand polarised wave (L-wave), which both propagate parallel to the magnetic field, $\mathbf{k} \parallel \mathbf{B}$. Both are circularly polarised, with the electric field vector of the R-wave rotating clockwise around magnetic field lines, and the electric field vector of the L-wave rotating anticlockwise around magnetic field lines, see figure 2.3. Where clockwise and anticlockwise are defined with respect to the waves direction of propagation. The second two forms are the Ordinary wave (O-wave) and Extraordinary wave (X-wave), which both propagate perpendicular to the magnetic field, $\mathbf{k} \perp \mathbf{B}$. The electric field vector of the O-wave oscillates parallel to the magnetic field and the electric field vector of the X-wave oscillates perpendicular to the magnetic field, see figure 2.3. The electric field vector of the X-wave is elliptically polarised such that its components \mathbf{E}_x and \mathbf{E}_y oscillate 90° out of phase, this results in \mathbf{E} moving in an ellipse.[29]

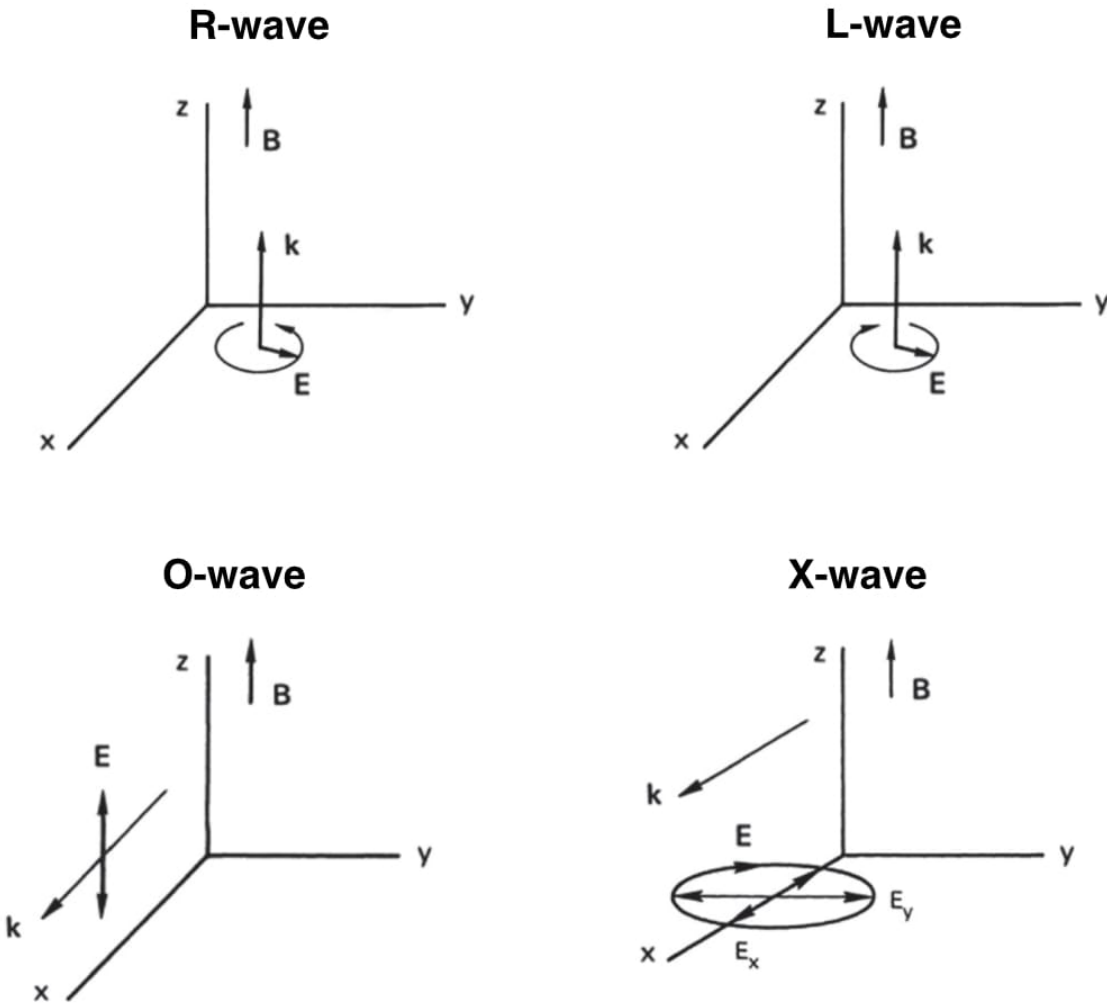


Figure 2.3: Diagrams showing the direction of the wave vector, \mathbf{k} , and the electric field vector, \mathbf{E} , in relation to the magnetic field, \mathbf{B} , for the R-wave, L-wave, O-wave and X-wave. Reproduced from F.F. Chen[29].

These waves are highly dependent on the oscillations of electrons within the plasma and are therefore known as electromagnetic electron waves.

Electromagnetic Waves Parallel to the Magnetic Field, $\mathbf{k} \parallel \mathbf{B}$

R-wave - Right-Hand Polarised wave, $\mathbf{E} \odot \mathbf{B}$

L-wave - Left-Hand Polarised wave, $\mathbf{E} \circlearrowleft \mathbf{B}$

Electromagnetic Waves Perpendicular to the Magnetic Field, $\mathbf{k} \perp \mathbf{B}$

O-wave - Ordinary wave, $\mathbf{E} \parallel \mathbf{B}$

X-wave - Extraordinary wave, $\mathbf{E} \perp \mathbf{B}$

To determine the conditions at which each wave experiences cutoff and resonance, a fluid model can be used to describe a cold collisionless plasma with a nonzero background magnetic field. This fluid model is then used to find the dispersion relations for each wave, see equations 2.1 to 2.4, where the refractive index is defined as $\frac{ck}{2\pi f_m}$, c is the speed of light in m/s, k is the wave vector in m^{-1} , f_m is the microwave frequency in Hz, $f_{p,e}$ is the frequency of the electrons in the plasma in Hz as defined by equation 2.5, $f_{c,e}$ is the frequency at which electrons rotate around magnetic field lines in Hz as defined by equation 2.6 and lastly $f_{UH} = \sqrt{f_{p,e}^2 + f_{c,e}^2}$ is the Upper Hybrid Resonance (UHR) frequency in Hz. [31][29]

$$\text{R-wave dispersion relation: } \left(\frac{ck}{2\pi f_m} \right)^2 = 1 - \frac{f_{p,e}^2/f_m^2}{1 - (f_{c,e}/f_m)} \quad (2.1)$$

$$\text{L-wave dispersion relation: } \left(\frac{ck}{2\pi f_m} \right)^2 = 1 - \frac{f_{p,e}^2/f_m^2}{1 + (f_{c,e}/f_m)} \quad (2.2)$$

$$\text{O-wave dispersion relation: } \left(\frac{ck}{2\pi f_m} \right)^2 = 1 - \frac{f_{p,e}^2}{f_m^2} \quad (2.3)$$

$$\text{X-wave dispersion relation: } \left(\frac{ck}{2\pi f_m} \right)^2 = 1 - \frac{f_{p,e}^2(f_m^2 - f_{p,e}^2)}{f_m^2(f_m^2 - f_{UH}^2)} \quad (2.4)$$

The electron plasma frequency, $f_{p,e}$, is defined by equation 2.5, where e is the elementary charge in C, n_e is the plasma electron density in m^{-3} , ε_0 is the permittivity of free space in Fm^{-1} and m_e is the mass of an electron in kg.

$$f_{p,e} = \frac{1}{2\pi} \sqrt{\frac{e^2 n_e}{\varepsilon_0 m_e}} \quad (2.5)$$

Cutoff occurs when the wavelength of a wave in a plasma becomes infinite and the refractive index goes to zero. Resonance occurs when the wavelength of a wave in a plasma becomes zero and the refractive index goes to infinity. Making this substitution into equations 2.1 to 2.4 allows us to find the cutoff and resonant frequencies of each wave, see table 2.1.

Table 2.1: The cutoff and resonant frequencies for the four types of electromagnetic waves that can occur in a plasma.

	CUTOFF ($k = 0$)	RESONANCE ($k = \infty$)
R-wave	$\frac{f_{p,e}^2/f_m^2}{1-(f_{c,e}/f_m)} = 1$	$f_{c,e} = f_m$
L-wave	$\frac{f_{p,e}^2/f_m^2}{1+(f_{c,e}/f_m)} = 1$	NA
O-wave	$f_m = f_{p,e}$	NA
X-wave	$\frac{f_{p,e}^2/f_m^2}{1-(f_{c,e}/f_m)} = 1 \quad \& \quad \frac{f_{p,e}^2/f_m^2}{1+(f_{c,e}/f_m)} = 1$	$f_{UH} = f_m$

As can be seen from table 2.1, only the R-wave and the X-wave can achieve resonance, so only these waves will be considered from here on. To better interpret table 2.1, the cutoff and resonant frequencies can be plotted in a Clemmow-Mullaly-Allis (CMA) Diagram, see figure 2.4, where $(f_{p,e}/f_m)^2$, which is proportional to the plasma's electron density, is on the x-axis, and $f_{c,e}/f_m$, which is proportional to the magnetic field strength, is on the y-axis.

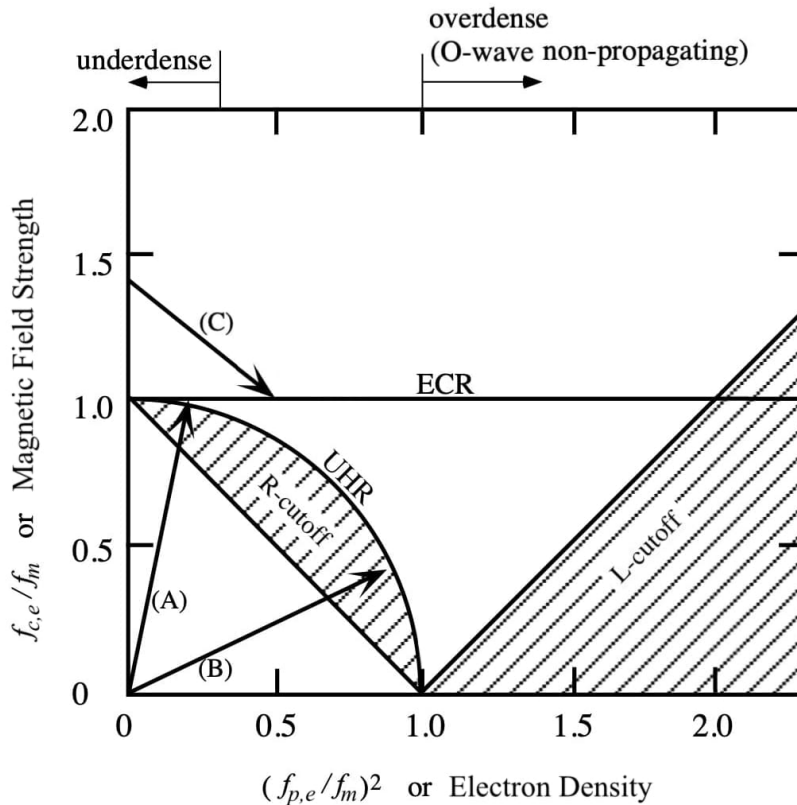


Figure 2.4: Expected propagation, resonance and cutoff regions of microwaves in a cold plasma. Presented as a Clemmow-Mullaly-Allis (CMA) Diagram. Reproduced from I. Funaki[32].

The R-wave is cutoff in the shaded region labeled R-cutoff, while the X-wave is cutoff in both the R-cutoff and L-cutoff shaded regions. The horizontal line labeled ECR is the location at which the R-wave achieves resonance, and the curved line labeled UHR is where the X-wave achieves resonance.

Microwaves are generated outside of the thruster and are propagated into the plasma. In figure 2.4 this is represented as starting at zero on the x-axis and moving right. If an R-wave is propagated from a region of low magnetic field strength ($f_{c,e}/f_m < 1$), it has to pass through the R-cutoff region to reach its ECR resonance condition, see figure 2.4 arrow (A). Similarly, if an X-wave is propagated from a region of low magnetic field strength ($f_{c,e}/f_m < 1$), it also has to pass through the R-cutoff region to reach its UHR resonance condition, see figure 2.4 arrow (B).

In order for the microwaves to achieve resonance without passing through a cutoff region, the R-wave can be propagated from a region of high magnetic field strength ($f_{c,e}/f_m > 1$), see figure 2.4 arrow (C). By not passing through a cutoff region, more of the microwave energy reaches the resonance region where it is transferred to the electrons. This method of microwave energy transfer is highly efficient and is referred to as a magnetic beach[33].

An X-wave could be used instead of an R-wave. The X-wave however, can't achieve resonance in an overdense plasma ($(f_{p,e}/f_m)^2 > 1$) and so is less useful than the R-wave. High plasma densities are desirable, as more electrons/ions will result in increased thrust. Higher plasma densities can also be achieved by increasing the microwave frequency, f_m . However, the frequency is restricted to 2.45 GHz ± 0.05 GHz, as this is the industry standard microwave frequency, and as a result 2.45 GHz generators are considerably less expensive than higher frequency generators due to them being more developed[34].

A coaxial ECR thruster with a linear antenna emits a linearly polarised wave parallel to the magnetic field[35]. This linear polarised wave is the sum of a R-wave and a L-wave[36]. This means that the microwave field in the thruster is comprised only of R-waves and L-waves that propagate from a region of high magnetic field strength ($f_{c,e}/f_m > 1$). As L-waves do not achieve resonance, it is logical to assume that this thruster would only be able to couple a maximum of 50 % of its microwave energy into the plasma[36]. However, microwave coupling efficiencies of up to 98 % have been reported[7]. The generally accepted explanation for this is that the L-wave is converted into a different wave mode that can then be absorbed by the plasma[37][38][39]. This likely occurs when the L-wave is reflected off the thrust chamber's wall, inverting its polarisation, which turns it into an R-wave[40]. Future work could measure the polarisation of the waves in the thrusters chamber to verify this.

2.2 Electron Cyclotron Resonance (ECR) Heating

Electron Cyclotron Resonance (ECR) heating acts to convert the electromagnetic energy of the microwaves directly into the kinetic energy of the electrons. Section 2.3 explains how for magnetic nozzle thrusters, the final kinetic energy of the ions is directly proportional to the energy of the electrons at the thruster. This makes ECR heating a highly efficient method of indirectly increasing ion kinetic energy in magnetic nozzle thrusters.

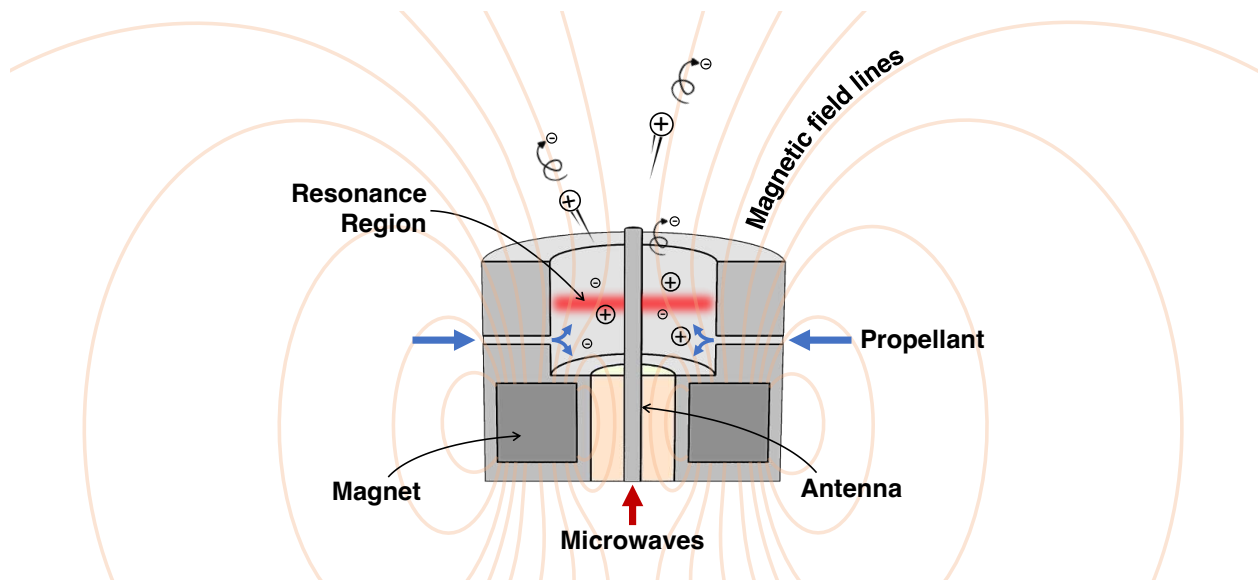


Figure 2.5: Simplified cross-sectional diagram of a coaxial ECR magnetic nozzle thruster.

ECR heating in the ECR magnetic nozzle thruster can be best explained with the help of figure 2.5. Free electrons in the thruster's chamber, spin around magnetic field lines at their electron cyclotron frequency, $f_{c,e}$. See equation 2.6, where $f_{c,e}$ is the electron cyclotron frequency in Hz, e is the elementary charge in C, B is the magnetic field strength in T and m_e is the mass of an electron in kg.

$$f_{c,e} = \frac{eB}{2\pi m_e} \quad (2.6)$$

Microwaves are emitted from a central antenna at the frequency $f_m = 2.45$ GHz. At a specific magnetic field strength, $B = B_0 = 87.5$ mT, the electron cyclotron frequency, $f_{c,e}$, is equal to the frequency of these microwaves, f_m . This creates a highly efficient transfer of energy from the microwaves to the electrons that is known as Electron Cyclotron Resonance (ECR) heating. The location of this resonance region, where the electrons resonantly absorb microwave energy, is highlighted in red in figure 2.5.

2.2.1 Collisionless Heating Model

The thruster's antenna generates a linearly polarised microwave field within the thruster's chamber[35]. This field comprises two counter-rotating circularly polarised waves, an R-wave and an L-wave[36]. The amplitude of the R-wave, E_R , equals the amplitude of the L-wave, E_L , and the sum of these amplitudes equals the amplitude of the net microwave field, $E = E_R + E_L$ [16][41]. The R-wave rotates in the right-hand sense around the magnetic field, while the L-wave rotates in the left-hand sense around the magnetic field. When the cyclotron frequency of an electron matches the frequency of these waves and is coincidentally in phase, the electron experiences a constant energy gain from the R-wave, see figure 2.6. Conversely, if the electron is coincidentally out of phase with the wave it experiences a constant energy loss. However, the electrons are found to experience a net energy gain and are stochastically heated[42][43].

Force due to the R-wave: $\vec{F}_R = -e \vec{E}_R$

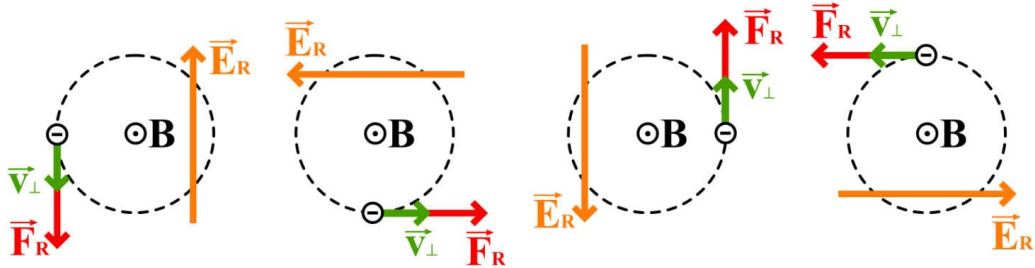


Figure 2.6: Vector arrows for the amplitude of the R-wave \vec{E}_R , the electrons tangential velocity \vec{v}_\perp and the force on the electron due to the R-wave \vec{F}_R at four points though the electrons rotation. Wave and electron in phase. Reproduced from M.A. Lieberman[41].

The L-wave, rotating in the opposite direction to the electron, acts to slow down and speed up the electron alternately, with no net energy gain, see figure 2.7.

Force due to the L-wave: $\vec{F}_L = -e \vec{E}_L$

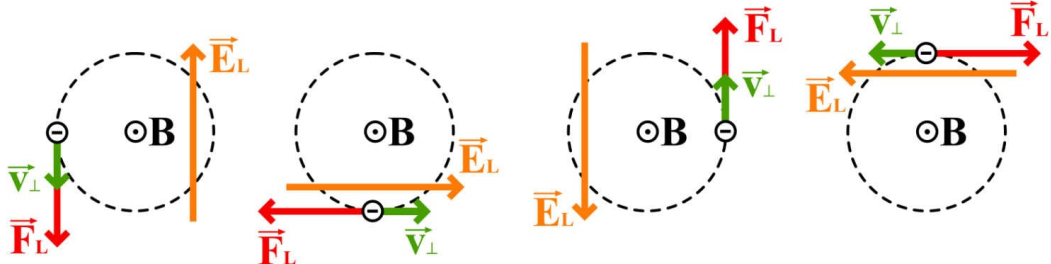


Figure 2.7: Vector arrows for the amplitude of the L-wave \vec{E}_L , the electrons tangential velocity \vec{v}_\perp and the force on the electron due to the L-wave \vec{F}_L at four points though the electrons rotation. Reproduced from M.A. Lieberman[41].

The change in electron energy resulting from the combination of \vec{F}_R and \vec{F}_L is modelled for an in phase electron. Figure 2.8 shows the change in electron energy as the electron moves through the resonance region. For the example in figure 2.8 an electron travels 20 mm at a constant axial velocity, $v_{\parallel} = 2.3 \times 10^6$ m/s, through a region of constant magnetic field strength gradient, $|\frac{\partial B}{\partial x}| = 5.36$ T/m. The frequency of both the R-wave and L-wave is $f_m = 2.45$ GHz. The ripples in the primary waveform are produced from the alternating energy gain and loss generated by the L-wave.

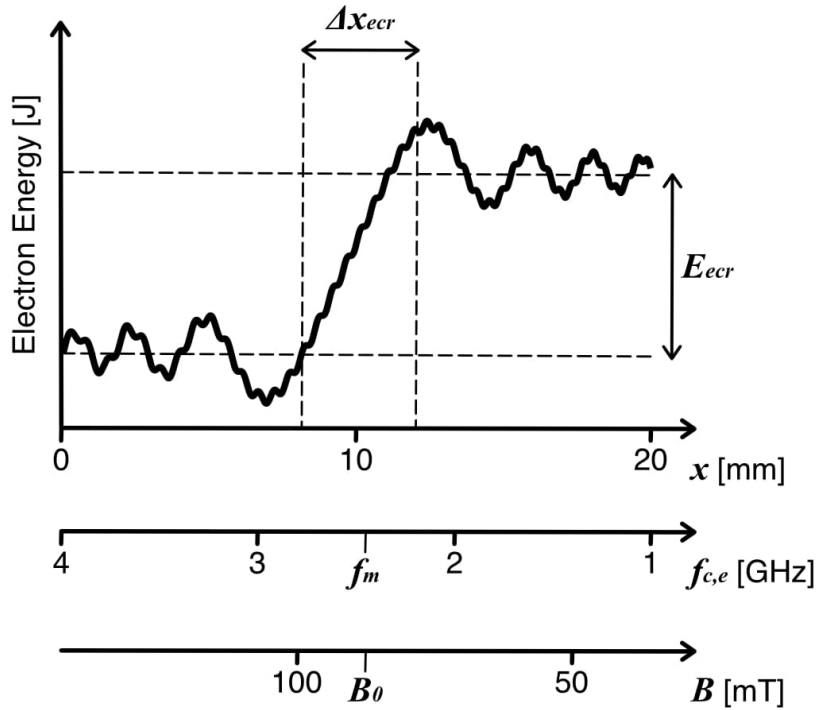


Figure 2.8: The energy gain of an electron in one pass through a resonance region. Produced using my collisionless heating model of the R-wave and L-wave with an in phase electron.

An increase in electron energy, E_{ecr} , is observed to occur over a distance, Δx_{ecr} . Δx_{ecr} is the thickness of the resonance region and is calculated using equation 2.7 to be 3.9 mm for the example in figure 2.8, where B_0 is the magnetic field strength at resonance in T, v_{\parallel} is the electrons mean axial velocity in m/s, f_m is the driving microwave frequency in Hz and $|\frac{\partial B}{\partial x}|$ is the magnetic field strength gradient in T/m.[41]

$$\Delta x_{ecr} = \sqrt{\frac{B_0 v_{\parallel}}{f_m |\frac{\partial B}{\partial x}|}} \quad (2.7)$$

This range in location at which ECR occurs, Δx_{ecr} , corresponds to a range in magnetic field strength at which ECR occurs, see figure 2.8. By assuming a constant magnetic field strength gradient, this range of magnetic field strength can be calculated using equation 2.8.

$$\Delta B_{ecr} = \left| \frac{\partial B}{\partial x} \right| \Delta x_{ecr} \quad (2.8)$$

The energy gained by the electron from one pass through the resonance region, E_{ecr} , is calculated using equation 2.9, where E_{ecr} is measured in J, e is the elementary charge in C, E_R is the amplitude of the R-wave in V/m and m_e is the mass of an electron in kg.[41]

$$E_{ecr} = \frac{e^2 E_R^2 B_0}{2m_e f_m \left| \frac{\partial B}{\partial x} \right| v_{\parallel}} \quad (2.9)$$

Absorbed power per unit area can now be calculated by numerically integrating equation 2.9 over the flux of electrons, $n_e v_{\parallel}$, incident on the resonance region, see equation 2.10, where S_{ecr} is the absorbed power per unit area of the resonance region in W/m² and n_e is the number density of electrons in m⁻³.[41]

$$S_{ecr} = \frac{n_e e^2 E_R^2 B_0}{2m_e f_m \left| \frac{\partial B}{\partial x} \right|} \quad (2.10)$$

Equations 2.7, 2.9 and 2.10 define the collisionless ECR heating of electrons and their derivations can be found in M.A. Lieberman[41]. Waves that are not absorbed and instead pass through the resonance region can become evanescent and decay exponentially, preventing their energy from being transferred to the electrons. It is therefore important to increase S_{ecr} so as to minimise the microwave power that passes through the resonance region and is lost. S_{ecr} increases when magnetic field strength gradient, $\left| \frac{\partial B}{\partial x} \right|$, is decreased. It is therefore desirable to decrease $\left| \frac{\partial B}{\partial x} \right|$ as much as possible, to increase the fraction of microwave power that is transferred to the electrons. As S_{ecr} is a measurement of absorbed power per unit area, it is desirable to reduce $\left| \frac{\partial B}{\partial x} \right|$ over as large an area as possible so as to maximise this transfer of power.[44]

2.2.2 Doppler Broadened Resonance Region

In an ECR magnetic nozzle thruster, energetic electrons are repelled from the magnet and accelerate away from the thruster. This positively charges the thruster, creating a potential drop that attracts the low-energy electrons back towards the thruster. These electrons pass through the resonance region a second time, gaining further thermal energy. Before the electrons reach the back of the chamber, they are repelled via the magnetic mirror effect and are accelerated out of the thruster, through the resonance region once more. This bouncing between the electrostatic field and magnetic mirror can happen multiple times for each electron, increasing their thermal velocity significantly[45]. This increases their mean velocity parallel to the magnetic field lines, v_{\parallel} , sufficiently so that the electrons experience

a Doppler shifted microwave frequency, $f_m + \frac{1}{2}\Delta f_D$. A Gaussian distribution in electron velocities results in the resonance region taking on a Gaussian shape with a full width at half maximum of Δf_D in the frequency domain, see equation 2.11.[46]

$$\Delta f_D = 4\sqrt{\ln(2)} f_m \frac{v_{\parallel}}{c} \quad (2.11)$$

The range in resonant frequencies, $f_m \pm \frac{1}{2}\Delta f_D$, creates a corresponding range in the magnetic field strengths at which resonance occurs, $B_0 \pm \frac{1}{2}\Delta B_D$. Equation 2.6 can then be used to find equation 2.12.

$$\Delta B_D = \frac{2\pi m_e \Delta f_D}{e} \quad (2.12)$$

The resonance region thickness due to Doppler broadening, Δx_D , can then be calculated from equation 2.12. Δx_D can be seen to increase as $|\frac{\partial B}{\partial x}|$ decreases.

$$\Delta x_D = \frac{\Delta B_D}{|\frac{\partial B}{\partial x}|} \quad (2.13)$$

Total Resonance Region Thickness ($\Delta x_{ecr} + \Delta x_D$)

In a study by J. Porto et al.[45], a particle in cell simulation shows electrons gaining tangential energy in a region with a full width at half maximum of ~ 4.4 mm. The model used $f_m = 2.45$ GHz, $B_0 = 875$ G, $|\frac{\partial B}{\partial x}| = 1.77$ T/m and $v_{\parallel} = 1.1 \times 10^6$ m/s. From equations 2.7 and 2.13 the two resonance region thicknesses can be calculated as $\Delta x_{ecr} = 4.7$ mm and $\Delta x_D = 0.6$ mm, which gives a total resonance region thickness of $\Delta x_{ecr} + \Delta x_D = 5.3$ mm. The proximity of this value of resonance region thickness to the value of 4.4 mm found from the particle in cell simulation helps to validate the model for electron heating that is described in section 2.2.

2.3 Ion Acceleration in a Magnetic Nozzle

The fundamental physical mechanism by which any electrostatic/electromagnetic propulsion system generates thrust is the acceleration of ions. To develop and improve upon a thruster, it is necessary to first understand how the ions are accelerated. Gridded Ion Thrusters and Hall Effect Thrusters generate a strong electric field that accelerates their ions. Conversely, ECR magnetic nozzle thrusters accelerate their ions using a strong magnetic field.

Ion acceleration in a magnetic nozzle can be broken down into four parts: **(i)** Electron Acceleration, **(ii)** Ion Acceleration, **(iii)** Momentum Transfer and **(iv)** Electron Detachment.

(i) Electron Acceleration

High energy electrons are generated in the thruster's chamber where they are exposed to a strong magnetic field. The movement of the electron within the magnetic field generates a force in a direction perpendicular to both the electron's velocity and the magnetic field. This force is known as the Lorentz force and is defined using equation 2.14, where \mathbf{F} is the Lorentz force in N, e is the elementary charge in C, \mathbf{E} is the electric field in V/m, \mathbf{v} is the electron's velocity in m/s and \mathbf{B} is the magnetic field in T.

$$\mathbf{F} = e(\mathbf{E} + \mathbf{v} \times \mathbf{B}) \quad (2.14)$$

The Lorentz force causes the electron to spin around magnetic field lines. The electron's velocity can therefore be split into its velocity perpendicular to magnetic field lines, v_{\perp} , and its velocity parallel to magnetic field lines, v_{\parallel} , see figure 2.9.

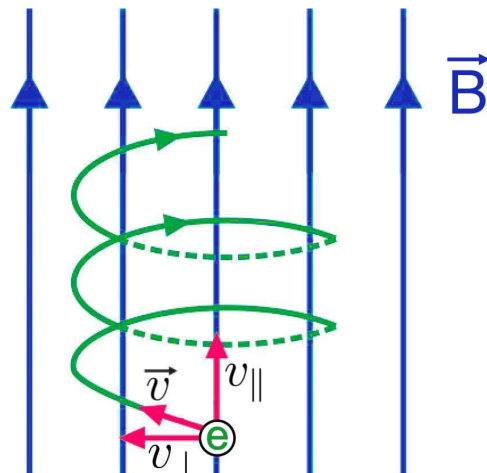


Figure 2.9: Diagram showing how an electron spirals around magnetic field lines. Reproduced from X. Sun[47].

The rotation of electrons around magnetic field lines can produce cyclotron radiation. There is no evidence that this radiation plays a significant role in the ion acceleration of ECR magnetic nozzle thrusters, however it can produce electromagnetic noise that could interfere with instruments onboard a satellite.[48]

The electrons magnetic moment can be defined by equation 2.15, where μ_e is the electrons magnetic moment in J/T, m_e is the electrons mass in kg, v_\perp is the electron's velocity perpendicular to magnetic field lines in m/s and B is the local magnetic field strength in T.

$$\mu_e = \frac{m_e v_\perp^2}{2B} \quad (2.15)$$

The high magnetic field strength gradient causes these electrons to be accelerated downstream away from the magnet, see equation 2.16, where \dot{v}_\parallel is the electrons acceleration downstream in m/s², and $(\frac{\partial B}{\partial x})_\parallel$ is the gradient of the magnetic field parallel to magnetic field lines in T/m. The derivation of which can be found in F.F. Chen[29].

$$\dot{v}_\parallel = -\frac{\mu_e}{m_e} \left(\frac{\partial B}{\partial x} \right)_\parallel \quad (2.16)$$

From equation 2.16 it can be seen that a high magnetic field strength gradient is desirable, as it results in greater electron acceleration downstream. This highlights the design challenges for ECR magnetic nozzle thrusters, as a low magnetic field strength gradient is also desirable to increase electron heating, see equation 2.9.

Combining equations 2.15 and 2.16 gives us equation 2.17, which shows that the acceleration of electrons downstream, \dot{v}_\parallel , is highly dependent on the electron's velocity perpendicular to magnetic field lines, v_\perp .

$$\dot{v}_\parallel = -\frac{v_\perp^2}{2B} \left(\frac{\partial B}{\partial x} \right)_\parallel \quad (2.17)$$

As was shown in section 2.2, Electron Cyclotron Resonance (ECR) heating acts to directly increase v_\perp , and therefore \dot{v}_\parallel . ECR heating is therefore well suited to the acceleration of electrons in a magnetic nozzle.

(ii) Ion Acceleration

Equation 2.17 shows how the electron tangential velocity, v_\perp , that is generated during ECR heating is converted into the parallel velocity, v_\parallel , of the electron downstream. To determine how this movement of electrons downstream affects the ions, it is essential to take into account the average velocity of all the electrons together. This is known

as the average thermal velocity of the electrons, v_{th} . This is then converted into the average kinetic energy of the electrons, see equation 2.18, which can be more easily measured. T_e is the electron temperature and is a measure of the average electron kinetic energy in eV. Within the spacecraft electric propulsion community, electron temperature is often displayed with the units eV. 1 eV is the kinetic energy of an electron that has been accelerated through a potential difference of 1 V and is equal to 1.602×10^{-19} J. As electric propulsion research often studies electrons that have been accelerated through potential differences, this makes the eV a more useful unit than the J when displaying electron temperature.

$$eT_e = \frac{1}{2}m_e v_{th}^2 \quad (2.18)$$

As the electrons are accelerated downstream, they are separated from the ions. This charge separation creates a potential drop downstream of the thruster that can be found using equation 2.19. This is known as an ambipolar electric field, where ϕ_{max} is the maximum potential drop in the plume, T_{e0} is the electron temperature at the thruster's exit plane in eV and γ_e is the polytropic coefficient which is determined experimentally and is thought to be between 1.0 and 1.2[49].

$$\phi_{max} = -T_{e0} \frac{\gamma_e}{\gamma_e - 1} \quad (2.19)$$

As can be seen from equation 2.19, the maximum potential drop in the plume is proportional to electron temperature at the thruster's exit plane. This is expected, as higher electron temperature means that the electrons thermal velocity is increased. From equation 2.17 we can see that an increased electron tangential velocity results in a greater electron acceleration downstream which then produces a larger charge separation and therefore a larger potential drop in the plume.

This potential drop in the plume acts to accelerate the ions towards the electrons and out of the thruster, see figure 2.10. This method of accelerating the ions is known as charged separation coupling[50]. The maximum energy of the ions, $E_{i,max}$, can be calculated by adding a term into equation 2.19 to account for ion acceleration in the presheath, before the thruster's exit, see equation 2.20[49]. The equation is multiplied by the elementary charge, e , to convert the units of ion energy from eV to J.

$$E_{i,max} = eT_{e0} \left(\frac{\gamma_e}{\gamma_e - 1} + \frac{1}{2} \right) \quad (2.20)$$

Equations 2.17 to 2.20 therefore show how electron tangential velocity, v_{\perp} , is converted into ion kinetic energy, $E_{i,max}$, in a magnetic nozzle. A highly efficient way to increase

$E_{i,max}$ is therefore increased to increase v_{\perp} . Electron Cyclotron Resonance (ECR) heating acts to directly increase v_{\perp} , and is therefore a highly efficient means of increasing ion energy.

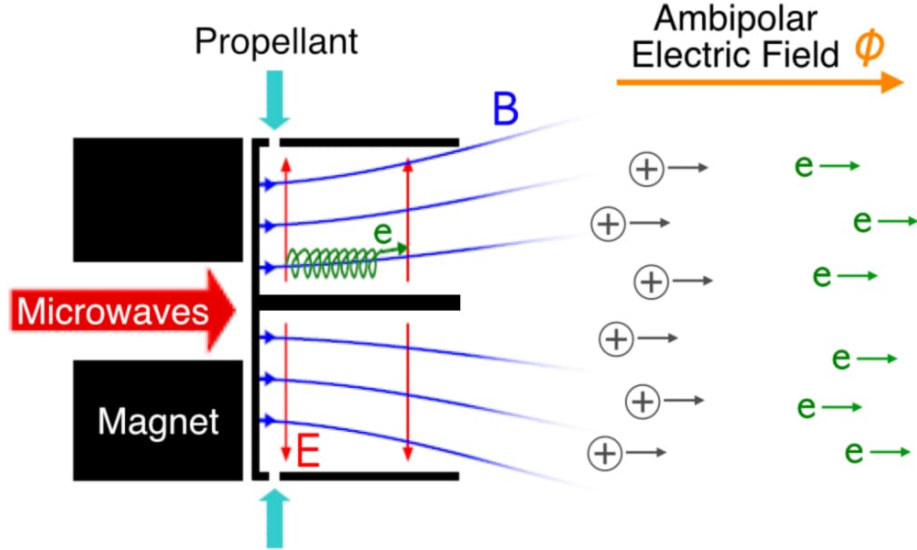


Figure 2.10: Diagram showing how an ambipolar electric field forms in the plume of an ECR thruster and acts to accelerate the ions downstream. Reproduced from D. Packan[51].

(iii) Momentum Transfer

The acceleration of ions in the magnetic nozzle results in a change to the momentum of the plume. The transfer of this momentum to the thruster's applied magnetic field produces thrust. It is necessary then to determine the mechanism by which momentum is transferred from the plasma to the thruster.

The trajectory of an electron spinning around magnetic field lines can be seen to resemble the coils of an electromagnet, see figure 2.9. Like an electromagnet, each electron in a magnetic nozzle generates an azimuthal current that forms its own magnetic field. If the generated magnetic field opposes the applied magnetic field in the magnetic nozzle, it is called a diamagnetic field, and the current that generates it is called a diamagnetic current. The sum of the individual electron diamagnetic fields in a magnetic nozzle creates a net diamagnetic field that opposes the applied magnetic field, see figure 2.11. This diamagnetic field creates a Lorentz force that acts to both reduce the divergence of the electrons and push against the applied magnetic field. This force on the thruster's magnetic field from the diamagnetic field is the primary mechanism by which the momentum of the plasma is transferred to the thruster.[25][52]

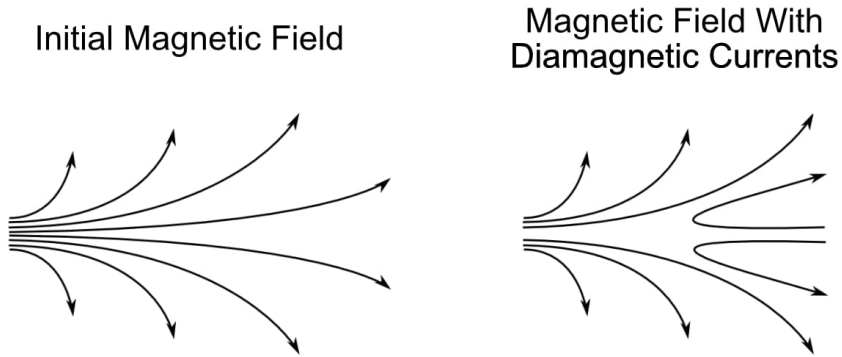


Figure 2.11: Magnetic field lines showing the magnetic field in a magnetic nozzle (left) and in a magnetic nozzle containing a plasma induced diamagnetic current (right). Reproduced from F.H. Ebersohn[53].

It should be noted that this is a complex field of ongoing research, many aspects of which have been omitted for brevity. The plume contains many different plasma induced currents that generate a magnetic field far more complex than the one shown in figure 2.11. Because the plasma, electric fields and magnetic fields are all coupled, numerically modelling the plume proves highly difficult.

(iv) Electron Detachment

As all magnetic field lines form closed loops, the electrons must detach from them, or else they would circle round and impinge on the back of the thruster. This would cancel out the ambipolar electric field, resulting in no ion acceleration. The divergence of these magnetic field lines, and the location at which the electrons detach, heavily influences the ion plume divergence and therefore the thruster's beam divergence efficiency, η_b .

There are two types of plasma detachment, collisional and non-collisional. Collisional detachment can be caused two different ways. The electrons in the jet can recombine with the ions, producing a neutral atom that does not follow the magnetic field lines. Alternately, the electrons collide elastically with the ions or neutrals, bending their trajectory. However, these two mechanisms are infrequent in magnetic nozzle plasma thrusters and their effect is presumed to be negligible[15].

Non-collisional detachment is the more widely accepted cause of plasma detachment in magnetic nozzle plasma thrusters. But again there are multiple different mechanisms through which this is thought to happen. The simplest explanation is that the electrons are traveling so fast downstream that the weak magnetic field is insufficient to overcome the electrons inertia, causing the electrons to detach from the magnetic field lines[54]. However, as the mass of electrons is low, so too is their inertia, meaning that this method of detachment would only occur to the highest energy electrons in the

plasma. The ions, accelerated by the electrons, have a far larger mass than the electrons, and therefore a greater inertia. A second non-collisional detachment mechanism is therefore proposed, in which the ions inertia breaks them free from the weak magnetic field lines downstream. This creates an electric potential that pulls the electrons towards the ions, off their field lines[55], see figure 2.12. Lastly, a third mechanism for non-collisional detachment is presented in which the plasma jet acts to deform the downstream magnetic field lines such that they never loop back around to the thruster. This “freezing” of magnetic field lines would negate the need for plasma detachment all-together[56].

In reality no one mechanism is solely correct, and plasma detachment is most likely a combination of all the mechanisms discussed. Whilst a brief overview of plasma detachment has been provided here, the nuances of this complex topic are ultimately beyond the scope of this thesis.

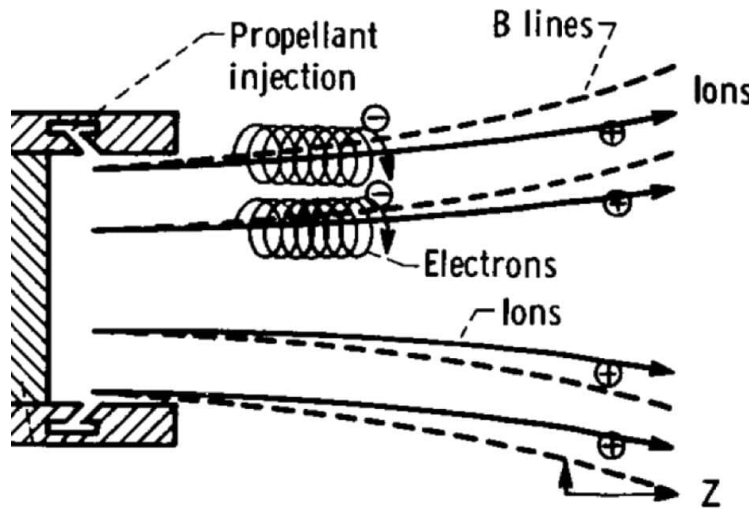


Figure 2.12: Detachment of the electrons from magnetic field lines (B lines), due to the electric field produced by downstream ions. Reproduced from H.G. Kosmahl et al.[50]

2.4 Development of the Coaxial ECR Thruster at ONERA

The coaxial ECR thruster uses a coaxial cable to propagate microwaves into the thruster and a central antenna to emit them into a plasma. The development of the coaxial ECR thruster has been led by the ONERA French Aerospace Lab, and three PhD theses outline this development from inception to the current state of the art.

PhD Thesis: F. Cannat, 2015

In this first thesis, the ECR thruster's permanent magnet was replaced with an electromagnetic coil. This allowed for a variety of different magnetic topologies to be tested. The modularity of the thruster also allowed for the location of the ECR region and the diameter of the inner thruster chamber to be varied. It was found that mass utilisation efficiency was increased when the ECR region lay downstream of the propellant injectors, such that all propellant passes through the resonance region. Mass utilisation efficiency was maximised when the resonance region was in close proximity to the propellant injectors.

Mass utilisation efficiency was also increased when the thruster chamber diameter increased from 13 mm to 27 mm. This increases the ratio of plasma volume to wall area, decreasing plasma wall losses. This also decreases the neutral propellant density which results in less collisions and therefore higher electron temperatures. Higher divergence efficiencies were linked to a lower neutral density, due to the decreased collision rate and higher electron temperatures.

By including a DC block in the thruster's microwave line, it is possible to electrically float the thruster. The potential that the thruster floats at is therefore defined by the plasma that surrounds it, and is known as the thruster floating potential. The ambipolar electric field produced by charge separation in the plume was found to produce a thruster floating potential of over 200 V. Unfortunately, this high thruster floating potential critically damaged the thrusters DC block. This has since been solved by instead floating the thruster using a wireless waveguide transmission.[16]

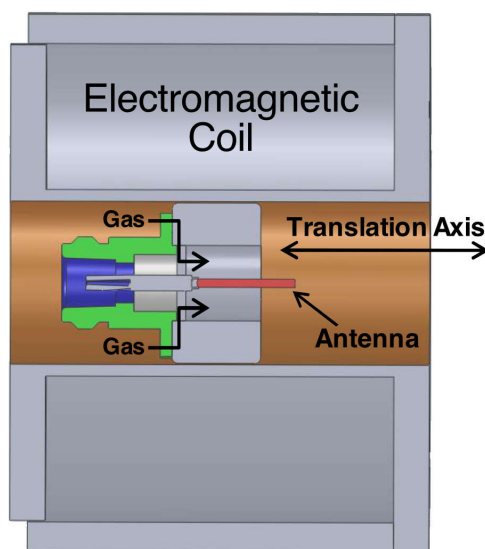


Figure 2.13: Electromagnet ECR thruster prototype. Reproduced from F. Cannat[57].

PhD Thesis: T. Vialis, 2018

This next thesis outlines the adaptation of ONERA's electromagnetic ECR thruster into one that uses permanent magnets to increase the thruster's efficiency. Adaptation of the thruster's design to fit on a thrust balance was also required so that thrust could be measured directly for the first time, instead of indirectly using electrostatic probes. This involved using waveguides to wirelessly transfer microwave power to the thruster. This had the added effect of floating the thruster, lifting the restrictions on the thruster's floating potential. The thruster was found to float at approximately 300 V, with this higher floating potential correlating to an increase in performance.

Different thruster geometries were tested, with the aim of increasing the thrust produced. The thrust chamber diameter remained fixed at 27.5 mm, as this had already been determined to be the diameter that produced the highest thrust by F. Cannat[16]. The length of the thrust chamber that produced the highest thrust was found to be $L = 20$ mm, see figure 2.14. Thrust was also seen to peak for an antenna length of $l = 20$ mm and diameter of $D = 2.3$ mm. [15]

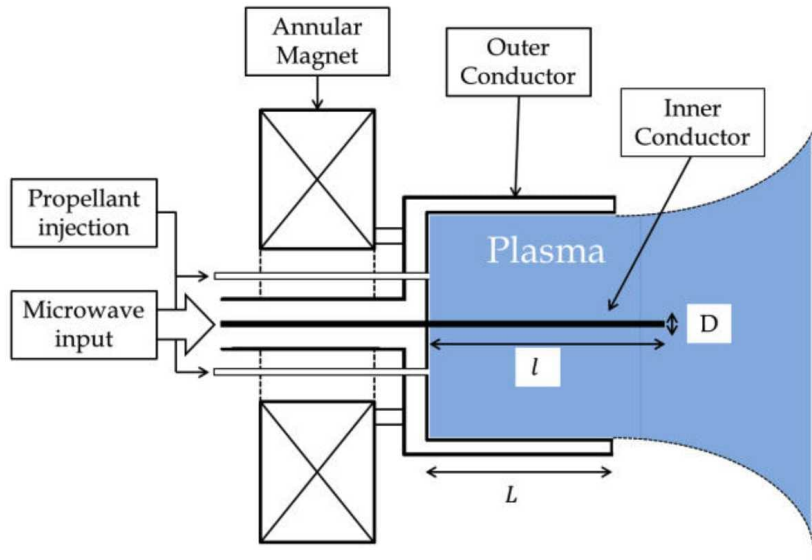


Figure 2.14: Permanent magnet ECR thruster prototype. Reproduced from T. Vialis[15].

PhD Thesis: S. Peterschmitt, 2020

The most recent PhD thesis on ONERA's ECR thruster was submitted by S. Peterschmitt in 2020[36]. This thesis outlines the current state of the art in ECR thrusters, see figure 2.15.

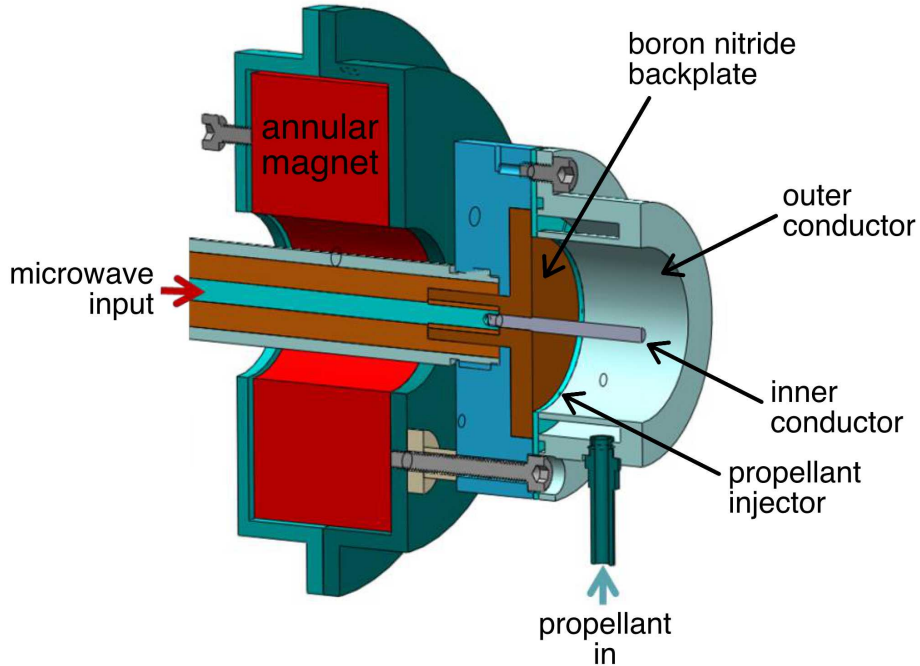


Figure 2.15: Diagram of ONERA's latest ECR thruster with 27.5 mm outer conductor diameter. Reproduced from S. Peterschmitt[36].

Erosion of the inner conductor was identified as the limiting factor of thruster lifetime. Graphite was chosen to be the material from which to make the inner and outer conductors due to its low erosion rate and high performance. Lifetime tests were extrapolated to predict that the inner conductor could last for over 1000 hours before it is critically eroded. A novel magnetic field topology was seen to increase thrust by 20 %. This used two opposing annular magnets to create a more divergent magnetic field.

Erosion marks on the back of the thruster suggested that a small fraction of plasma was not separating from the magnetic field lines and was impinging on the back of the thruster. By adding a dielectric plate around the exit of the thruster this flow is interrupted. This back-flowing plasma must have had a net negative charge, as this interruption resulted in a 40 % increase in thruster floating potential. This increase in ambipolar electric field strength then resulted in a 20 % increase in trust.

With all these insights, a larger thruster was built, that increased the diameter of the outer conductor from 27.5 mm to 70.0 mm, see figure 2.16. This allowed for more power and higher mass flow rates to be used without increasing the plasma density within the thruster to critical levels where cutoff could occur. A performance comparison between the 2015 electromagnet ECR thruster, the state of the art 2020 permanent magnet ECR thruster as well as its larger configuration can be seen in table 2.2. Unfortunately, some key design

elements of both 2020 thrusters that are responsible for their high performance remain the private and protected intellectual property of ONERA.[36]

Table 2.2: The performance improvement of the coaxial ECR thruster due to its development at ONERA from 2015[16] to 2020[36].

	Year	2015	2020	2020
Outer Conductor Diameter [mm]		27.0	27.5	70.0
Power [W]		30	25	146
Mass Flow Rate [mg/s]		0.10	0.10	0.25
Thruster Efficiency [%]		16	44	43
Thrust [mN]		1.0	1.5	5.6
Specific Impulse [s]		1000	1580	2310
Thrust to Power [mN/kW]		33	60	38

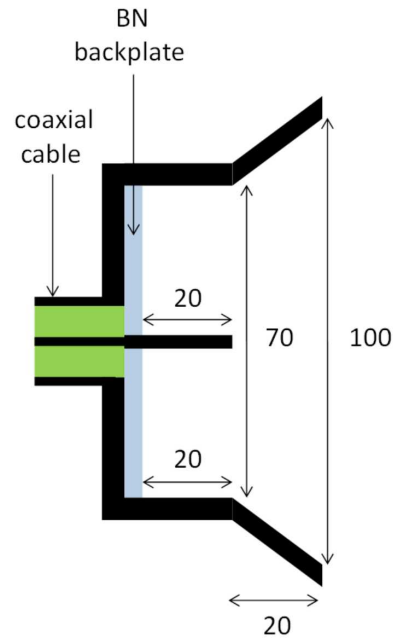
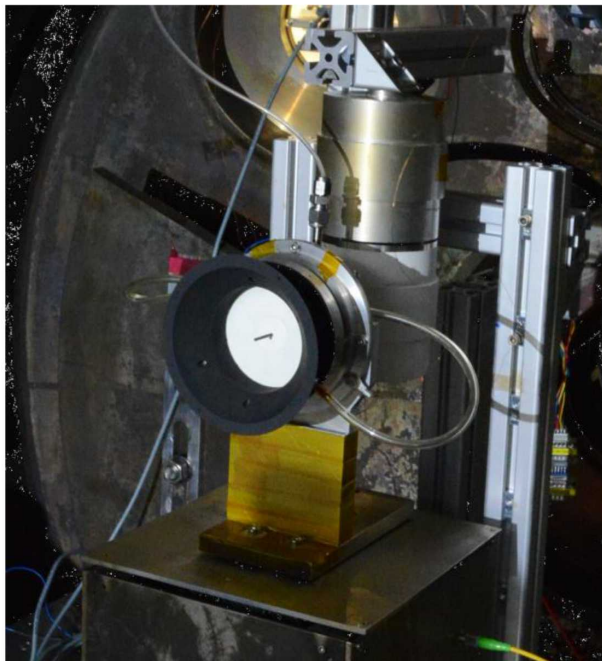


Figure 2.16: Photo and corresponding diagram of ONERA's 70 mm outer conductor diameter ECR thruster. The geometries shown here have been altered to protect the intellectual property of ONERA. All dimensions in millimetres. Reproduced from S. Peterschmitt[36].

2.5 University of Michigan's ECR Thruster

The University of Michigan has been developing their own ECR magnetic nozzle thruster. This development is summarised in a thesis by B.N. Wachs[24]. The novelty of this work largely lies in the use of two frequencies and pulsed waveforms. Advancements in our understanding of facility effects were also made, which are discussed in section 2.6.

As explained in sections 2.2 and 2.3, any increase in the energy imparted to electrons via ECR heating should result in a corresponding increase in ion energy and therefore thruster performance. A novel way to increase electron energy was proposed, in which two different frequencies are combined before being fed into the thruster. This has the effect of creating two distinct resonance regions in the thruster, see figure 2.17.

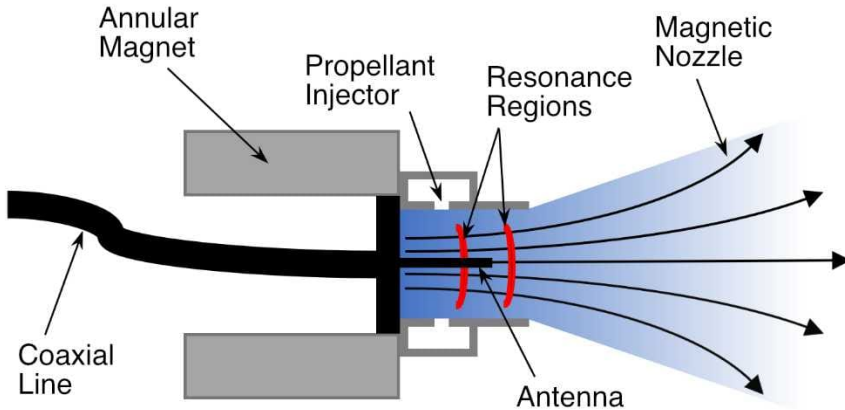


Figure 2.17: ECR thruster schematic showing the two resonance regions created by the two microwave frequencies. Reproduced from B.N. Wachs[58].

Unfortunately, adding a second microwave frequency did not improve thruster performance. By splitting microwave power between two frequencies, electric field intensity at the resonance region decreases. The conclusion was drawn that microwave power coupling was partially dependent on the local electric field intensity at the resonance region. This would also explain why waveguide ECR thrusters have such low power coupling efficiencies[59]. Similarly, pulsed waveforms did not show improved thruster performance. This was hypothesised to be caused by neutrals escaping the thruster between pluses, reducing mass utilisation efficiency.[24]

2.6 Facility Effects

The lack in development of ECR thrusters has been largely blamed on the thrusters unique relationship to facility effects. Conventional HET's and GIT's perform better in a vacuum chamber than they do in space. This is because they can ingest the background gas in a vacuum chamber, ionising it and accelerating it which artificially increases propellant mass flow rate and therefore the amount of thrust that is produced.

ECR magnetic nozzle thrusters however, experience decreased thrust when subject to this background gas. This is because unlike HET's and GIT's, which accelerate their propellant over a short distance within the thruster, acceleration in an ECR magnetic nozzle thruster occurs over a distance greater than several thruster radii outside of the thruster[60]. Background gas that collides with electrons in the plume decreases the strength of the ambipolar electric field that acts to accelerate the ions, thus decreasing thrust[26]. Due to the large distance over which acceleration occurs, smaller vacuum chambers can intercept the ambipolar electric field, which can also decrease its strength. Figure 2.18 shows how the thrust produced by an ECR thruster increases as background pressure is decreased. An increase in thrust is also observed when switching to a larger vacuum chamber.

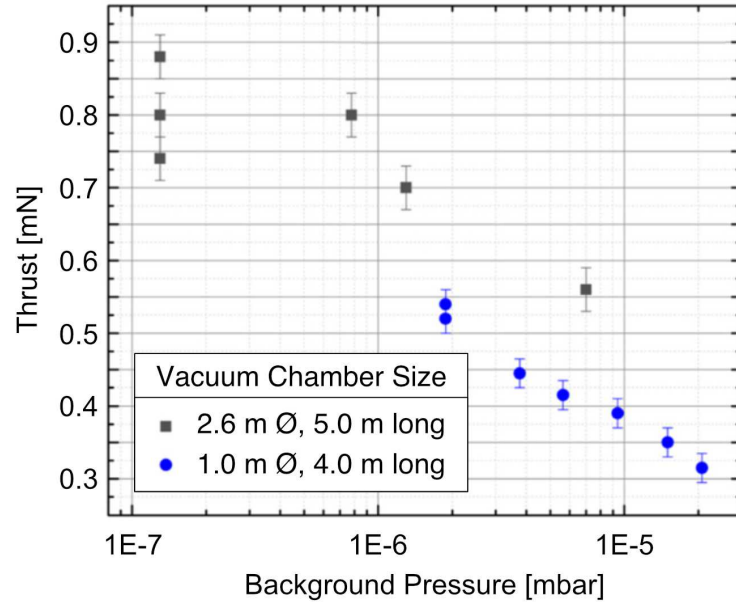


Figure 2.18: Thrust produced by the same ECR thruster at different background pressures and vacuum chamber sizes. Reproduced from V. Dèsangles et al.[7].

Given the limited size of the vacuum chambers used for ECR thruster research in 1965, as well as their limited pumping speed, it is no wonder that ECR thrusters displayed poor performance and were not investigated more thoroughly when they were first invented[11]. Since these first studies, the minimum achievable background pressure during testing has decreased from 3.3×10^{-5} mbar to 1.2×10^{-7} mbar, while vacuum chamber size has increased from 1.2 m diameter and 1.8 m long to 2.6 m diameter and 5.0 m long[11][7]. This has

significantly improved ECR thruster performance and has allowed for them to operate more similarly to how they would in space. However, the effect of facility size and background pressure on ECR thruster performance has yet to be fully characterised and understood. It is for this reason that it is essential that an ECR thruster be flown in space so that its in space performance can be measured and compared to its performance during ground tests.

2.6.1 Background Pressure

High background pressures result in a higher density of neutral particles that the electrons and ions in the plume get accelerated past. These neutral particles can act to decrease thrust by colliding with energetic ions and electrons in the plume. Ion-neutral collisions can result in the exchange of charge, ionising the neutral particle, while the ion gets deionised. The energy losses associated with this transfer of charge results in a reduction of thrust. However, experiments have shown that the energy loss due to these ion-neutral collisions are negligible when compared to the energy losses due to electron-neutral collisions in the plume. Electron-neutral collisions can cause the neutral particle to be ionised, resulting in the loss of the electron, or the electron can donate its energy to excite the neutral particle. Both types of these electron-neutral collisions act to decrease the total kinetic energy of the electrons, reducing the strength of the ambipolar electric field that accelerates the ions and generates thrust. An experimental study by B. Wachs[26] has shown that electron ionisation and excitation collisions results in 39 % of the power of the plume being lost at a background pressure of 3.5×10^{-5} mbar. Notably, this power loss reduces to just 1.6 % at 1.3×10^{-6} mbar, see figure 2.19.

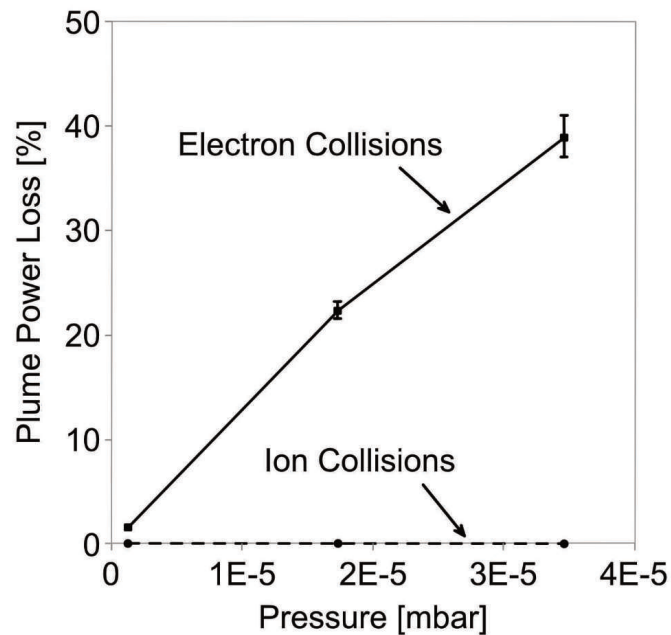


Figure 2.19: Percentage of plume power lost to electron collisions and ion collisions from 1.3×10^{-6} mbar to 3.5×10^{-5} mbar. Reproduced from B. Wachs[26].

Experimental tests by the ONERA French Aerospace Lab[7] show that thrust is reduced by 40 % when background pressure is increased from 2×10^{-6} mbar to 2×10^{-5} mbar, see figure 2.18. It can be seen from equations 1.9 and 1.7 that thrust is directly proportional to the square root of the power of the plume $T \propto \sqrt{P_{jet}}$. Therefore, this decrease in thrust of 40 % corresponds to a decrease in plume power of 64 %. This is a far greater power loss than would be suggested by the results in figure 2.19. It is evident then that more work needs to be done to be able to fully predict the behaviour of ECR thrusters under different background pressures. This will be essential to the eventual use of ECR thrusters in space, as a good prediction of their in-space performance will be required.

The pumping system used for all ECR thruster tests detailed in this thesis is capable of maintaining a background pressure between 6×10^{-6} mbar and 8×10^{-6} mbar, depending on the flow rate of the propellant through the thruster. This makes most results comparable to those taken by ONERA in their smaller vacuum chamber[36].

2.6.2 Facility Size & Conductivity

During testing at the ONERA French Aerospace Lab, it was noticed that an increase in thrust is experienced when the thruster is moved into a larger vacuum chamber[7]. This thrust increase is measured at approximately 0.15 mN and appears to remain constant over a range of background pressures, see figure 2.18. Extrapolating the data in figure 2.18 shows that switching to the larger chamber increases thrust by approximately 30 % at 2e-5 mbar, but only 20 % at 2e-6 mbar, indicating that facility size could have a larger impact on thruster performance at higher background pressures.

The vacuum chamber used for all ECR thruster tests detailed in this thesis is 3.0 m in length, and 1.5 m in diameter. This makes most results comparable to those taken by ONERA in their smaller 1.0 m diameter, 4.0 m long vacuum chamber. It should be noted however, that a lack of data means that no conclusions can be drawn about the effect of facility size on ECR thruster performance as of yet.

Studies at the University of Michigan have attempted to artificially reduce the facility size by introducing a steel plate downstream of the thruster[28]. This reduces the space that the plume has available to propagate downstream from over 5 meters to just 0.7 meters, however no significant change in thrust was measured. As background pressures were kept below 4×10^{-7} mbar, this apparent insensitivity to facility size could be due to facility size having a smaller effect at this low background pressure. The plate was then biased from -200 V to +200 V in an attempt to perturb the ambipolar electric field that acts to accelerate the ions. While this had no effect on the thrust produced, it did have a significant effect on the thruster's floating potential, suggesting that the ambipolar electric field in the plume changes with the plate to ensure that the gradient of the ambipolar electric field is maintained.

A recent study at ONERA[17] has found that covering the walls of their vacuum chamber with a dielectric film produced an increase in thrust. This is thought to be because the conductive walls of the vacuum chamber can allow for current to flow across magnetic field lines, effectively shorting out the ambipolar electric field. Adding a dielectric film prevents this, increasing thrust and making performance more representative of the thrusters in-space performance.

2.7 Thesis Objectives

Primary Objective: Find Novel Techniques to Enhance ECR Thruster Performance

Since the mechanism driving the high performance of ONERA's ECR thrusters remains unknown, developing a new approach to increase thruster performance is required for these thrusters to be commercially viable. Thruster efficiencies are currently $\sim 10\%$ [27][28] and likely need increasing to above 40 % to achieve commercial success.

Sub Objectives:

- 1. Increase thruster performance by decreasing magnetic field strength gradient...**
 - (a) using an electromagnet, see Ch. 5.**
 - (b) using a ferromagnetic material, see Ch. 8.**

As shown in section 2.2, the microwave energy that an electron absorbs when passing through the resonance region is inversely proportional to the magnetic field strength gradient at resonance, $|\frac{\partial B}{\partial x}|$, so decreasing the magnetic field strength gradient should increase the temperature of the electrons. In section 2.3 it was shown that the maximum kinetic energy of the ions is directly proportional to the temperature of the electrons at the thrusters exit. Therefore, decreasing the magnetic field strength gradient at resonance should result in a proportional increase to ion velocity and specific impulse, increasing the thruster performance.

- 2. Increase thruster performance by adding a magnetic mirror trap, see Ch. 6.**

Another way to increase the temperature of the electrons is to make them pass through the resonance region multiple times. The addition of a magnetic mirror trap to the exit of the thruster can reflect electrons back towards the resonance region, increasing their energy. These hotter electrons should result in a proportional increase to ion velocity and specific impulse, increasing the thruster performance.

- 3. Investigate the effect of resonance region location on thruster performance, see Ch. 7.**

The location of the resonance region within the thruster can determine how much microwave power can be delivered to the plasma. It also determines the fraction of plasma losses to the wall of the thruster, making it an important variable to characterise with respect to the thruster performance.

- 4. Increase thruster performance by adding a second microwave frequency, see Ch. 9.**

The addition of a second microwave frequency should produce two distinct resonance regions within the thruster. This has already been investigated by B. Wachs[61] and was found to not significantly improve thruster performance. However, the frequency difference between the two signals was never less than 50 MHz. The reduction of the frequency difference into the kHz range could act to merge the two resonance regions, creating one thickened resonance region that could increase thruster performance.

3 EXPERIMENTAL SETUP

This thesis presents multiple novel mechanisms designed to improve ECR thruster performance. In order to determine their effectiveness, thruster performance is measured directly using a thrust balance. ECR thruster performance is highly dependent on its environment. It is necessary then to recreate the environment of space as accurately as possible. This requires the use of a vacuum chamber and pumping system to reduce the background pressure to near zero. It is also desirable for the vacuum chamber to be as large as possible so as to reduce the interaction of the plasma plume with the chamber walls. The setup of the vacuum facility, the microwave line to deliver power to the thruster, and the thrust balance to measure thrust, is detailed in these first three sections:

3.1	Vacuum Chamber	44
3.2	Microwave Line	47
3.3	Torsional Thrust Balance	49

To better understand the thrust generating mechanisms described in sections 2.2 and 2.3, it is necessary to measure the properties of the electrons and ions in the thruster's plume. A Langmuir probe is a type of electron/ion collector that can be used to determine the energy of the electrons in the plume and the strength of the ambipolar electric field. A Faraday probe is a type of ion collector that can be swept through the plume to determine the total ion current that the thruster generates. It can also be used to determine the divergence of the plume and thus the divergence efficiency of the thruster. Lastly, a Retarding Potential Analyser (RPA) is a type of ion analyser that can be used to determine the energy of the ions. The setup and calibration of these instruments is detailed in these last three sections:

3.4	Langmuir Probe (Electron Measurements)	51
3.5	Faraday Probe (Ion Beam Measurements)	58
3.6	Retarding Potential Analyser (Ion Energy Measurements)	64



Figure 3.1: The “Daedalus” vacuum chamber within which all test campaigns were conducted.

3.1 Vacuum Chamber

Thruster tests were conducted within the “Daedalus” vacuum chamber at the University of Surrey’s Spacecraft Electric Propulsion Laboratory, see figure 3.1. The pumping system comprises a cryopump (Marathon CP-12, 3,600 l/s N₂) and a cryopanel (660 mm diameter, 16,800 l/s Xe[62]). These pumps use the energy absorbed by helium during its phase change to cool down metal panels to under 40 °K. This is cold enough that most xenon atoms that impinge on the panel immediately condense, sticking to the panel, which reduces the background pressure within the vacuum chamber. As can be seen from figure 3.2, 40 °K is cold enough to condense xenon at background pressures below 10⁻¹⁰ mbar. However, krypton will only condense at background pressures above 10⁻⁷ mbar, and argon will only condense at background pressures above 10⁻³ mbar. These minimum condensation pressures define the minimum pressures at which each propellant can be used. As the vacuum chamber in use cannot achieve background pressures below 10⁻⁶ mbar, both xenon and krypton can be used without the concern of significantly elevated background pressures.

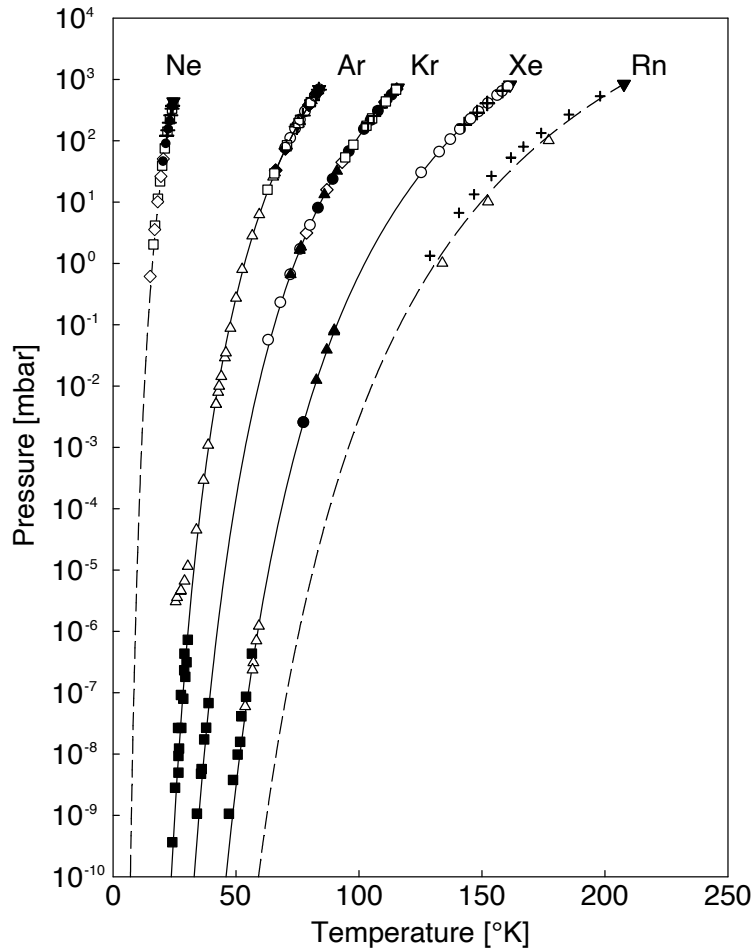


Figure 3.2: Sublimation curves of the rare gases. Reproduced from A. Ferreira[63].

Pressure readings are taken with a Penningvac PTR 90 pressure gauge that uses a cold cathode to measure pressures between 1×10^{-3} and 5×10^{-9} mbar. Pressure readings that are

taken with a non-zero propellant flow rate need to be corrected to account for the difference in gas properties. This is achieved using equation 3.1 [64], where p_c is the corrected pressure, p_i is the indicated pressure, p_{base} is the base pressure and κ_g is the gas correction factor. Gas correction factors for different gases can be found in table 3.1. Unfortunately, outgassing of H₂O from the vacuum chamber walls acts to significantly increase the minimum pressure achievable by this pumping system. The corrected background pressures for a range of different propellants and mass flow rates are shown in table 3.2.

$$p_c = \frac{p_i - p_{base}}{\kappa_g} + p_{base} \quad (3.1)$$

Table 3.1: Gas correction factors for a nitrogen calibrated pressure gauge.[65][66][67][68]

Gas	Gas correction factor (κ_g)
Xe	2.87
Kr	1.94
Ar	1.29
Air	1.00

Table 3.2: Corrected background pressures at given mass flow rates for xenon, krypton and argon. Six readings were taken for each flow rate with standard errors from 2×10^{-8} mbar to 3×10^{-7} mbar. Vacuum pump maintenance between test campaigns resulted in faster pumping speeds for the large ECR thruster. The base background pressure was 4.8×10^{-6} mbar for all tests.

Thruster(s)	Mass Flow Rate [mg/s]	Corrected Background Pressure [$\times 10^{-6}$ mbar]		
		Xenon	Krypton	Argon
AVS-UK & Small	0.08	6.4	-	-
	0.14	6.9	-	-
	0.25	7.7	-	-
Large	0.39	6.9	6.9	13.4
	0.49	7.6	7.6	14.7
	0.59	8.3	8.3	16.0

Three ECR thrusters have been tested. First a thruster developed by AVS-UK Ltd. in partnership with the University of Surrey was tested. Second, a small thruster was developed and tested. Third, a large thruster was developed and tested. I independently developed and tested both the small and large thrusters for this thesis. A diagram of the test configuration and equipment for the large thruster is shown in figure 3.3. The AVS-UK thruster and the small thruster used a similar test configuration to the large thruster, which is shown in appendix B. Photos of the two setups, highlighting their differences, are shown in figure 3.4. Chapter 4 presents results from all three thrusters. Chapters 5 and 6 present results from just the small thruster, and chapters 7, 8 and 9 present results from just the large thruster.

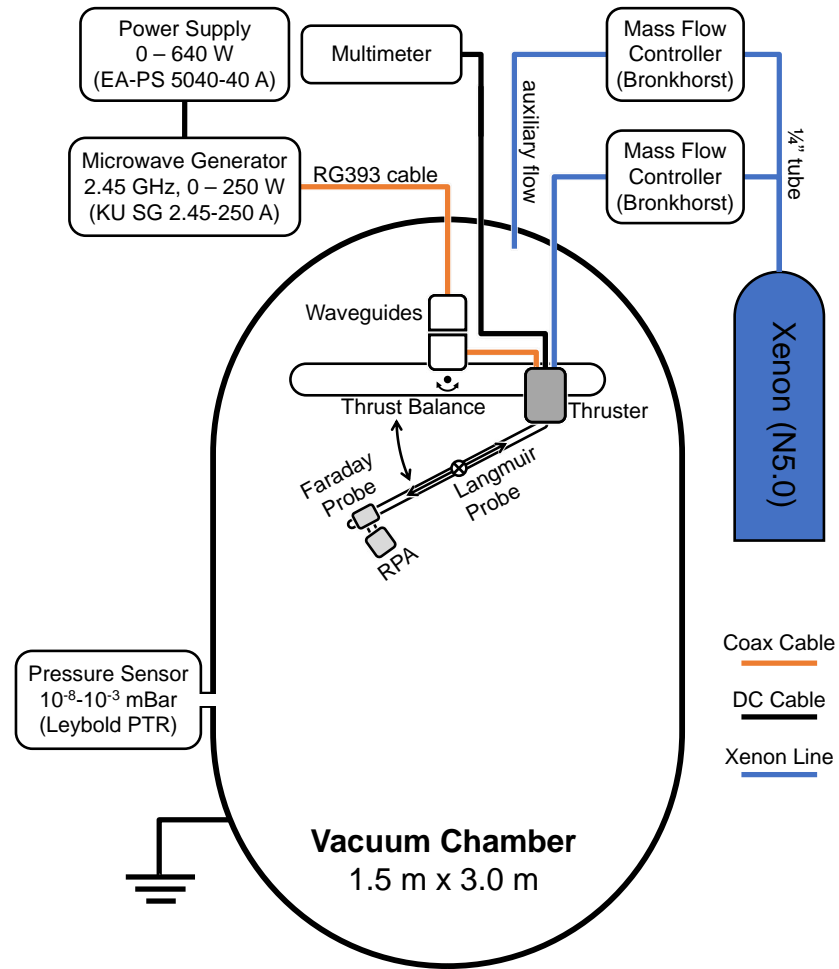


Figure 3.3: Diagram of the test configuration and equipment for the large ECR thruster.

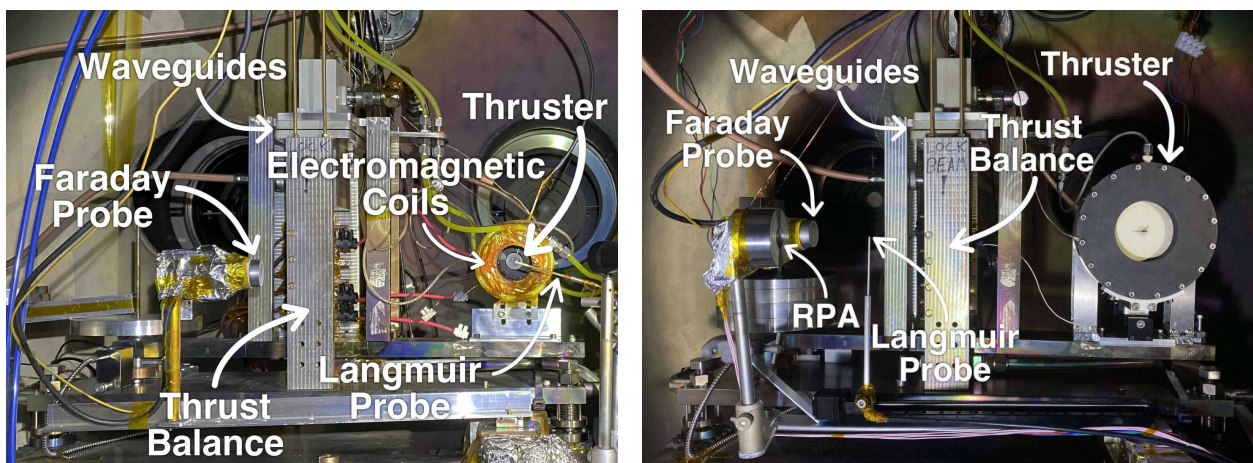


Figure 3.4: Test setup for the small ECR thruster (left) and large ECR thruster (right).

3.2 Microwave Line

A 2.40 GHz to 2.50 GHz solid-state microwave generator was used to produce up to 240 W of microwave power which is delivered to the thruster via coaxial cables, see figure 3.3. Forward power, P_{fwd} , is measured at the generator, but some of this power is lost to the coaxial cables, feedthrough and waveguides before it reaches the thruster. By replacing the thruster with an Anritsu MA24105A power meter and perfectly matched dummy load, it is possible to measure what fraction of the power is lost to the microwave line, see figure 3.5. This is known as the insertion loss, IL . The measured insertion loss of the microwave line was 0.39, meaning that the thruster receives 61 % of the forward microwave power produced by the microwave generator. When running the thruster, the load is the plasma within the thruster. If this load is not a perfectly matched 50 Ohms, some of the microwave power is reversed and travels back up the line. This reverse power can then be measured at the generator as P_{rev} . These readings of forward and reverse microwave power, as well as the insertion loss calculated earlier, allows for the microwave power delivered to the thruster, $P_{thruster}$, to be calculated, see equation 3.2.[27]

$$P_{thruster} = P_{fwd}(1 - IL) - \frac{P_{rev}}{(1 - IL)} \quad (3.2)$$

Sweeping the frequency of the microwaves between 2.40 GHz and 2.50 GHz is shown to vary the reverse power. Therefore a frequency is chosen that minimises P_{rev} , and thereby maximises $P_{thruster}$.

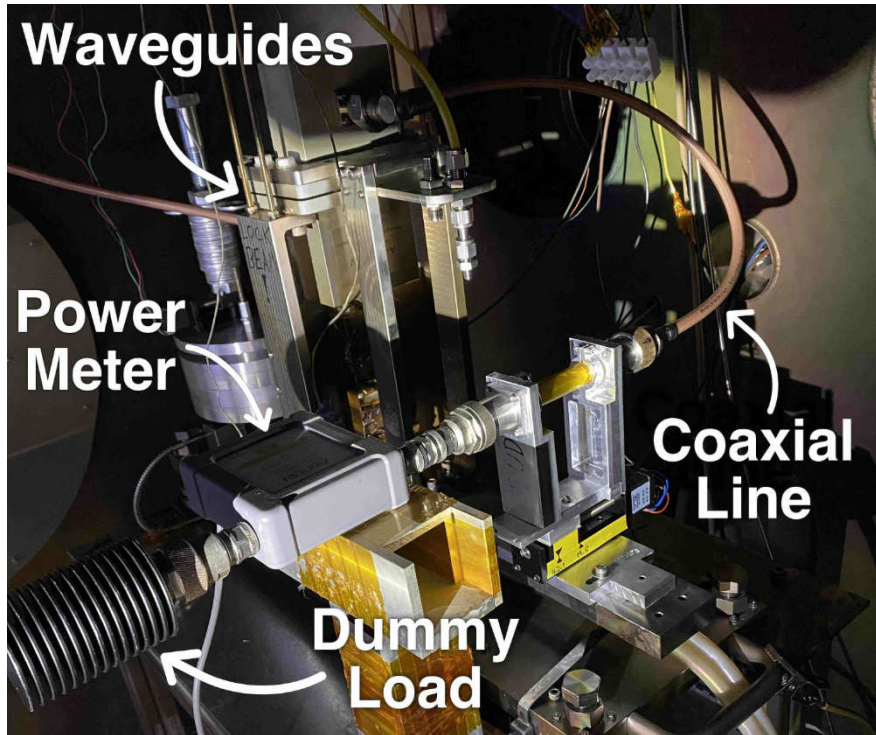


Figure 3.5: The replacement of the thruster with a power meter and dummy load to calculate the insertion loss, IL , of the microwave line.

Discharges in the Coaxial Line

Working with coaxial cables in vacuum was one of the most challenging and expensive parts of this thesis. This is because the connectors kept burning, resulting in a loss of power to the thruster. Almost all coaxial connectors have a gasket to provide weather sealing and prevent water or debris from getting inside a connection. However, these gaskets are not designed to withstand vacuum, and allow for air trapped in the connection to slowly vent to vacuum over time. When the connection is operating near its maximum power, the electric field produced between the inner and outer conductor can be strong enough to cause electron emission from the material's surface. At atmospheric pressure this is of no concern. At low pressures however, the mean free path of the electron can be larger than the distance between the inner and outer conductors, allowing for emitted electrons to impact the opposite surface. This causes more electrons to be emitted via secondary electron emission. This process repeats itself, increasing signal noise and heating the inside of the connector. This phenomenon is known as a multipactor discharge. The multipactor discharge does not destroy the connector itself, however it can vaporise some of the dielectric material inside of the connector. This creates a gas that can build up and subsequently breakdown[69]. If this ionisation breakdown is not stopped it can result in the total destruction of the connector, see figure 3.6. Ionisation breakdown can also occur due to trapped air in the connector that has not had sufficient time to vent.

The solution to this is to drill a small hole in the connector, allowing for any vaporised material to vent out. This prevents the build up of pressure within the connector that would lead to ionisation breakdown and the destruction of the connector. A single 1.0 mm diameter hole in an N-type connector was found to be sufficient to prevent the ionisation breakdown. However, imperfect connectors with a high Voltage Standing Wave Ratio (VSWR) could require more ventilation, and so four evenly spaced holes of 1.5 mm diameter were drilled in the connectors, see figure 3.7. No increase in insertion loss or reflected power was observed.

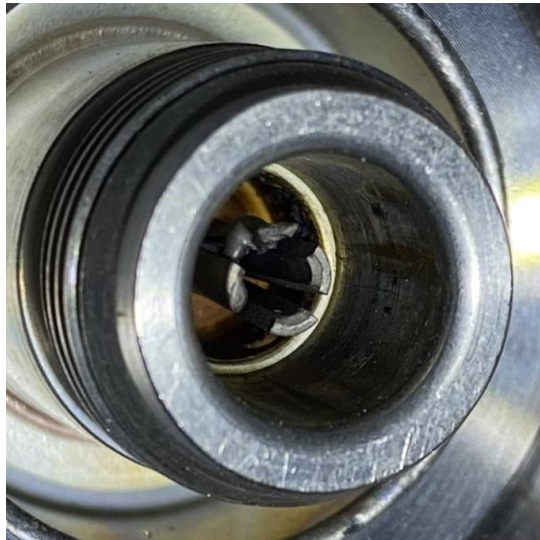


Figure 3.6: Photo of an unmodified N-type connector with burnt PTFE dielectric and melted inner conductor.



Figure 3.7: Photo of a correctly modified N-type connector with 1.5 mm diameter holes, indicated with red circles.

3.3 Torsional Thrust Balance

To measure thrust, the thruster was mounted to a torsional thrust balance[70], see figure 3.4. Thrust that is generated by the thruster pushes back on the arm of the thrust balance, rotating it about a central torsional pivot. As the displacement of this arm is directly proportional to the thrust, it can be used to calculate the thrust produced by the thruster. The stiff coaxial cables that carry the microwave power to the thruster act to reduce this displacement, reducing the accuracy of thrust measurements. As their stiffness is seen to change with temperature, this also adds a significant error to thrust measurements. Therefore, a pair of waveguides is used to wirelessly transmit the microwave power, increasing the accuracy of thrust measurements.

Measurements of displacement were taken using a PHILTEC muDMS125 optical fibre displacement sensor. To determine the relationship between displacement and thrust, it was essential to take measurements of displacement during the application of known force values to the balance. A Newport 8302-V piezo-motor was used to incrementally push a Novatech F329 load cell against the balance, imitating the force that the thruster would produce. By plotting the force required to move the balance a certain distance, the relationship between thrust and displacement is found, see figure 3.8.

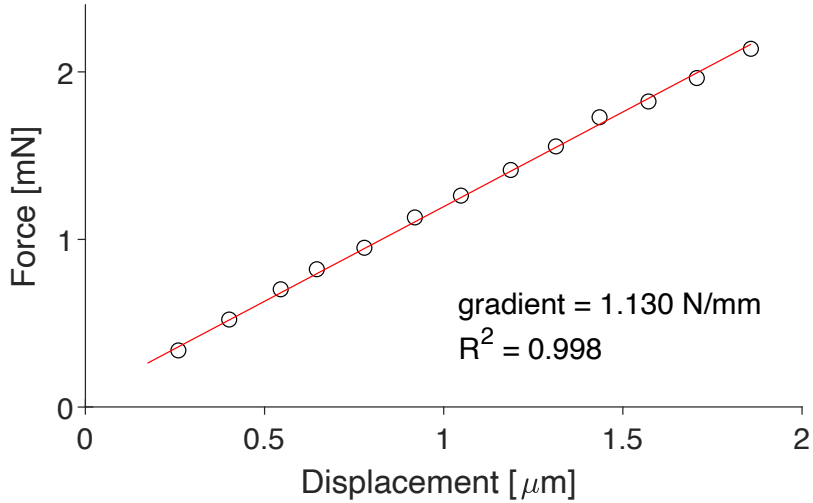


Figure 3.8: Torsional thrust balance calibration. A line of best fit is applied to thirteen individual measurement points. The gradient of this line defines the relationship between force and the displacement of the thrust balance.

To measure the force produced by the thruster, the thruster is ignited and kept lit until a thermal steady state is achieved. The microwave power to the thruster is then cut, such that the thrust balance returns to its point of equilibrium. Displacement measurements during this power cutoff are shown in figure 3.9, where the microwave power is cut at 47 seconds,

leaving the thrust balance to oscillate about its new equilibrium point. By averaging the data and fitting a line to the “power on” and “power off” sections separately, the displacement can be determined. This is known as a thrust step, due to the sudden step in the recorded displacement. Three thrust steps are taken for each test condition, and the displacement is averaged.

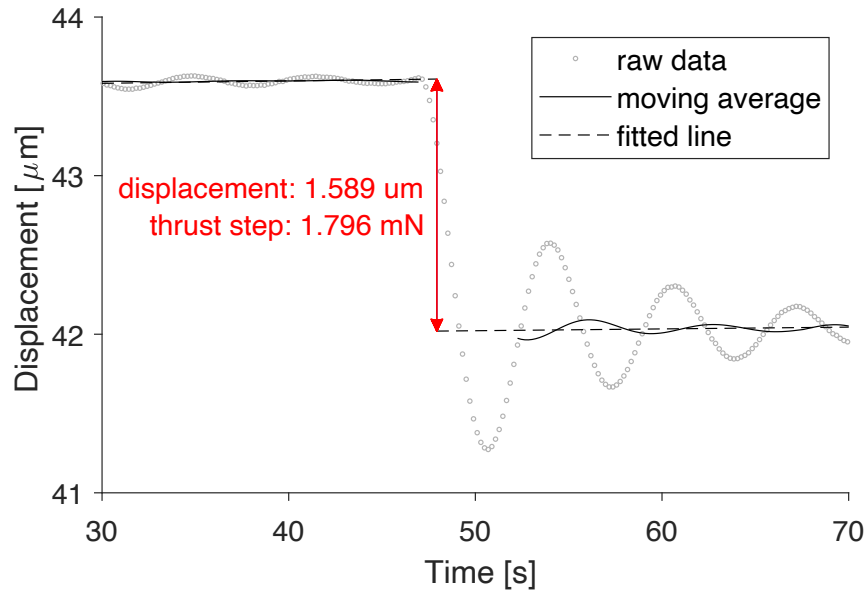


Figure 3.9: A thrust step measurement on the torsional thrust balance. Displacement before the thrust step is averaged and a line of best fit is applied. Displacement after the thrust step is also averaged and a line of best fit is applied. The displacement difference between these two lines is used to calculate thrust.

As the propellant mass flow rate to the thruster remains constant during this thrust step, the thrust measured does not include the thrust due to the expulsion of cold gas. This makes interpreting the thrust measurements easier, as there is one less variable to consider.

For the AVS-UK thruster and the small thruster, thermal steady state was unable to be obtained without burning the microwave connector. This decreased the accuracy of the thrust measurements. The small thruster also used an electromagnet that could be attracted to any ferromagnetic material in its surroundings. However, current to the electromagnet was kept constant during the thrust step so that there was no change to magnetic field strength that could affect the thrust measurements. The large thruster was able to obtain thermal steady state for all powers used, and did not implement electromagnets.

3.4 Langmuir Probe (Electron Measurements)

A Langmuir probe, also known as an electron probe, is an exposed section of wire that is placed within the plasma of a thruster, usually in the thruster's plume. By positively biasing the potential of the wire, electrons are attracted towards it and a current is generated. By analysing the change in current as the probe potential changes, many properties of the electrons can be determined, which helps us to characterise the plasma and better understand the mechanisms behind plasma thrusters. This relationship between probe bias potential and current is known as an I–V curve, an example of which is shown in figure 3.10.

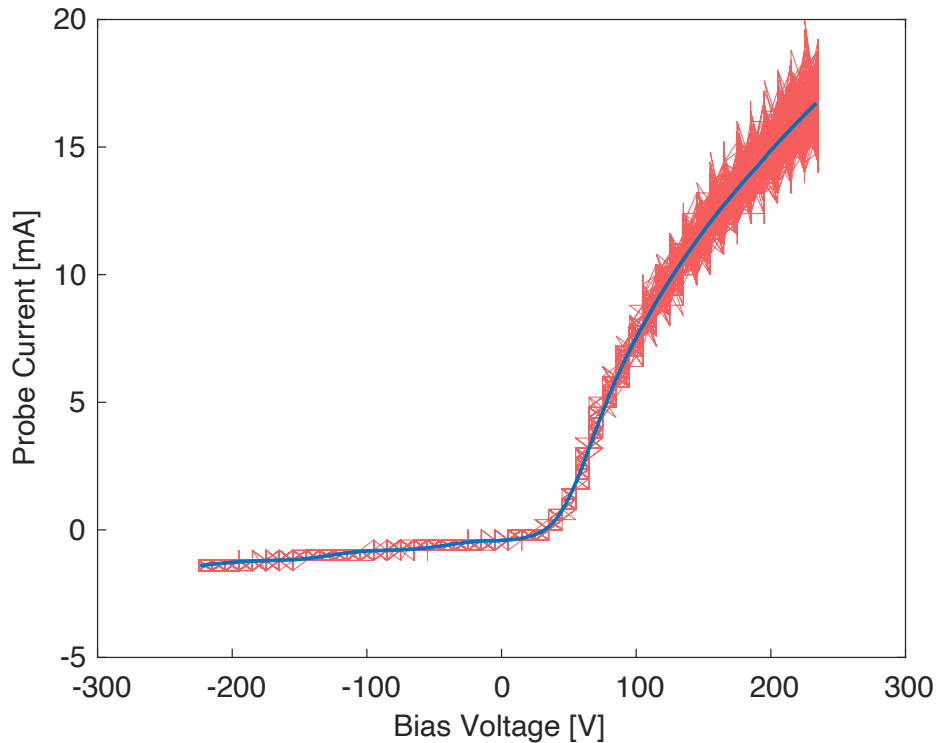


Figure 3.10: Langmuir probe current as a function of bias voltage with respect to the grounded vacuum chamber. Raw data in red, smoothed data in blue.

Probe Design

As the electrode of a Langmuir probe can be subject to high currents, it is made from tungsten wire with a melting point of 3,400 °C. An alumina ceramic tube houses the tungsten wire, shielding it from the plasma, such that only the exposed end of the wire can collect a current, this exposed end is referred to as the electrode. It is desirable to keep the size of the electrode as small as possible, so as to disturb the plasma as little as possible. This is especially important in an ECR magnetic nozzle thruster, as a probe could perturb the ambipolar electric field that is responsible for ion acceleration.

Electrons in a magnetic field spiral around magnetic field lines. The radius of the rotation of the electrons around a magnetic field line is known as its Larmor radius, r_L . The large ECR thruster has a much stronger magnetic field, giving the electrons a smaller Larmor radius, see

equation 3.3, where m is the electrons mass in kg, v_{\perp} is the electrons perpendicular velocity in m/s, e is the elementary charge in C and B is the magnetic field strength in T.

$$r_L = \frac{mv_{\perp}}{eB} \quad (3.3)$$

This smaller Larmor radius confines electrons more tightly to the magnetic field lines. This limits electron diffusion across magnetic field lines towards the probe, which reduces the electron current that the probe can collect. This had the effect of decreasing the signal to noise ratio making electron measurements less accurate for the large ECR thruster. To increase probe current, and therefore accuracy, the electrode length and radius is scaled up, see table 3.3. The probe is also always aligned perpendicular to magnetic field lines. This has the effect of maximising the collection area of the probe which also maximises probe current, minimising the effect of magnetic field strength on electron measurements.

Table 3.3: Dimensions and position of the Langmuir probe's electrode for the small ECR thruster whose results are presented in chapters 4, 5 and 6, and large ECR thruster whose results are presented in chapters 4, 7, 8 and 9.

	Electrode used for Small Thruster	Electrode used for Large Thruster
length [mm]	2.0	6.3
radius, r_{lp} [mm]	0.19	0.59
cross-sectional area, A_{lp} [mm ²]	0.76	7.43
distance downstream [mm]	49.0	variable

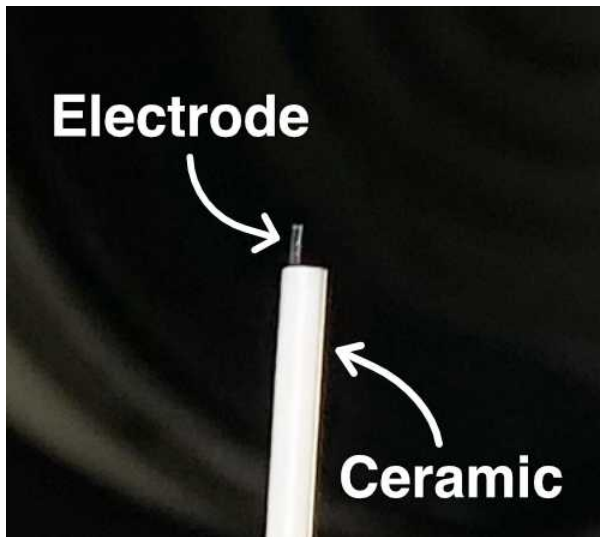


Figure 3.11: Langmuir probe for the small ECR thruster whose results are presented in chapters 4, 5 and 6.

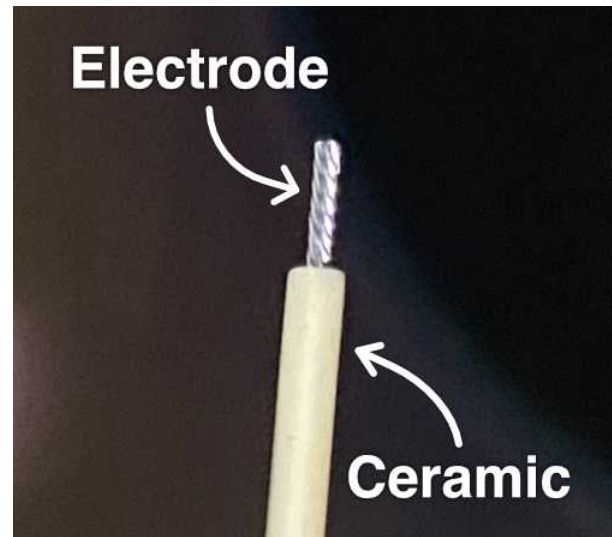


Figure 3.12: Langmuir probe for the large ECR thruster whose results are presented in chapters 4, 7, 8 and 9.

Plasmas that are generated using a Radio Frequency (RF) method can induce an RF signal in the electrode. In order for this to not decrease the accuracy of electron measurements via a decreased signal to noise ratio, it is necessary to compensate for the RF signal. This can be achieved by adding inductors into the probe circuitry to filter out these high frequency signals, this is known as an RF choke. Fortunately, the frequency of ECR plasmas is so high that the probe does not pick them up and no compensation is required.[71]

Operation

The Langmuir probe circuitry that is used to record the I-V curve was developed by M. Tisaev.[72]

First, a triangular wave is generated using a Thandar TG2001 function generator. This is then amplified using a KEPCO BOP 500M bipolar amplifier which biases the electrode from -235 V to +235 V with respect to chamber ground. This large voltage range was selected due to the high plasma potential of the plume that can reach up to 130 V. The electrons that are attracted towards the electrode generate a current in the probe. A shunt resistor is used to convert the collected probe current into a voltage that can be measured. An Analog Devices AD8479TRZ-EP differential amplifier is then used to remove the common mode voltage, producing a voltage relative to ground that is directly proportional to the probe current. This voltage is measured with a Rohde & Schwarz RTC1002 Oscilloscope, alongside the triangular wave bias. This allows for the measured voltage, which is a measure of the probe current, to be plotted as a function of the probe bias as seen in figure 3.10.

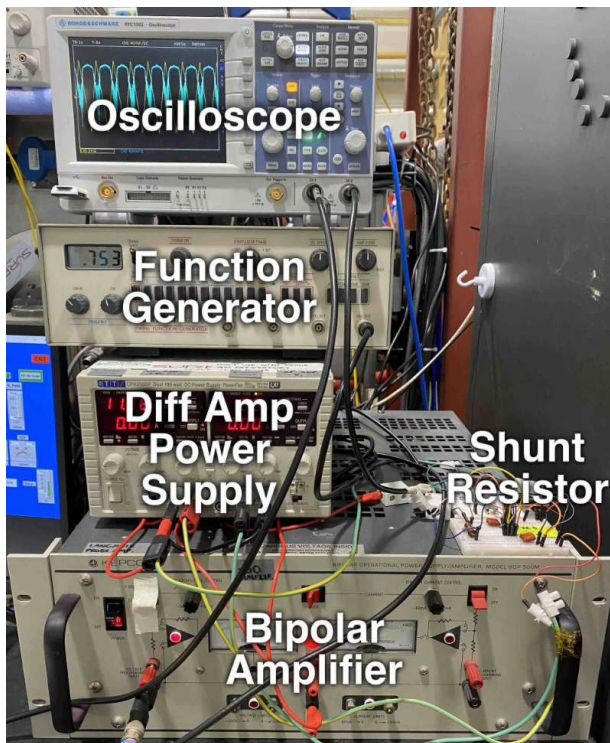


Figure 3.13: Photo of the equipment used to operate the Langmuir probe.

Data Processing

“Recommended Practice for Use of Langmuir Probes in Electric Propulsion Testing” by R.B. Lobbia et al.[73] guided the Langmuir probe data processing outlined in this section. For each operating point, the probe potential was swept from -235 V to +235 V with respect to chamber ground eight times, with each sweep taking 0.8 seconds to complete. The data processing outlined in this section was conducted on each of these sweeps individually. This results in eight values for each plasma property, from which the mean and standard error are calculated to assess the accuracy of each value.

By plotting the raw current data as a function of the raw voltage data, the probe current profile can be obtained, see the red line in figure 3.10. The probe current profile contains significant noise, so a Savitzky-Golay filter is used to produce an I–V curve, see the blue line in figure 3.10. The Savitzky-Golay filter was chosen, as other filters break down at the beginning and end of the data set, causing the curve to sporadically diverge from its path.

The first property that can be found from figure 3.10 is the floating potential of the plasma. This is found by identifying the bias voltage of the probe at which the probe current is zero, see the red circle in figure 3.14. This is the voltage at which there is no net movement of charge on or off the probe. The probe attracts a small number of positive ions when biased below the plasma potential (plasma potential is the average potential in the space between charged particles in a plasma, a value for which will be found later). This ion current is responsible for the linear slope that is seen when the bias voltage drops below the floating potential. It is necessary to remove this ion current from the data to obtain the electron current of the probe (the current due to electrons only). A line of best fit is applied to the data that lies beneath the floating potential, see the red dotted line in figure 3.14. This line of best fit is then subtracted from the data to obtain the electron current, see figure 3.15. This is a crude approximation of ion current which will be refined later. The plasma potential is then defined as the voltage at which the derivative of the electron current is at its maximum, see figure 3.16.

Electron temperature is a measure of the average kinetic energy of the electrons. To find electron temperature, the natural logarithm of electron current is plotted against bias voltage. A line of best fit is applied to the data that lies between the floating potential and the plasma potential. The electron temperature is defined as the inverse of the gradient of this line of best fit, see equation 3.4, where T_e is the electron temperature in eV, I_e is the electron current in A and ϕ_B is the bias voltage in V.

$$T_e = \left(\frac{d \ln I_e}{d \phi_B} \right)^{-1} \quad (3.4)$$

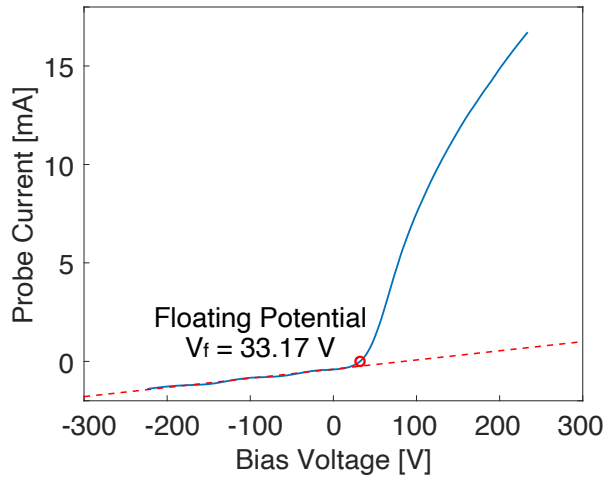


Figure 3.14: Langmuir probe current as blue line. Ion current as red dashed line. The ion current is a line of best fit applied to the data that lies beneath the floating potential.

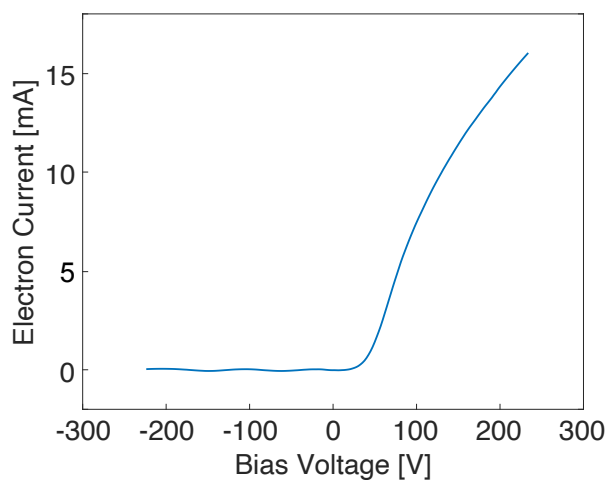


Figure 3.15: Electron current as a function of bias voltage. The electron current is the probe current minus the ion current.

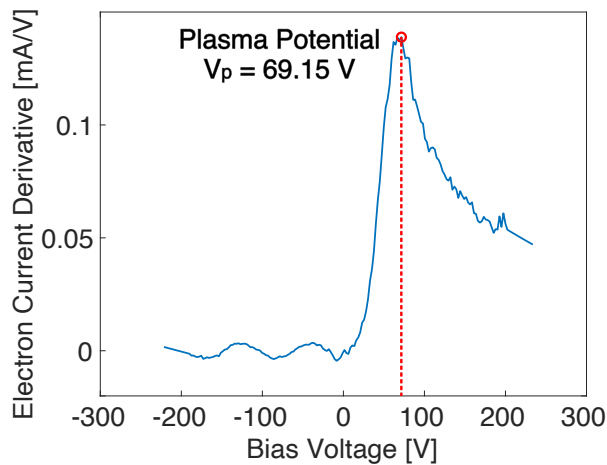


Figure 3.16: Electron current derivative as a function of bias voltage. Plasma potential defined by highest point, red circle.

Electron saturation current, $I_{e,sat}$, is defined as the electron current at the point where the bias voltage equals the plasma potential, figure 3.15 can be used to find this value. Electron density can then be computed using equation 3.5, where n_e is electron density in m^{-3} , e is the elementary charge in C, A_{lp} is the collection area of the probe in m^2 (see table 3.3), m_e is the electron mass in kg and T_e is electron temperature in eV.

$$n_e = \frac{I_{e,sat}}{eA_{lp}} \sqrt{\frac{2\pi m_e}{eT_e}} \quad (3.5)$$

As electrons are more mobile than ions, when the electrode is inserted into the plasma the electrons have a higher flux in/out of the electrode. This biases the surrounding plasma, creating an electric field in a region around the electrode known as the Debye sheath. The Debye length is a measure of the thickness of this sheath and can then be calculated from equation 3.6, where λ_D is Debye length in m, ε_0 is the permittivity of free space in Fm^{-1} , T_e is electron temperature in eV and e is the elementary charge in C.[29]

$$\lambda_D = \sqrt{\frac{\varepsilon_0 T_e}{n_e e}} \quad (3.6)$$

By dividing the Langmuir probe's electrode radius by the Debye length, the relative thickness of the sheath can be determined, see table 3.4, where r_{lp} is the probe radius in m and λ_D is Debye length in m.

Table 3.4: The values of the probe radius to Debye length ratio that define the sheath. Different data processing methods are required for each of the three different sheaths.

$\frac{r_{lp}}{\lambda_D} < 3$	= Orbital Motion-Limited (Thick) Sheath
$3 < \frac{r_{lp}}{\lambda_D} < 50$	= Transitional Sheath
$50 < \frac{r_{lp}}{\lambda_D}$	= Thin Sheath

The calculation of ion density is highly dependent on the size of the probe's sheath. During testing of the ECR thruster, the probe radius to Debye length ratio was found to always lie beneath three. Therefore an orbital motion-limited sheath can be assumed. Ion density can now be calculated using equation 3.7. Note that this equation can only be used when an Orbital Motion-Limited (thick) sheath is assumed, where n_i is ion density in m^{-3} , A_{lp} is the collection area of the probe in m^2 , m_i is ion mass in kg, e is the elementary charge in C, I_{probe} is the probe current in A and ϕ_B is the bias voltage in V. Note that equation 3.7 is only accurate when an orbital motion-limited sheath is assumed and a cylindrical probe is used.[73]

$$n_i = \frac{1}{2\sqrt{\pi}A_{lp}} \sqrt{2\pi m_i} e^{-(3/2)} \left[-\frac{dI_{probe}^2}{d\phi_B} \right]^{1/2} \quad (3.7)$$

$[-dI_{probe}^2/d\phi_B]$ is found by plotting I_{probe}^2 against ϕ_B for all values of ϕ_B below the floating potential and applying a line of best fit. $[-dI_{probe}^2/d\phi_B]$ in equation 3.7 can then be substituted for the gradient of this line of best fit.

When the sheath around the Langmuir probe electrode is thin, the assumption can be made that all ions entering the sheath are collected by the probe. However, when the sheath is thick, the collection of the ions is orbital motion-limited. This means that the proportion of ions entering the sheath that also reach the probe electrode is dependent on probe bias as

well as the angular momentum and energy distribution of the ions. As the sheath has been determined to be thick, see table 3.4, ion current can be calculated from equation 3.8, where I_i is ion current in A, e is the elementary charge in C, n_i is ion density in m^{-3} , A_{lp} is the collection area of the probe in m^2 , ϕ_p is plasma potential in V, ϕ_B is bias voltage in V and m_i is ion mass in kg. Note that equation 3.8 is only accurate when an orbital motion-limited sheath is assumed, and a cylindrical probe is used.

$$I_i(\phi_B) = \frac{en_i A_{lp}}{\pi} \sqrt{\frac{2e(\phi_p - \phi_B)}{m_i}} \quad (3.8)$$

This new ion current approximation can then be plotted on figure 3.14 to create figure 3.17.

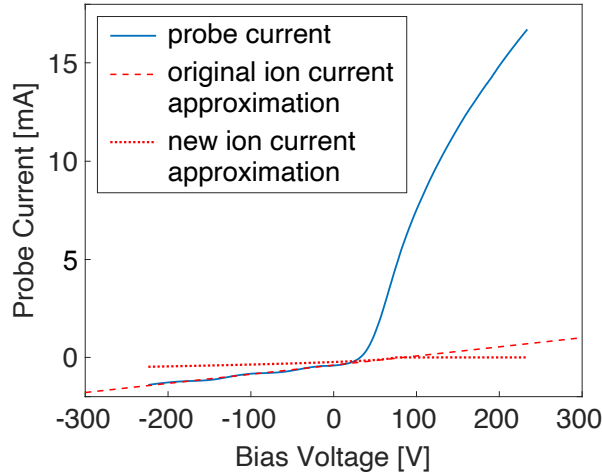


Figure 3.17: Probe current as a function of bias voltage. Comparing the original ion current approximation against the new ion current approximation.

As can be seen from figure 3.17, the new ion current approximation calculated from equation 3.8 is different to the original ion current approximation. By subtracting this new ion current from the probe current, a new electron current profile can be found. This means that all plasma properties calculated from the electron current now need recalculating.

The Electron Energy Distribution Function (EEDF) can now be calculated from equation 3.9, where \mathcal{E} is the electron energy in eV and is calculated as the local plasma potential minus the probe bias potential, e is the elementary charge in C, A_{lp} is the collection area of the probe in m^2 , m_e is the mass of an electron in kg and $\frac{d^2 I_e}{d\mathcal{E}^2}$ is the second derivative of the electron current. The EEDF is a probability density function that describes the energy distribution of the electrons.[73]

$$f(\mathcal{E} = \phi_p - \phi_B) = \frac{2}{e^2 A_{lp}} \sqrt{2m_e e \mathcal{E}} \frac{d^2 I_e}{d\mathcal{E}^2} \quad (3.9)$$

3.5 Faraday Probe (Ion Beam Measurements)

A Faraday probe is a type of ion probe that measures the current density of the ions in a thruster's plume. By negatively biasing a metallic disk, electrons are repelled, such that the disk only collects ions. The current generated by this influx of ions can be used to calculate the ion current density in the thruster's plume. By rotating the probe 90° about the thruster such that it starts by facing the plume head on, and ends facing the side of the thruster, the thruster's plume can be mapped. This can be used to determine the divergence of the plume, as well as the total ion current of the plume.

Probe Design

The Faraday probe detailed in this section was developed by S. Masillo.[74]

The Faraday probe comprises a cylindrical collector that is housed within a coaxial guard ring, see figure 3.18. Both are biased to the same negative potential so as to repel electrons and collect only ions. The guard ring acts to shield the sides of the collector, such that ions only impinge on the front face of the collector. In addition, the guard ring creates a uniform sheath in front of the collector, limiting edge effects that could affect the collected current.



Figure 3.18: Faraday probe collector and coplanar guard ring.

The guard ring and collector are both made from high-purity molybdenum due to its low sputter erosion rate and low Secondary Electron Emission (SEE) yield. Their dimensions are shown in table 3.5. The 0.30 mm gap between the collector and the guard ring is large enough to keep them electrically isolated, while being small enough that only a small fraction of ions incident on the probe will fall down this gap. The ions that fall into this gap are accounted for during data processing.

Table 3.5: Faraday probe dimensions.

Guard Ring	inner radius, r_{gr} [mm]	10.30
	height, h_{gr} [mm]	10.00
Collector	radius, r_c [mm]	10.00
	height, h_c [mm]	10.00

For the small thruster whose results are presented in chapters 4, 5 and 6, the Faraday probe is mounted at a radius of 277 mm from the thruster. For the large thruster whose results are presented in chapters 4, 7, 8 and 9, the Faraday probe is mounted at a radius of 427 mm from the thruster. A LabVIEW script was used to control and record the position of the probe with respect to the collected current. A TTi 1604 digital multimeter was used to measure the current of the collector.

Data Processing

The probe current measured in testing needs to be converted into ion current density in order for it to be comparable with Faraday probe measurements in other facilities. Ion current density can be calculated from equation 3.10, where j is the ion current density in Am^{-2} , I_{FP} is the Faraday probe current in A, A_c is the cross-sectional area of the collector face in m^2 , κ_G is the correction factor for ions collected in the gap between collector and guard ring, and κ_{SEE} is the correction factor for secondary electron emission at the collector surface.[75]

$$j = \frac{I_{FP}}{A_c + \kappa_G} \kappa_{SEE} \quad (3.10)$$

A_c can be calculated from the value of r_c in table 3.5, where $A_c = \pi r_c^2$. κ_G can be calculated from equation 3.11, where r_{gr} is the guard ring inner radius in m, h_c is the collector height in m, and h_{gr} is the guard ring height in m.

$$\kappa_G = \pi(r_{gr}^2 - r_c^2) \left(\frac{2\pi r_c h_c}{2\pi r_c h_c + 2\pi r_{gr} h_{gr}} \right) \quad (3.11)$$

κ_{SEE} can then be calculated from equation 3.12, where Ω_k is the ion current fraction of the k^{th} ion species, γ_k is the SEE yield from the k^{th} ion species, and Z_k is the k^{th} ion species charge state, see table 3.6.

$$\kappa_{SEE} = \frac{1}{1 + \sum_k \frac{\Omega_k \gamma_k}{Z_k}} \quad (3.12)$$

Multiply charged ions are produced when a particle loses more than one electron. As these can increase the collector current it is important to know what fraction of the plume contains multiply charged ions, so that this increase in collector current can be accounted for. A.J. Sheppard et al.[76] has used an E×B probe (ion velocity filter) to determine the ion

species composition of an ECR thruster. They found that when using xenon propellant, the plume is comprised almost entirely of singly charged ions, with no evidence of triply charged ions. Doubly charged ions comprised only 4 % of the collected current on average, see table 3.6. Importantly, the ion species composition seemed not to vary with changing mass flow rate to power ratio.

Table 3.6: Ion current fraction for an ECR thruster[76] and SEE yield of molybdenum[75].

Ion charge state	ion current fraction	SEE yield of molybdenum
Z_k	Ω_k	γ_k
+1	0.96	0.022
+2	0.04	0.20

Using the data from table 3.6, κ_{SEE} is calculated to be 0.98. This allows for the calculation of ion current density from the measured probe current using equation 3.10. Ion current density can then be mapped at different points throughout the plume to determine how the ion beam current and ion beam shape changes under different operating conditions.

Assuming that the plume is axially symmetric and that the ions travel radially out from a point source, the total ion beam current can be calculated by numerically integrating the ion current density across the rotation of the probe, see equation 3.13, where r_{fp} is the Faraday probe's radius of rotation in m, j is the ion current density in Am^{-2} and θ_{fp} is the Faraday probe's angle of rotation.[75]

$$I_{beam} = 2\pi r_{fp}^2 \int_0^{\frac{\pi}{2}} j(\theta_{fp}) \sin(\theta_{fp}) d\theta_{fp} \quad (3.13)$$

By adding the term $\cos(\theta_{fp})$, the ion beam current that is travelling axially with respect to the thruster can be calculated, see equation 3.14, where I_{axial} is the axial ion beam current in A.

$$I_{axial} = 2\pi r_{fp}^2 \int_0^{\frac{\pi}{2}} j(\theta_{fp}) \cos(\theta_{fp}) \sin(\theta_{fp}) d\theta_{fp} \quad (3.14)$$

The half-angle divergence of the beam, θ_b , can now be calculated from equation 3.15.

$$\theta_b = \cos^{-1} \left(\frac{I_{axial}}{I_{beam}} \right) \quad (3.15)$$

Beam divergence efficiency can then be calculated using equation 1.12. Unfortunately the ratio of single, double and triple charged ions in the plume was not measured, so accurate calculations of mass utilisation efficiency or thrust from this Faraday probe data are not possible. Calculations of mass utilisation efficiency from Faraday probe data regularly exceeded unity, indicating at a high fraction of multiply charged ions in the plume[77]. Additionally, Faraday probes have been seen to overestimate the thrust of ECR magnetic nozzle thrusters by between 20 % and 80 %[36]. This overestimation far exceeds what is expected for HETs[78] and is thought to be due to the peculiarities of the magnetic nozzle.

Probe Bias for Small Thruster

In order for the Faraday probe to measure the ion current in the plume, both the collector and guard ring must be biased to a negative voltage to repel the electrons and collect only ions. To determine what voltage to use, the bias voltage is swept down from 0 V. This repels more electrons, increasing the probe current. When decreasing the bias voltage results in no further increase in probe current, all electrons have been repelled and the probe is in “ion current saturation”. A probe bias voltage too large could perturb the plume and affect the performance of the thruster itself, therefore the lowest bias voltage at which ion current saturation is achieved should be used.[75]

In figure 3.19, probe current is plotted against bias voltage. This allows for us to see when the probe achieves ion current saturation. This bias voltage sweep is conducted at five different angles throughout the plume to ensure that the probe achieves ion current saturation throughout the whole plume. For conventional hall-effect and gridded ion thrusters it is generally accepted that ion current saturation has been achieved when the gradient of these curves are all less than 1 %/V. This is usually achieved at bias potentials between -10 V and -30 V[79]. As seen from figure 3.19, this condition is achieved for all rotation angles at approximately -50 V. However, the probe current does not plateau and instead continues to rise. This is due to the presence of high energy electrons in the plume of ECR thrusters, which can require bias voltages up to 300 V to reach ion current saturation[10].

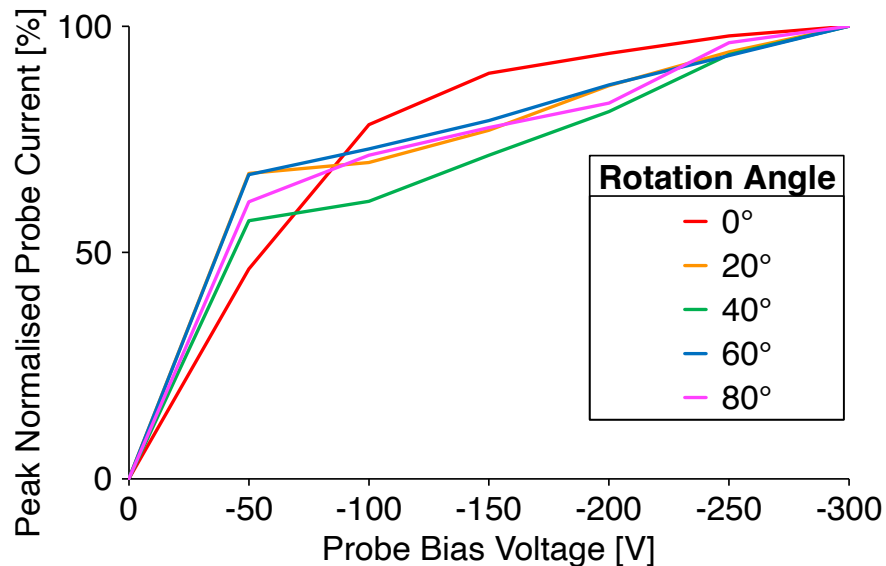


Figure 3.19: Peak normalised probe current as a function of bias voltage at different probe rotation angles. Small ECR thruster, 73 W thruster power, 0.10 mg/s xenon mass flow rate, 2 A electromagnet current.

A better way to find the bias voltage that achieves “ion current saturation” is then to map the current of the plume for different bias potentials, see figure 3.20. Here it can be seen that a highly energetic electron population in the centre of the plume creates a dip in collector current at a rotation angle of 0° . This is thought to be due to highly energetic electrons not being repelled from the probe at these low bias voltages. This dip is eliminated at a bias voltage of -300 V. The apparent elimination of this electron artefact lead to the decision to select -300 V as the Faraday probe bias voltage for the small ECR thruster.

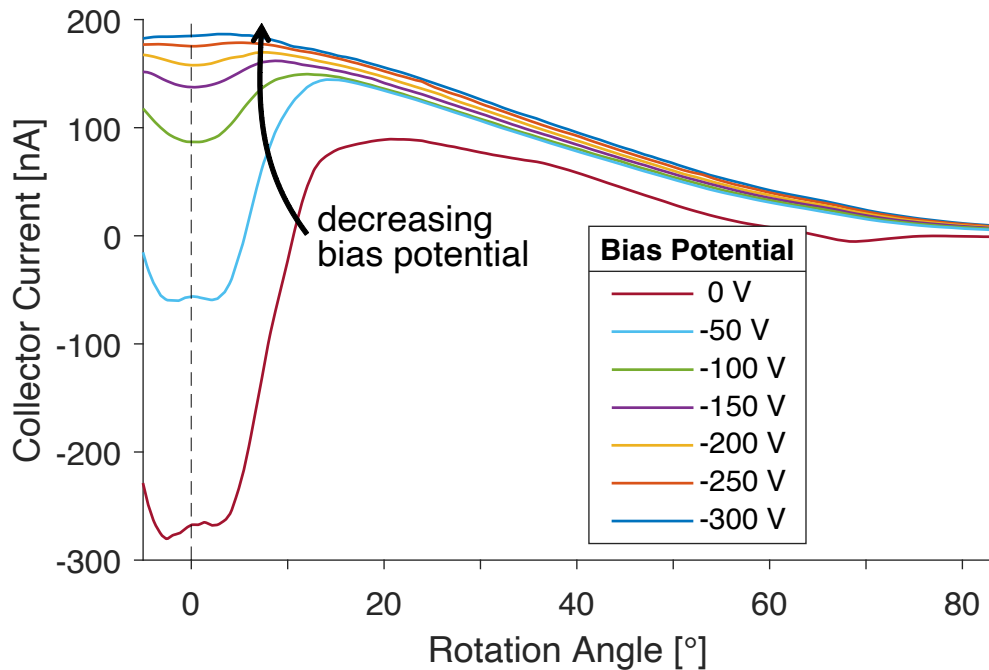


Figure 3.20: Faraday probe collector current as a function of rotation angle for different bias potentials. At 0° the probe is aligned with the centreline of the thruster. Small ECR thruster, 73 W thruster power, 0.10 mg/s xenon mass flow rate, 2 A electromagnet current.

Probe Bias for Large Thruster

The correct probe bias also needed to be found for the large ECR thruster, whose results are presented in chapters 4, 7, 8 and 9. To do this, the current in the plume was mapped at different bias potentials, see figure 3.21. The slight asymmetry around the 0° rotation angle is likely due to the fact that the thruster is not located in the centre of the vacuum chamber and is closer to the wall on one side, see figure 3.3.

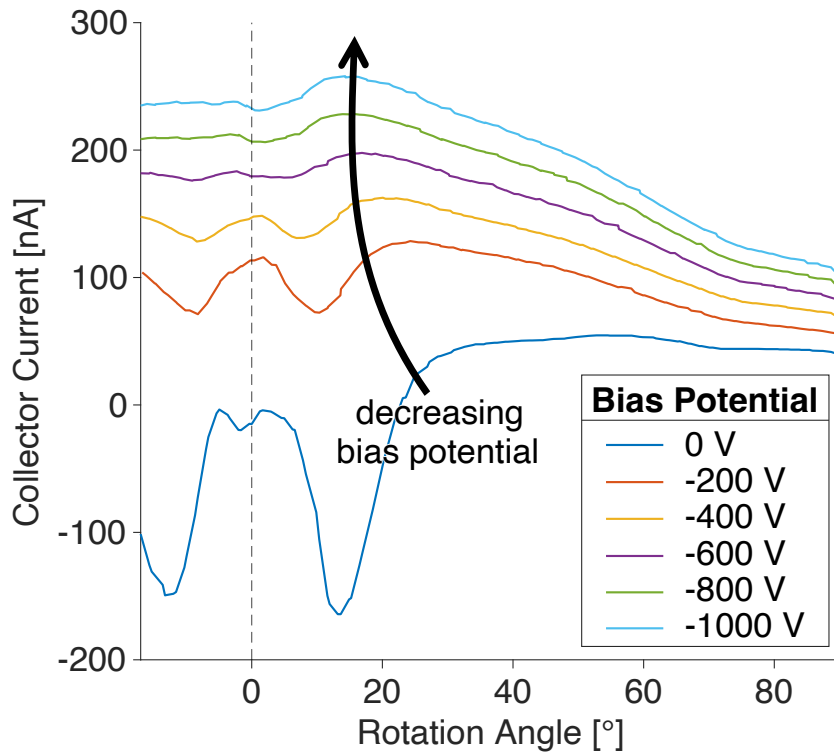


Figure 3.21: Faraday probe collector current as a function of rotation angle for different bias potentials. At 0° the probe is aligned with the centreline of the thruster. Large ECR thruster without iron ring, 145 W thruster power, 0.39 mg/s xenon mass flow rate.

Unlike the current map for the small thruster seen in figure 3.20, the current map for the large thruster in figure 3.21 does not appear to converge. A TTI 1604 digital multimeter was used to measure collector current, which has a maximum bias voltage of -1000 V , limiting the bias potential of the probe. An annular trough in ion current is observed at 0 V bias potential. This indicates that the high energy electrons responsible for this trough are not generated uniformly within the thruster's chamber, but are instead concentrated in an annular shape. A probe bias potential of -1000 V was chosen to be used for the large thruster as this is believed to achieve the most accurate measurement of ion current. This disparity in probe bias potential should be considered when comparing Faraday probe results between the small and large thrusters. However, the thruster's insensitivity to downstream potential, as described in section 2.6.2, means the thruster's performance is unlikely to be affected by the probes highly negative potential[28].

3.6 Retarding Potential Analyser (Ion Energy Measurements)

A Retarding Potential Analyser (RPA), also known as a Retarding Field Energy Analyser (RFEA) or gridded energy analyzer, is used to measure the energy distribution of the ions in a thruster's plume. By making the assumption that the ions are singly charged and all of their energy is kinetic in the direction of the probe's axis, this ion energy distribution can be used to find the velocity of the ions, see equation 3.16, where v_i is the ion velocity in m/s, e is the elementary charge in C, E_i is ion energy in J and m_i is the ion mass in kg.[76]

$$v_i = \sqrt{\frac{2E_i}{m_i}} \quad (3.16)$$

Thrust and specific impulse are both directly proportional to the velocity of the ions, see equations 1.4 and 1.5 where v_{ex} can be substituted for v_i . Therefore, directly measuring ion velocity is a key step to understanding the underlying physical mechanisms that allow the thruster to operate. This RPA was built after the test campaign for the small thruster had concluded. Therefore the RPA was only used with the large thruster, and its measurements are presented in chapters 7 and 8.

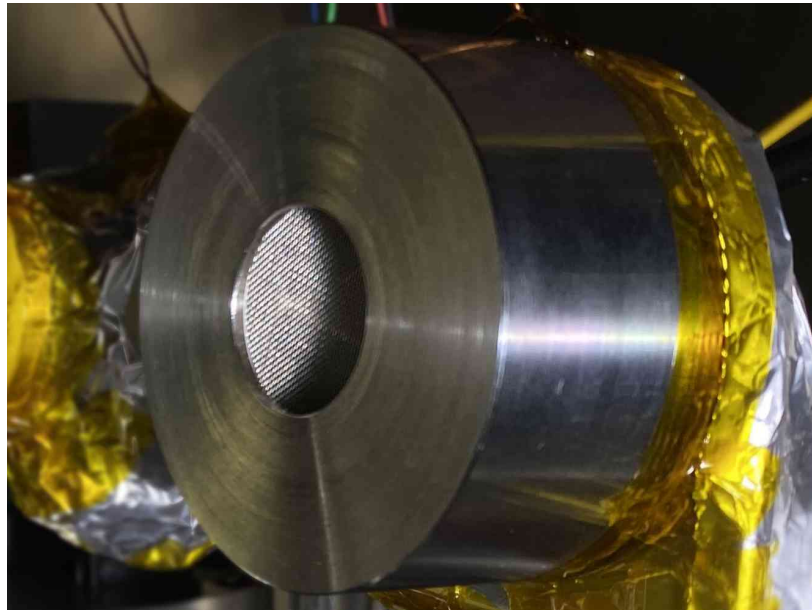


Figure 3.22: Photo of the RPA with grid visible behind grounded enclosure.

RPA Design

The RPA comprises a graphite collector and four stainless steel mesh grids that are separated by ceramic spacers, see figures 3.23 and 3.24. This assembly is contained within a ceramic housing (not shown) that acts to electrically insulate the grids and collector. This is then housed within a stainless steel enclosure that is grounded to prevent any build up of charge on the RPA, see figure 3.22.

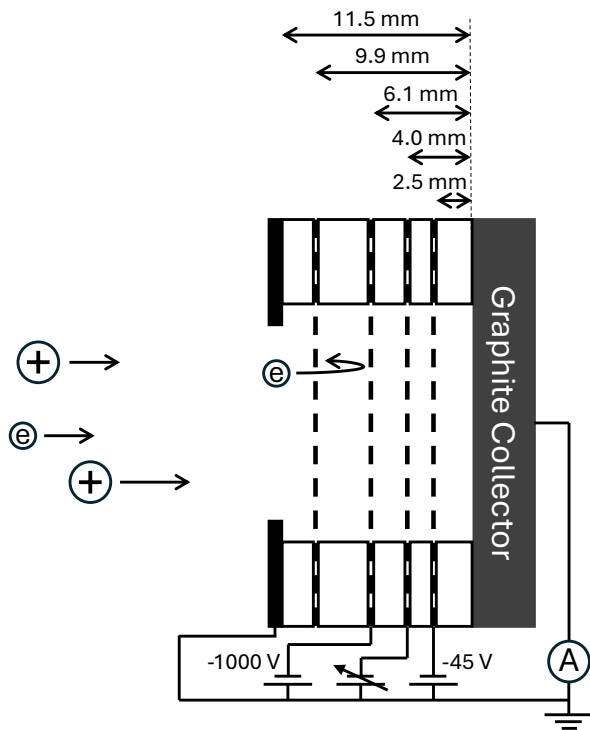


Figure 3.23: Cross-sectional diagram showing the distance of each grid from the collector.



Figure 3.24: Photo of RPA grids, spacers and collector, with grounded enclosure removed.

The ions and electrons enter the RPA as shown in figure 3.23. The first grid that they pass through is left to float at the plasma potential so as to minimise any disturbance to the plasma plume. The second grid that the electrons and ions encounter is biased at a highly negative potential, so as to reflect all the electrons such that only the ions pass through. The potential of the third grid is swept from 0 V to 300 V. At 0 V all the ions are allowed to pass through and are collected by the graphite collector. As the potential of this grid is increased it starts to reflect the ions, with the lower energy (slower) ions being reflected at lower potentials, and higher energy (faster) ions getting reflected at higher potentials until all ions are reflected. By measuring the potential at which a drop in collector current is observed, the energy of these reflected ions can be calculated. When the ions impact the graphite collector, they can cause the collector to lose an electron through a process known as Secondary Electron Emission (SEE). In order for this to not affect the collector current, a fourth grid is added that is held at a potential of -45 V. This acts to reflect these SEE electrons back towards the collector where they are re-collected.

To make the RPA measurements of ion energy comparable to others in literature [76][80][35], the RPA's design was made as similar as possible to that described in M.J. Baird et al.[81]. The collector was manufactured from graphite due to its low rate of secondary electron emission. The ceramic spacers and insulation are all machined from Alumina. The grids and outer housing are all 316 Stainless Steel. The opening in the grounded outer housing for the ions to enter is 21.0 mm in diameter, and the ceramic spacers have an inner diameter of 25.4 mm. The first (floating) grid has 23.6 wires per cm with a wire diameter of 0.19 mm.

The second (electron repelling) grid has 31.5 wires per cm with a wire diameter of 0.12 mm. The final two grids have 39.4 wires per cm with a wire diameter of 0.10 mm. The RPA is attached to a rotational stage, see figure 3.3, at a radius of 431 mm from the thruster.

Grid Bias

To ensure that the collector current is solely due to the ions, it is necessary to check that all electrons are being reflected by the electron repelling grid. This is achieved by sweeping the potential of the electron repelling grid from 0 V down to more negative potentials. As the grid potential decreases, more electrons are repelled and the collector current rises. Ion current saturation is achieved when the collector current plateaus, indicating that all electrons have been repelled[82], see figure 3.25. Facing the RPA head on to the thruster (0° off-axis) required an electron repelling grid potential of -2.0 kV to achieve ion current saturation. This is likely due to the highly energetic electrons that reside between 0° and 20° off-axis, as seen when finding the correct bias potential for the Faraday probe, see figure 3.21. Unfortunately, bias potentials in excess of -1.0 kV are unable to be used due to laboratory equipment limitations. By rotating the RPA to 20° off-axis, the electron repelling grid potential required for ion current saturation decreases to -1.0 kV, see figure 3.25. Therefore the RPA's location was fixed at 20° off-axis and the potential of the electron repelling grid was fixed at -1.0 kV. Such high electron repelling grid potentials are not required when testing HETs and GITs. This is because ECR thrusters have significantly higher energy electrons in their plume. This is a result of the direct transfer of energy to the electrons in the resonance region[59], see section 2.2.

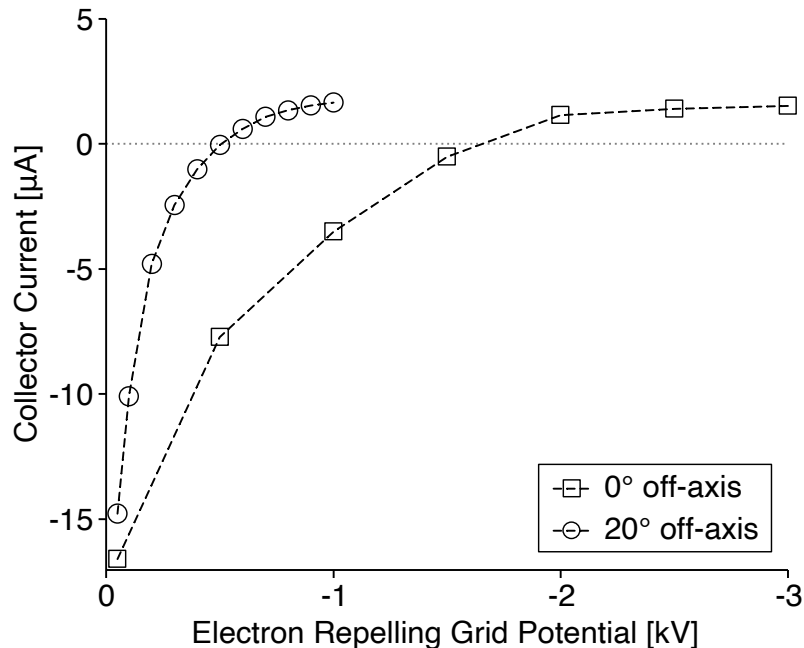


Figure 3.25: Collector current as a function of the electron repelling grid potential. Potential of the ion selection grid maintained at 0 V to allow for all ions to be collected. Large ECR thruster without iron ring, 145 W thruster power, 0.39 mg/s xenon mass flow rate.

Data Processing

The collector current is recorded as the bias of the ion selection grid is swept from 0 V to 300 V, see figure 3.26. This current is defined by equation 3.17, where I is the collector current in A as a function of the grid bias voltage ϕ_B in V, e is the elementary charge in C, n_i is the ion density in m^{-3} , A_c is the area of the collector in m^2 , m_i is the ion mass in kg, $f(E_i)$ is the ion energy distribution function and E_i is the ion energy in J.[83]

$$I(\phi_B) = -\frac{e^2 n_i A_c}{m_i} \int f(E_i) dE_i \quad (3.17)$$

By differentiating equation 3.17, the ion energy distribution function can be found, see equation 3.18.

$$\frac{dI}{d\phi_B} = -\frac{e^2 n_i A_c}{m_i} f(E_i) \quad (3.18)$$

Here it can be seen that the ion energy distribution function, $f(E_i)$, is directly proportional to $-dI/d\phi_B$. Therefore, differentiating the collector current in figure 3.26 allows for the ion energy distribution to be found. This ion energy distribution is normalised and plotted in figure 3.26. A moving average is also applied to smooth the data.

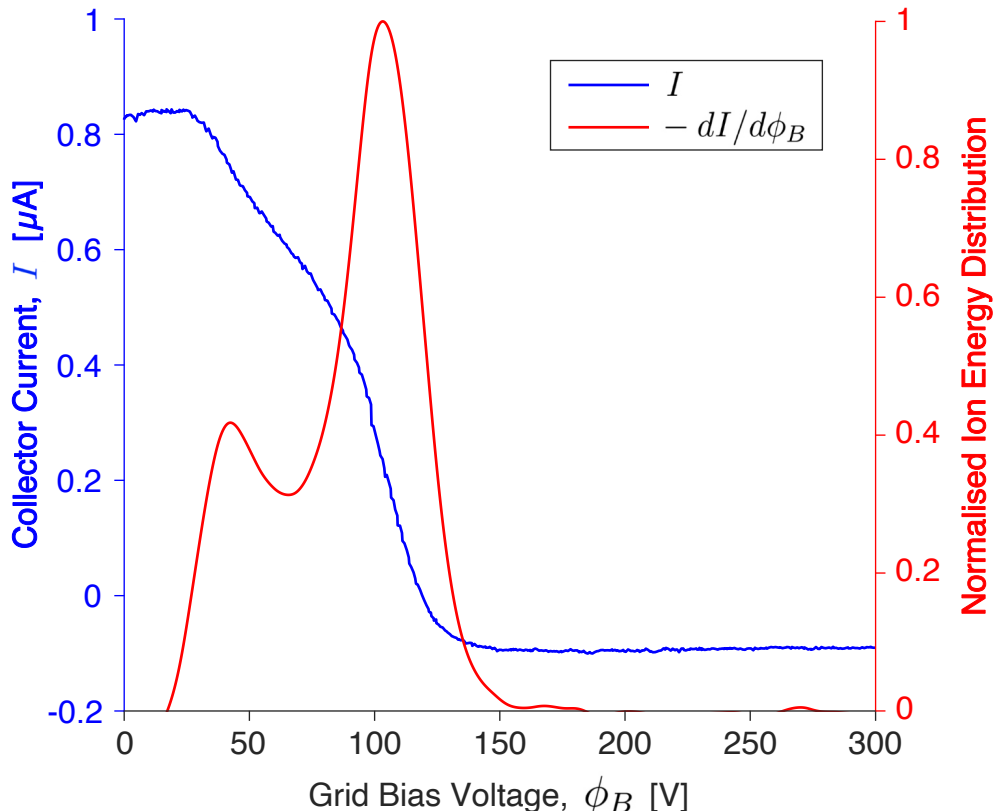


Figure 3.26: Collector current and normalised ion energy distribution for the large ECR thruster without iron ring. 29 W thruster power, 0.39 mg/s xenon mass flow rate.

Here it can be seen that there are two peaks in the ion energy distribution. This is unexpected, as according to section 2.3 the ions that are generated in the thruster are all accelerated by the same ambipolar electric field, which would produce a single peak in ion energy. J. Jarrige et al.[84] has found that the lower energy peak is created by slow ions that have been generated in the plume. These slow ions are generated from electron-neutral and ion-neutral collisions with the background gas. The lower energy peak should then reduce in intensity as background pressure is decreased.

While this double peaked ion energy distribution could be evidence that a Current-Free Double Layer (CFDL) has been generated within the plume, the formation of a CFDL is highly unlikely, and more detailed measurements of the potential gradient in the plume would be required to prove its existence. A CFDL can be thought of as a highly compressed ambipolar electric field. While the ambipolar electric field spans meters, the CFDL has a much smaller thickness, typically between $10\lambda_D$ and $100\lambda_D$, where λ_D is the Debye length[85]. This produces a much stronger potential gradient within the CFDL. This strong potential gradient produces a collimated beam of high energy ions that works to split the ion energy distribution into two peaks. While the CFDL splits the ion energy distribution into two peaks, it does not add any momentum to the ion beam and so does not affect thruster performance[86][87].

Ion Energy Approximation

The RPA was rotated 90° , such that it points perpendicular to the thruster and is radial-facing. As the ions generated in the thruster have a high axial velocity, they cannot enter the rotated RPA and so the high energy peak that they create in the ion energy distribution is shrunk significantly[88], see figure 3.27. As ion acceleration in an ECR magnetic nozzle thruster has been seen to occur over a distance greater than several thruster radii outside of the thruster[60], ions generated via electron-neutral and ion-neutral collisions in the plume are also accelerated axially. This means that the majority of ions responsible for the lower energy peak also cannot enter the rotated RPA. There exists a small number of ions generated adjacent to the RPA that have yet to be accelerated by the ambipolar electric field. These ions are known as (stationary) thermal ions, and as they do not have a large axial velocity they can make their way into the RPA. This results in the low energy peak shifting to a lower grid bias voltage in figure 3.27, as only these low energy thermal ions can enter the rotated RPA. The grid bias voltage at which this peak occurs is therefore the local plasma potential at the RPA, ϕ_p , see figure 3.27. This method of rotating the RPA is commonly used to find the local plasma potential for RF magnetic nozzle thrusters[88][89].

An ion energy distribution was also taken with the RPA pointing towards the thruster, see figure 3.27. This ion energy distribution can be seen to start when the grid bias voltage, ϕ_B , equals the local plasma potential, ϕ_p . The grid bias voltage at which the high energy peak occurs is known as the ion beam potential, ϕ_b [88][90]. To calculate the energy of the ions, the local plasma potential must first be subtracted[91], see equation 3.19, where E_i is ion energy in J, ϕ_B is the bias voltage of the analysis grid in V and ϕ_p is the potential of the local plasma in V. To calculate the energy of the ions at the ion beam potential, ϕ_B can be substituted for ϕ_b . From figure 3.27 the ion energy at the ion beam potential is found to be 126 eV. Using equation 3.16, the velocity of these ions is 13,600 m/s.

$$E_i = e(\phi_B - \phi_p) \quad (3.19)$$

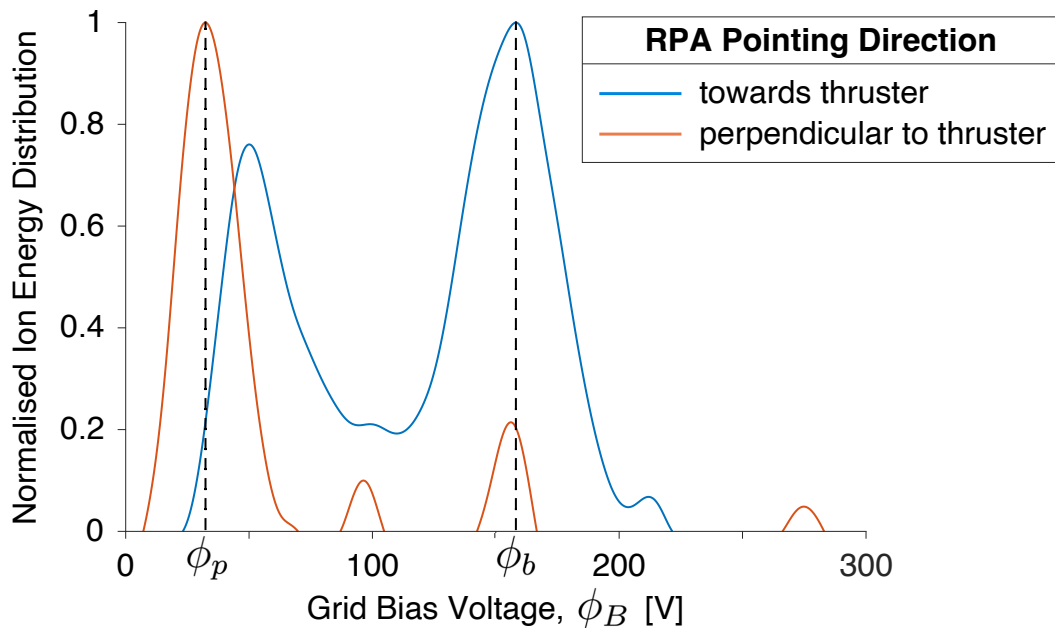


Figure 3.27: Normalised ion energy distribution for the large ECR thruster without iron ring. RPA facing the thruster and RPA facing perpendicular to the thruster. 115 W thruster power, 0.39 mg/s xenon mass flow rate.

Unfortunately, the RPA is unable to be rotated every time that an ion energy distribution is taken. This means that the RPA will be fixed pointing towards the thruster, preventing a direct measurement of the local plasma potential, ϕ_p . However, it is possible to make a crude calculation of ϕ_p from the ion energy distribution when the RPA is pointing towards the thruster. The local plasma potential will always lie below the grid bias voltage of the first peak. From figure 3.27, ϕ_p can therefore be approximated as the grid bias voltage of the first peak when the RPA is pointing towards the thruster multiplied by 0.64. This is only a crude approximation of the local plasma potential, ϕ_p , but allows for the calculation of ion energy from equation 3.19 when ϕ_p cannot be directly measured.

Data Verification

Biasing the electron repelling grid to below -1.0 kV, resulted in arcing between the grids of the RPA. If ionisation between the grids of the RPA also occurs at an electron repelling grid potential of -1.0 kV, this could artificially increase collector current, decreasing the accuracy of the ion energy distribution. To verify that no ionisation was occurring within the RPA, propellant was injected into the thruster with the microwave generator turned off. Therefore, any ionisation that resulted in collected current at the RPA must be due to ionisation within the RPA itself. No significant current was observed as the bias potential of the RPA was swept. This indicates that no ionisation is occurring within the RPA.

4 THRUSTER GEOMETRY OPTIMISATION

The optimisation of ECR thruster geometry is split into three sections:

4.1	Chamber Geometry	71
4.2	Injector Position	79
4.3	Antenna Length & Shape	81

Additionally, antenna material and thruster potential are investigated in the last two sections:

4.4	Antenna Material	84
4.5	Thruster Floating Potential	86

Three different ECR thrusters were tested over three test campaigns:

YEAR	THRUSTER
2021	AVS-UK Thruster Developed by AVS-UK Ltd. in partnership with the University of Surrey, with testing conducted by Dr J. Stubbing and myself at the University of Surrey.
2023	Small Thruster I developed and tested this independently for this thesis.
2024	Large Thruster I developed and tested this independently for this thesis.

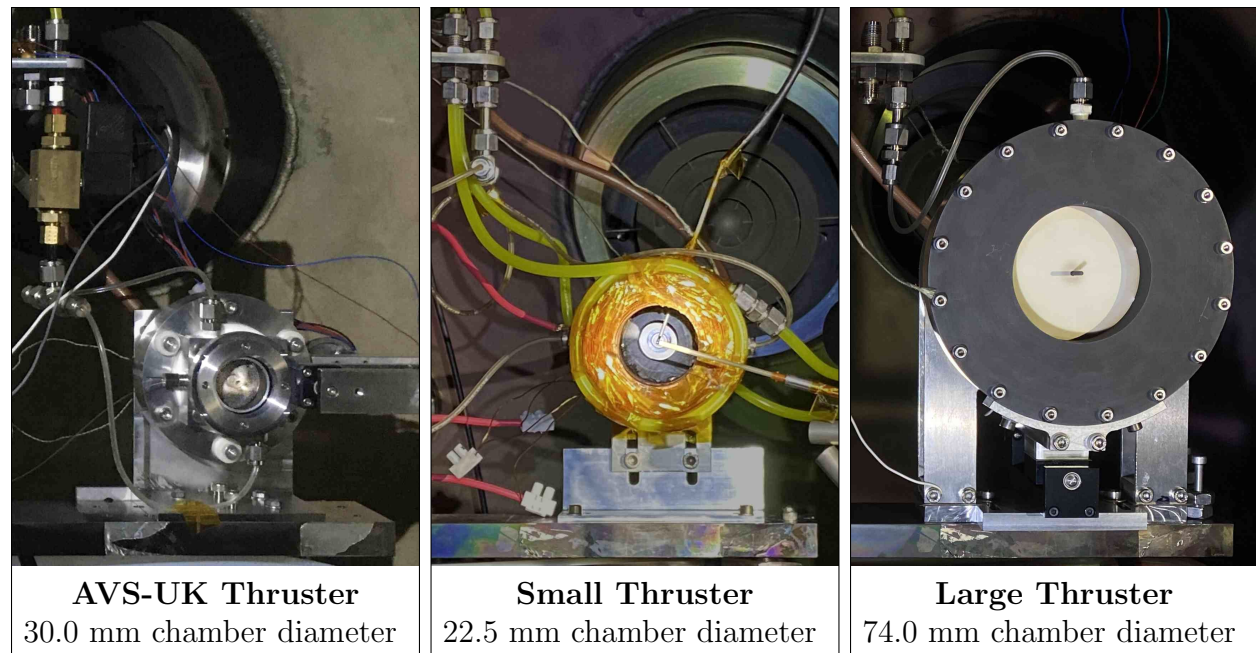


Figure 4.1: Comparison of the three ECR thrusters used for this geometry study.

4.1 Chamber Geometry

The geometry of the thruster chamber plays a large role in confining the neutral propellant so that it can be more easily ionised and accelerated. Optimising for a high neutral propellant density results in a long and thin chamber. However, this also leads to an increase in plasma losses to the walls. Therefore a trade off must be made to ensure sufficient neutral propellant density with minimal plasma wall losses.

AVS-UK Thruster

The AVS-UK ECR thruster is a coaxial ECR thruster. It has a linear antenna made from tungsten, chosen for its relatively low sputtering yield. Its backplate is made from boron nitride due to its moisture resistance and its chamber walls are machined from Aluminium 5083 due to its corrosion resistance. The novelty of this thruster's design lies in its motorised telescopic chamber, allowing for the chamber length to be changed without venting the vacuum chamber. The thruster was designed and manufactured by AVS-UK in partnership with the University of Surrey, and tested at the University of Surrey under the UK Space Agency's National Space Technology Programme (grant reference number NSTP3-FS1-021).[27]

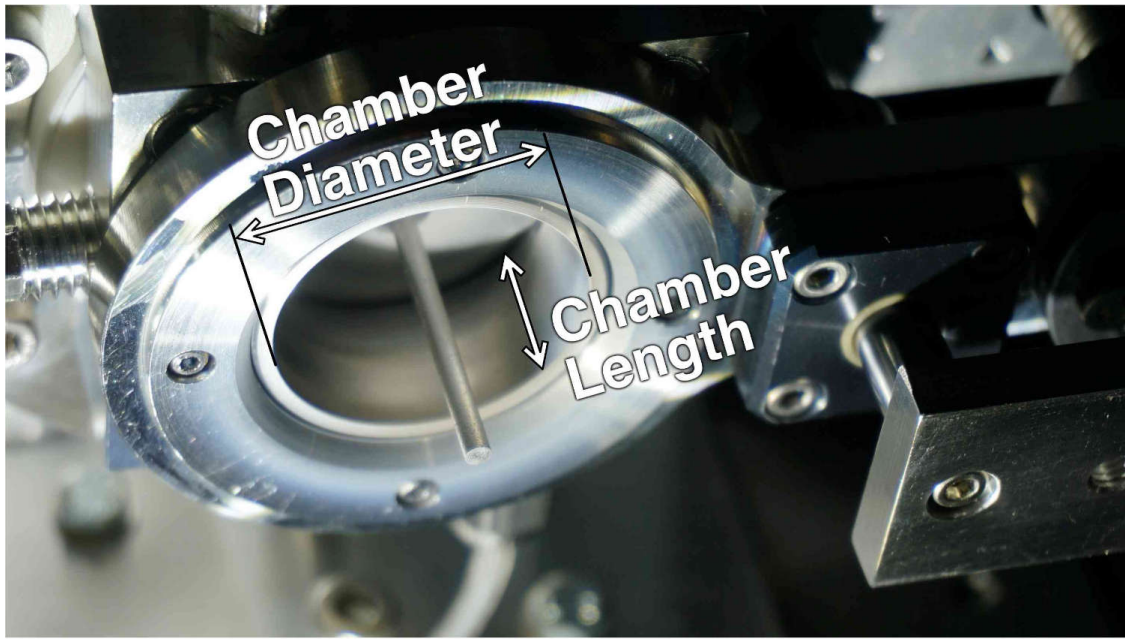


Figure 4.2: AVS-UK ECR thruster. 30.0 mm chamber diameter, 16.0 mm chamber length.

As ECR thrusters have historically suffered from low efficiencies, the aim of the AVS-UK ECR thruster test campaign was to increase thruster efficiency by as much as possible. Instead of independently evaluating the effects of thruster power and propellant mass flow rate on thruster performance, thruster performance is plotted as a function of the ratio of thruster power to propellant mass flow rate. This ratio then simplifies to the energy absorbed

per unit mass of propellant. These plots therefore show how efficiently the absorbed energy is being converted into the kinetic energy of the ions.

First, the length of the chamber was swept from 16 mm to 26 mm, see figure 4.3. The shorter 16 mm chamber length demonstrated higher thruster performance at lower specific energies. Therefore the 16 mm chamber length was selected for the following tests. The ions and electrons follow magnetic field lines[54]. The longer chamber walls intersect more of these magnetic field lines, likely resulting in more plasma losses to the walls which reduces thruster performance.

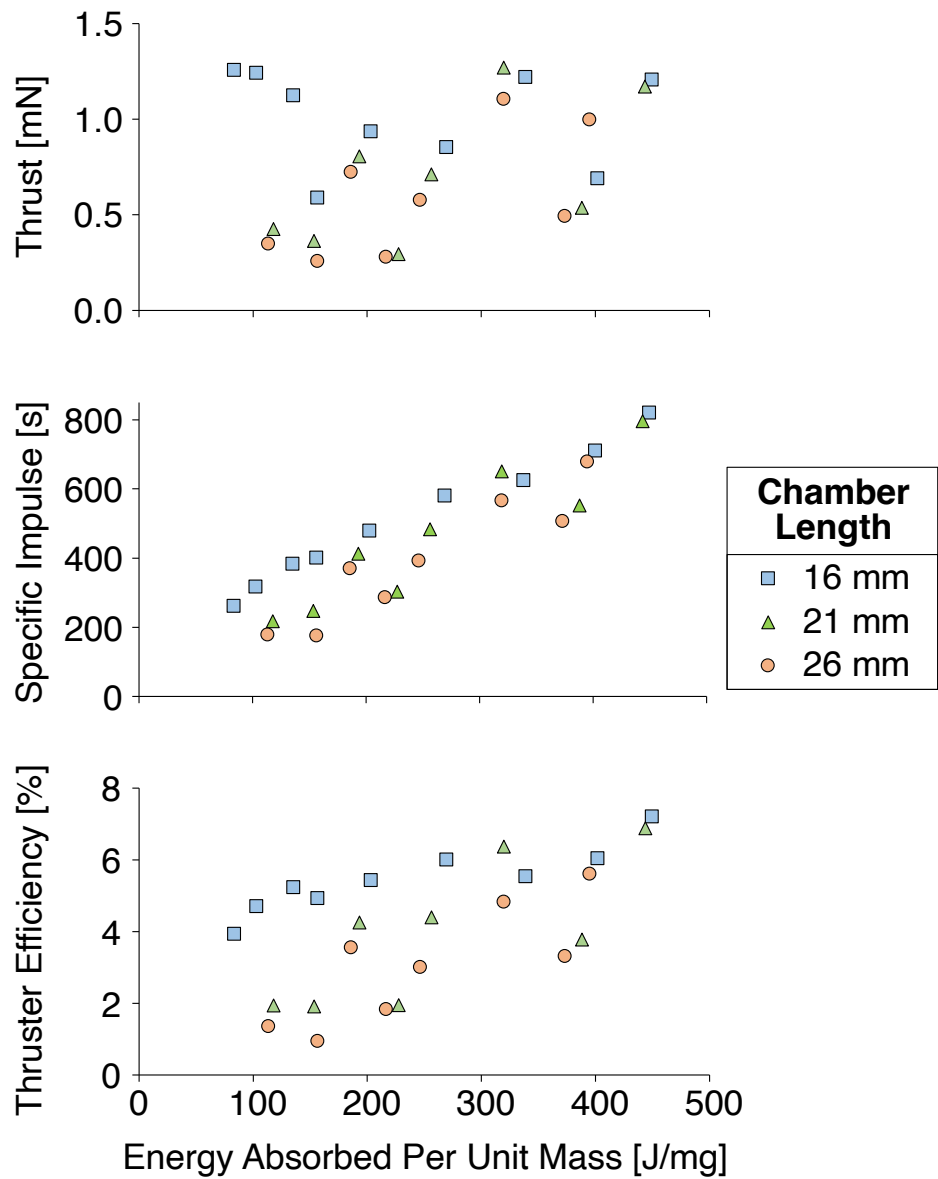


Figure 4.3: Thrust, specific impulse and thruster efficiency as a function of the energy absorbed per unit mass of propellant. Xenon mass flow rates between 0.10 mg/s and 0.50 mg/s were used. AVS-UK ECR thruster, 30 mm chamber diameter, linear antenna.

Next the diameter of the thruster's chamber was changed from 30 mm to 24 mm, see figure 4.4. Here, the 30 mm chamber diameter can be seen to approximately double the thruster efficiency for all values of specific energy. Therefore the 30 mm chamber diameter was selected for the following tests. This could indicate that the smaller chamber is producing an excessively high plasma density, resulting in increased plasma wall losses and lower thruster performance.

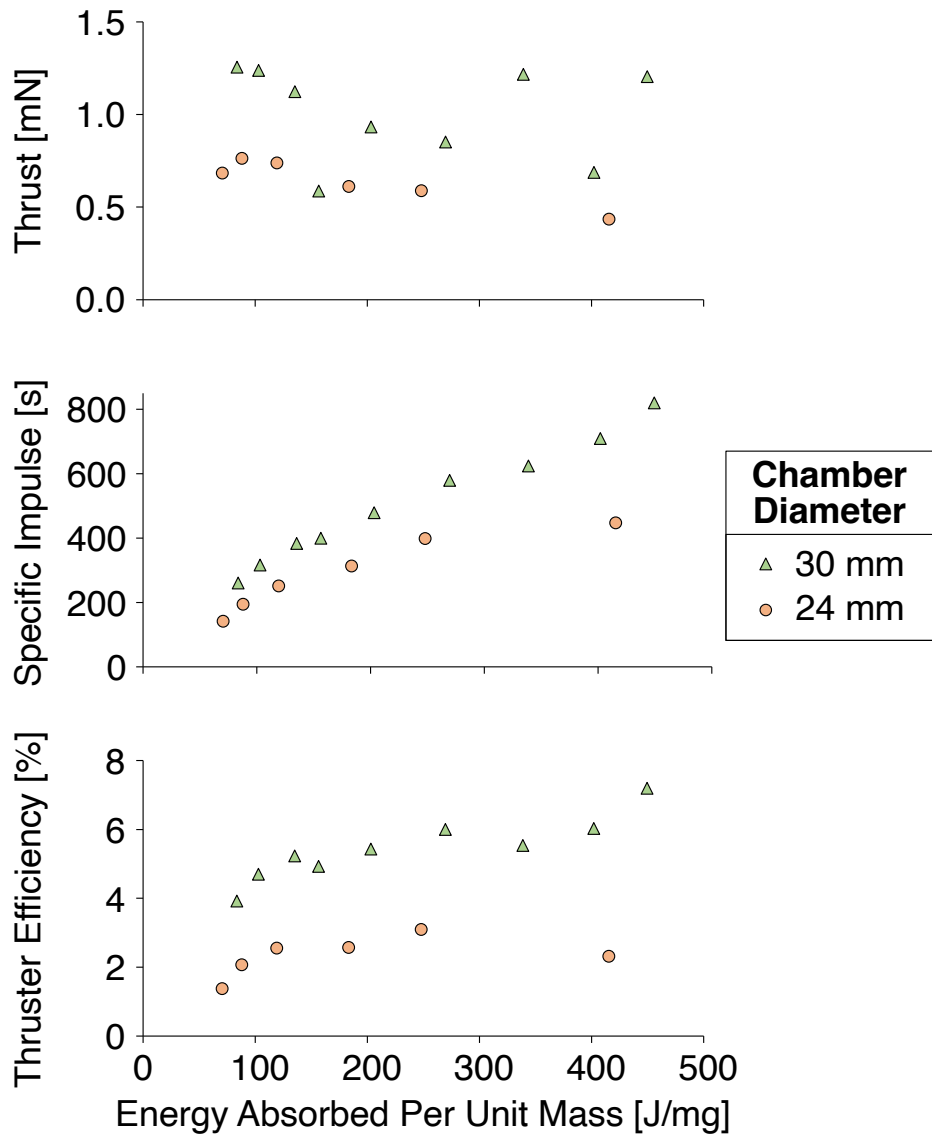


Figure 4.4: Thrust, specific impulse and thruster efficiency as a function of the energy absorbed per unit mass of propellant. Xenon mass flow rates between 0.10 mg/s and 0.50 mg/s were used. AVS-UK ECR thruster, 16 mm chamber length, linear antenna.

Small Thruster

A new thruster was designed to continue research into ECR thrusters after the test campaign on the AVS-UK thruster had concluded. This ECR thruster is smaller than the AVS-UK thruster, as shown in figure 4.5. The design of this small thruster has been optimised for simplicity and a low mass. Specifically, the Samarium Cobalt permanent magnet (Sm₂Co₁₇ 28/20) has been shrunk in size to significantly reduce total thruster mass. The permanent magnet has an outer diameter of 45.0 mm, inner diameter of 15.0 mm and height of 17.5 mm. A plot of the thruster's magnetic field along its central axis can be found in figure 5.3. Isostatic graphite was chosen to make the chamber walls and linear antenna. This was due to new research by S. Peterschmitt[36] showing that a graphite antenna provided higher thrust with a lower erosion rate when compared to stainless steel and molybdenum. A copper heatsink was added to the rear of the thruster to prevent the PTFE from melting and the magnet from demagnetising during periods of high thermal load.

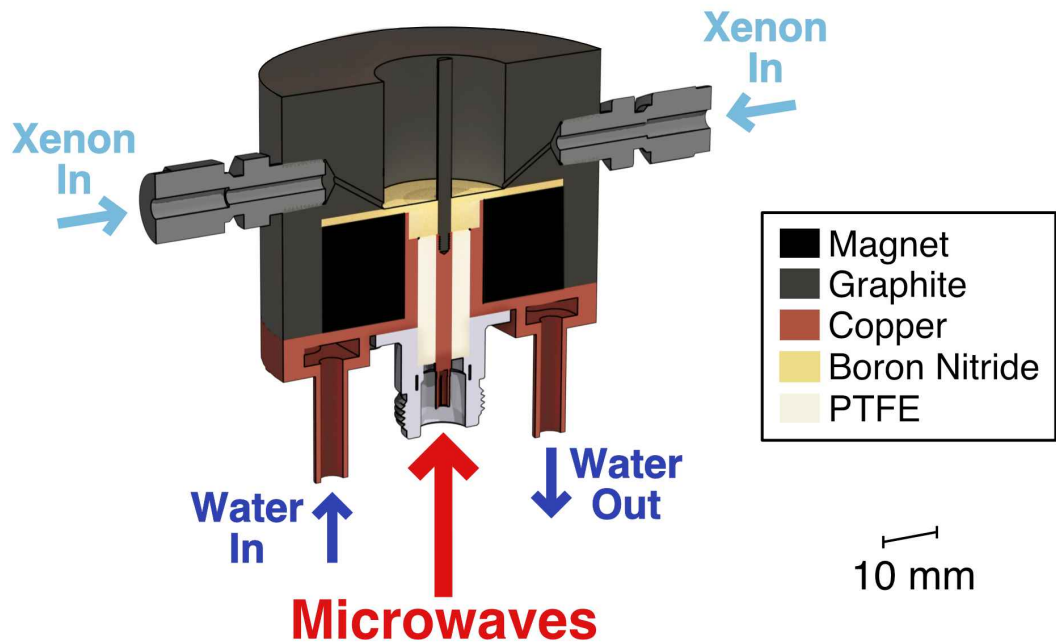


Figure 4.5: Cross-sectional view of the small thruster. 22.5 mm chamber diameter, 21.0 mm chamber length, 2.5 mm antenna diameter, 23.0 mm antenna length.

A higher neutral propellant density within the chamber should lead to increased performance. But the intersection of magnetic field lines with the chamber wall acts to decrease thruster performance. This is partly due to axial momentum loss to the chamber wall, which is investigated in detail by K. Takahashi et al.[92]. In this paper a modified helicon magnetic

nozzle thruster is constructed such that its back wall is mechanically separate from its lateral wall, see figure 4.6. This allows for separate measurements of thrust from the back and lateral walls. It was found that whilst the back of the chamber produces positive thrust, the lateral wall produces a negative thrust that subtracts from the total thrust. This is thought to occur due to ions accelerating off-axis, hitting the lateral wall and imparting their momentum. For xenon, the negative thrust contribution of the lateral wall varies between 50 % and 80 % of that from the back wall.

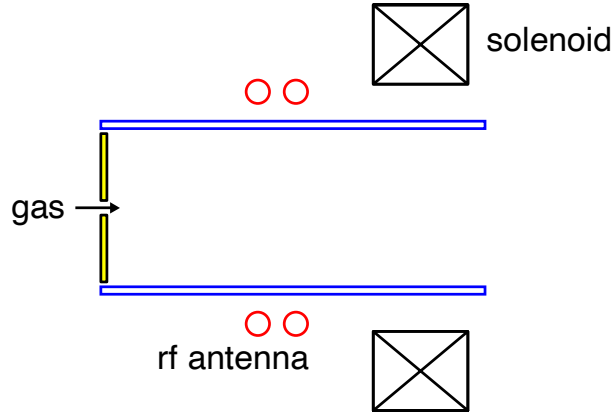


Figure 4.6: Cross-sectional diagram of a helicon thruster with mechanically separated back wall (yellow) and lateral wall (blue). Reproduced from K. Takahashi et al.[92].

Presuming that this loss in thrust due to momentum loss to the lateral wall also occurs in ECR thrusters, this is a source of inefficiency that should be reduced. As well as momentum loss to the wall, plasma is also lost to the wall. Ions that are lost to the wall can no longer be accelerated to generate thrust, while the loss of electrons is thought to reduce the strength of the ambipolar electric field that accelerates the ions, further decreasing thrust. One way to reduce momentum and plasma losses to the lateral wall is to taper the wall outwards, so that ions and electrons with a divergence angle lower than the angle of the wall taper will not hit the wall. 7.5° and 15.0° convex wall tapers were tested, however these produced high reflected powers which resulted in a negligible thrust. This high reflected power was likely due to the angled chamber producing a high VSWR. The other geometries tested were a concave stepped chamber wall and a nozzle that was added to the exit of the thruster, see figure 4.7. Both these geometries were designed to increase the neutral propellant density within the thruster, with the aim of increasing thruster performance. Thruster performance is plotted as a function of thruster power for each chamber geometry, see figure 4.8. Here it can be seen that the stepped wall produces significantly lower performance, likely due to increased plasma wall losses. The nozzle also appears to decrease performance slightly and so only the straight wall was used for the following tests.

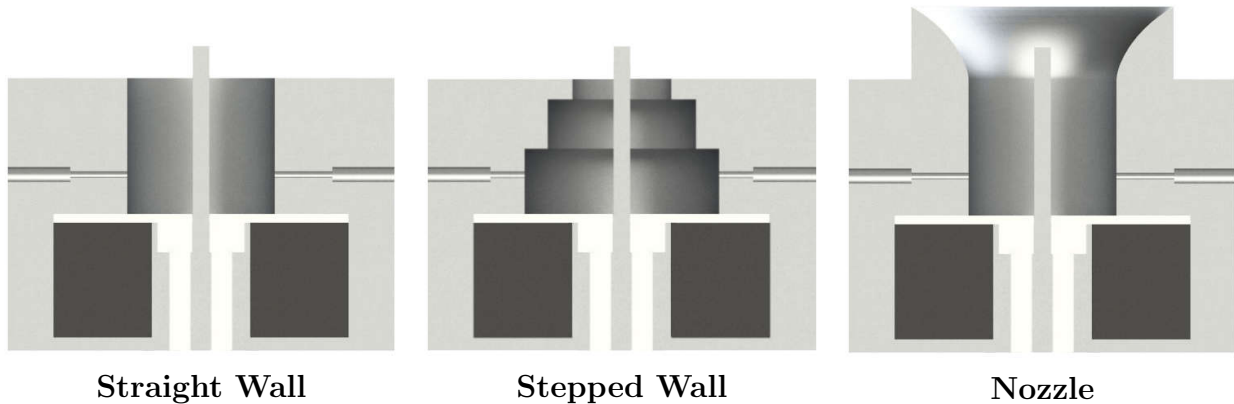


Figure 4.7: The three chamber geometries tested with the small ECR thruster. Conductive material in light grey, ceramic in white and permanent magnet in dark grey. Xenon propellant injected from two 1 mm diameter injectors, 6 mm downstream of the backplate.

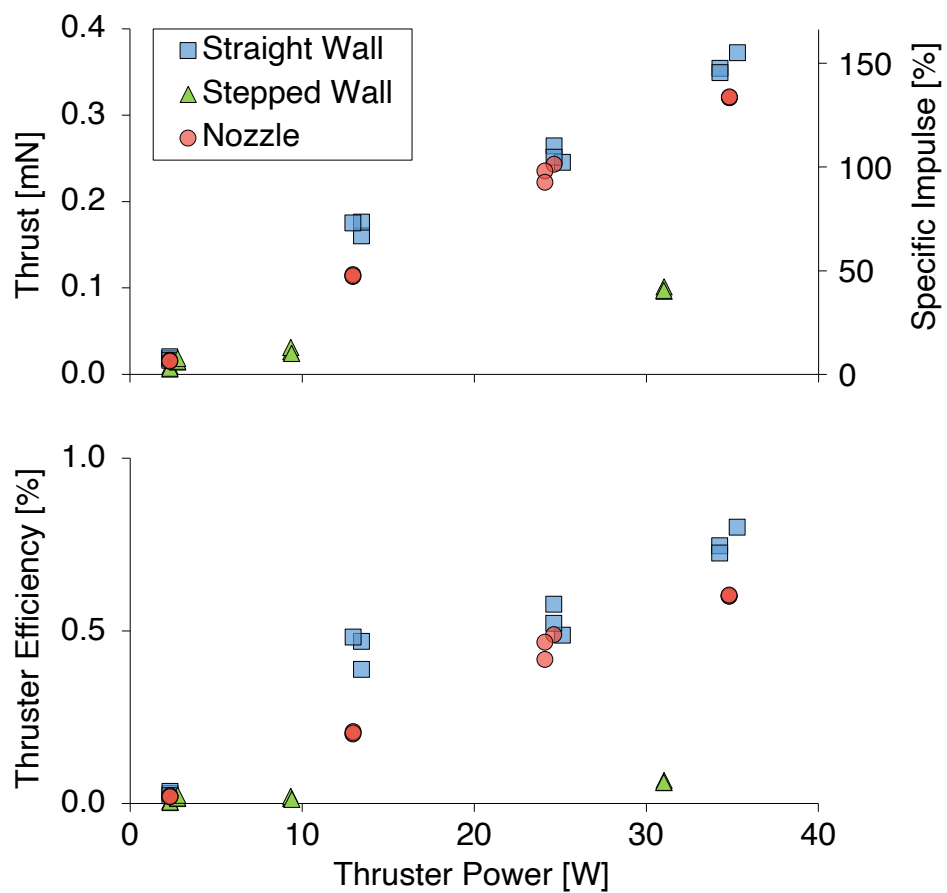


Figure 4.8: Thrust, specific impulse and thruster efficiency as a function of thruster power for three different chamber geometries. Small ECR thruster, 0.25 mg/s xenon mass flow rate. Three readings taken for each test condition, standard errors from 0.001 mN to 0.007 mN.

Large Thruster

A large thruster was later designed with the aim of increasing thrust. Similar to the small thruster, the chamber walls and antenna were machined from isostatic graphite, the backplate was made from boron nitride and the permanent magnet was Samarium Cobalt (Sm₂Co₁₇ 28/20).

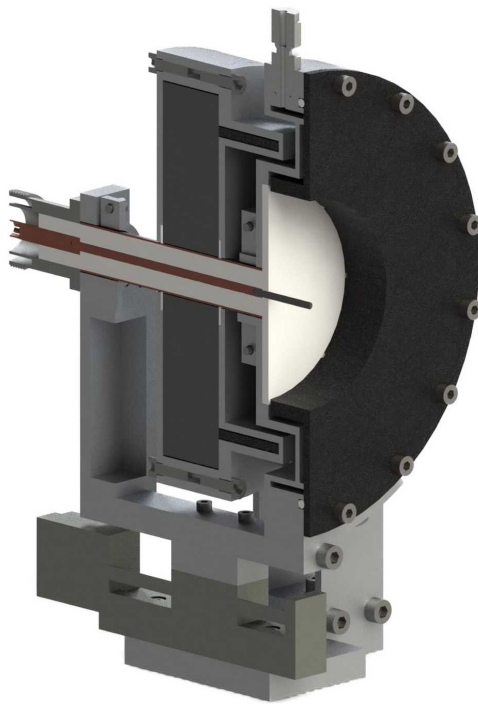


Figure 4.9: Cross-sectional view of the large ECR thruster. 74.0 mm chamber diameter, 20.0 mm chamber length, 2.5 mm antenna diameter, 20.0 mm antenna length.

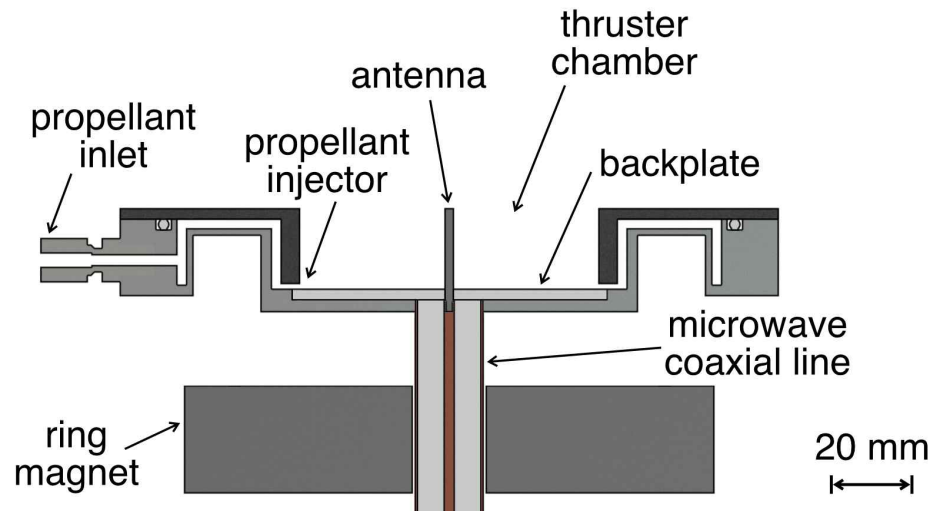


Figure 4.10: Labeled cross-sectional view of the large thruster.

Propellant is injected more evenly, as eight $1\text{ mm} \times 2\text{ mm}$ injector holes are used instead of the two 1 mm diameter injector holes that were used on the small ECR thruster. Two opposite and equidistant orifices that are not visible on figure 4.10 ensure symmetrical propellant injection. The ring magnet is not in contact with the thruster so as to avoid high temperatures that could cause demagnetisation. A thicker thruster coaxial line was designed using a copper inner conductor, boron nitride dielectric and aluminium foil outer conductor. The switch from a PTFE dielectric to a ceramic dielectric prevented the line from melting and/or burning, while the larger coaxial line allowed for a more efficient and reliable transfer of microwave power. The large ECR thruster reflected significantly less microwave power than the small ECR thruster. This results in more power to the thruster for the same forward power at the microwave generator, see figure 4.11. The VSWR is a measure of how much of the forward microwave power is reflected back towards the generator, with a lower VSWR producing less reflected power. The small ECR thruster had a mean VSWR of 2.42, meaning that 17.2 % of forward power was reflected. While the large ECR thruster had a mean VSWR of 1.13, meaning that 0.4 % of forward power was reflected.

The larger chamber diameter requires a higher minimum xenon mass flow rate of 0.39 mg/s to sustain a plasma in the thruster, compared with the small thruster's 0.08 mg/s minimum xenon mass flow rate. This results in an increase to the thrust but a decrease to the specific impulse, see figure 4.11. Thruster efficiency is largely unchanged.

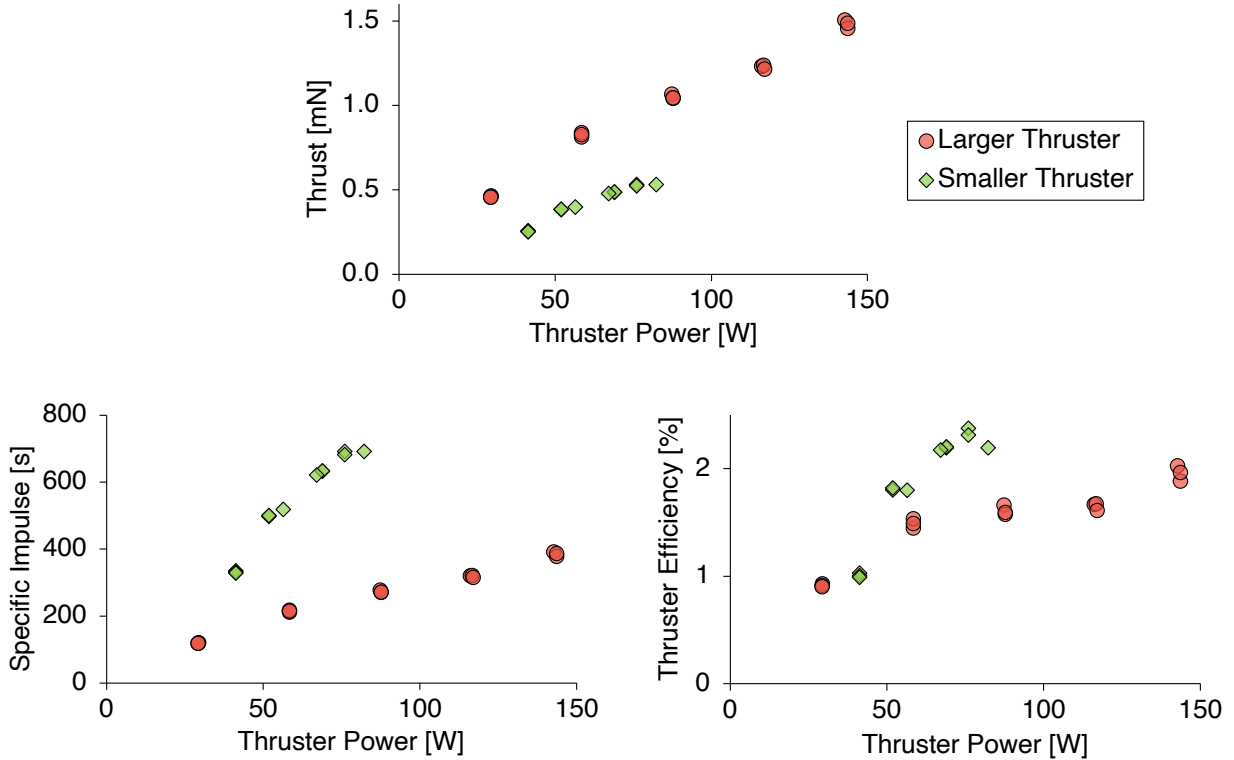


Figure 4.11: Thrust, specific impulse and thruster efficiency as a function of thruster power for the small and large ECR thrusters. 0.08 mg/s xenon mass flow rate for the small thruster and 0.39 mg/s for the large thruster with resonance region 10 mm from backplate. Three readings taken for each test condition, standard errors from 0.002 mN to 0.015 mN.

4.2 Injector Position

Previous research has indicated that mass utilisation efficiency is increased when the propellant injectors are located close to both the resonance region and the backplate.[16]

Small Thruster

Propellant is injected into the chamber radially through two opposite holes, each 1 mm in diameter. Two configurations were tested, one where the injectors were positioned at the back of the chamber, adjacent to the dielectric backplate, and one where the injectors were displaced 6 mm downstream, near the middle of the chamber and closer to the resonance region, see figure 4.12. Forward power at the microwave generator was increased from 10 W to 30 W to 50 W and finally to 70 W. The thrust produced by both injector displacements was measured and is plotted as a function of the thruster power in figure 4.13.

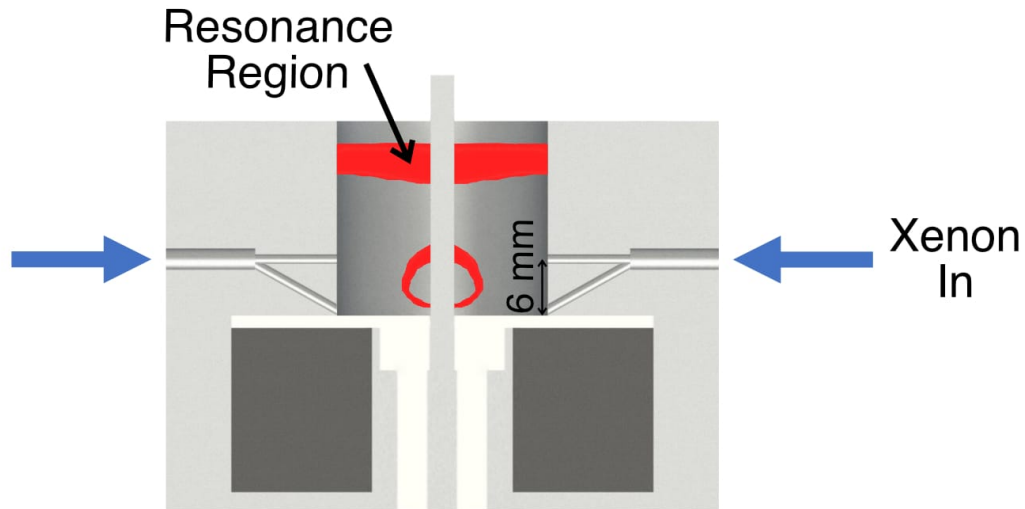


Figure 4.12: Cross-sectional diagram of the small ECR thruster with both injector displacements visible. Resonance region highlighted in red (modelled using FEMM[93]).

No significant change in performance between the two configurations can be seen for the two highest power levels. However, for the third highest power level the 6 mm injector displacement reflects far more power than the 0 mm injector displacement, shifting it left and down in figure 4.13. This shows that the 0 mm injector displacement is able to couple more power into the plasma at lower power levels, making it the more stable configuration. In this configuration, the propellant has a greater distance over which it can spread out, creating a more even propellant density distribution within the chamber before it reaches the resonance region. This likely reduces the fraction of the microwaves that experience

cutoff and are reflected. A 0 mm injector displacement is therefore used for all the following tests.

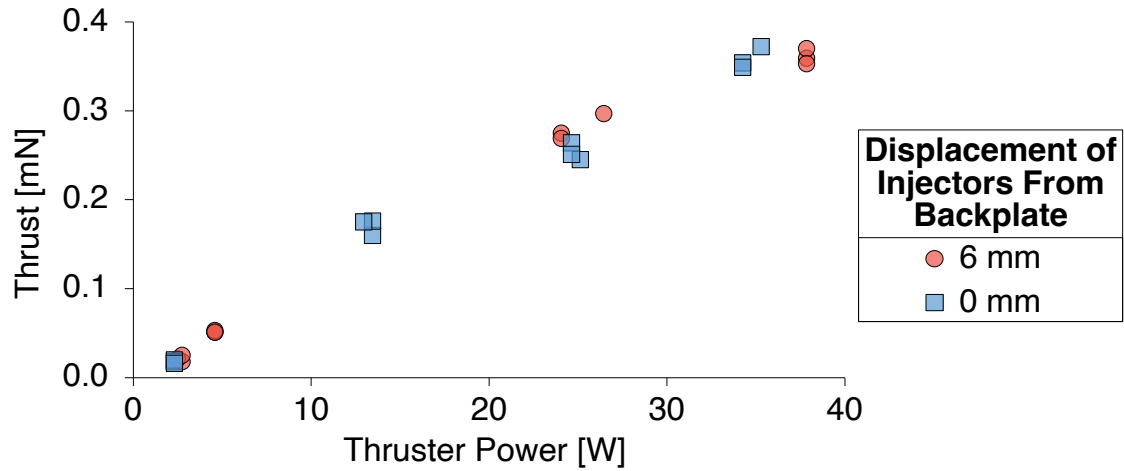


Figure 4.13: Thrust as a function of thruster power with varying injector displacement. Small ECR thruster, 0.25 mg/s xenon mass flow rate. Three readings taken for each test condition, standard errors from 0.001 mN to 0.006 mN.

4.3 Antenna Length & Shape

An ECR thruster's antenna is responsible for the emission and polarisation of microwave energy. By optimising the radiation pattern of the antenna, performance can be increased. Numerically modelling an antenna that is immersed within a plasma is highly complex. Therefore it is usually faster and more representative to experimentally test different antenna geometries.

AVS-UK Thruster

A helical antenna was manufactured for the AVS-UK ECR thruster. Helical antennas emit circularly polarised waves instead of the linearly polarised waves that linear antennas emit. They also have a more directional radiation pattern and have a much shorter length than a linear antenna[94]. The linear antenna that was used in all prior tests, was replaced and compared to the helical antenna as seen in figure 4.14. Both antennas are machined out of tungsten due to tungsten's low sputtering yield.

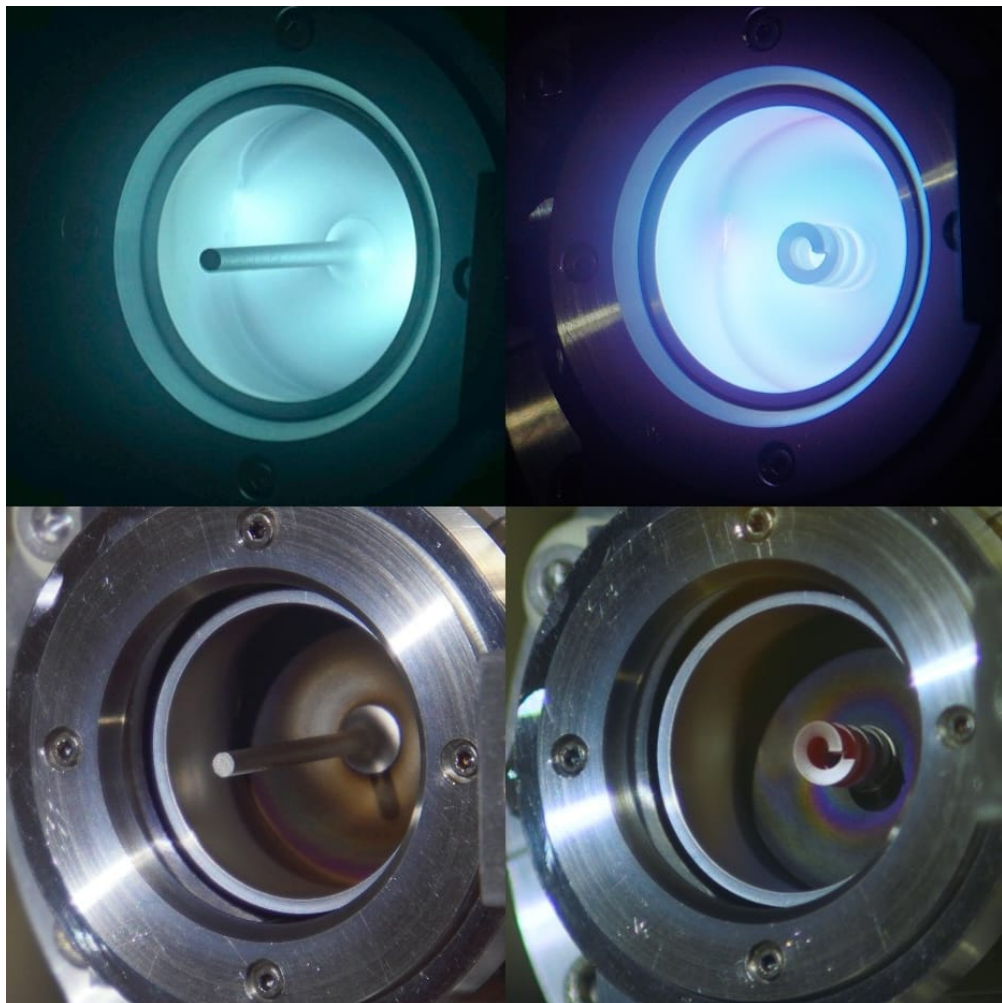


Figure 4.14: AVS-UK ECR thruster with linear antenna (left) and helical antenna (right). During operation (top), after operation (bottom).

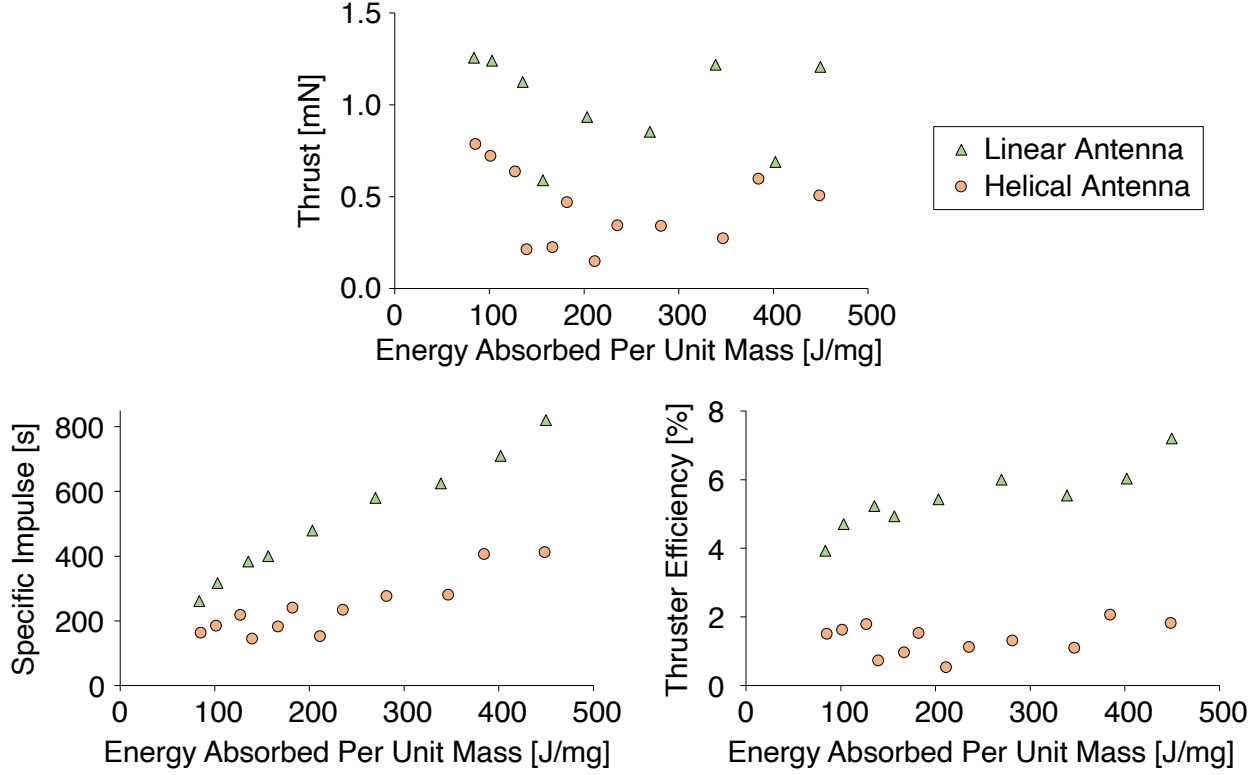


Figure 4.15: Thrust, specific impulse and thruster efficiency as a function of the energy absorbed per unit mass of propellant. Xenon mass flow rates between 0.10 mg/s and 0.50 mg/s were used. AVS-UK ECR thruster, 16 mm chamber length, 30 mm chamber diameter.

From figure 4.15 it can be seen that the helical antenna delivers significantly lower thruster efficiency at every level of specific energy. This is in agreement with results obtained by A.J. Thomas[35]. However, unlike the right-hand oriented helical antenna used by A.J. Thomas, the helical antenna in this study is oriented in a left-hand sense. This means that it emits left-hand polarised waves that cannot be absorbed via ECR, instead of right-hand polarised waves that can be absorbed[95]. It is worth noting that this polarisation does invert when the waves are reflected off the chamber walls, allowing for microwave energy to be resonantly absorbed[40].

There could be several reasons for the observed decrease in thruster performance. In figure 4.14 a high intensity plasma can be seen in the gaps between the coil of the helical antenna. This conductive plasma could act to electrically bridge these gaps, effectively turning the helical antenna into a linear antenna. The high intensity plasma in these coil gaps poses another problem however, as a large fraction of it impinges on the antenna. This increases plasma losses and also contributes to antenna heating. The antenna was observed to glow red for a few seconds after the thruster was switched off, see the bottom right photo in figure 4.14. It could also turn out that the more omnidirectional radiation pattern of the linear antenna makes it better suited to evenly distributing the microwave energy throughout the chamber, instead of concentrating it in one spot. Further work is therefore required to determine the primary mechanism for the helical antenna reducing thruster performance.

Small Thruster

To maximise the efficiency of the linear antenna, its length should be an integer fraction of the wavelength of the microwaves. The highest thruster powers, and therefore the highest performance, should then be seen at an antenna length of 15.3 mm, as this is exactly $\frac{1}{8}$ th the wavelength of the 2.45 GHz microwaves. The thrust as a function of the thruster power for each antenna length can be seen in figure 4.16.

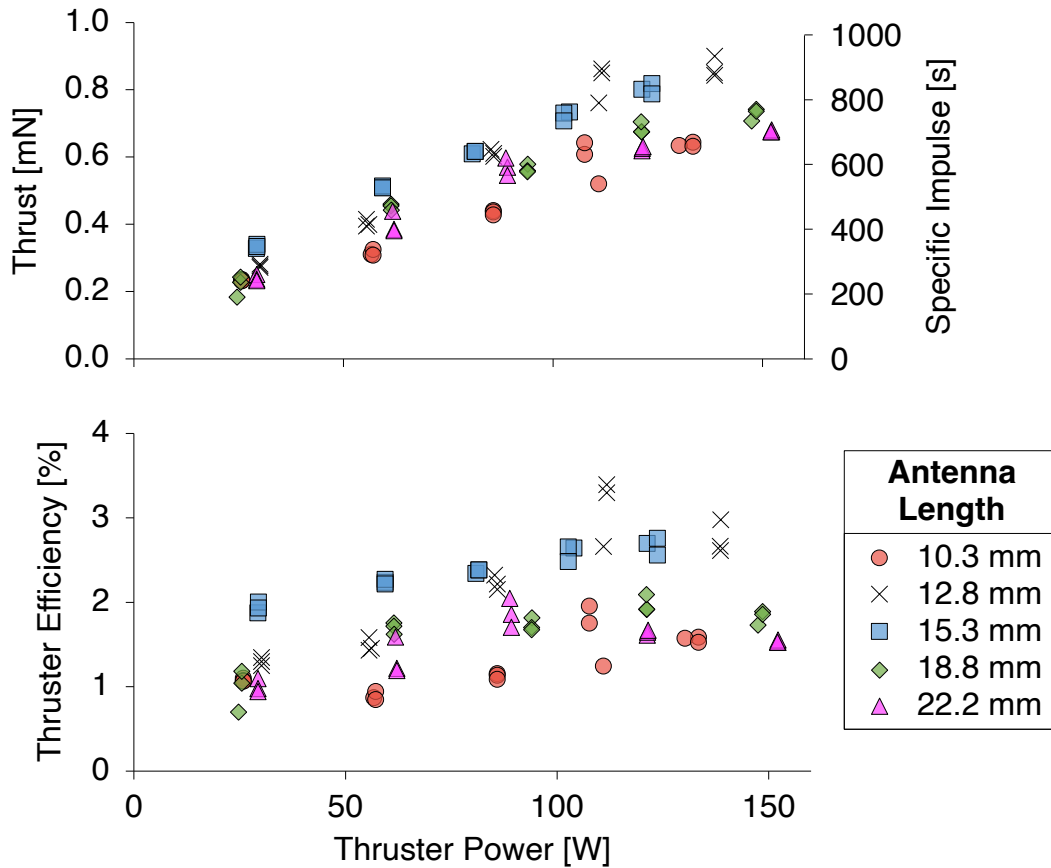


Figure 4.16: Thrust, specific impulse and thruster efficiency as a function of thruster power for five different lengths of antenna. Small ECR thruster, 0.10 mg/s xenon mass flow rate. Three readings taken for each test condition, standard errors from 0.003 mN to 0.036 mN.

From figure 4.16 it can be seen that the 15.3 mm antenna achieves the highest thruster performance for thruster powers under 100 W. The 12.8 mm antenna can be seen to exceed the performance of the 15.3 mm antenna when thruster power exceeds 100 W. This could be because the conductive plasma that is concentrated around the antenna is artificially extending the antenna. This would work to lengthen the antenna, bringing the 12.8 mm antenna closer to the ideal $\frac{1}{8}$ th wavelength, while moving the 15.3 mm antenna away from the ideal $\frac{1}{8}$ th wavelength. A 20 mm antenna is used for all future tests to ensure the results are more comparable with those from other ECR thrusters[7].

4.4 Antenna Material

A comprehensive study by S. Peterschmitt[36] on antenna material for ECR thrusters found that pure graphite resulted in a higher thruster performance and lower erosion rate than both stainless steel and molybdenum. The reason for this increased performance is unknown. Various boron nitride coatings were also tested, which were found to decrease thruster performance. This could be due to the coating decreasing the local electric field intensity[59].

Small Thruster

Diamond Like Carbon (DLC) coatings have shown promise for use in plasma neutralisers[96]. This is because DLC can have large Secondary Electron Emission (SEE) yields. A larger SEE yield means that when an electron impacts the surface, more secondary electrons are emitted from the surface as a result. These electrons are donated to the plasma and can help to increase plasma density. Electrical conductivity of the coating is required to replenish the lost electrons, and adding hydrogen to the coating can further increase the SEE yield[97]. The SEE yield of graphite is no higher than 1.0, whereas the maximum SEE yield of DLC is greater than 8.0[98][99], see table 4.1. As the antenna of the ECR thruster is fully immersed in the plasma, the high SEE yield of DLC could increase the plasma density and boost thruster performance. An isostatic graphite antenna was coated in a 1 μm layer of conductive and hydrogenated DLC by Wallwork Heat Treatment Ltd, see figure 4.17.

Table 4.1: Maximum SEE yields for a range of antenna materials[98][99]. Note that SEE yield is dependent on the energy of the impinging electron, which is not constant for the values here.

Maximum SEE Yield	
Graphite, Aluminium	1.0
Steel, Copper, Molybdenum, Tungsten	1.3 - 1.4
Diamond Like Carbon (DLC)	> 8.0

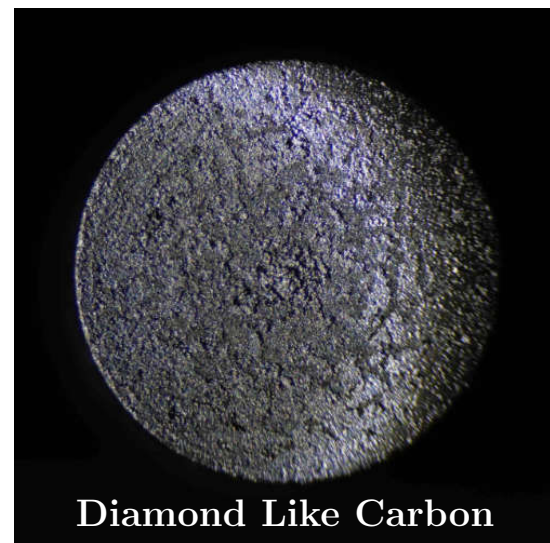
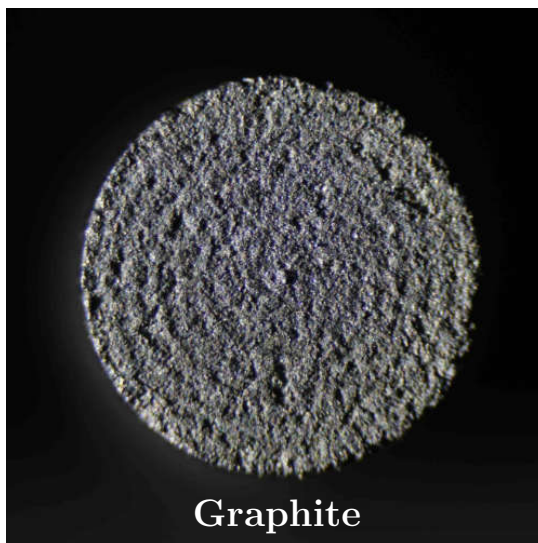


Figure 4.17: Microscope images of the end of a 2.5 mm \varnothing antenna. Pure graphite with machining circles visible (left), 1 μm Diamond Like Carbon (DLC) coating (right).

A Scanning Electron Microscope (SEM) was used to compare the DLC coated antenna to the pure graphite antenna, see figure 4.18. The majority of the antenna was coated in DLC, although the coating had flaked off in some areas, see the right image in figure 4.18. Energy-Dispersive X-Ray Spectroscopy was also used to determine the chemical composition of the antenna surface. This found the graphite antenna to be composed of 100 % carbon and the DLC coated antenna to be composed of 89 % carbon and 11 % Silicone. From figure 4.19 the pure graphite antenna can be seen to produce the same thrust as the DLC antenna for every thruster power tested. This is evidence that the SEE yield of the antenna does not affect thruster performance. Therefore, different material properties must be responsible for the performance enhancement seen by S. Peterschmitt[36] when switching from a steel/molybdenum antenna to a graphite antenna. As a result it was decided to use a pure graphite antenna for the remainder of the test campaign to reduce costs.

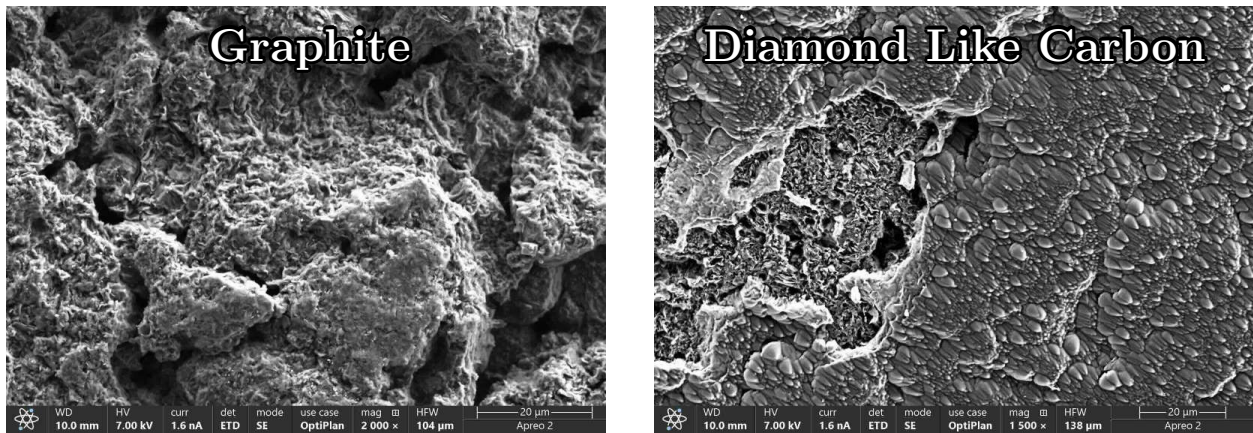


Figure 4.18: SEM images of the tip of the antenna. Pure graphite antenna (left). 1 μ m Diamond Like Carbon (DLC) coating with graphite visible beneath the layer (right).

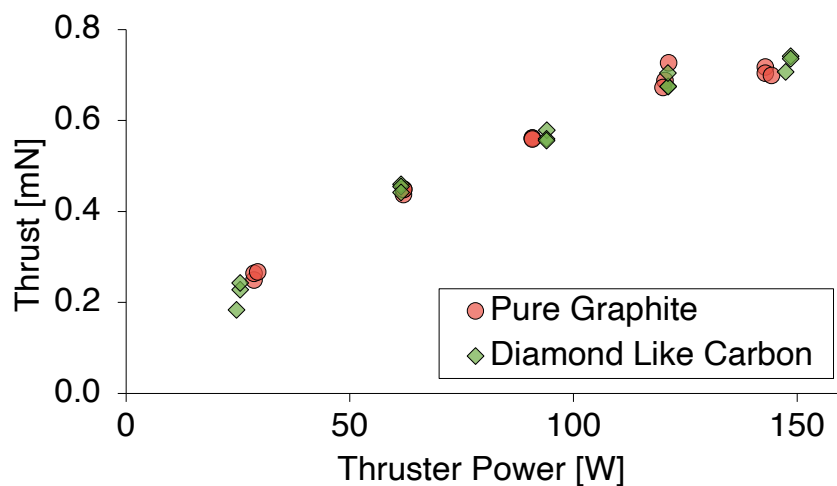


Figure 4.19: Thrust as a function of thruster power for a pure graphite antenna and Diamond Like Carbon (DLC) coated antenna. Small ECR thruster, 0.10 mg/s xenon mass flow rate. Three readings taken for each test condition, standard errors from 0.001 mN to 0.018 mN.

4.5 Thruster Floating Potential

As the thruster is electrically insulated from the thrust balance, it is free to float at the floating potential of the surrounding plasma. The thruster's floating potential can therefore be a good indicator as to the strength of the ambipolar electric field that accelerates the ions. Previous research shows that the ratio of ECR thruster floating potential to total energy of the ion beam remains constant[15]. The thruster's floating potential can therefore be a good indicator of thruster performance.

Small Thruster

It was observed that increasing thruster power had a positive effect on both the thruster floating potential and the measured thrust, see figure 4.20.

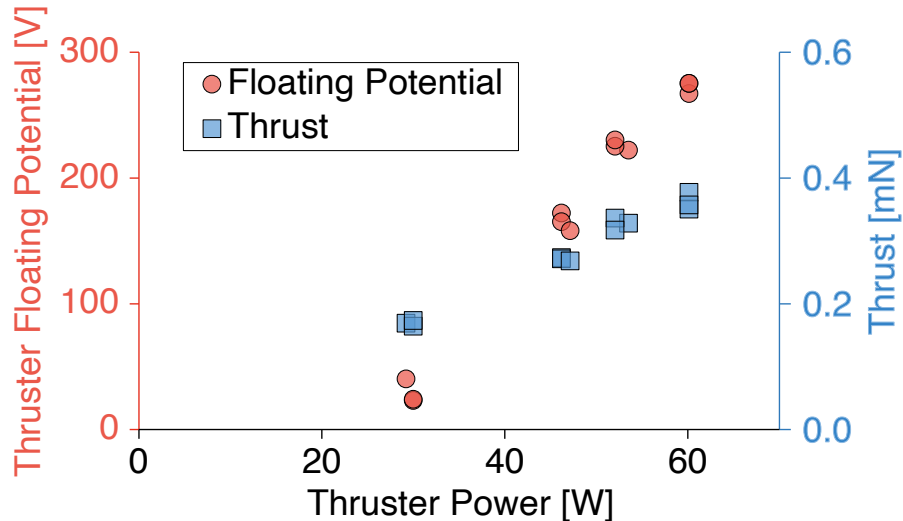


Figure 4.20: Thruster floating potential and thrust as a function of thruster power with 0.08 mg/s xenon mass flow rate. Three readings taken for each test condition, standard errors from 3 V to 4 V and 0.001 mN to 0.008 mN respectively.

As floating potential has a positive correlation with performance, it is worth finding out if it is a contributor to the increased performance or merely an inconsequential side effect of it. Connecting a power supply to the thruster and sweeping the thruster's potential from -300 V to +300 V had no effect on thruster performance. This is likely due to the same effect described in section 2.6.2, where the potential of the ambipolar electric field in the plume changes to ensure that the gradient of the ambipolar electric field is maintained[28].

Research by S. Peterschmitt[36] showed that placing a dielectric sheet in the exit plane of an ECR thruster could significantly increase thrust. This is thought to be because it blocks any back-streaming electrons from flowing to the back of the thruster. To try and replicate these results, a 180 mm diameter mica dielectric sheet was added to the thruster's exit, see figure 4.21. As shown in figure 4.22, the addition of the dielectric sheet shows no significant increase to thrust. The sheet was therefore removed for all the following tests.



Figure 4.21: The small ECR thruster with dielectric sheet in its exit plane.

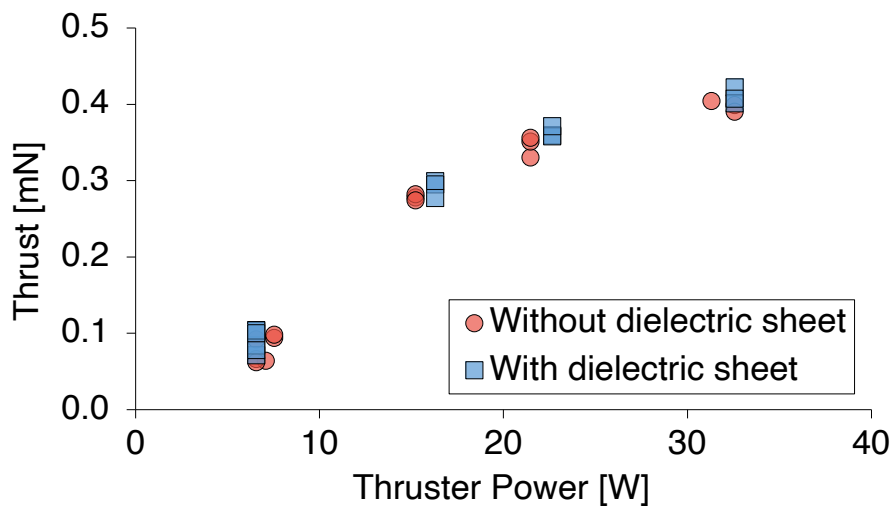


Figure 4.22: Thrust as a function of thruster power for the small ECR thruster both without and with a dielectric sheet in its exit plane. 0.25 mg/s xenon mass flow rate. Three readings taken for each test condition, standard errors from 0.002 mN to 0.008 mN.

4.6 Conclusion

Three ECR thrusters are tested, each with distinct geometries. It is found that for a chamber diameter of 30.0 mm, a 16 mm chamber length produces higher thruster performance than longer chambers. While reducing the chamber diameter to 24 mm is seen to reduce thruster performance. A straight thruster chamber wall was determined to produce the highest thruster performance as it was seen to result in the lowest reflected powers. A large ECR thruster with a 74.0 mm diameter chamber was then developed, which was seen to produce higher thrust at a sacrifice to specific impulse. An improved coaxial design also allowed for higher thruster powers.

Positioning the injector holes at the rear of the thruster's chamber was seen to increase power coupling at low mass flow rates, likely due to the propellant being more evenly dispersed when it reaches the resonance region. A linear antenna was found to produce higher thruster performance than a helical antenna. And an antenna length of 15.3 mm was determined to produce the highest thruster performance, as it is an integer fraction of the wavelength of the microwaves.

Antenna material was also investigated, as it was theorised that an antenna with an increased SEE yield could increase plasma density and boost thruster performance. The graphite antenna was coated in Diamond Like Carbon, which has a SEE yield >8.0 , but this failed to improve thruster performance. Lastly, a dielectric sheet was added to the thruster's exit plane, with the aim of blocking back-streaming electrons. However, this also failed to improve thruster performance. Both the Diamond Like Carbon coating and the dielectric sheet were not used for all the following tests.

Table 4.2: Key dimensions of the final configurations of the two thrusters that are used for all following tests in this thesis, as well as their maximum performance values. Compared against the two thrusters that have been developed at ONERA[36]. * Performance values for the ONERA thrusters are those taken in the smaller B61 vacuum chamber to enable a more representative comparison[7].

	Developed For Thesis		Developed By ONERA*	
	Smaller Thruster	Larger Thruster	Smaller Thruster	Larger Thruster
Chamber Diameter [mm]	22.5	74.0	27.5	70.0
Chamber Length [mm]	21.0	20.0	20.0	20.0
Antenna Length [mm]	23.0	20.0	20.0	20.0
Thrust [mN]	0.5	1.5	0.5	2.0
Specific Impulse [s]	700	400	600	1000
Thruster Efficiency [%]	2	2	6	8

5 EFFECTS OF MAGNETIC FIELD GRADIENT AT RESONANCE

In section 2.2 it was found that decreasing the magnetic field strength gradient $|\frac{\partial B}{\partial x}|$ within the resonance region increases the power that the electrons absorb when passing through. The small ECR thruster that was geometrically optimised in chapter 4 uses a permanent magnet, and therefore has a permanent magnetic field strength gradient. The addition of an electromagnet downstream of the small ECR thruster allows for its magnetic field strength gradient at resonance to be decreased. This decrease in magnetic field strength gradient results in a proportional increase in thrust, indicating that reducing the magnetic field strength gradient at resonance can significantly increase thruster performance due to increased electron heating.

This section on decreasing the magnetic field strength gradient at resonance via the use of an additional electromagnet is split into six parts:

5.1	Magnetic Model	90
5.2	Magnetic Field Strength Gradient at Resonance Effects	94
5.3	Mass Flow Rate Effects	101
5.4	Thruster Power Effects	104
5.5	Background Pressure Effects	107
5.6	Conclusion	111

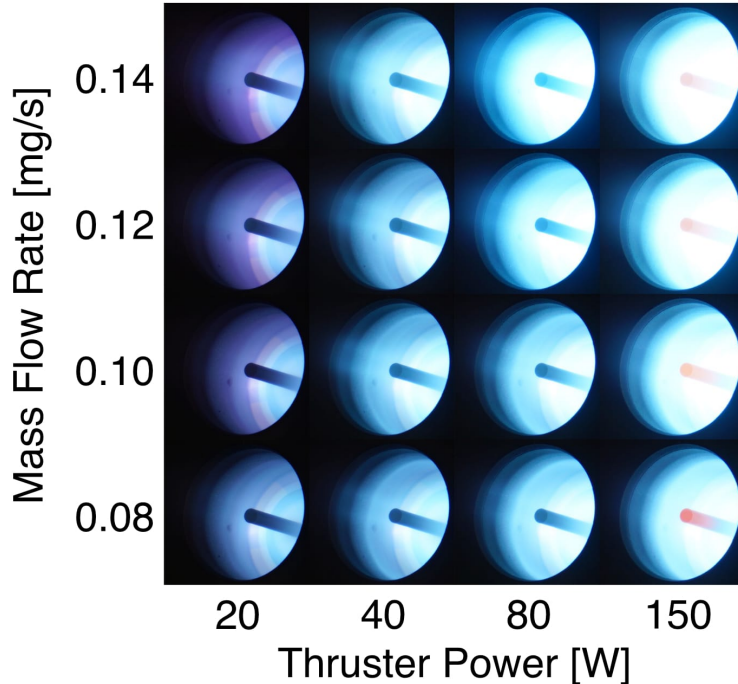


Figure 5.1: Sixteen photos of the small ECR thruster with electromagnetic coil removed, comparing mass flow rates and thruster powers. 1/40 s, f/6.3 and ISO 100.

5.1 Magnetic Model

This section describes the magnetic field of the small ECR thruster and how it changes when an electromagnetic coil is added into the magnetic circuit. The geometrical design of the small ECR thruster is detailed in section 4.1. It should be noted that adding an electromagnetic coil downstream of the thruster does alter the thruster's performance.

An electromagnetic coil was added 24.0 mm downstream of the small ECR thruster's permanent magnet, see figure 5.2. This coil comprises 1300 turns of 0.75 mm diameter aluminium wire, has an outer diameter of 80.0 mm, inner diameter of 44.0 mm and height of 48.0 mm.

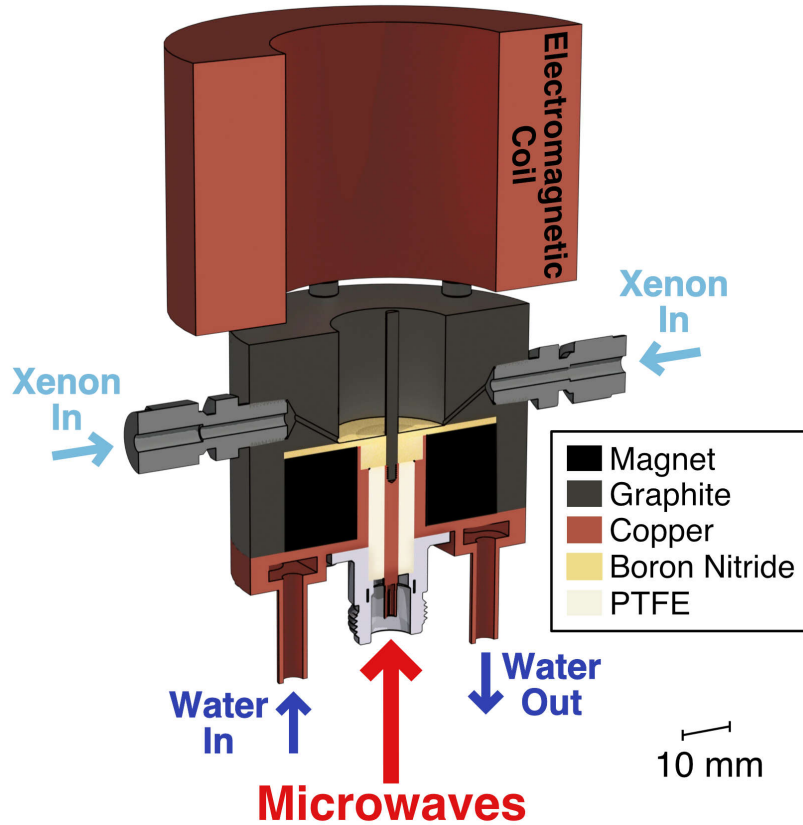


Figure 5.2: Cross-sectional view of the small ECR thruster with electromagnetic coil.

An axisymmetric magnetic field model of the thruster was created using Finite Element Method Magnetics[93]. By sweeping the current through the electromagnetic coil, the magnetic field strength gradient at resonance can be varied. By plotting the magnetic field strength along the thruster's central axis, this change in magnetic field strength gradient can be observed, see figure 5.3.

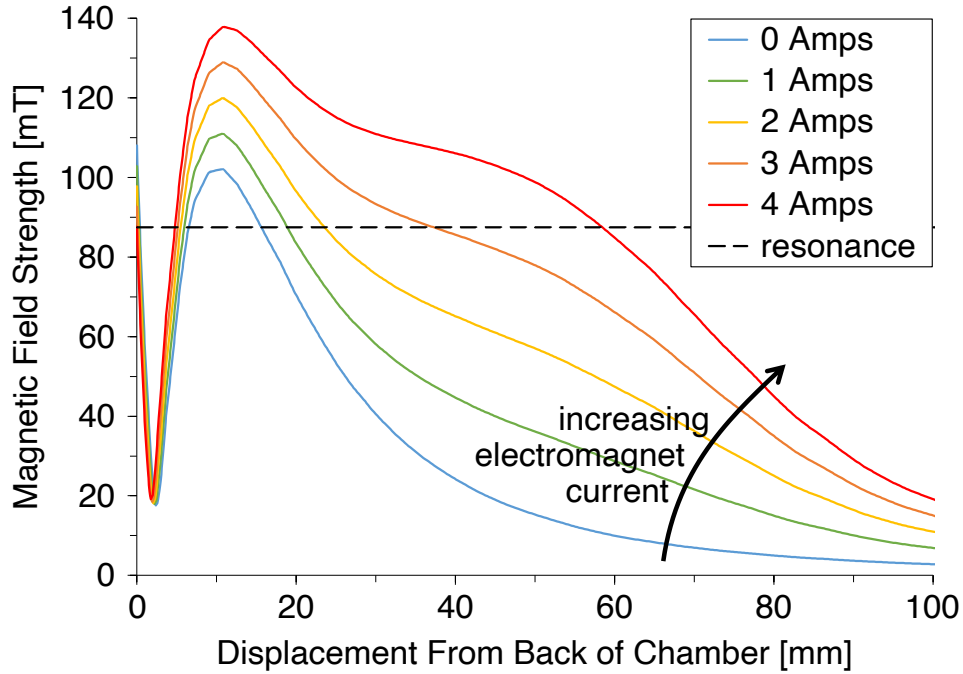


Figure 5.3: Magnetic field strength plot for the small ECR thruster with varying coil currents. Each solid line shows the change in magnetic field strength with respect to displacement from the back of the thruster's chamber along its central axis. The dashed line shows the magnetic field strength at which resonance occurs, 87.5 mT. Modelled using FEMM[93].

By measuring the gradient of each curve as it passes through resonance (the black dashed line), $|\frac{\partial B}{\partial x}|$ is found and recorded in table 5.1. The resonance regions that lie before 10 mm displacement from the back of the chamber can be ignored, as these are much smaller and so should have a minimal effect on electron heating. Now that $|\frac{\partial B}{\partial x}|$ is found, the total resonance region thickness, $\Delta x_{ecr} + \Delta x_D$, can be calculated using equations 2.7 and 2.13, see table 5.1. This assumes the same axial electron velocity as J. Porto et al.[45] of 1.1×10^6 m/s. From table 5.1, the total resonance region thickness, $\Delta x_{ecr} + \Delta x_D$, can be seen to be greatest at 3 A of coil current.

Table 5.1: Values that define the resonance region along the central axis of the small ECR thruster for each electromagnetic coil current.

Coil Current	0 A	1 A	2 A	3 A	4 A
$ \frac{\partial B}{\partial x} $ [T/m]	3.82	3.69	2.31	0.69	1.66
Δx_{ecr} [mm]	3.2	3.3	4.1	7.5	4.9
Δx_D [mm]	0.3	0.3	0.5	1.6	0.6
B_{0U} [mT]	94.2	94.1	92.8	90.6	92.1
B_{0L} [mT]	80.8	80.9	82.2	84.4	82.9

Ideally, the absorbed power per unit area of the resonance region, S_{ecr} , would now be calculated for each value of magnetic field strength gradient in table 5.1. This would allow for the prediction of the ECR thruster's performance based on how much energy is absorbed in the resonance region. Using equations 2.7 and 2.10, S_{ecr} can be defined in terms of Δx_{ecr} , see equation 5.1, where S_{ecr} is the absorbed power per unit area of the resonance region in W/m^2 , n_e is the number density of electrons in m^{-3} , e is the elementary charge in C, E_R is the amplitude of the R-wave, m_e is the mass of an electron in kg, v_{\parallel} is the electrons mean axial velocity in m/s and Δx_{ecr} is the thickness of the resonance region in m.

$$S_{ecr} = \frac{n_e e^2 E_R^2}{2 m_e v_{\parallel}} \Delta x_{ecr}^2 \quad (5.1)$$

From equation 5.1 it can be seen that to calculate S_{ecr} , values for electron density, n_e , and amplitude of the driving electromagnetic wave, E_R , must first be found. These are not trivial to find and therefore have the potential to introduce significant errors into the value of S_{ecr} . By making the assumption that n_e , E_R and v_{\parallel} remain constant as the magnetic field strength gradient changes, it can be stated that that $S_{ecr} \propto \Delta x_{ecr}^2$. It can therefore be assumed that any increase in Δx_{ecr}^2 results in a directly proportional increase to the power absorbed by the electrons.

As the rate of change of magnetic field strength gradient is relatively small, the assumption can be made that magnetic field strength gradient remains constant within the resonance region. This allows for the calculation of the lower and upper bounds of the resonance region, see equations 5.2 and 5.3, where B_{0U} and B_{0L} are the upper and lower bounds of the resonance region in T, B_0 is the magnetic field strength at resonance in T, Δx_{ecr} is the thickness of the resonance region in m, Δx_D is the resonance region thickness due to Doppler broadening in m and $|\frac{\partial B}{\partial x}|$ is the magnetic field strength gradient at resonance in T/m.

$$B_{0U} = B_0 + \frac{\Delta x_{ecr} + \Delta x_D}{2} \left| \frac{\partial B}{\partial x} \right| \quad (5.2)$$

$$B_{0L} = B_0 - \frac{\Delta x_{ecr} + \Delta x_D}{2} \left| \frac{\partial B}{\partial x} \right| \quad (5.3)$$

Equations 5.2 and 5.3 can be seen to account for Doppler broadening, as this is thought to increase the energy absorbed by electrons passing through the resonance region. The size of the resonance region can now be visualised as the region between the upper and lower bounds of the resonance region, B_{0U} and B_{0L} . This is shown as the red regions in figure 5.4. This assumes that there is a negligible change in magnetic field strength gradient in the radial direction.

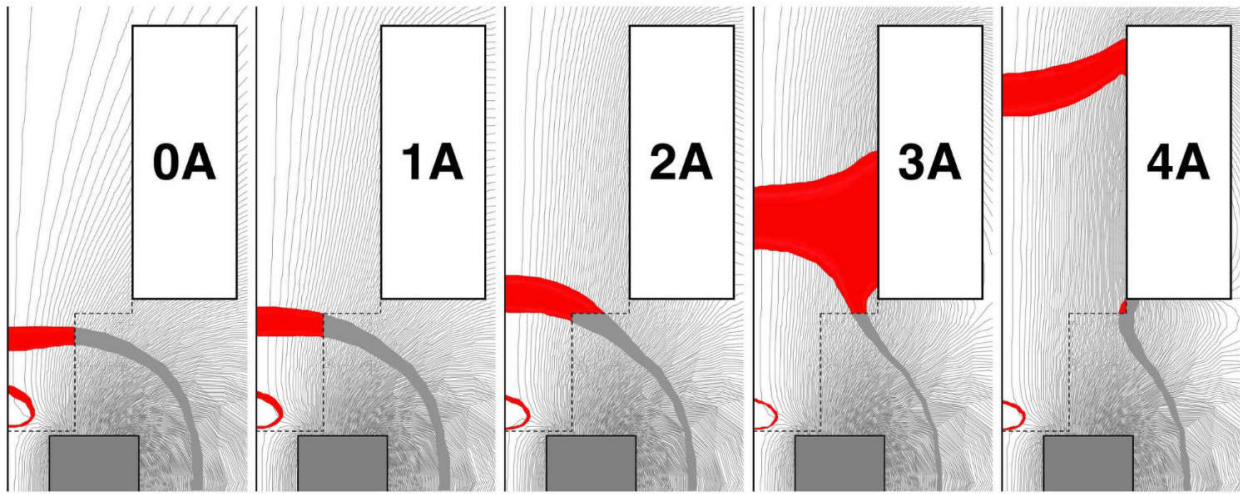


Figure 5.4: Five axisymmetric magnetic field models of the small ECR thruster, with varying electromagnetic coil currents. Permanent magnet indicated by grey box, electromagnet indicated by white box, dashed lines outline the chamber. Resonance region defined as the region between B_{0U} and B_{0L} and indicated in red when inside the chamber, or grey when outside the chamber. Modelled using FEMM[93].

The observable change in the area of the red resonance region in figure 5.4 shows how the thickness of the resonance region changes as the coil current is increased. By measuring the area of the red region in figure 5.4, the cross-sectional resonance region area can be calculated. Unlike Δx_{ecr} , the value of cross-sectional resonance region area takes into account the thickness of the resonance region across the radius of the thruster. This makes it a more accurate measurement of the net resonance region thickness in the thruster. As it has been determined that $S_{ecr} \propto \Delta x_{ecr}^2$, any increase to the cross-sectional resonance region area should result in a proportional increase to the energy absorbed by the electrons in the resonance region.

5.2 Magnetic Field Strength Gradient at Resonance Effects

By sweeping the current to the electromagnet, the magnetic field strength gradient at resonance can be decreased, increasing both the thickness and the cross-sectional area of the resonance region, see figures 5.3 and 5.4. Equation 5.1 has shown that the square of resonance region thickness is directly proportional to the power absorbed in the resonance region. As the cross-sectional resonance area can be thought of as a measurement of the net resonance region thickness in the thruster, the increase in cross-sectional resonance area should result in a corresponding increase to the power absorbed at the resonance region. This should then result in an increase to the thruster performance.

Thrust Measurements

Direct thrust measurements were taken at varying electromagnetic coil currents and are plotted in figure 5.5. These are plotted alongside the normalised cross-sectional resonance area, which is simply the area of the red regions in figure 5.4, normalised so that the area at 0 A coil current is equal to 1. The thrust can be seen to peak at 3 A and shows a strong correlation with the size of the cross-sectional resonance area. The thruster power is 74 W for all data points and refers to the microwave power deposited in the thruster, it does not account for power used by the electromagnet. The xenon mass flow rate is 0.10 mg/s for all measurements.

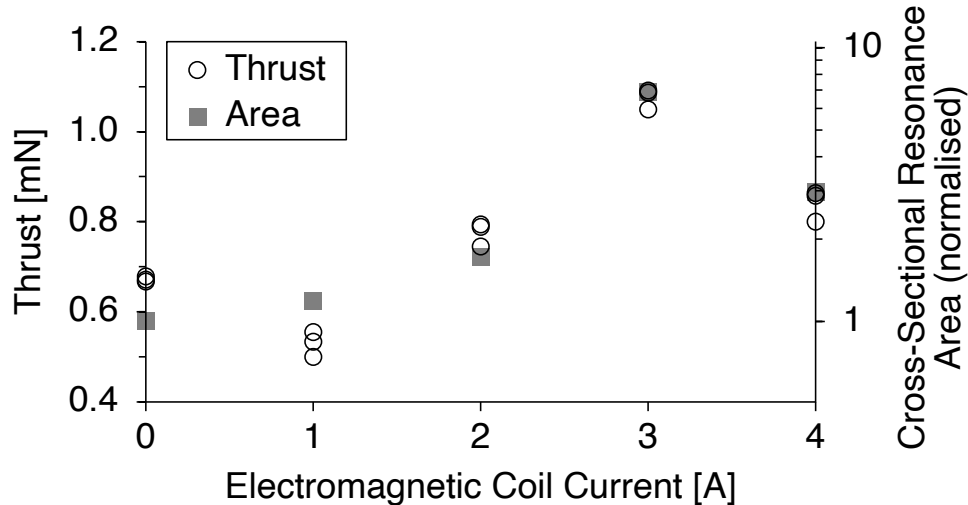


Figure 5.5: Thrust and cross-sectional resonance area (normalised) as a function of the electromagnetic coil current. Small ECR thruster, 74 W thruster power, 0.10 mg/s xenon mass flow rate. Three measurements taken for each coil current, standard errors from 0.003 mN to 0.016 mN. Cross-sectional resonance area is calculated from the red regions in figure 5.4.

Looking again at Figure 5.4, it can be seen that as the coil current is increased, fewer magnetic field lines intersect the walls of the thruster. This could reduce plasma wall losses, resulting in the thrust increase seen in figure 5.5. However, this cannot explain how from 3 A to 4 A, the thrust decreases. The conclusion must then be made that the thrust is highly dependent on the cross-sectional resonance area, as no other variables peak at 3 A of coil

current. This accurately reflects the proportional relationship between the power absorbed in the resonance region and the resonance region thickness, $S_{ecr} \propto \Delta x_{ecr}^2$, as shown by equation 5.1. A higher absorbed power then results in a higher thrust.

From figures 5.5 and 5.6 it can be seen that increasing the electromagnetic coil current from 0 A to 3 A has increased both thrust and specific impulse by 60 %. From figure 5.7 it can be seen that the thruster efficiency is increased by 16 %, or 174 % if the power to the electromagnetic coil is ignored. This study therefore presents strong evidence that optimising for a thickened resonance region can significantly increase the thruster performance.

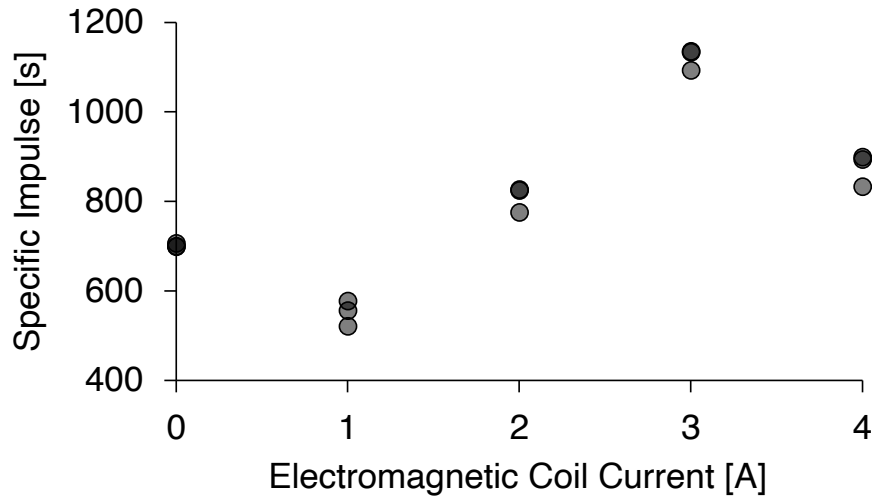


Figure 5.6: Specific impulse as a function of the electromagnetic coil current. Small ECR thruster, 74 W thruster power, 0.10 mg/s xenon mass flow rate. Three measurements taken for each coil current, standard errors from 3 s to 16 s.

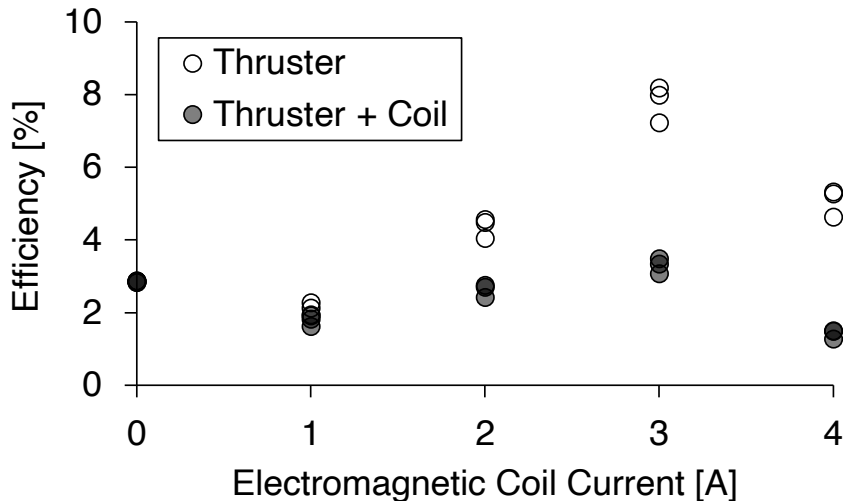


Figure 5.7: Efficiency as a function of the electromagnetic coil current. Thruster efficiency not accounting for coil power shown by white circles, accounting for coil power shown as dark circles. Small ECR thruster, 74 W thruster power, 0.10 mg/s xenon mass flow rate. Three measurements taken for each coil current, standard errors from 0.01 % to 0.29 %.

T. Vialis[15] found that positioning the resonance region further from the backplate decreased the thruster performance. However, figures 5.4 and 5.5 show the thrust mostly increasing as the resonance region moves further from the backplate. This leads to the conclusion that the negative effect of the resonance region's position on the thruster performance appears to be weaker than the positive effect of the increased cross-sectional resonance area.

Ion Beam Measurements

A Faraday probe was used to map out the ion beam profile of the thruster at different coil currents, see figure 5.8. Ions produced in the resonance region with trajectories that are highly divergent from the central axis, normally collide with the thruster walls. When the resonance region is close to the thruster exit however, they can escape. Figure 5.4 shows that the resonance region is closest to the thruster exit at 4 A coil current. This is thought to be the cause of the hump in the ion beam profile between 20° and 70° for this coil current value, see figure 5.8. Ion current density along the thruster's axis (at 0° rotation angle) can be seen to be greatest at 3 A coil current. All data is taken for a fixed thruster power of 71 W and a fixed xenon mass flow rate of 0.10 mg/s.

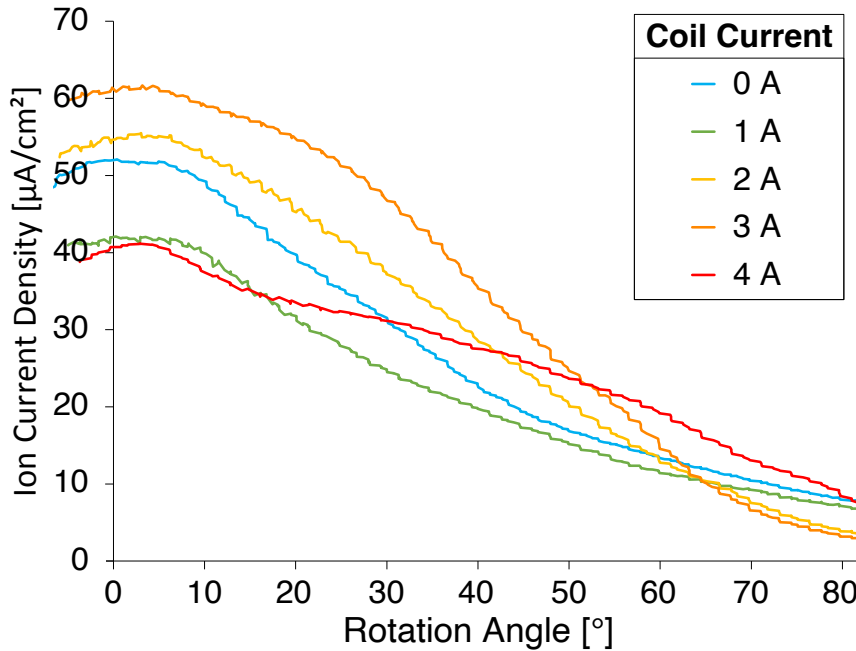


Figure 5.8: Ion current density as a function of rotation angle of the Faraday probe at five different electromagnetic coil currents. Probe swept three times for each coil current, mean value at each angle is used. Small ECR thruster, 71 W thruster power, 0.10 mg/s xenon mass flow rate.

The data presented in figure 5.8 were taken in steps of 1 A of coil current. In figure 5.9, the coil current is instead increased in steps of 0.5 A. The ion current density can be seen to peak at a coil current between 2.5 A and 3.0 A.

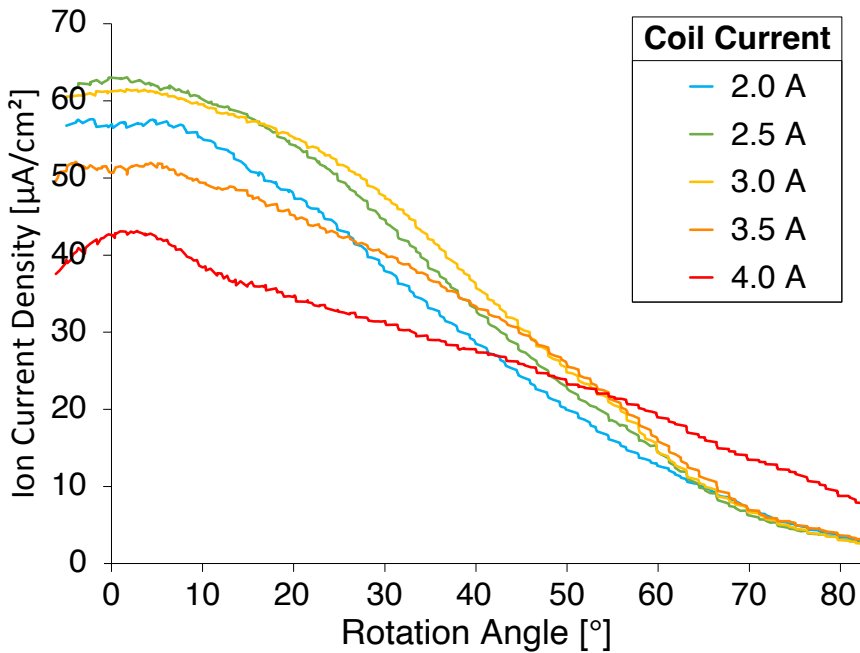


Figure 5.9: Ion current density as a function of rotation angle of the Faraday probe at five different electromagnetic coil currents. Probe swept three times for each coil current, mean value at each angle is used. Small ECR thruster, 69 W thruster power, 0.10 mg/s xenon mass flow rate.

By numerically integrating the ion current density curves in figure 5.8, values for the total current of the ion beam can be calculated. These are plotted alongside the thrust as a function of coil current in figure 5.10. A good correlation between the ion beam current and the thrust, indicates that the increase in thrust is in part due to an increase in ion beam current. In figure 5.10 thrust and ion beam current are also plotted with respect to cross-sectional resonance area. Here it can be clearly seen that larger cross-sectional resonance areas result in increased thrust and ion beam current. This is suggestive that the resonant heating of electrons plays a large role in the ion production mechanism, and therefore a larger resonance region produces an increase to the mass utilisation efficiency.

In figure 5.10 thrust and ion beam current are also plotted as a function of the magnetic field strength gradient at resonance. This clearly shows that decreasing the magnetic field strength gradient at resonance results in increased thruster performance. The values of magnetic field strength gradient at resonance have been taken from the centre of the resonance region, see table 5.1, and so do not represent the whole resonance region, whereas the values of cross-sectional resonance area do account for the whole resonance region. For this reason, values of cross-sectional resonance area are more representative of thruster performance than values of the magnetic field strength gradient at resonance.

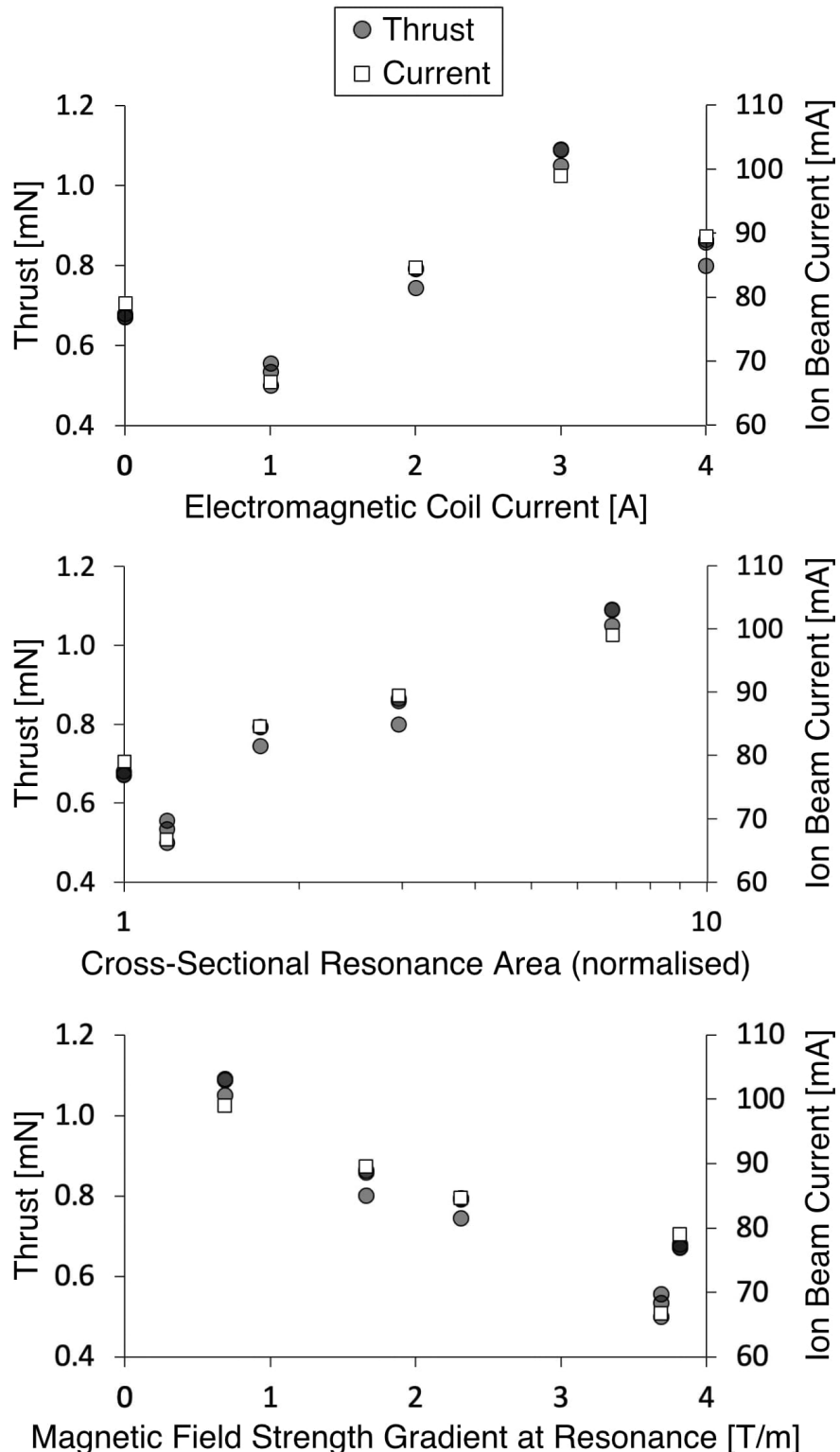


Figure 5.10: Thrust and ion beam current as a function of electromagnetic coil current (top), normalised cross-sectional area of the resonance region (middle) and magnetic field strength gradient on the central axis (bottom). Small ECR thruster, 71 W thruster power, 0.10 mg/s xenon mass flow rate. Three thrust measurements taken for each coil current, standard errors from 0.003 mN to 0.016 mN. Cross-sectional resonance area calculated from the red regions in figure 5.4.

Electron Measurements

Langmuir probe measurements of the electron temperature, taken 49 mm downstream of the electromagnet along the thrusters central axis, are shown in figure 5.11. The electron temperature can be seen to peak at 3 A of coil current, indicating that increased electron heating is occurring within the thicker resonance region.

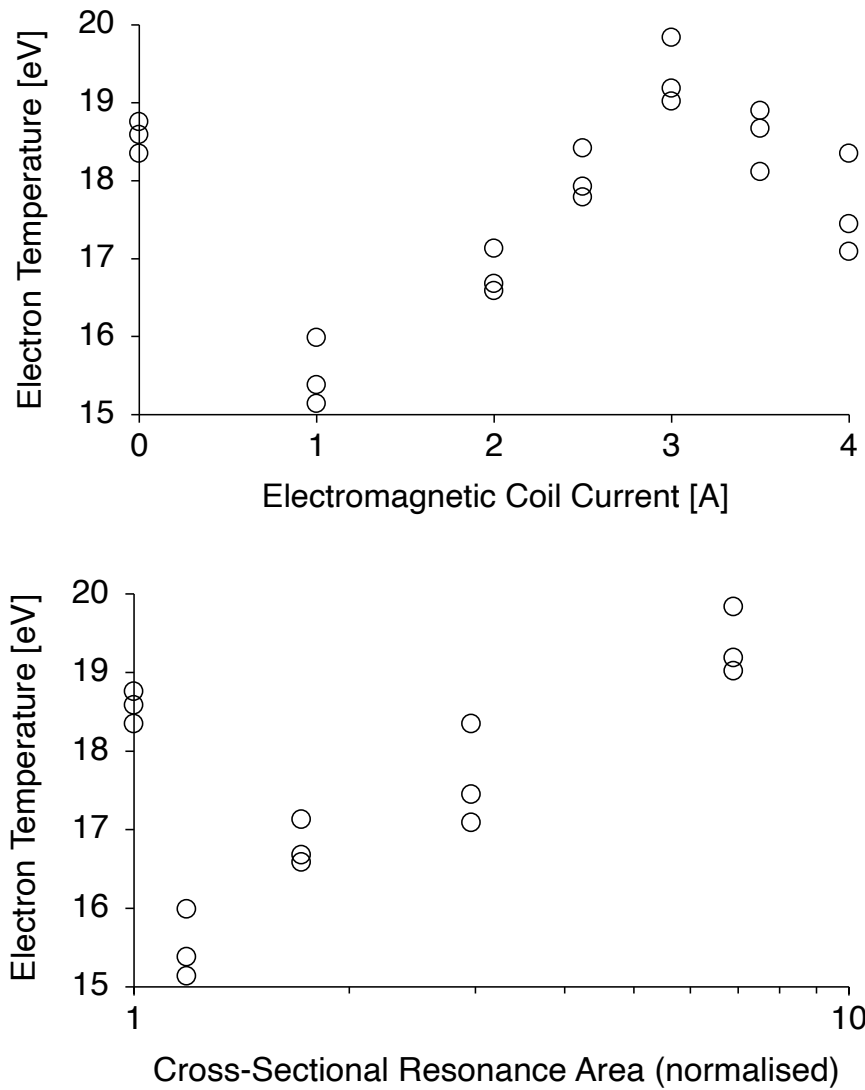


Figure 5.11: Electron temperature as a function of electromagnetic coil current (top) and cross-sectional area of the resonance region (bottom). Cross-sectional resonance area was only calculated for integer values of coil current, hence the bottom plot only contains values for coil currents of 0 A, 1 A, 2 A, 3 A and 4 A. Small ECR thruster, 69 W thruster power, 0.10 mg/s xenon mass flow rate. Three measurements taken for each coil current, standard errors from 0.17 eV to 0.37 eV.

In figure 5.11 electron temperature is also plotted as a function of cross-sectional resonance area for coil currents of 0 A, 1 A, 2 A, 3 A and 4 A. At this Langmuir probe location it can be seen that larger cross-sectional resonance areas produce hotter electrons. However, this relationship is seen to not hold true for a coil current of 0 A. This discrepancy could be due to the significant change to the divergence of the magnetic field when current is increased from 0 A to 1 A, see figure 5.4. This could act to change the gradient of the ambipolar electric field, which would act to change the rate of electron cooling in the magnetic nozzle. Therefore, a change in ambipolar electric field gradient would likely change the temperature of the electrons at the Langmuir probe's location, even if the electrons at the resonance region remained the same temperature. A solution to this would be to measure the temperature of the electrons at the resonance region, however this is likely not possible with a Langmuir probe due to it perturbing the local plasma.

The increased electron thermal energy at higher cross-sectional resonance areas produces a stronger ambipolar electric field which accelerates the ions to greater velocities. This increase in ambipolar electric field strength is indicated by the increase in both thruster floating potential and plasma potential seen in figure 5.12. The plasma potential is measured at the same location as the electron temperature, 49 mm downstream of the electromagnet along the thrusters central axis.

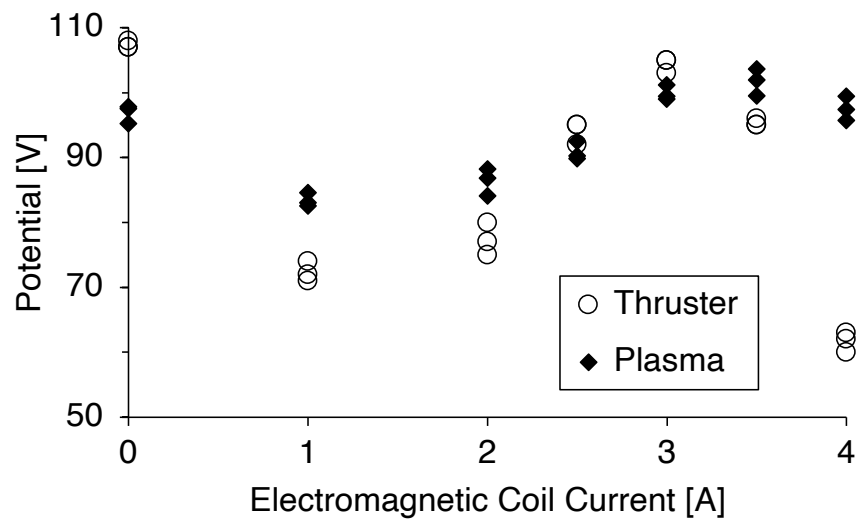


Figure 5.12: Thruster floating potential and plasma potential as a function of electromagnetic coil current. Small ECR thruster, 69 W thruster power, 0.10 mg/s xenon mass flow rate. Three measurements taken for each test condition, standard errors from 0.33 V to 1.45 V and 0.60 V to 1.21 V respectively.

5.3 Mass Flow Rate Effects

In section 5.2 it was determined that 3 A of electromagnetic coil current produced both the thickest resonance region and the highest thruster performance. Therefore a coil current of 3 A is used for all tests in section 5.3. Thruster power refers to the microwave power deposited in the thruster, and does not account for power used by the electromagnet.

Thrust Measurements

Thrust measurements were taken at three different xenon mass flow rates to better characterise the thruster, see figure 5.13.

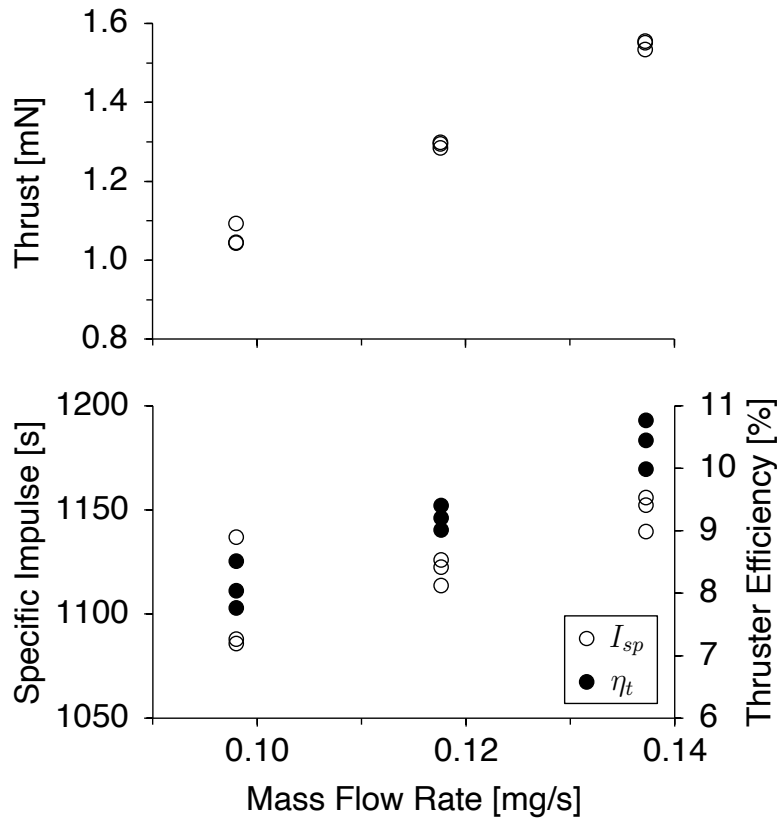


Figure 5.13: Thrust, specific impulse and thruster efficiency as a function of xenon mass flow rate. Small ECR thruster, 78 W thruster power, 3 A coil current. Three readings taken for each mass flow rate, standard errors from 0.004 mN to 0.016 mN. Thruster efficiency does not account for electromagnetic coil power.

As can be seen from Figure 5.13, between 0.10 mg/s and 0.14 mg/s the thruster performance scales linearly with mass flow rate. Higher mass flow rates are required to determine the performance ceiling for this thruster. It should be noted that the power of the electromagnetic coils was not accounted for in the calculation of thruster efficiency in figure 5.13. A later iteration of the thruster has achieved a magnetically thickened resonance region without the use of electromagnets. Therefore, not accounting for electromagnetic coil power in calculations of thruster efficiency, enables us to compare the two.

Ion Beam Measurements

A Faraday probe was used to map out the ion beam profile of the thruster at three different mass flow rates, see figure 5.14. The ion beam current was then calculated and is displayed in figure 5.15. The ion beam current shows a positive linear correlation with the mass flow rate.

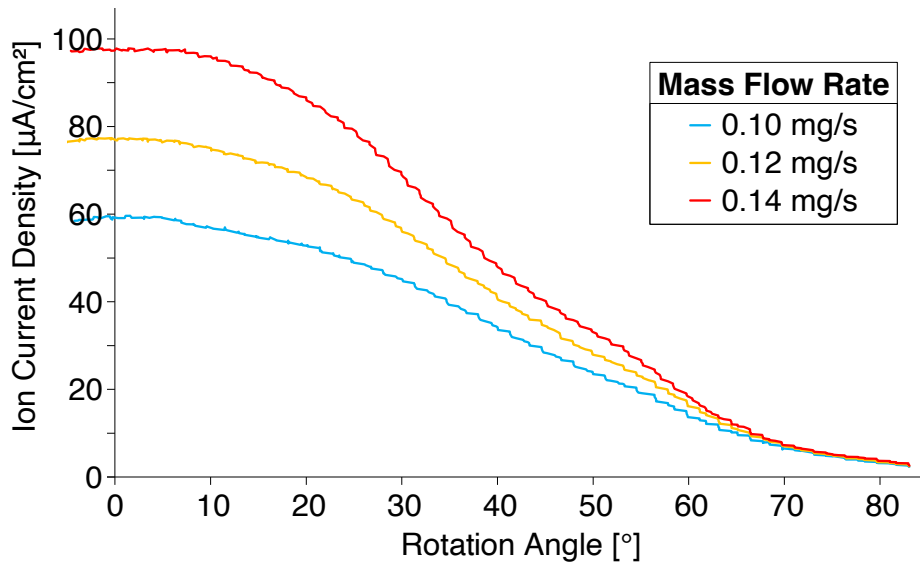


Figure 5.14: Ion current density as a function of rotation angle of the Faraday probe at three different mass flow rates. Probe swept three times for each mass flow rate, mean value at each angle is used. Small ECR thruster, 78 W thruster power, 3 A coil current.

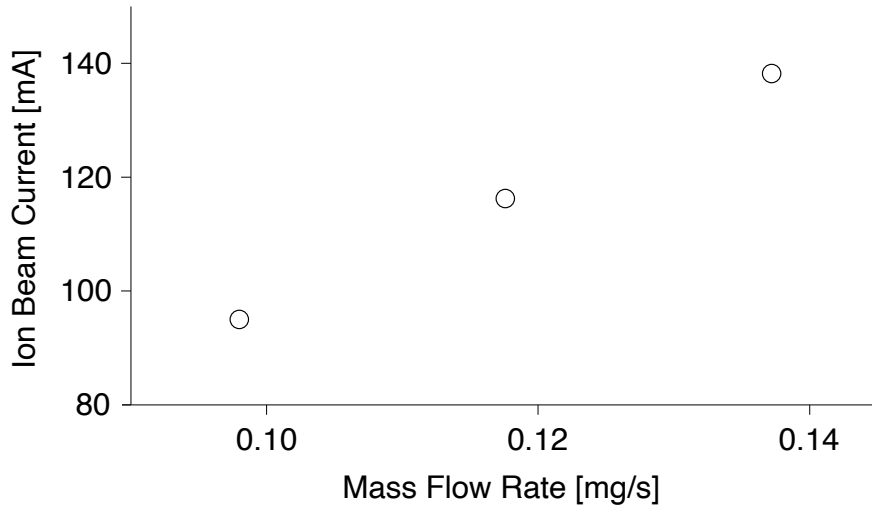


Figure 5.15: Ion beam current as a function of mass flow rate. Small ECR thruster, 78 W thruster power, 3 A coil current.

Electron Measurements

Langmuir probe measurements of the electron temperature and plasma potential, taken 49 mm downstream of the electromagnet along the thrusters central axis, are shown in figure 5.16. The mass flow rate can be seen to have only a small effect on the electron energy. This results in a similarly small change to the thruster floating potential and the plasma potential, as seen in figure 5.16. Electron temperature decreases by 9 % as the xenon mass flow rate is increased from 0.10 mg/s to 0.14 mg/s, while plasma potential decreases by 7 %. As discussed in section 2.2, individual electrons passing through the resonance region should gain the same energy from ECR heating, irrespective of the propellant mass flow rate. This agrees with the data shown in figure 5.16, as electron energies are seen to have little dependence on propellant mass flow rate, but might decrease at higher mass flow rates due to the increased probability of electron-neutral collisions.

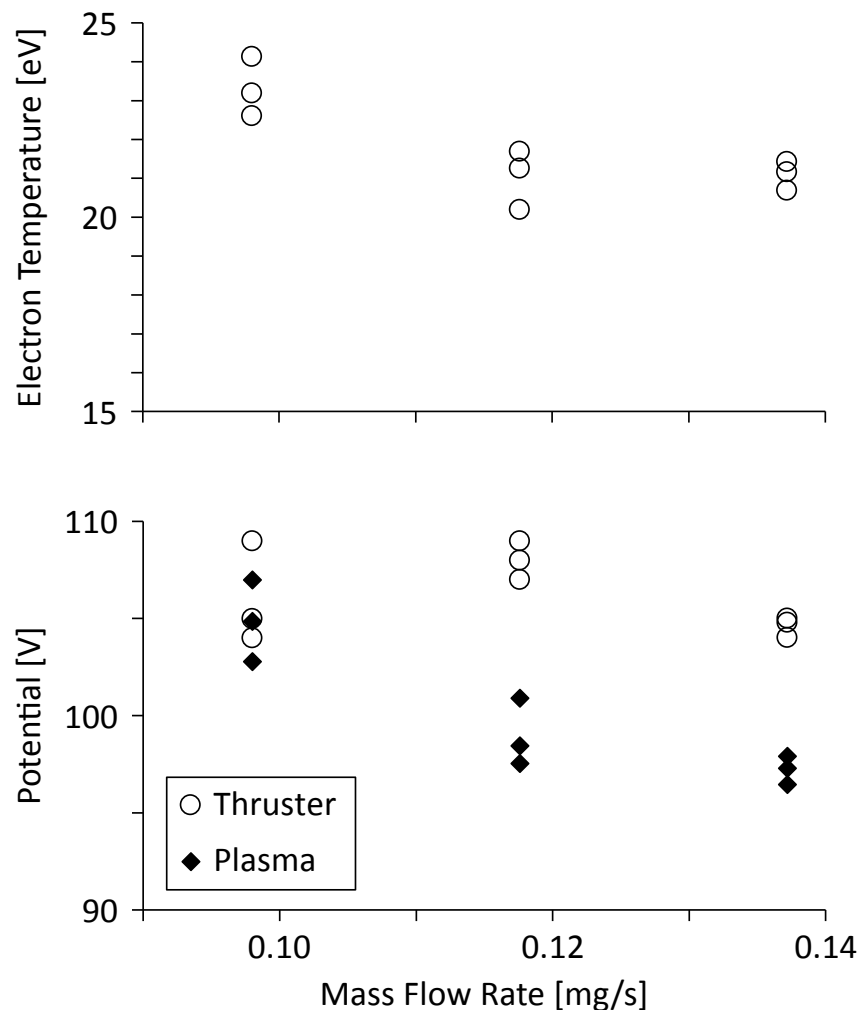


Figure 5.16: Electron temperature, thruster floating potential and plasma potential as a function of xenon mass flow rate. Small ECR thruster, 78 W thruster power, 3 A coil current. Three readings taken for each mass flow rate, standard errors from 0.20 eV to 0.44 eV, 0.33 V to 1.53 V and 0.44 V to 1.15 V respectively.

5.4 Thruster Power Effects

A coil current of 3 A and a xenon mass flow rate of 0.10 mg/s are used for all tests in section 5.4. The thruster power refers to the microwave power deposited in the thruster, and does not account for power used by the electromagnet.

Thrust Measurements

Thrust measurements were taken at three different forward microwave powers to better characterise the thruster, see figure 5.17. A change in reflected power is responsible for the spread in thruster powers between the three repeats.

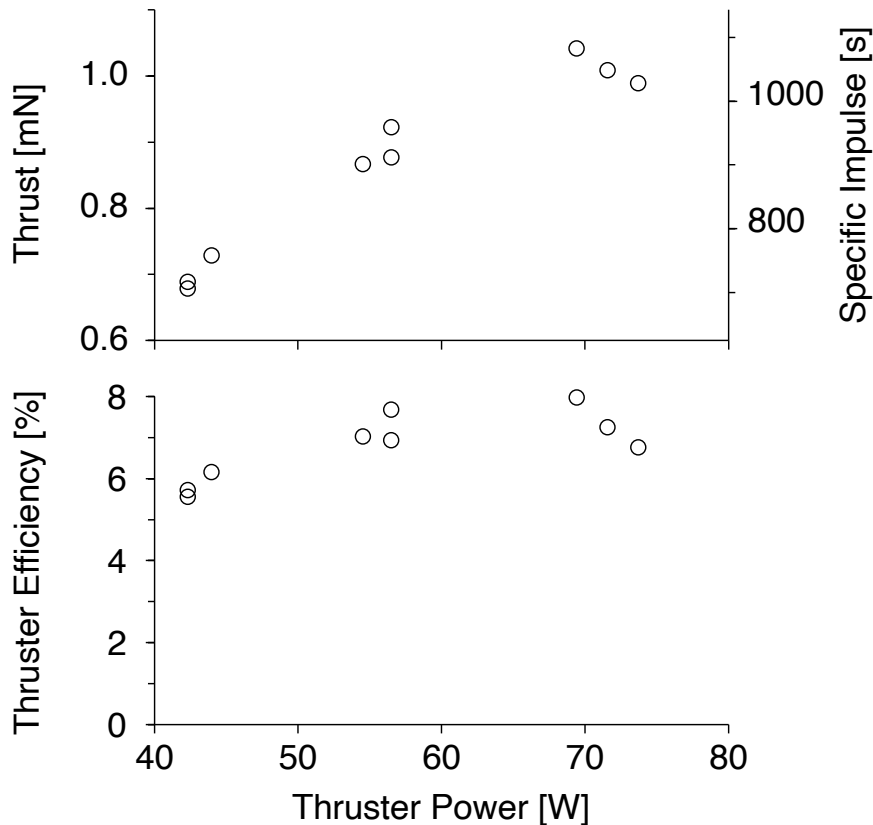


Figure 5.17: Thrust, specific impulse and thruster efficiency as a function of thruster power. Small ECR thruster, 0.10 mg/s xenon mass flow rate, 3 A coil current. Three readings taken for each power level, standard errors from 0.015 mN to 0.017 mN. Thruster efficiency does not account for electromagnetic coil power.

A positive correlation between thruster power and thrust indicates that higher microwave powers yield higher performance. This agrees with equation 2.10, that shows how the power absorbed per unit area of the resonance region is directly proportional to the amplitude of the electric field, $S_{ecr} \propto E_R$. As higher thruster powers increase the amplitude of the electric field, this leads to more absorbed power in the resonance region and a higher thruster performance.

Ion Beam Measurements

The ion current density profiles for thruster powers of 43 W, 56 W and 73 W were measured and are displayed in figure 5.18. Ion beam current was then calculated and is displayed in figure 5.19. Ion beam current appears to start plateauing for higher thruster powers, indicating that increasing thruster powers further will only result in a marginal increase to ion beam current and mass utilisation efficiency.

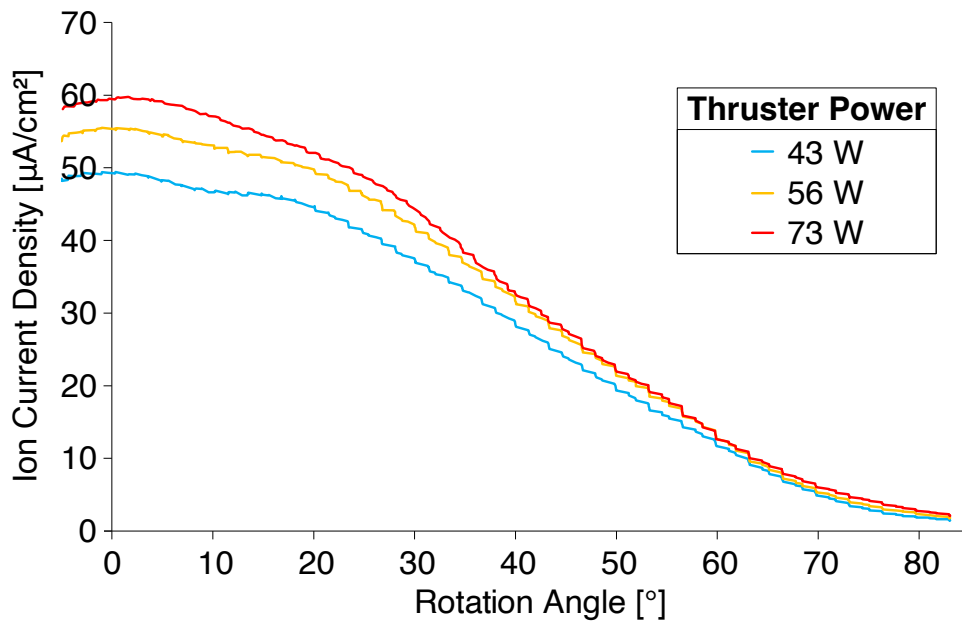


Figure 5.18: Ion current density as a function of rotation angle of the probe at three different thruster powers. Probe swept three times for each power, mean value at each angle is used. Small ECR thruster, 0.10 mg/s xenon mass flow rate, 3 A coil current.

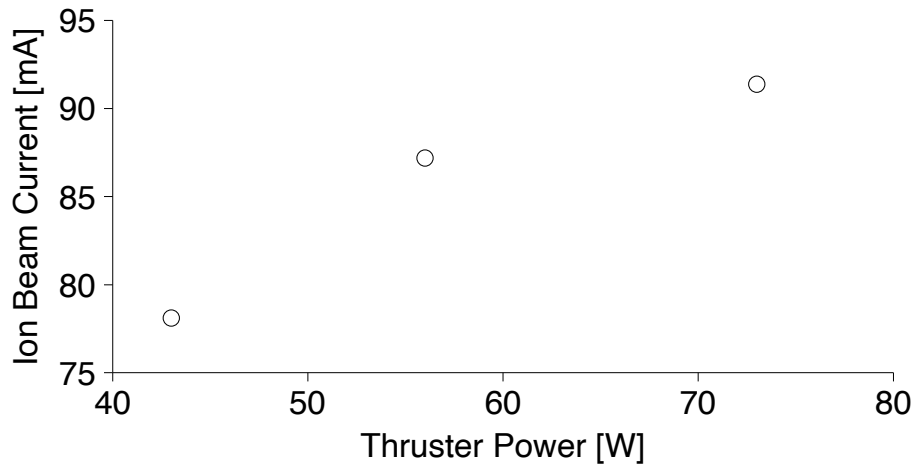


Figure 5.19: Ion beam current as a function of thruster power. Small ECR thruster, 0.10 mg/s xenon mass flow rate, 3 A coil current.

Electron Measurements

Langmuir probe measurements of the electron temperature and plasma potential, taken 49 mm downstream of the electromagnet along the thrusters central axis, are shown in figure 5.20. The increase in thruster power results in an increase in measured electron temperature, see figure 5.20. This results in a corresponding increase to the strength of the ambipolar electric field, as indicated by the increase to thruster floating potential and plasma potential seen in figure 5.20. In section 2.3 it was determined that ion energy was directly proportional to both the electron temperature at the thruster's exit plane and the maximum potential drop in the plume. The results in figure 5.20 therefore indicate that thruster power has a significant effect on ion energy, this is supported by the corresponding increase to specific impulse shown in figure 5.17.

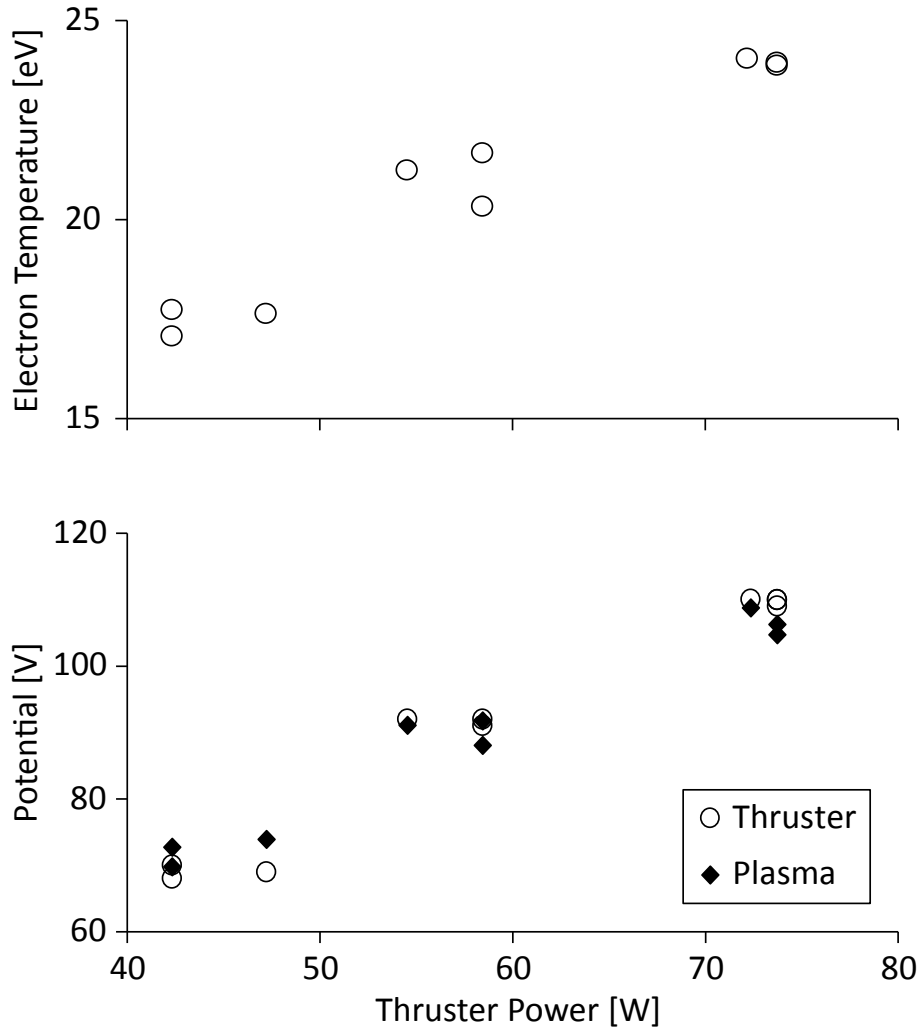


Figure 5.20: Electron temperature, thruster floating potential and plasma potential as a function of thruster power. Small ECR thruster, 0.10 mg/s xenon mass flow rate, 3 A coil current. Three readings taken for each power level, standard errors from 0.07 eV to 0.30 eV, 0.33 V to 0.58 V and 1.10 V to 1.51 V respectively.

5.5 Background Pressure Effects

A coil current of 3 A, a xenon mass flow rate of 0.10 mg/s and a thruster power of ~ 70 W are used for all tests in section 5.5. The thruster power refers to the microwave power deposited in the thruster, and does not account for power used by the electromagnet.

Thrust Measurements

ECR magnetic nozzle thrusters use a magnetic nozzle to accelerate electrons away from the thruster. This generates an ambipolar electric field that acts to accelerate the ions out of the thruster. At higher background pressures, more electrons collide with the neutral particles in the background gas. This reduces the electron temperature and the strength of the ambipolar electric field, reducing the acceleration of the ions. This decrease in performance at higher background pressures introduces significant uncertainty when attempting to predict the in-space performance of these thrusters.[26]

To study these effects, the background pressure is artificially increased by introducing an auxiliary flow of xenon into the vacuum chamber, see figure 3.3. When the background pressure is decreased from 5×10^{-5} mBar to 6×10^{-6} mBar, the thrust can be seen to increase from 0.8 mN to 1.0 mN, see figure 5.21. A similar linear relationship between performance and the natural logarithm of background pressure was observed by ONERA, the French Aerospace Lab, down to pressures of 8×10^{-7} mBar.[7]

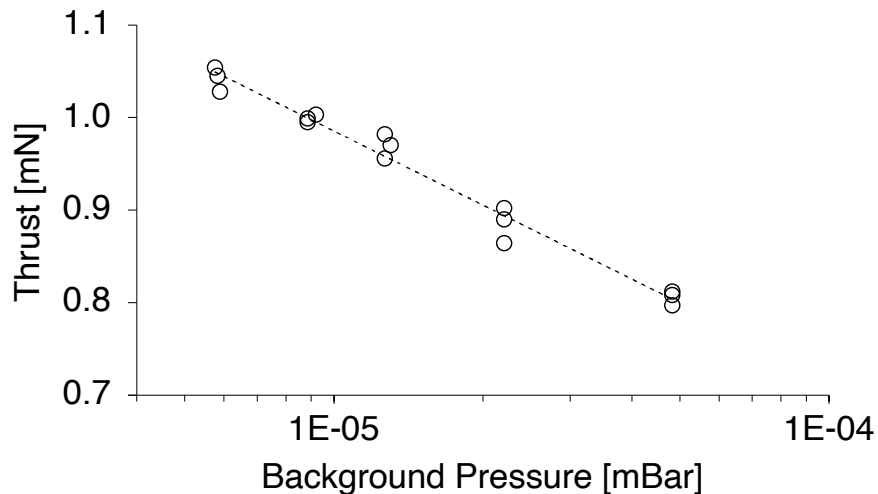


Figure 5.21: Thrust as a function of background pressure. Small ECR thruster, 68 W thruster power, 0.10 mg/s xenon mass flow rate, 3 A coil current. Three readings taken for each background pressure, standard errors from 0.002 mN to 0.011 mN.

The background pressure at which this linear relationship plateaus has yet to be found. It is therefore important that the testing of ECR thrusters be conducted at as low a background pressure as possible. Efforts should be made to fly an ECR thruster in space as soon as possible, so that its in-space performance can be determined. This can be achieved by measuring how much the thruster changes the trajectory of a spacecraft.

Ion Beam Measurements

A Faraday probe is used to measure the thruster's ion current density profile at different background pressures, see figure 5.22. Lower ion current densities along the thruster's central axis (0° rotation angle) are observed at higher background pressures. This is believed to be one of the causes for the decrease in thrust at higher background pressures, as seen in figure 5.21. Another cause is thought to be a decrease in the ion energy. A retarding potential analyser was later used to measure this decrease in ion energy, with its results presented in section 8.5.

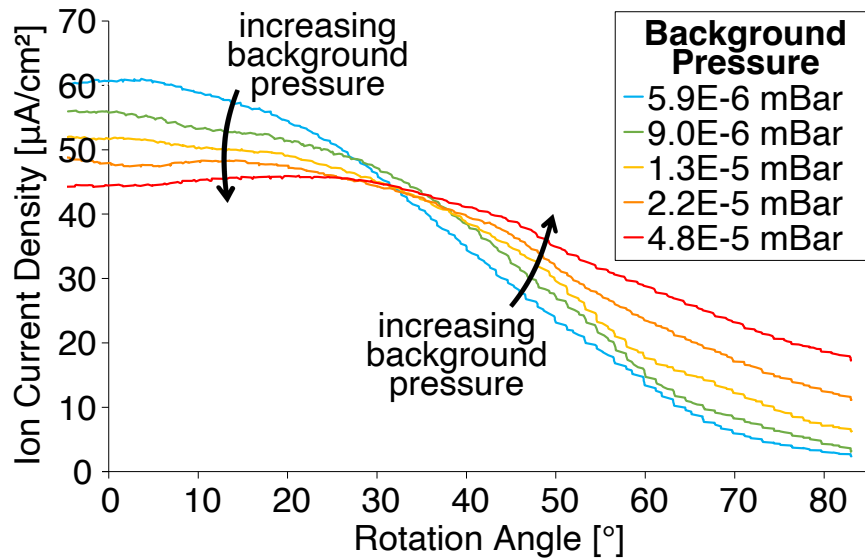


Figure 5.22: Ion current density as a function of rotation angle, showing the ion beam profile of the thruster at different background pressures. Small ECR thruster, 70 W thruster power, 0.10 mg/s xenon mass flow rate, 3 A coil current. 0° is when the probe is aligned with the central axis of the thruster. Probe swept three times for each background pressure, mean value at each angle is used.

The ion current density is seen to increase with background pressure for rotation angles greater than $\sim 40^\circ$. The increase in the number of neutral particles at these higher pressures increases the frequency of ion-neutral and electron-neutral collisions in the plume. This results in increased ion scattering, where the ions deviate from their original trajectory, increasing ion beam divergence. This also results in an increase to the frequency of charge exchange collisions in the plume. Charge exchange collisions create low-energy ions with mostly random trajectories that are more easily captured by the Langmuir probe at large rotation angles, increasing ion beam divergence[100]. Hall effect thrusters usually experience an increase in ion current density at all rotation angles, resulting in an increase to thruster performance at higher background pressures[101]. This is due to entrained neutrals

artificially increasing the propellant mass flow rate.

From figure 5.23 it can be seen that the total ion beam current increases with background pressure. This indicates that like in hall effect thrusters, entrained neutrals are artificially increasing the propellant mass flow rate[102]. However, because the increased background pressure also decreases the strength of the ambipolar electric field, the ion current density at the central axis decreases. This results in a significant decrease to the divergence efficiency, see figure 5.23.

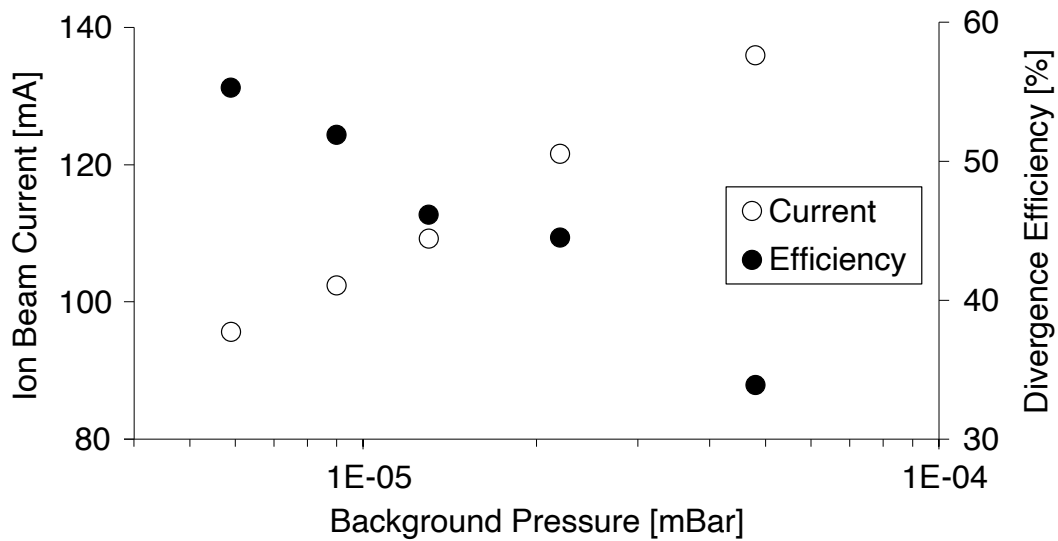


Figure 5.23: Ion beam current and divergence efficiency as a function of background pressure. Small ECR thruster, 70 W thruster power, 0.10 mg/s xenon mass flow rate, 3 A coil current.

Electron Measurements

Langmuir probe measurements of the electron temperature and plasma potential, taken 49 mm downstream of the electromagnet along the thrusters central axis, are shown in figure 5.24. It can be seen that both electron temperature and plasma potential decrease as background pressure increases. This observation is in agreement with B. Wachs et al.[26] who has demonstrated that the decrease in performance at higher background pressures is predominately due to the increased electron-neutral collisions in the plume. These collisions decrease the net energy of the electrons, which in turn decreases the ambipolar electric field strength that is responsible for accelerating the ions. A decrease in ambipolar electric field strength is indicated by the decrease in the thruster floating potential and the plasma potential in figure 5.24.

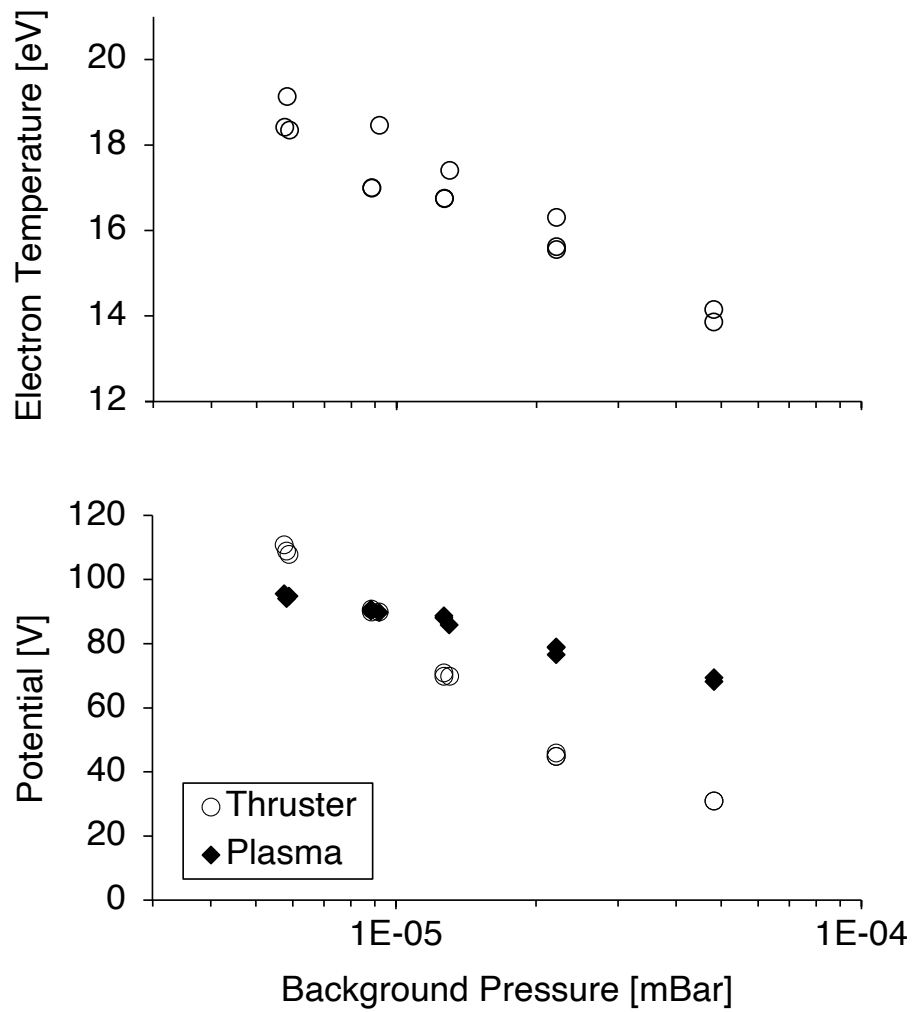


Figure 5.24: Electron temperature, thruster floating potential and plasma potential as a function of background pressure. Small ECR thruster, 68 W thruster power, 0.10 mg/s xenon mass flow rate. Three readings taken for each background pressure, standard errors from 0.15 eV to 0.49 eV, 0.33 V to 1.00 V and 0.24 V to 0.39 V respectively.

5.6 Conclusion

The addition of an electromagnetic coil at the exit of the small ECR thruster, allows for the magnetic field strength gradient to be decreased. This reduction in magnetic field strength gradient results in a thicker resonance region that delivers more energy to the electrons. This is supported by measurements of the electron temperature that increase as the resonance region is thickened. This increase in electron energy acts to increase the strength of the ambipolar electric field. This is supported by measurements of the thruster floating potential and plasma potential that both increase as the resonance region is thickened. This strengthened ambipolar electric field accelerates more ions to a greater velocity. This is supported by measurements of the ion beam current that increase as the resonance region is thickened. Measurements of ion velocity using a retarding potential analyser were taken in a follow up study and are presented in chapter 8. The increase in the number and velocity of ions acts to increase thruster performance. This is confirmed using direct thrust measurements that increase as the resonance region is thickened.

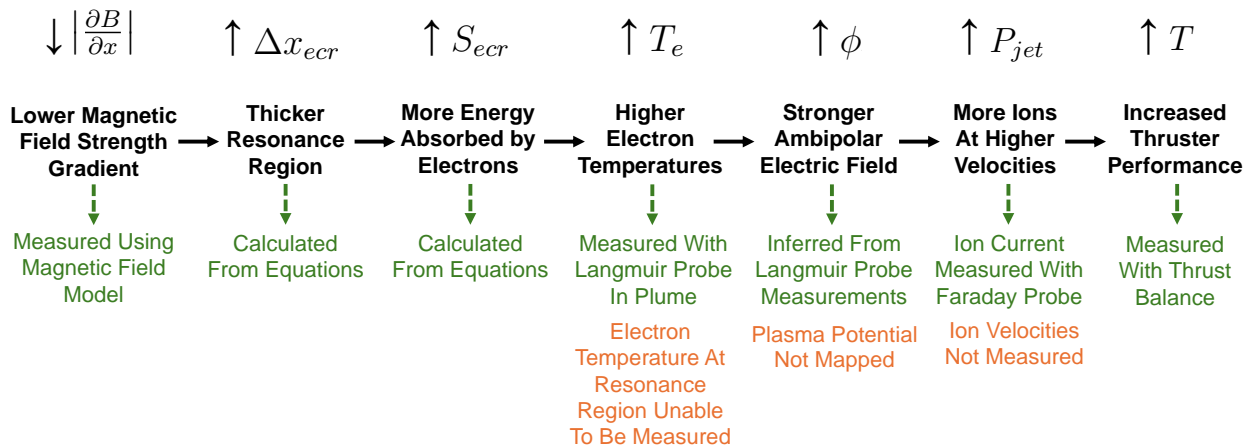


Figure 5.25: Flowchart showing the theorised sequence of events and the variables that are increased/decreased as a result. The method with which each variable was measured is shown in green.

Increasing the thickness of the resonance region has increased both thrust and specific impulse by 60 %, see figure 5.5. The thruster efficiency is increased by 16 %, or 174 % if the power to the electromagnet is ignored. This study therefore presents strong evidence that optimising for a thickened resonance region can significantly increase thruster performance. Achieving this thickening with passive magnetic components instead of an electromagnet, can significantly increase the thruster efficiency. This is the subject of chapter 8.

6 EFFECTS OF ADDING A MAGNETIC MIRROR TRAP

Chapter 2 has shown that the energy of the ions is directly proportional to the temperature of the electrons at the thruster's exit plane. Thruster performance is therefore highly dependent on the energy of the electrons. Chapter 5 exploits this dependence, increasing electron heating in the resonance region to increase thruster performance.

A new method with which to increase the energy of the electrons is proposed. The addition of a second permanent magnet creates a region of high magnetic field strength at the thruster's exit. This acts to confine electrons to the thruster's chamber via the magnetic mirror effect. The trapped electrons bounce around the inside of the thruster's chamber, passing through the resonance region multiple times before escaping. By increasing the number of times that the electrons pass through the resonance region, their energy is increased, increasing the thruster performance.

This section on adding a magnetic mirror trap to the small ECR thruster is split into four parts:

6.1	Magnetic Mirror Theory	113
6.2	Magnetic Model	116
6.3	Thruster Performance	118
6.4	Conclusion	125

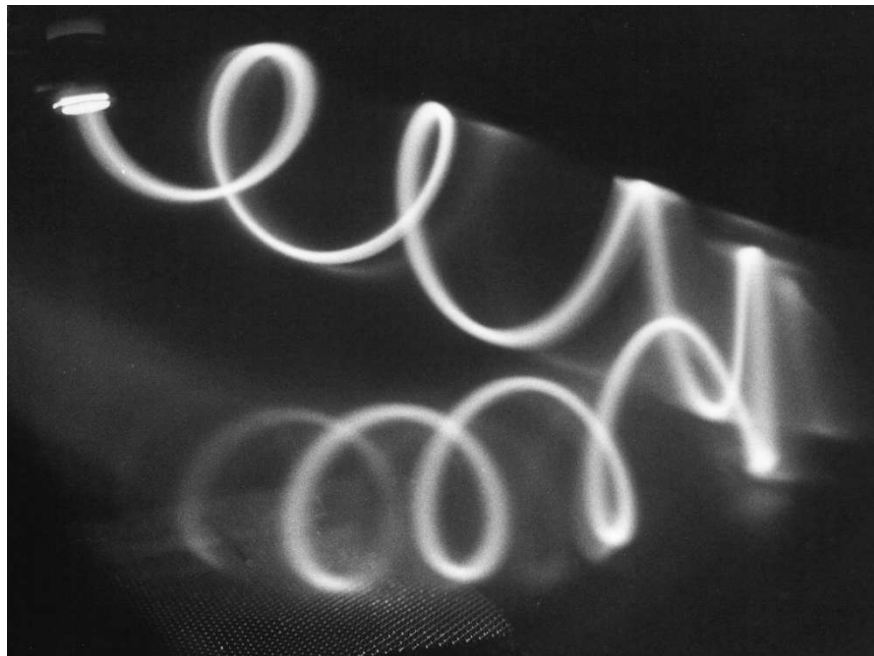


Figure 6.1: Magnetic mirror reflection of an electron beam. The guiding centre of the reflected beam does not follow that of the incident beam due to grad-B drift and curvature drift in a non uniform field. Reproduced from R. Stenzel[103].

6.1 Magnetic Mirror Theory

Electrons in a magnetic field spin around magnetic field lines in a helical motion, such that their velocity can be split into their velocity perpendicular to magnetic field lines, v_{\perp} , and their velocity parallel to magnetic field lines, v_{\parallel} , see figure 2.9. If the magnetic field is diverging, such that magnetic field strength decreases, the perpendicular velocity of the electrons is converted to its parallel velocity, accelerating it in the direction of the magnetic field. This is the principle of magnetic nozzles used for electron acceleration in ECR thrusters. However, if the magnetic field is converging, such that magnetic field strength increases, the electrons parallel velocity is converted to its perpendicular velocity, decelerating it in the direction of the magnetic field. This deceleration continues until the electrons parallel velocity reaches zero and inverts, the electron then begins accelerating in the opposite direction, see figures 6.1 and 6.2. This is known as a magnetic mirror.

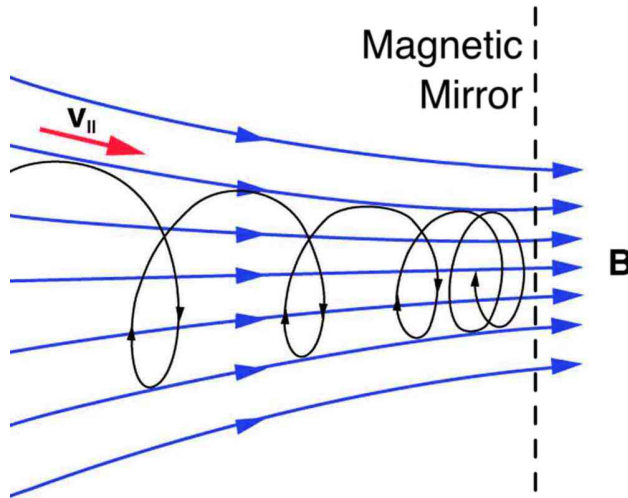


Figure 6.2: An electron that travels into a region with a stronger magnetic field will have its velocity parallel to magnetic field lines reduced. If the magnetic field is strong enough, this velocity will then reverse. Reproduced from P.P. Uroine[104].

Electrons can pass through the magnetic mirror only if their parallel velocity exceeds the value shown in equation 6.1, where v_{\parallel} is the electron's velocity parallel to magnetic field lines in m/s, v_{\perp} is the electron's velocity perpendicular to magnetic field lines in m/s, B_{max} is the maximum magnetic field strength within a magnetic mirror in T and B_{min} is the minimum magnetic field strength within a magnetic mirror in T.

$$\text{Electron escape condition: } v_{\parallel} > v_{\perp} \sqrt{\frac{B_{max}}{B_{min}} - 1} \quad (6.1)$$

As an example, for a mirror ratio $\frac{B_{max}}{B_{min}} = 5$, equation 6.1 simplifies to $v_{\parallel} > 2v_{\perp}$. Assuming an isotropic pitch angle distribution and a Maxwellian temperature distribution, the fraction of electrons that satisfy this condition, $v_{\parallel} > 2v_{\perp}$, and escape the magnetic mirror is found to be $e^{-2} = 13.5\%$, with the remainder getting reflected. Since ECR heating acts to directly increase v_{\perp} , this further decreases the fraction of electrons that can escape the magnetic mirror.[8]

Grad-B Drift

As seen in figure 6.1, electrons are not perfectly reflected and instead experience a drift that acts to move them off the original magnetic field line about which they were rotating. This drift can occur due to the magnetic field strength gradient not aligning with magnetic field lines, see figure 6.3. This causes the electrons radius of rotation (Larmor radius) to change throughout the period of the electrons rotation. This results in the electrons drifting in a direction perpendicular to both the magnetic field lines and the magnetic field gradient at the velocity $v_{\nabla B}$, see equation 6.2, where $v_{\nabla B}$ is the electrons grad-B drift velocity in m/s, v_{\perp} is the electron's velocity perpendicular to magnetic field lines in m/s, r_L is the electrons Larmor radius in m, \mathbf{B} is the magnetic field strength in T and $\nabla \mathbf{B}$ is the magnetic field strength gradient in T/m.

$$\mathbf{v}_{\nabla \mathbf{B}} = \frac{1}{2} v_{\perp} r_L \frac{\mathbf{B} \times \nabla \mathbf{B}}{B^2} \quad (6.2)$$

As ECR heating acts to directly increase v_{\perp} , there is the potential for a significant grad-B drift velocity, $v_{\nabla B}$, within ECR magnetic nozzle thrusters. However, as the grad-B drift velocity is directly proportional to $\mathbf{B} \times \nabla \mathbf{B}$, grad-B drift will only occur in regions where the magnetic field gradient, $\nabla \mathbf{B}$, is not parallel to the magnetic field, \mathbf{B} . This is only seen to occur in/near the thruster, see figure 6.5, meaning that while there is a significant grad-B drift velocity in/near the thruster, there is a negligible grad-B drift velocity in the far field of the plume. ECR magnetic nozzle thrusters typically aim to limit drift as much as possible, as any movement of electrons across magnetic field lines could result in them impacting and being lost to the thruster's chamber walls, reducing thruster efficiency. Conventional ECR thrusters should then aim to have a magnetic field gradient parallel to the magnetic field. This can be achieved by locating the thruster's chamber further from the permanent magnet.

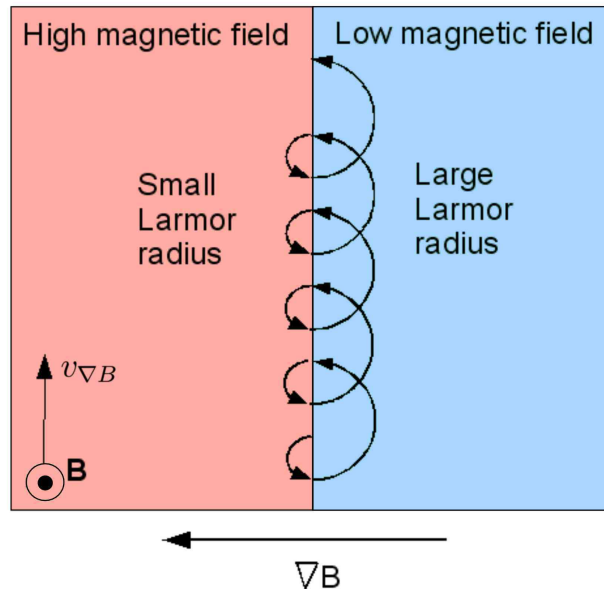


Figure 6.3: Grad-B drift of an electron in a magnetic field where the magnetic field strength gradient is orthogonal to magnetic field lines. Reproduced from A. Peeters[105].

Curvature Drift

The other cause for electrons drifting from the original magnetic field line about which they were rotating is the curvature of a magnetic field. In a curved magnetic field, electrons follow magnetic field lines in an arc with radius r_{Bc} , see figure 6.4. The centrifugal force that these electrons experience, gives them a velocity orthogonal to both the magnetic field and the radius of curvature, see equation 6.3, where \mathbf{v}_R is the electrons curvature drift velocity in m/s, m_e is the electrons mass in kg, v_{\parallel} is the electrons velocity parallel to magnetic field lines in m/s, e is the elementary charge in C, B is the magnetic field strength in T and r_{Bc} is the magnetic field's radius of curvature in m.

$$\mathbf{v}_R = \frac{m_e v_{\parallel}^2}{e B^2} \frac{\mathbf{r}_{Bc} \times \mathbf{B}}{r_{Bc}^2} \quad (6.3)$$

The addition of a second ring magnet to create a magnetic mirror trap increases the curvature of magnetic field lines within the thruster, see figure 6.5. Therefore, the curvature drift velocity, \mathbf{v}_R , can be expected to be greater when the second ring magnet is added.

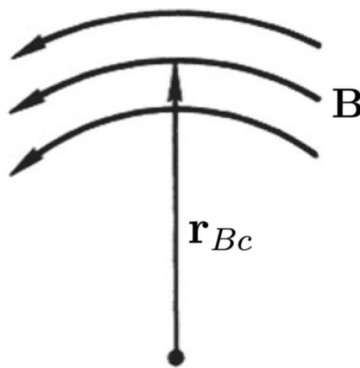


Figure 6.4: Curvature of a magnetic field. Reproduced from F.F. Chen[29].

The addition of the magnetic mirror trap in figure 6.5 also causes a larger fraction of magnetic field lines to intercept the thruster walls. Electrons following these field lines rely on grad-B and curvature drift, as well as collisional events, to move onto other magnetic field lines and escape the thruster. Without these drifts and collisional events the electrons would eventually impact the thruster walls, decreasing thruster efficiency.

6.2 Magnetic Model

This section describes the magnetic field of the small ECR thruster and how it changes when a second ring magnet is added into the magnetic circuit. The geometrical design of the small ECR thruster is detailed in section 4.1, while the electromagnet that allows for the the magnetic field to be optimised is detailed in section 5.1.

To confine the electrons to the thruster's chamber, a magnetic field was designed that uses the magnetic mirror effect to reflect electrons from the thruster's exit. This was achieved via the addition of a permanent ring magnet around the chamber's throat, see figure 6.5.

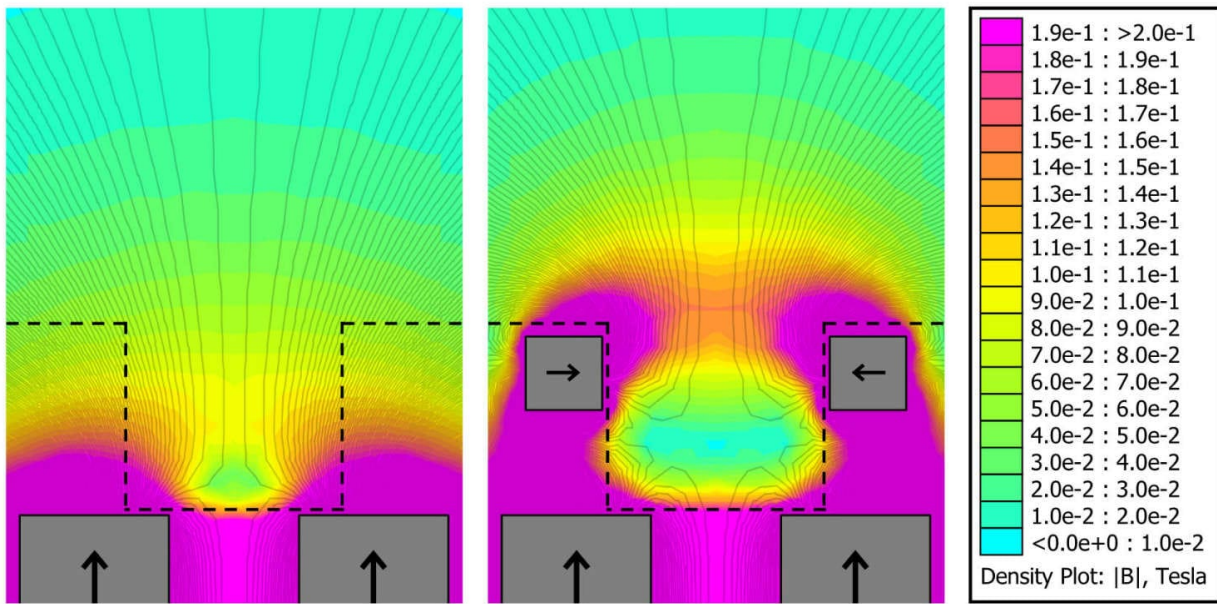


Figure 6.5: Axisymmetric magnetic field model of the smaller ECR thruster with one permanent magnet (left) and two permanent magnets (right). Magnetic field strength shown with colours, chamber outlined with black dashed line, ring magnets shown as grey boxes with arrows showing their direction of magnetisation, resonance region shown in yellow. Modelled using FEMM[93].

Expected Effects of Adding a Magnetic Mirror Trap:

1) Increased Electron Temperature

As can be seen from figure 6.5, the addition of a second ring magnet creates a region of high magnetic field strength at the exit of the thruster's chamber. This magnetic mirror reflects electrons back into the chamber where they pass through the resonance region again, absorbing more energy. This should result in a net increase in electron temperature, as electrons will have passed through the resonance region more times before escaping the magnetic mirror trap. Note that this effect is less significant when the electromagnet is added, as this thickens the downstream resonance region, increasing the energy that electrons gain outside of the magnetic mirror trap, see figure 6.8.

2) Decreased Mass Utilisation Efficiency

This reflection of electrons back into the thruster's chamber also acts to increase the electron density within the thruster. This increase in electron density increases the rate

of electron-neutral collisions, increasing the ionisation rate within the chamber, which should increase mass utilisation efficiency. However, this new magnetic field topology also results in more magnetic field lines intersecting the chamber walls, see figure 6.5. This will likely increase plasma losses to the walls, resulting in a net decrease in mass utilisation efficiency.

3) Lower Propellant Mass Flow Rate Required for Ignition

It was noticed during previous test campaigns that a large xenon mass flow rate (0.7 mg/s) is required to ignite the thruster. This is thought to be because the conventional magnetic field allows the initial free electrons within the propellant to accelerate downstream before they have had the opportunity to ionise the neutrals. The magnetic confinement of these free electrons increases their retention time within the chamber, increasing the rate of ionisation collisions. This should result in a lower propellant mass flow rate required to ignite a plasma.

From the magnetic field models in figure 6.5, the magnetic field strength as a function of displacement from the back of the thruster's chamber can be plotted, see figure 6.6.

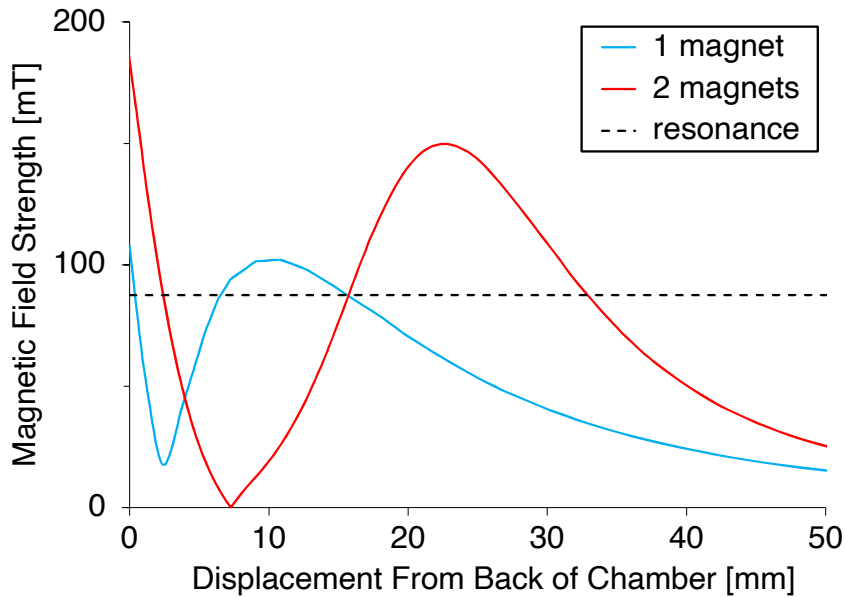


Figure 6.6: Magnetic field strength as a function of displacement from the back of the small ECR thruster's chamber along the thruster's central axis, for the thruster with a single magnet and two magnets. Dashed line shows the magnetic field strength at resonance. Modelled using FEMM[93].

From figure 6.6 it can be seen that the magnetic field strength at the exit of the chamber (21.0 mm displacement from the back of the chamber) is significantly increased for the 2 magnet thruster configuration. A magnetic null point is also introduced at approximately 8 mm displacement from the back of the chamber. This increase in the ratio of $\frac{B_{max}}{B_{min}}$ works to increase the fraction of electrons that are reflected by the magnetic mirror, as shown by equation 6.1. Note that the values of B_{max} and B_{min} are specific to each electron and depend on their individual trajectory. Most do not follow the linear trajectory shown in figure 6.6.

6.3 Thruster Performance

Direct thrust measurements were taken before and after adding the secondary ring magnet to the throat of the thruster. The comparison of these results shows if performance has been increased. The use of a Langmuir probe allows for the measurement of electron temperature to see if the magnetic mirror works to increase the net electron energy. A Faraday probe is also used to measure changes to ion beam current and divergence.

It was observed that the xenon mass flow rate required for ignition reduced from 0.7 mg/s to 0.1 mg/s when the secondary ring magnet was added. This is thought to be because without the magnetic mirror trap, free electrons within the propellant are immediately accelerated out of the thruster. The magnetic mirror trap reflects these escaping electrons, increasing the electron density within the thruster. This increases the electron-neutral collision rate within the thruster such that plasma ignition can occur.

Magnetic Field Optimisation Using Electromagnetic Coil

In chapter 5 it was determined that adding an electromagnetic coil downstream of the thruster could significantly improve performance. The same electromagnetic coils were therefore added to the thruster with the second ring magnet installed. Direct thrust measurements were then taken to determine the coil current at which performance was maximised, see figure 6.7. A thruster power of 74 W and a xenon mass flow rate of 0.10 mg/s was used, coil current was limited to a maximum of 4 A to avoid melting the coils.

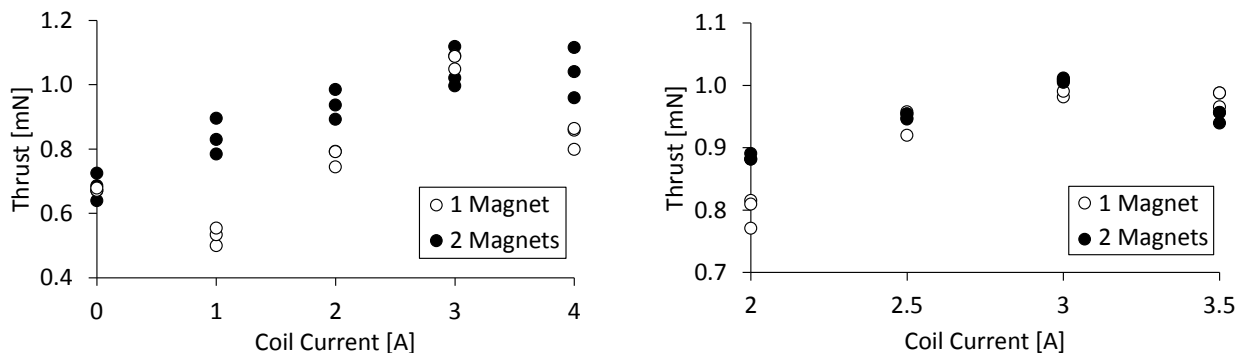


Figure 6.7: Thrust as a function of electromagnetic coil current in steps of 1.0 A (left) and 0.5 A (right). 74 W thruster power for the 1 magnet configuration, 124 W thruster power for the 2 magnet configuration. Small ECR thruster, 0.10 mg/s xenon mass flow rate. Three readings taken for each test condition, standard errors from 0.002 mN to 0.045 mN.

It can be seen from figure 6.7 that a coil current of 3 A achieves the highest thruster performance for both magnetic configurations. It should be noted that the addition of the second ring magnet significantly decreased reflected power, resulting in an increase of thruster power from 76 W to 124 W, see table 6.1. Therefore, despite the similar maximum thrust of the two magnetic configurations, the 2 magnet configuration uses 63 % more thruster power to achieve this. To determine why the reflected power is so low, the resonance region can be visualised in the same way as was done in figure 5.4, see figure 6.8.

Table 6.1: The respective microwave powers of the two thruster configurations at 3 A of electromagnetic coil current. Power to the electromagnet is not included.

No. of Permanent Ring Magnets	Power [W]			
	Forward at Generator	Forward at Thruster	Reflected at Thruster	Thruster
1	240	145	69	76
2	240	145	21	124

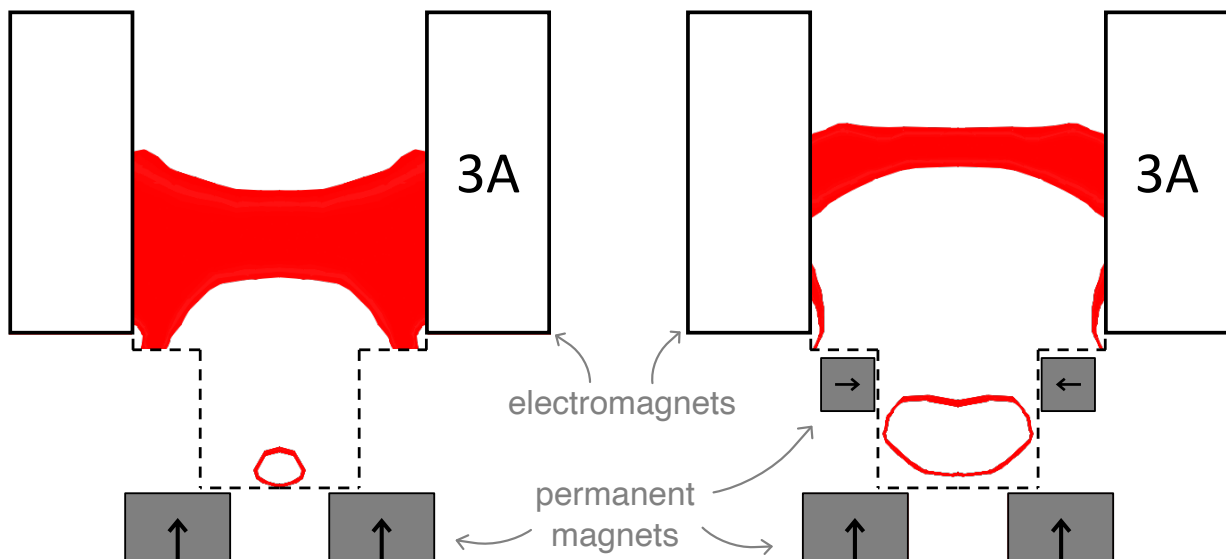


Figure 6.8: Axisymmetric magnetic field models of the small ECR thruster, with one ring magnet (left) and two ring magnets (right). Resonance region shown in red, chamber outlined with black dashed line, permanent ring magnets shown as grey boxes with arrows showing their direction of magnetisation, electromagnet shown as white boxes. Modelled using FEMM[93].

From figure 6.8 it can be seen that adding a second ring magnet increases the size of the upstream “spherical” resonance region within the thruster’s chamber close to the backplate. As this “spherical” resonance region now surrounds the majority of the antenna, it could absorb more of the microwave energy, leaving less to be reflected back to the generator. However, adding the second ring magnet also increases the fraction of magnetic field lines that intersect the thruster walls, see figure 6.9. This likely results in increased plasma losses to the walls, reducing mass utilisation efficiency, which is likely the reason for the two magnet thruster requiring more power to achieve the same thrust as the single magnet thruster. This theory is confirmed by the plot of ion current density in figure 6.10.

The larger red resonance region downstream is thinner for the two magnet configuration, see figure 6.8. This results in less energy getting delivered to the electrons in this region, which could reduce electron temperatures. Figure 6.9 shows that this resonance region lies downstream of the magnetic mirror trap, so electrons only pass through the larger downstream resonance region after they have escaped the magnetic mirror trap.

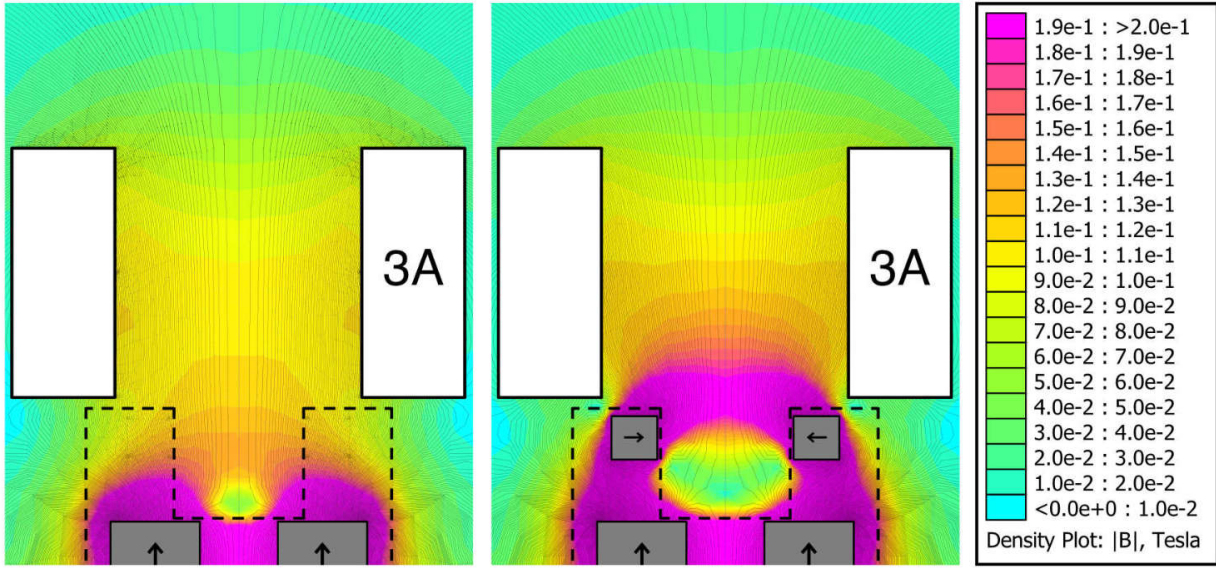


Figure 6.9: Axisymmetric magnetic field model of the smaller ECR thruster with one permanent magnet (left) and two permanent magnets (right). Magnetic field strength shown with colours, chamber outlined with black dashed line, permanent ring magnets shown as grey boxes with arrows showing their direction of magnetisation, electromagnet shown in white. Modelled using FEMM[93].

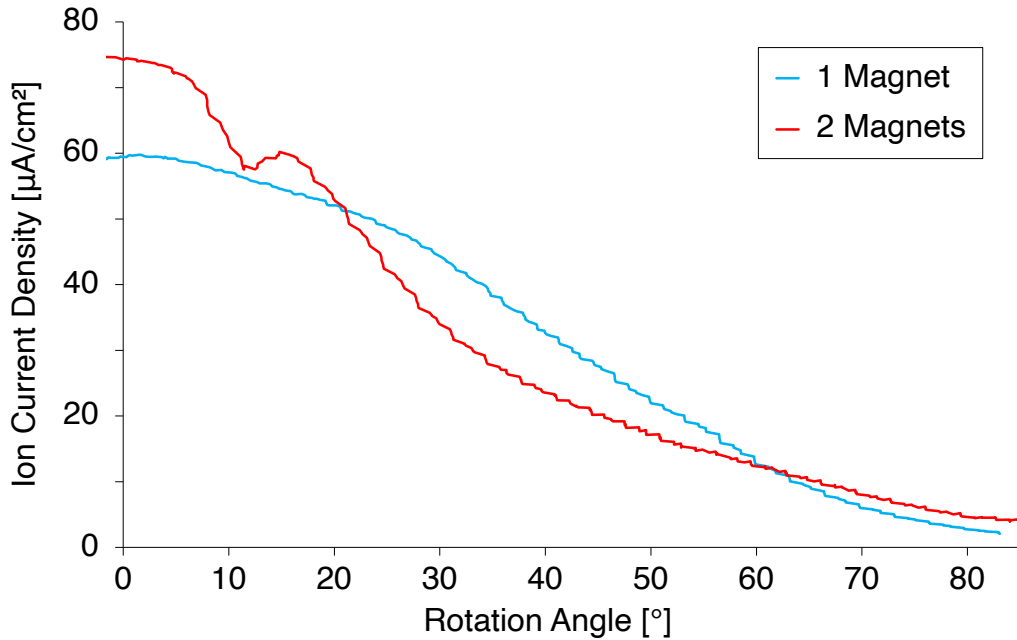


Figure 6.10: Ion current density as a function of rotation angle of the Faraday probe. Probe swept three times for each thruster configuration, mean value at each angle is used. Small ECR thruster, 73 W thruster power, 0.10 mg/s xenon mass flow rate, 3 A coil current.

Ion current density profiles were measured for both the single ring magnet thruster configuration and the two ring magnet thruster configuration with a thruster power of 73 W and

a xenon mass flow rate of 0.10 mg/s, see figure 6.10. Here it can be seen that the addition of a ring magnet decreases the divergence angle of the plume from 41° to 29° . Numerically integrating this plot however, reveals that the ion beam current is reduced 14 %, from 91 mA to 78 mA. This indicates a decrease to the mass utilisation efficiency which is likely due to plasma wall losses due to more magnetic field lines intersecting the chamber walls. A dip in ion current density is observed at approximately 12° rotation angle. The cause of this dip remains unclear, although it is seen to disappear at higher thruster powers.

Thruster Power Effects

The forward power at the microwave generator was increased from 144 W to 195 W to 240 W for a xenon mass flow rate of 0.10 mg/s. This allows for the relationship between thruster power and performance to be determined, see figure 6.11.

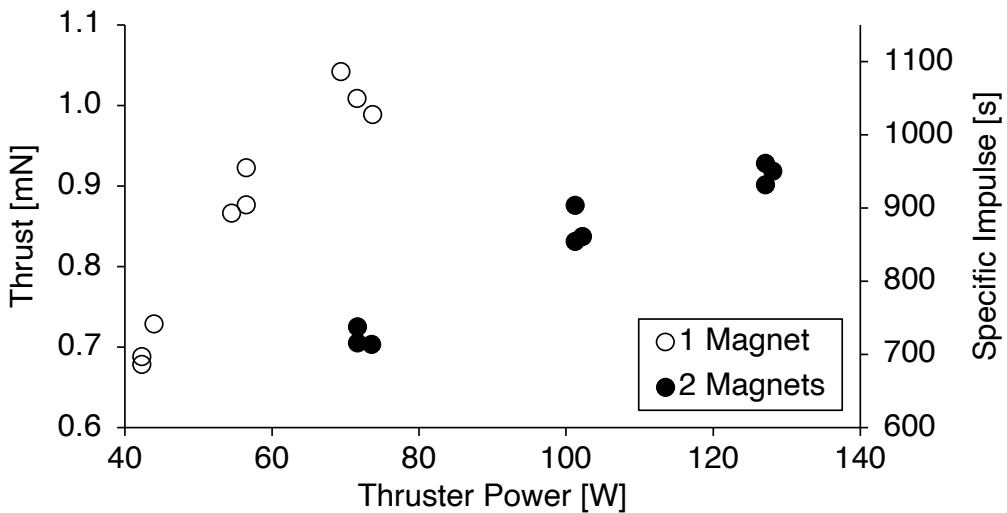


Figure 6.11: Thrust and specific impulse as a function of thruster power. Small ECR thruster, 0.10 mg/s xenon mass flow rate, 3 A coil current. Three readings taken for each test condition, standard errors from 0.007 mN to 0.015 mN.

The two magnet configuration reflects significantly less power than the single magnet configuration, resulting in higher thruster powers. This increased thruster power does not lead to a proportional increase in thruster performance, indicating a lower thruster efficiency. By plotting the thruster efficiency in figure 6.12, the two magnet configuration can be seen to have an efficiency below 4 %, while the efficiency of the single magnet configuration lies above 6 %.

Langmuir probe measurements of electron temperature, taken 49 mm downstream of the electromagnet, are shown in figure 6.13. This shows the two magnet configuration having significantly reduced electron temperatures for a given power level. This reduction in electron energy could be due to the decrease in resonance region thickness seen in figure 6.8. A thinner resonance region indicates that less energy is absorbed by electrons that pass through.

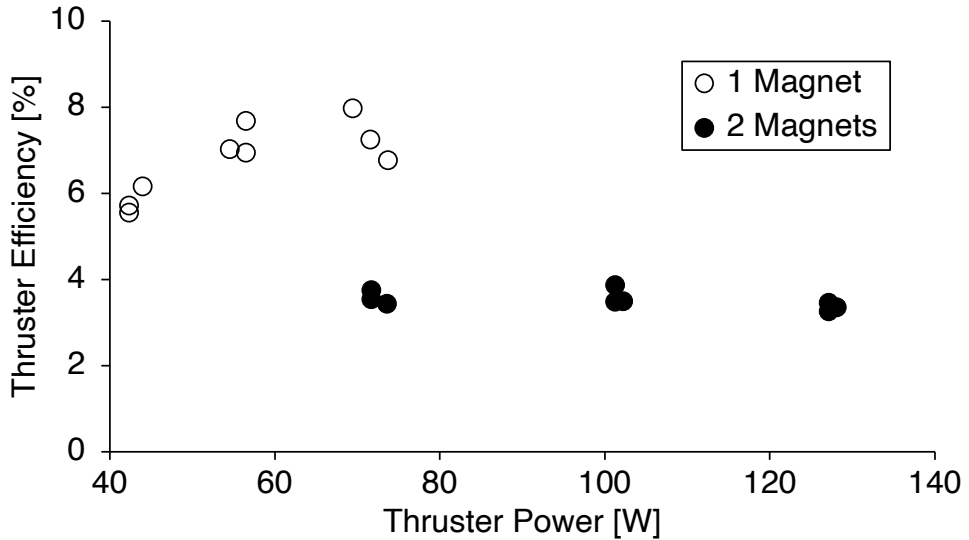


Figure 6.12: Thruster efficiency (not accounting for electromagnetic coil power) as a function of thruster power. Small ECR thruster, 0.10 mg/s xenon mass flow rate, 3 A coil current. Three readings taken for each test condition, standard errors from 0.06 % to 0.35 %.

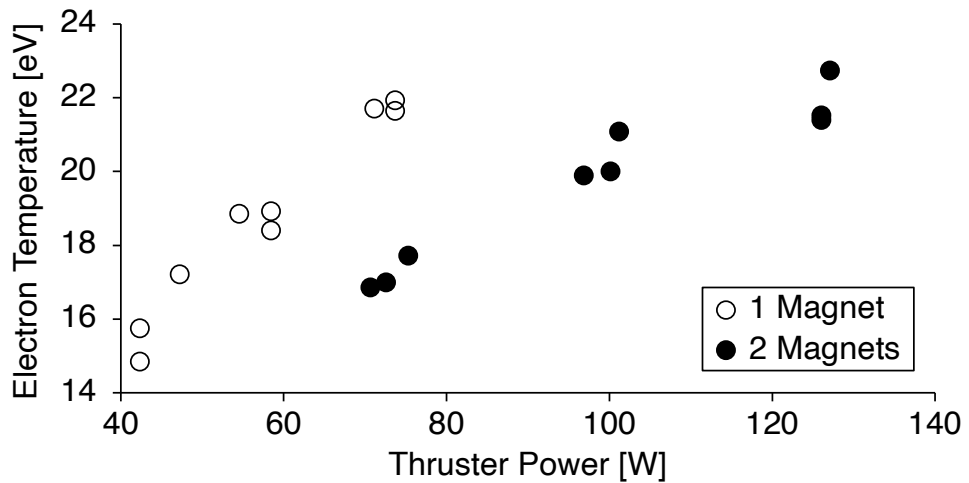


Figure 6.13: Electron temperature as a function of thruster power. Small ECR thruster, 0.10 mg/s xenon mass flow rate, 3 A coil current. Three readings taken for each test condition, standard errors from 0.15 eV to 0.69 eV.

These measurements verify the initial theory; the two magnet configuration increases power coupling, however electrons experience an energy decrease for a given thruster power due to the smaller downstream resonance region. The plasma formed within the chamber is also subject to higher wall losses with respect to the single magnet configuration, decreasing beam current and mass utilisation efficiency. Therefore the advantage of improved power coupling does not translate into higher thruster performance.

Mass Flow Rate Effects

By varying the mass flow rate between 0.10 mg/s, 0.12 mg/s and 0.14 mg/s of xenon, the relationship between performance and mass flow rate was determined, see figure 6.14. It should be noted that a constant generator power of 240 W was used, resulting in the single magnet configuration receiving a thruster power of 77 W, while the two magnet configuration received 120 W. Therefore these results should not be used to directly compare performance, but instead infer the relationship between performance and mass flow rate.

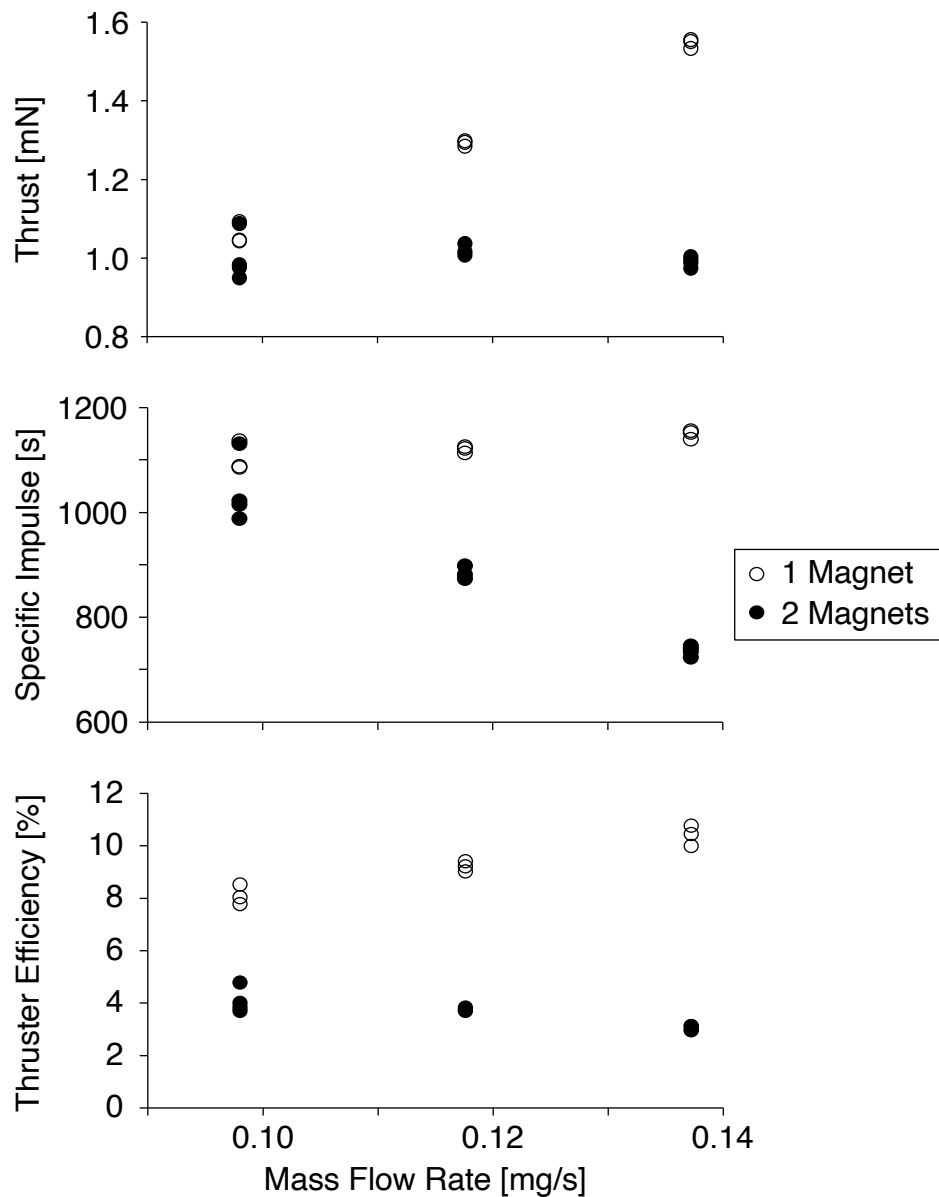


Figure 6.14: Thrust, specific impulse and thruster efficiency as a function of mass flow rate. 77 W thruster power for the 1 magnet configuration, 120 W thruster power for the 2 magnet configuration. Small ECR thruster, 3 A coil current. Three readings taken for each test condition, standard errors from 0.005 mN to 0.036 mN. Thruster efficiency does not account for electromagnetic coil power.

From figure 6.14 it can be seen that the performance of the single magnet configuration has a positive linear relationship with mass flow rate. The performance of the two magnet configuration however, is seen to have a negative linear relationship with mass flow rate. This indicates that a magnetic mirror trap might be able to provide an increase in performance for a small ECR thruster with an even lower mass flow rate.

Langmuir probe measurements of the electron temperature and density, taken 49 mm downstream of the electromagnet, are shown in figure 6.15. As higher mass flow rates create a higher neutral pressure within the thruster's chamber. This increases electron-neutral collisions, decreasing the net electron temperature. However, this negative relationship is far more pronounced for the two magnet configuration. As electron density is also seen to increase at these higher mass flow rates, the microwave electric field in the thruster could reduce in amplitude due to the heating of more electrons. This would then result in less energy delivered to each electron passing through the resonance region, see equation 2.9.

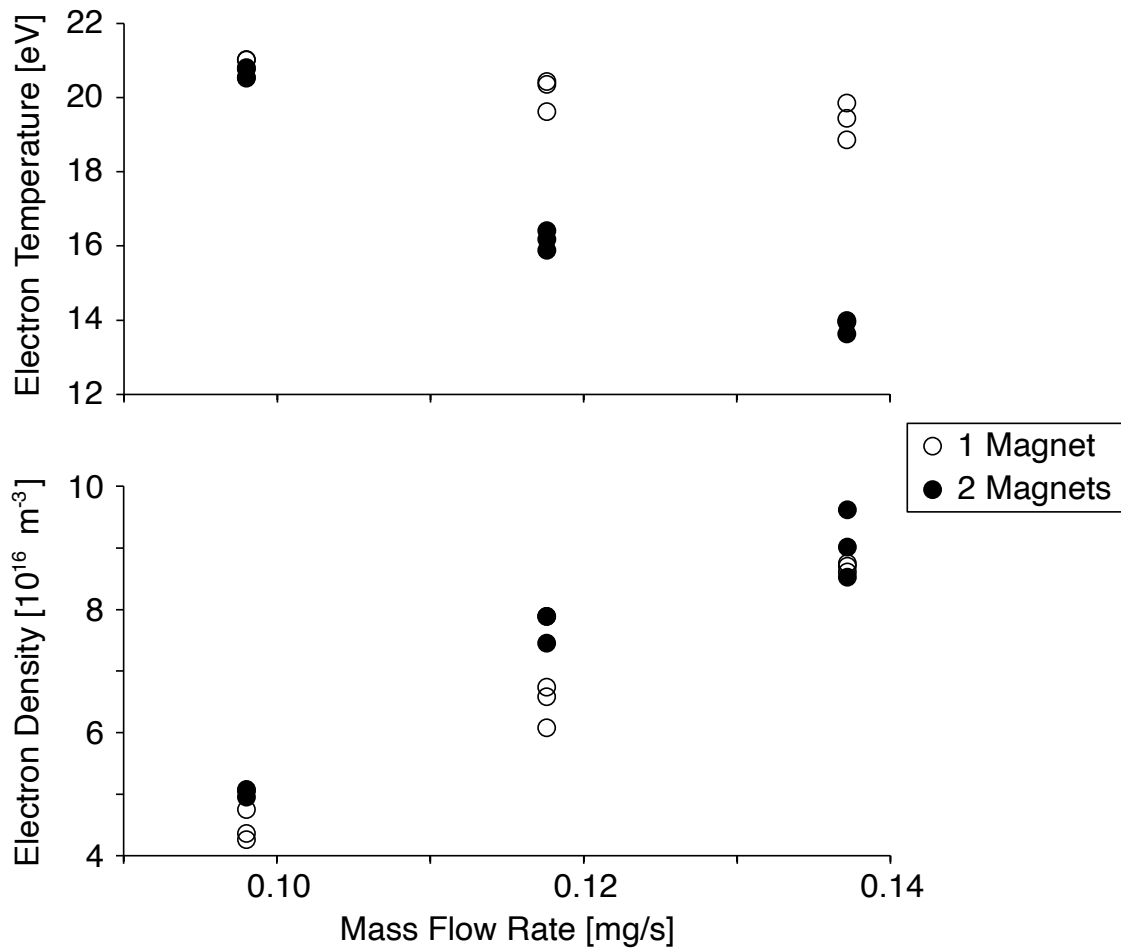


Figure 6.15: Electron temperature (top) and density (bottom) as a function of xenon mass flow rate. 77 W thruster power for the 1 magnet configuration, 120 W thruster power for the 2 magnet configuration. Small ECR thruster, 3 A coil current. Three readings taken for each test condition, standard errors from 0.12 eV to 0.36 eV and $3.7 \times 10^{14} \text{ m}^{-3}$ to $3.9 \times 10^{15} \text{ m}^{-3}$ respectively.

6.4 Conclusion

A second ring magnet was added to the throat of the small ECR thruster to generate a region of high magnetic field strength at the thruster's exit. This acted to reflect escaping electrons back into the thruster chamber where they could gain further energy from the upstream resonance region. The effects of adding this magnetic mirror trap were evaluated with the electromagnet downstream of the small ECR thruster.

Evaluation of Expected Effects:

1) Increased Electron Temperature ✗

Electron temperature measured downstream of the thruster was reduced by 21 % for the same thruster power. While adding the magnetic mirror should trap electrons, it also increased the magnetic field strength gradient at resonance of the downstream resonance region, decreasing the energy absorbed by electrons passing through. This is likely what caused a net decrease to electron energy in the plume for a given thruster power.

2) Decreased Mass Utilisation Efficiency ✓

Ion beam current was reduced by 14 % for the same thruster power, indicating a reduction to the mass utilisation efficiency. This is likely due to an increase in the fraction of magnetic field lines that intercept the thruster walls, causing higher plasma losses to the wall.

3) Lower Propellant Mass Flow Rate Required for Ignition ✓

Installing the second ring magnet reduced the xenon mass flow rate required to ignite the thruster from 0.7 mg/s to 0.1 mg/s. This is likely because the electrons had an increased retention time within the thruster's chamber, increasing the rate of ionisation.

Adding the magnetic mirror trap decreased thrust by 29 % and reduced the thruster efficiency from 7.3 % to 3.6 % for the same mass flow rate and thruster power. However, measurements of thrust and electron temperature show that the performance increases for lower mass flow rates. Therefore it is possible that a magnetic mirror trap could be useful for a miniaturised, low mass flow rate ECR thruster. A lack of performance for the current thruster however, has meant that a magnetic mirror trap will not be implemented in the following tests.

7 EFFECTS OF RESONANCE REGION LOCATION

Previous research on a small ECR thruster by F. Cannat[16] has shown that the thruster performance is increased when the resonance region is positioned near the back of the chamber. A large ECR thruster has been designed such that the thrust chamber's displacement from the ring magnet can be varied using a motorised translational stage. This enables the position of the resonance region to be swept from the back of the chamber to the front of the chamber, see figure 7.1. Thruster performance is observed to increase when the resonance region is positioned further away from the backplate, suggesting that scaling up an ECR thruster results in a change to the position of the resonance region that produces the highest thruster performance. Direct thrust measurements are taken to find the position at which the thruster performance is the greatest. A Faraday probe is used to measure variations in plume divergence and beam current. Langmuir probe measurements are used to identify trends in electron temperature and plasma potential. An RPA is also used to determine ion energies at different resonance region locations.

This section on varying the location of the resonance region is split into four parts:

7.1	Displacement Mechanism	127
7.2	Thruster Performance vs Location	129
7.3	Plume Measurements vs Location	131
7.4	Conclusion	135

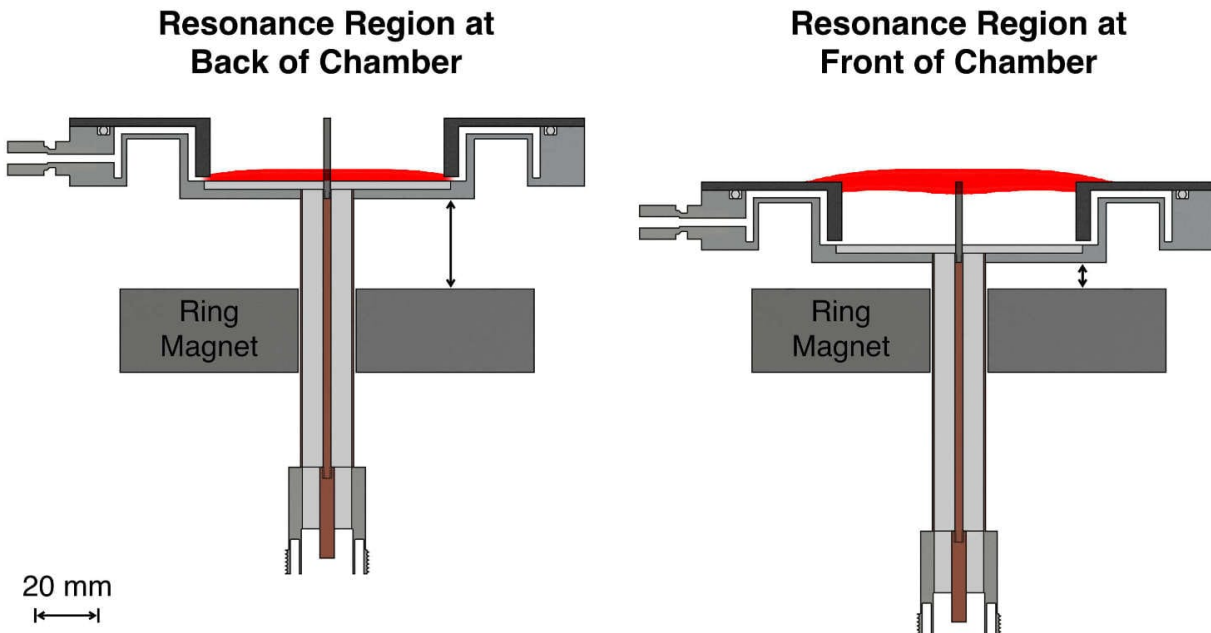


Figure 7.1: By varying the position of the thruster's chamber relative to the ring magnet, the position of the resonance region within the chamber can be varied. Resonance region shown in red (modelled using FEMM[93]).

7.1 Displacement Mechanism

This section describes the mechanism that is used to sweep the resonance region from the back to the front of the large ECR thruster's chamber. The geometrical design of the large ECR thruster is detailed in section 4.1.

The large ECR thruster was designed so that its ring magnet is mechanically separated from the thruster. The ring magnet is mounted directly to the thrust balance, while the thruster is mounted to a linear rail, allowing it to translate forwards and backwards, see figure 7.2.

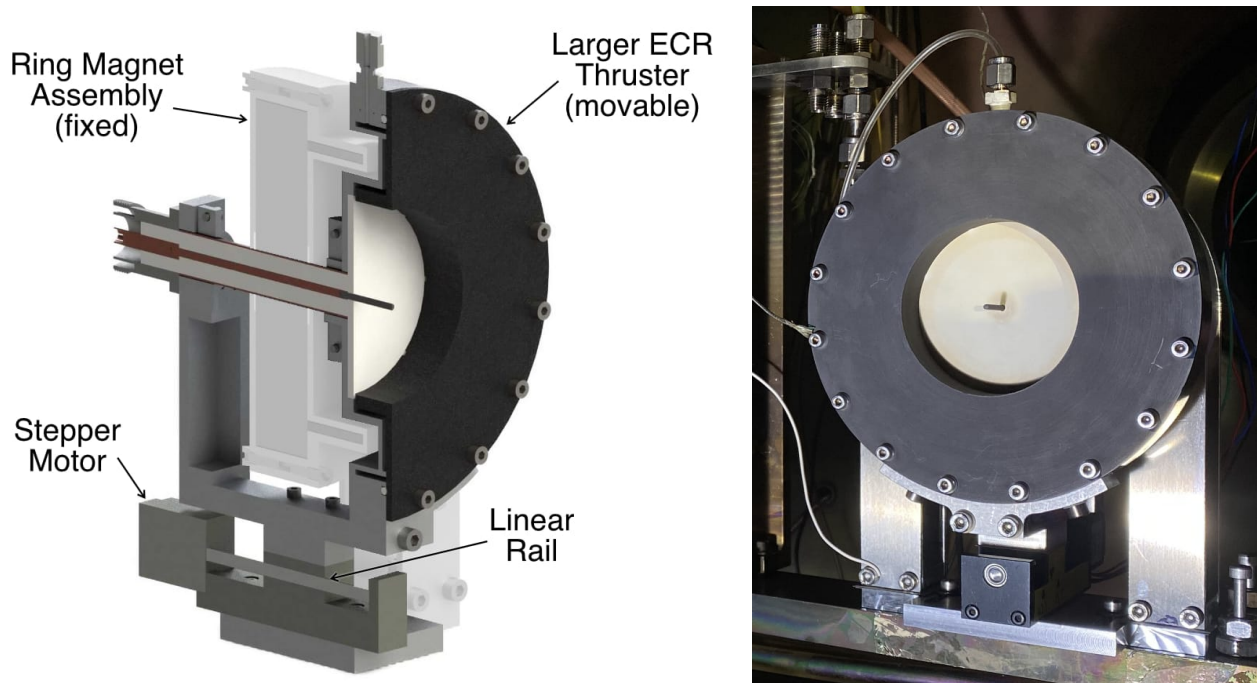


Figure 7.2: Cross-sectional view of the large ECR thruster on top of a motorised linear rail (left), fixed ring magnet assembly shown in faded white. Photo of the large ECR thruster installed on the thrust balance (right).

Using a stepper motor, the thruster was able to be displaced axially from the ring magnet. As the resonance region remains at a fixed distance from the ring magnet, this results in the resonance region getting displaced relative to the back of the thruster's chamber. The resonance region was able to be swept from the back of the thrust chamber (0 mm displacement) to the front of the thrust chamber (20 mm displacement), see figure 7.3.

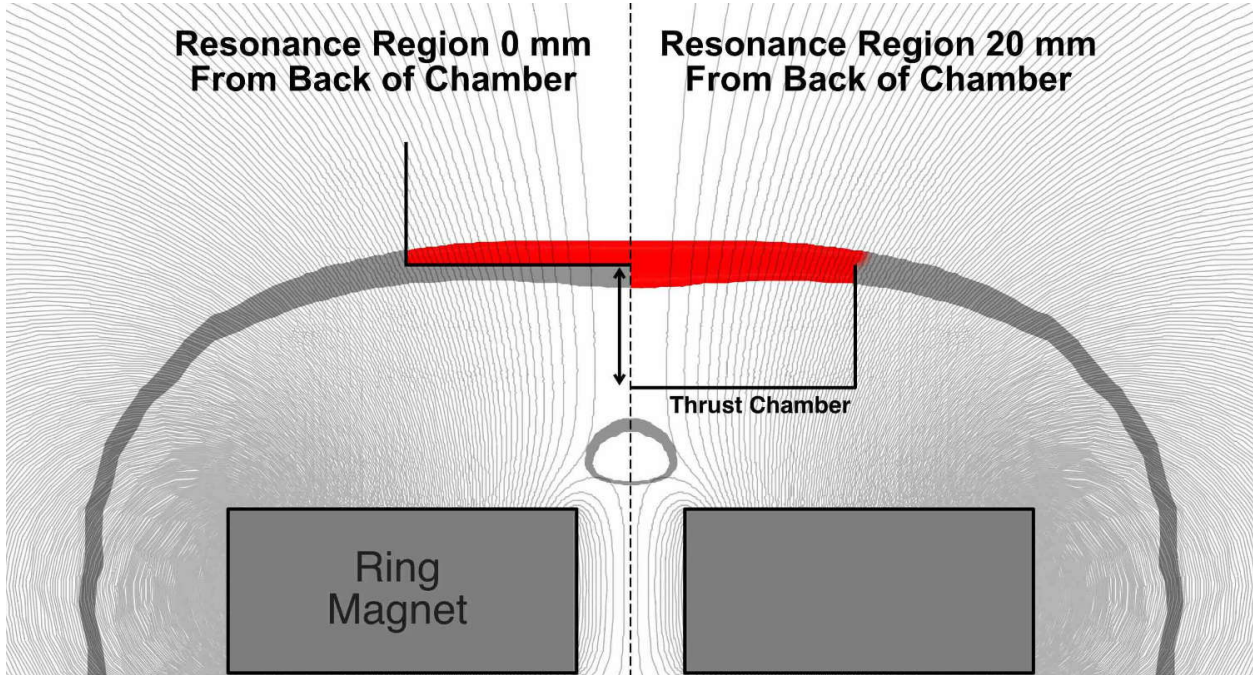


Figure 7.3: Magnetic field plot of the large ECR thruster, showing how the back of the thrust chamber is displaced from the resonance region. Resonance region shown in red when residing within the thrust chamber, and grey when residing outside of the thrust chamber. Modelled using FEMM[93].

Previous work by F. Cannat et al.[57] has shown that the ion current density is maximised when the resonance region is closer to the back of the thrust chamber, nearer the propellant injectors. However, that study was conducted on a thruster with a chamber 13 mm in diameter and 15 mm in length. This is significantly smaller than the 74 mm diameter, 20 mm long chamber of the large ECR thruster, which is likely the reason behind the seemingly contradictory results.

7.2 Thruster Performance vs Location

The large ECR thruster has a significantly lower VSWR than the small ECR thruster. This results in a significantly reduced reverse power, allowing for greater thruster powers and a lower thermal load across the microwave line. It was also noticed that for a fixed forward power at the generator of 240 W, reverse power measured at the generator appears to have a parabolic relationship with displacement, with the lowest reverse powers occurring when the resonance region is in the centre of the chamber at 10 mm displacement, see figure 7.4. A constant xenon mass flow rate of 0.39 mg/s was used during these tests. No measurements were able to be taken at 0 mm displacement, as the plasma was unable to be sustained.

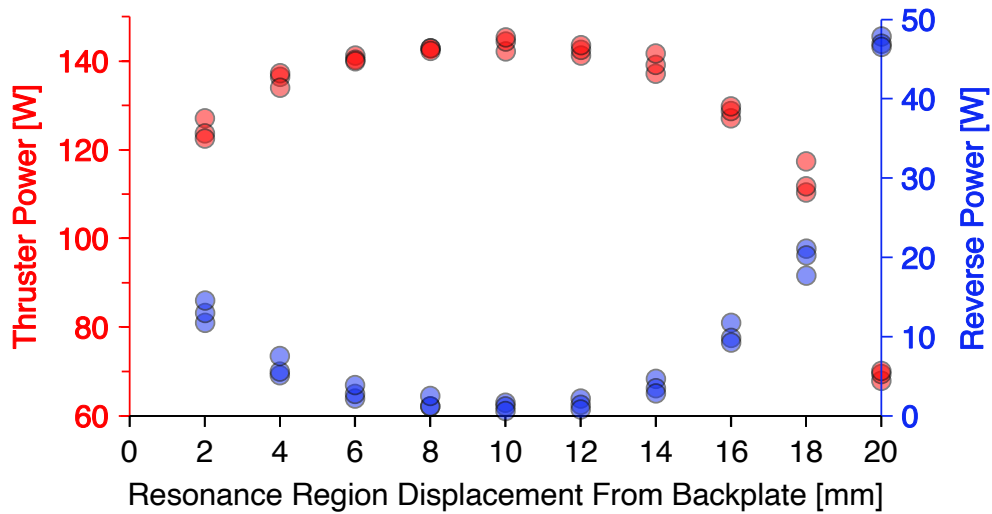


Figure 7.4: Thruster power and reverse microwave power measured at the generator as a function of the displacement of the resonance region from the backplate. Large ECR thruster, 240 W forward microwave power at the generator, 0.39 mg/s xenon mass flow rate. Three readings taken for each test condition, standard errors from 0.23 W to 1.61 W and 0.30 W to 1.00 W respectively.

The thrust is plotted against the resonance region's displacement from the backplate for a fixed forward power of 240 W, see figure 7.5. A decrease in thrust is seen at displacements below 8 mm, indicating that the thruster performs worse when the resonance region is near the backplate and/or injectors. It also appears that thruster performance plateaus for displacements of 8 mm and above. However, it can be seen from figure 7.4 that the net thruster power is significantly decreased at high displacements. Therefore, to get a better understanding of this change to thruster performance, the thruster efficiency is plotted in figure 7.5.

It can be seen from figure 7.5 that the thruster efficiency is significantly increased at 20 mm displacement due to it maintaining thrust at a significantly decreased thruster power. This increase in thruster performance with displacement of the resonance region from the

backplate contradicts the findings of F. Cannat et al.[57]. However, as the thruster they used was significantly smaller, this suggests that the displacement of the resonance region from the backplate that produces the highest thruster performance could change as the thruster is scaled. Note that there were also other differences to the thruster used by F. Cannat et al.[57], namely the use of an electromagnet instead of a permanent magnet, the use of aluminium for the thruster walls instead of graphite and the use of stainless steel for the antenna instead of graphite.

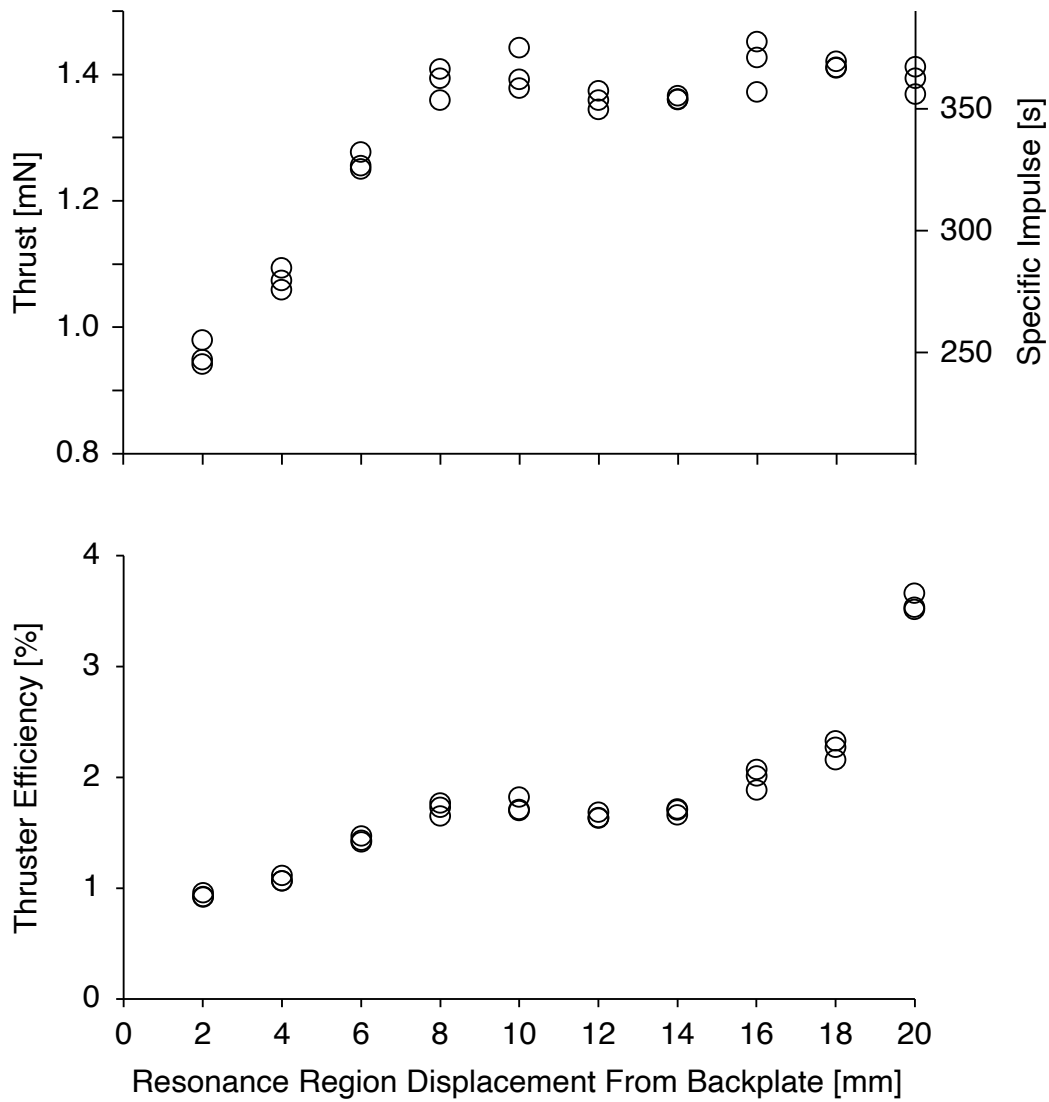


Figure 7.5: Thrust, specific impulse and thruster efficiency as a function of the displacement of the resonance region from the backplate. Thruster powers can be found from figure 7.4. Large ECR thruster, 0.39 mg/s xenon mass flow rate. Three readings taken for each test condition, standard errors from 0.002 mN to 0.029 mN.

7.3 Plume Measurements vs Location

Ion Beam Measurements

A Faraday probe was used to map out the ion beam profile of the thruster at varying displacements of the resonance region from the backplate, see figure 7.6.

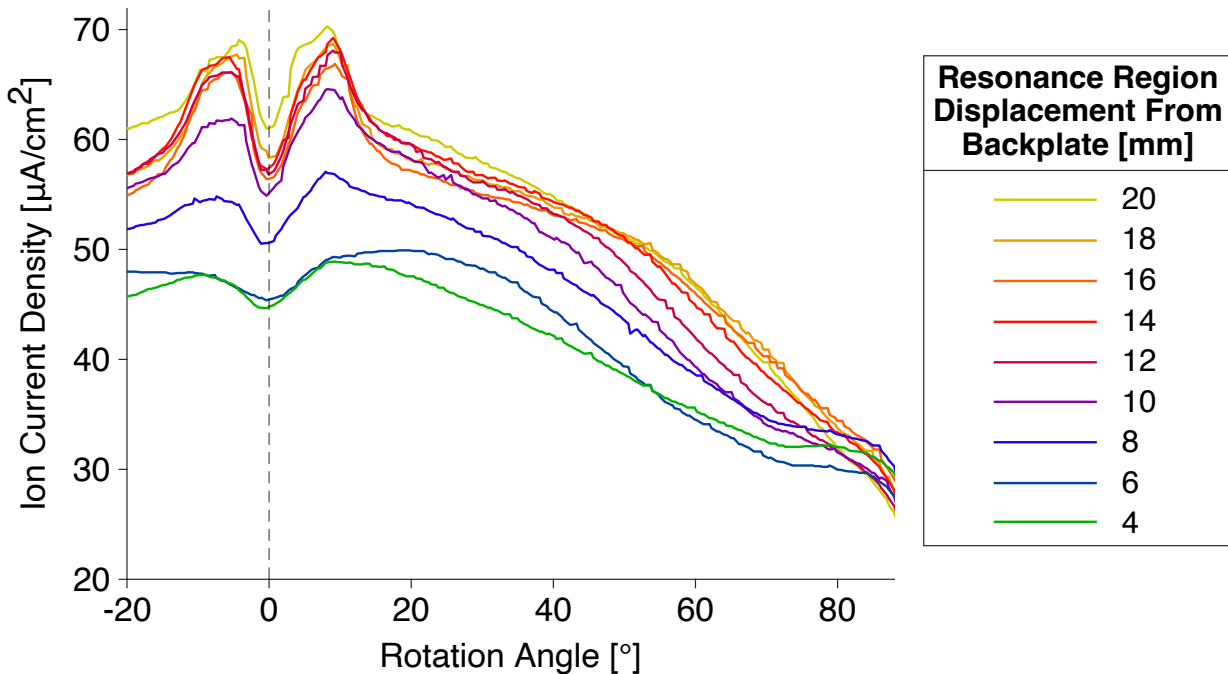


Figure 7.6: Ion current density as a function of rotation angle of the probe at nine different resonance region displacements. Probe swept three times for each displacement, mean value at each angle is used. Thruster powers can be found from figure 7.4. Large ECR thruster, 0.39 mg/s xenon mass flow rate.

From figure 7.6 it can be seen that the ion current density mostly increases with the displacement of the resonance region from the backplate. Calculations of the far field beam divergence angle show that the beam divergence remains at $55^\circ \pm 1^\circ$ for all resonance region displacements. Numerically integrating the ion current density curves allows for the calculation of the ion beam current, see figure 7.7. Noticeably, the ion beam current appears to be lower for resonance region displacements below 14 mm, with a larger drop in ion beam current for resonance region displacements below 8 mm, which aligns with the drop in thrust seen in figure 7.5.

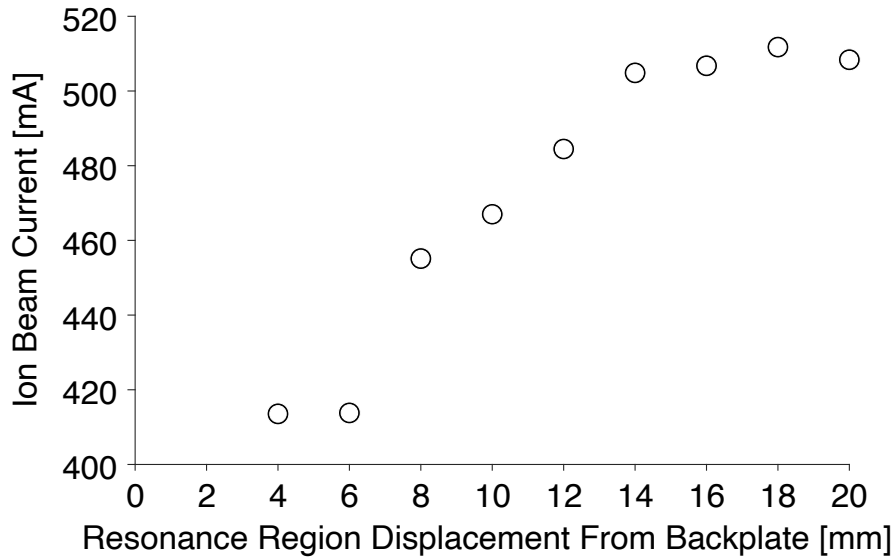


Figure 7.7: Ion beam current as a function of displacement of the resonance region from the backplate. Thruster powers can be found from figure 7.4. Large ECR thruster, 0.39 mg/s xenon mass flow rate.

Electron Measurements

Langmuir probe measurements of the electron temperature and plasma potential, taken 100 mm downstream of the thruster, are shown in figures 7.8 and 7.9.

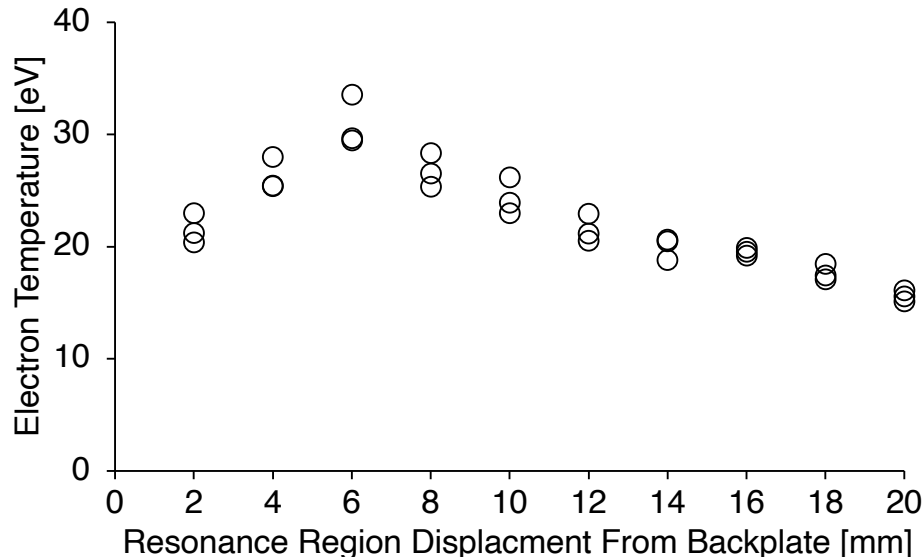


Figure 7.8: Electron temperature as a function of displacement of the resonance region from the backplate. Thruster powers can be found from figure 7.4. Large ECR thruster, 0.39 mg/s xenon mass flow rate. Three readings taken for each displacement, standard errors from 0.2 eV to 1.6 eV.

The electron temperature can be seen to increase as the resonance region is moved away from the backplate, with it peaking at a displacement of 6 mm before steadily decreasing. As the electrons are responsible for generating the ambipolar electric field, the trend in electron temperature can also be seen in the measurements of the thruster floating potential and plasma potential in figure 7.9.

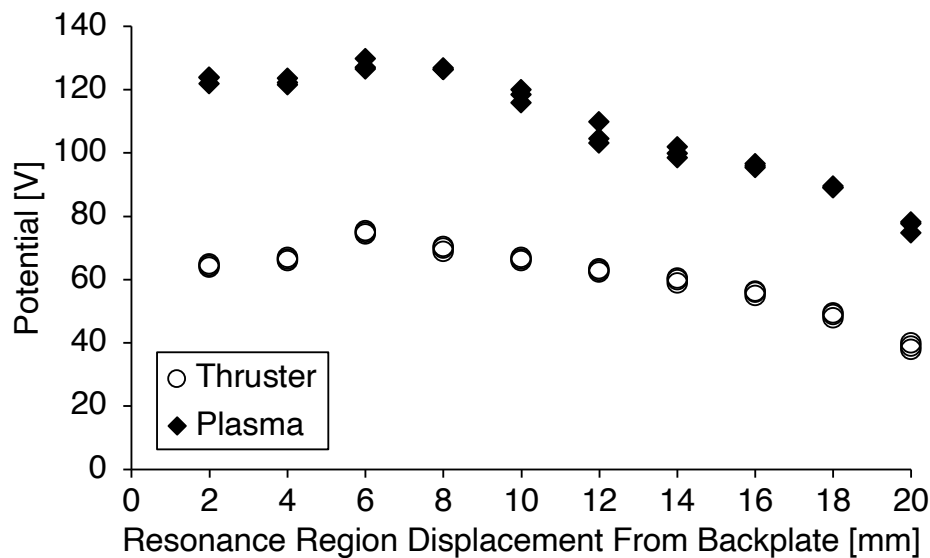


Figure 7.9: Thruster floating potential and plasma potential as a function of displacement of the resonance region from the backplate. Thruster powers can be found from figure 7.4. Large ECR thruster, 0.39 mg/s xenon mass flow rate. Three readings taken for each displacement, standard errors from 0.4 V to 0.6 V and 0.2 V to 1.5 V respectively.

RPA Measurements

The normalised ion energy distributions at different resonance region displacements from the backplate are plotted in figure 7.10. Here it can be seen that the higher energy ion peak moves to higher grid bias voltages as the resonance region is brought closer to the backplate. Displacements below 6 mm do not seem to follow this trend, likely because of an interaction of the resonance region with the backplate. By calculating the ion energy of the higher energy peaks in figure 7.10, the most probable energy of the ions in the ion beam can be plotted, see figure 7.11. This can be seen to follow the same trend as the electron temperature, thruster potential and plasma potential, with ion energy peaking at 6 mm displacement before steadily decreasing.

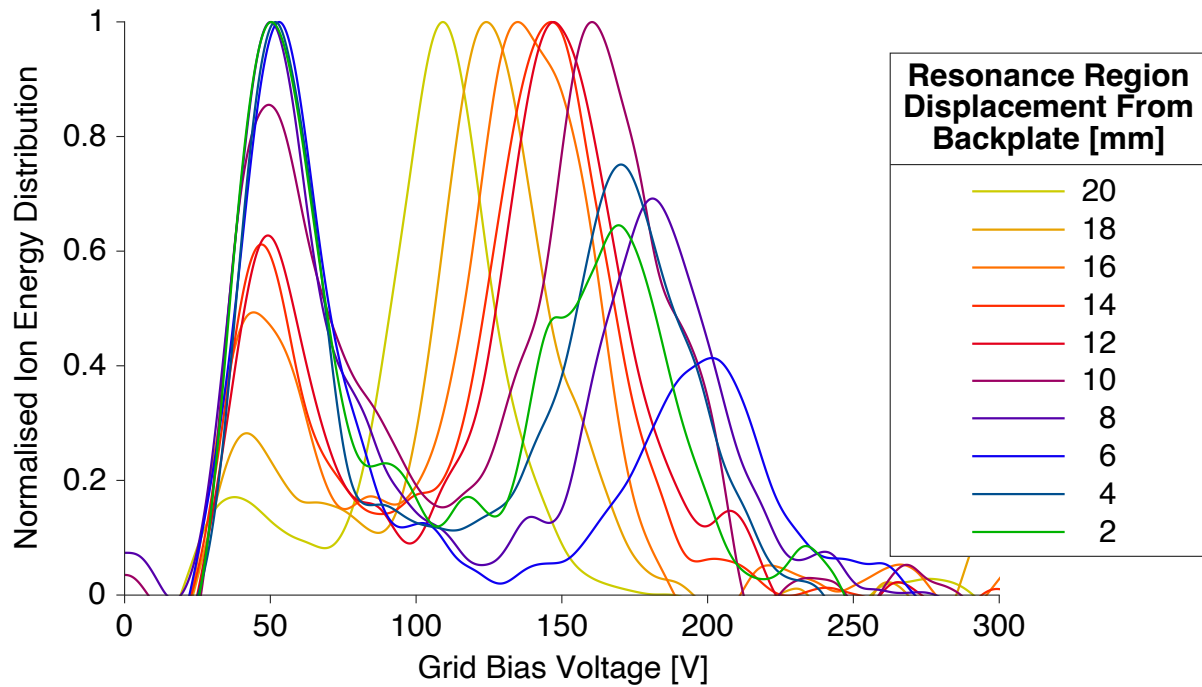


Figure 7.10: Normalised ion energy distribution at different resonance region displacements from the backplate. Thruster powers can be found from figure 7.4. Large ECR thruster, 0.39 mg/s xenon mass flow rate.

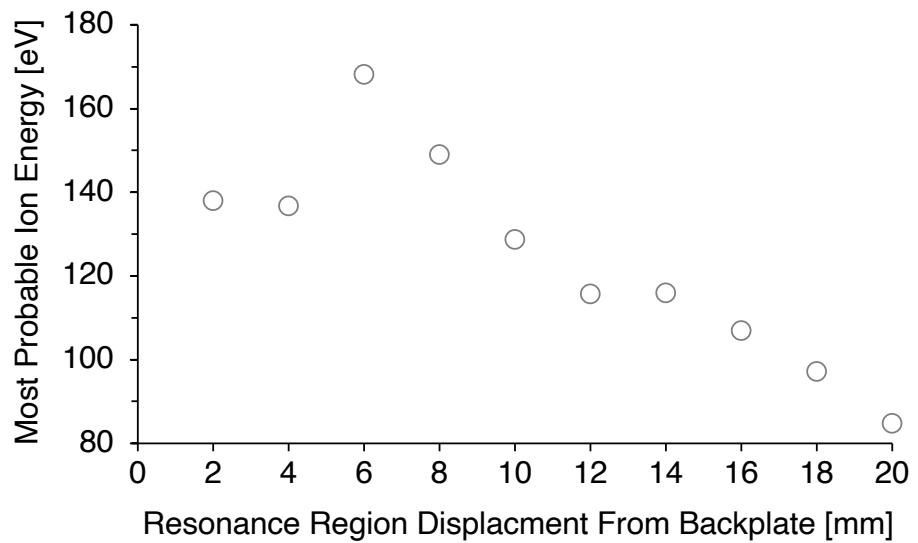


Figure 7.11: Most probable ion energy as a function of the displacement of the resonance region from the backplate. Most probable ion energy is approximated using the technique outlined in section 3.6. Thruster powers can be found from figure 7.4. Large ECR thruster, 0.39 mg/s xenon mass flow rate.

7.4 Conclusion

The plots produced from this study appear to comprise three distinct sections. These sections can be defined as the resonance region being near the backplate, in the middle of the chamber, or far from the backplate, see table 7.1.

Table 7.1: Mean measurements for the near, middle and far resonance region locations.

	Near	Middle	Far
Resonance Region Displacement From Backplate	≤ 6 mm	8 mm - 12 mm	≥ 14 mm
Thrust [mN]	1.1	1.4	1.4
Thruster Efficiency [%]	1.2	1.7	2.4
Ion Beam Current [mA]	414	469	508
Electron Temperature [eV]	26	24	18
Plasma Potential [V]	125	117	91
Most Probable Ion Energy [eV]	148	131	101

From table 7.1 it can be seen that when the resonance region is near the backplate, thruster performance is reduced. This appears to be due in part to a decrease in ion beam current. This decrease in the number of ions in the beam could be due to the resonance region residing nearer the propellant injectors. As the propellant is not as dispersed when it reaches the resonance region, areas of high and low neutral propellant density occur, which could result in the reflection of the microwaves. As the electric field is strongest near the antenna, these high neutral density areas close to the injectors also experience a weaker electric field, leading to less ionisation. Lastly, generating the plasma further back in the chamber results in more plasma losses to the wall, as more magnetic field lines can be seen to intercept the wall in figure 7.3. All these mechanisms could contribute to the decrease in ion beam current, and further work is required to characterise their individual effects.

Conversely, with the resonance region near the backplate, higher electron temperatures are produced in the plume. This results in an elevated plasma potential which in turn increases the most probable energy of the ions in the plume. All three of these variables are seen to peak when the resonance region is located 6 mm from the thruster's backplate.

Despite the higher thruster performance at the far resonance region location, all the following tests were conducted with a resonance region displacement from the backplate of 10 mm. This displacement was chosen as it resulted in the greatest thruster power and a high level of thrust. It also makes the results in this thesis more comparable to other ECR thruster studies, that have a resonance region residing near the backplate.

8 DECREASING MAGNETIC FIELD GRADIENT AT RESONANCE VIA PASSIVE COMPONENTS

As shown in chapter 5, reducing the magnetic field strength gradient at resonance can significantly increase thruster performance. Adding a ferromagnetic ring to the large ECR thruster allows for this effect to be replicated passively, without power loss to electromagnet, see figure 8.1. Experimental measurements indicate that this results in an increase to the strength of the ambipolar electric field and a decrease to the ion beam divergence. An increase in thrust and specific impulse of 15 % is observed, while the thruster efficiency increases by 32 %. This study presents strong evidence that decreasing magnetic field strength gradient at the resonance region can significantly enhance thruster performance.

This section on ferromagnetically decreasing the magnetic field strength gradient at resonance is split into eight parts:

8.1	Magnetic Model	137
8.2	Resonance Region Location Effects	142
8.3	Mass Flow Rate Effects	149
8.4	Thruster Power Effects	154
8.5	Background Pressure Effects	158
8.6	Alternative Propellants (Krypton & Argon)	166
8.7	Plasma Plume Map	171
8.8	Conclusion	174

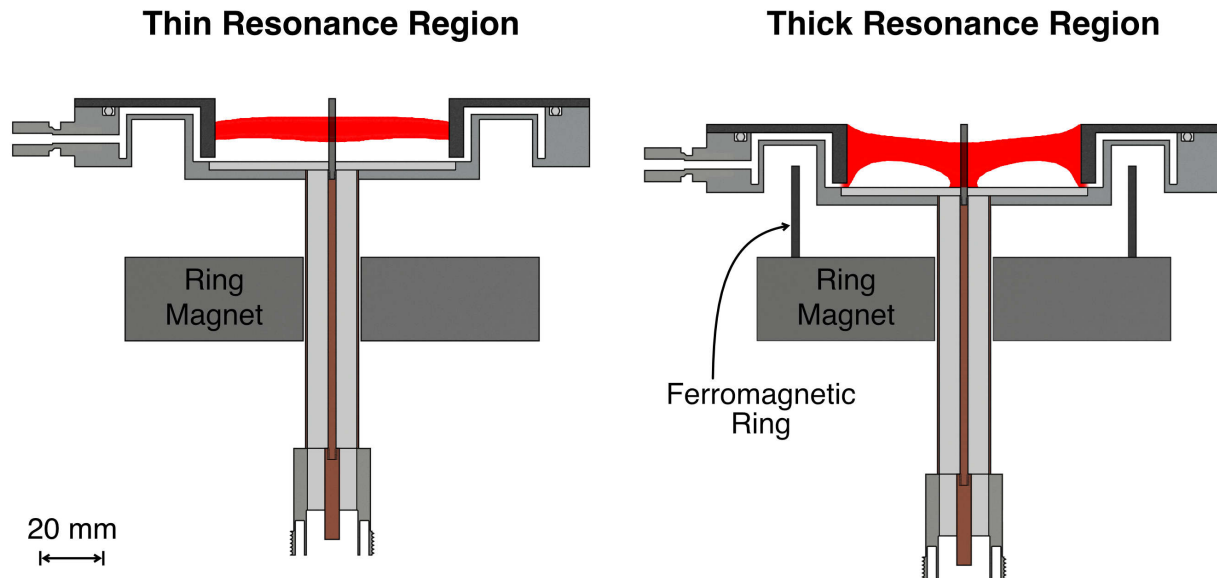


Figure 8.1: By adding a ferromagnetic ring, the magnetic field strength gradient at resonance can be decreased, increasing the thickness of the resonance region and the energy absorbed by electrons passing through. Large ECR thruster, resonance region shown in red (modelled using FEMM[93]).

8.1 Magnetic Model

This section describes the magnetic field of the large ECR thruster and how it changes when a ferromagnetic ring is added into the magnetic circuit. The geometrical design of the large ECR thruster is detailed in section 4.1, while the displacement mechanism that allows for the chamber to be positioned is detailed in section 7.1.

A disadvantage of the small ECR thruster is its power loss to the electromagnet, reducing the thruster efficiency. In this section, passively decreasing the magnetic field strength gradient at resonance is explored, via the use of ferromagnetic material. The addition of an iron ring immediately downstream of the permanent ring magnet decreases the magnetic field strength gradient at resonance, see figure 8.2. This results in a thicker resonance region and more power being absorbed by electrons that pass through, see figure 8.1.

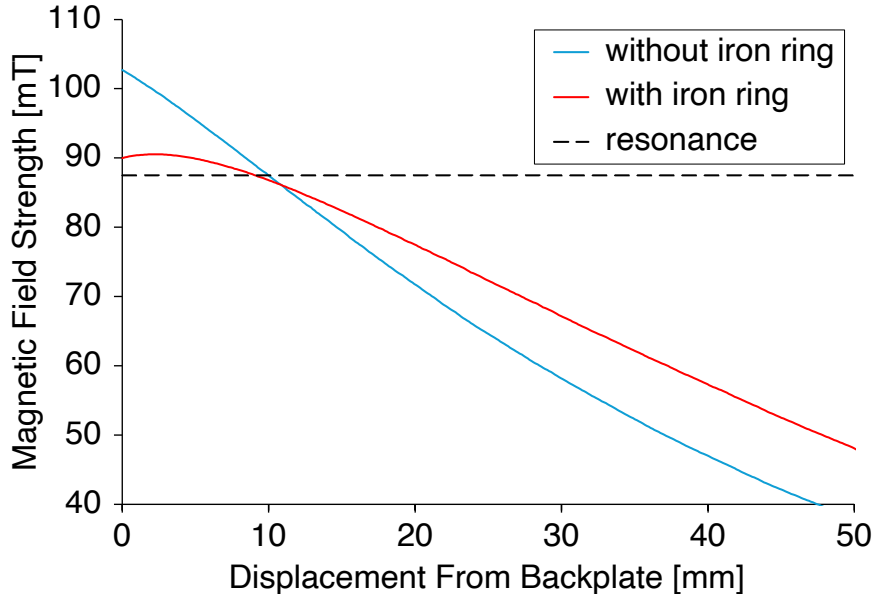


Figure 8.2: Magnetic field strength plot for the large ECR thruster without iron ring (thin resonance region) and with iron ring (thick resonance region). Solid lines show the change in magnetic field strength with respect to displacement from the backplate along the central axis. Dashed line shows the magnetic field strength at which resonance occurs, 87.5 mT. Data obtained from the same model shown in figure 8.3. Modelled using FEMM[93].

Using equations 2.7 and 2.13 the resonance region thickness, Δx_{ecr} , and resonance region thickness due to Doppler broadening, Δx_D , can be calculated, see table 8.1. The upper and lower bounds of the Doppler broadened resonance region can then be calculated using equations 5.2 and 5.3. The Doppler broadened resonance region defined by these bounds is shown in figure 8.3. The dimensions of the magnetic circuit and thrust chamber for the large ECR thruster with the iron ring are shown in figure 8.4.

Table 8.1: Values that define the resonance region along the central axis of the large ECR thruster without the iron ring (thin resonance region) and with the iron ring (thick resonance region).

	without iron ring	with iron ring
$ \frac{\partial B}{\partial x} $ [T/m]	1.68	0.73
Δx_{ecr} [mm]	4.8	7.3
Δx_D [mm]	0.6	1.5
B_{0U} [mT]	92.0	90.7
B_{0L} [mT]	83.0	84.3

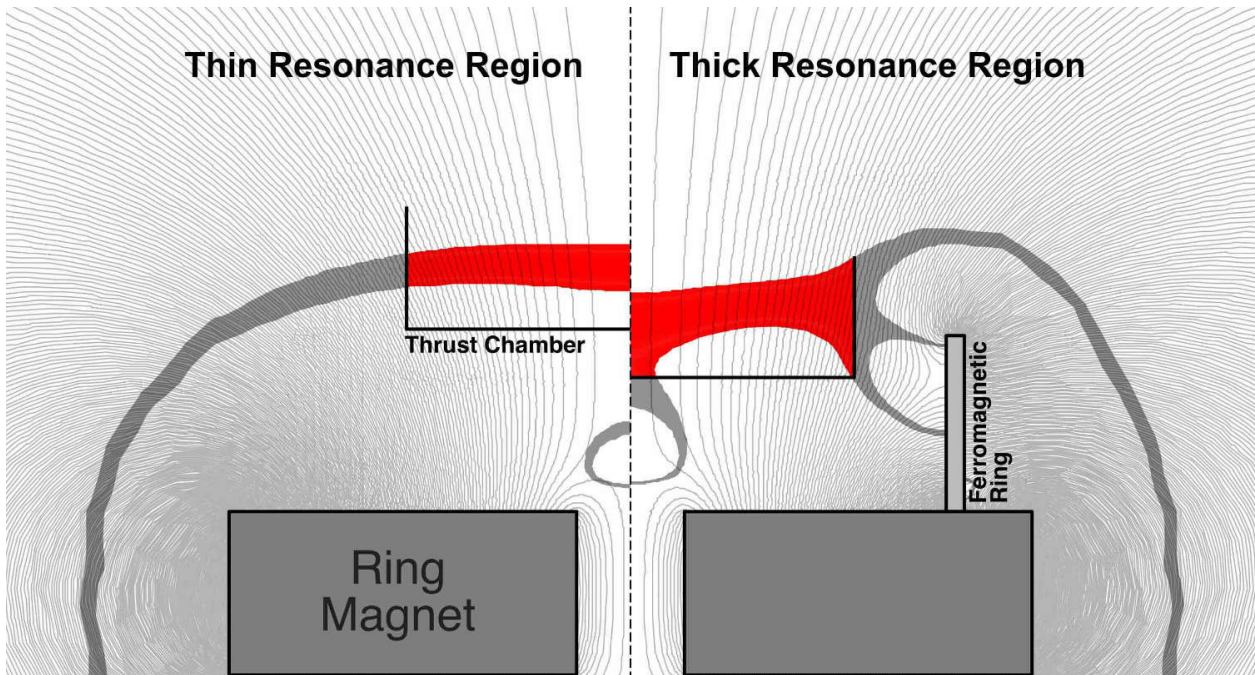


Figure 8.3: Axisymmetric magnetic field model of the large ECR thruster without the iron ring (thin resonance region) and the thruster with the ion ring (thick resonance region). The portion of the resonance region that resides inside the thrust chamber is shown in red. Resonance region that resides outside the thrust chamber shown in grey. Modelled using FEMM[93].

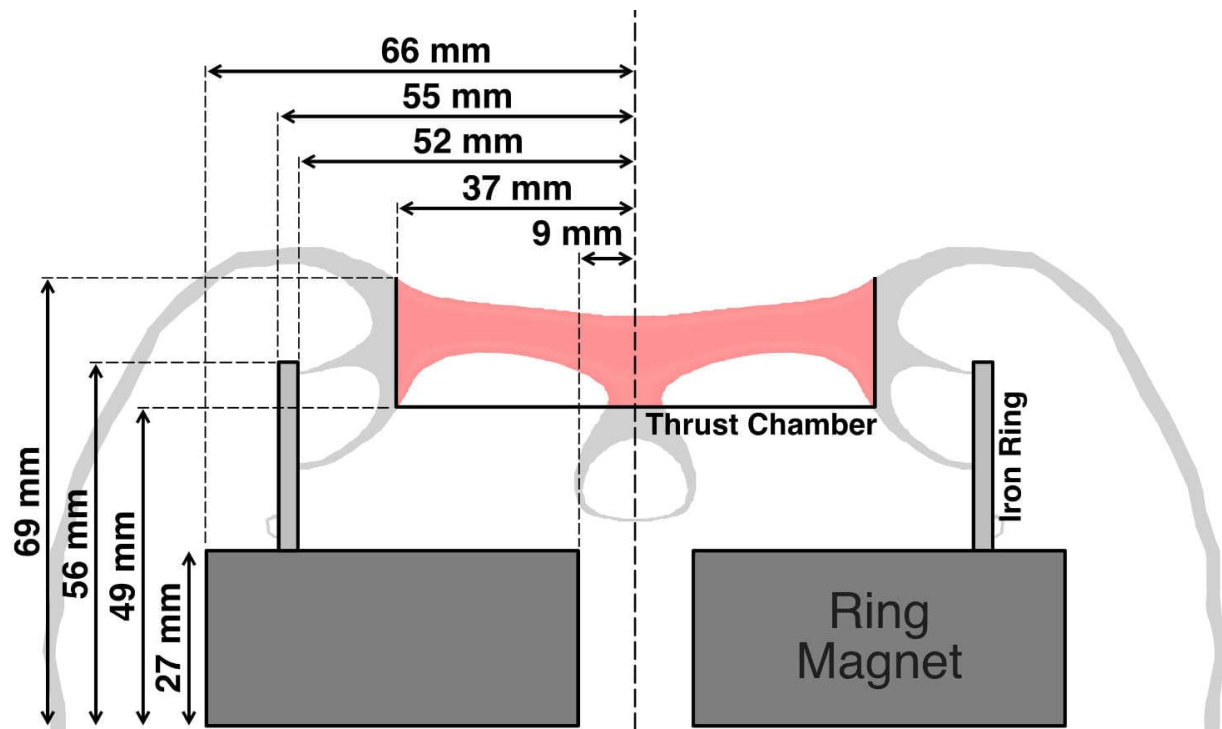


Figure 8.4: Key dimensions of the axisymmetric magnetic circuitry and thrust chamber for the large ECR thruster with the iron ring. The portion of the resonance region that resides inside the thrust chamber is shown in red. Resonance region that resides outside the thrust chamber shown in grey. Modelled using FEMM[93].

Magnetic Field Divergence

The beam divergence efficiency of ECR magnetic nozzle thrusters, as defined by equation 1.12, has been found to be highly dependent on the divergence of their magnetic field[36]. The red lines in figure 8.6 show how adding the iron ring leads to an unintended reduction in the magnetic field divergence. Figure 8.5.a shows the effect that adding the iron ring has on magnetic field divergence at a distance of 80 mm. However, this effect decreases with distance, and is negligible at a distance of 300 mm, see figure 8.5.b.

Electrons are accelerated out of the thruster and follow magnetic field lines until they detach at a certain distance downstream. The ions are observed to follow the path of these electrons along magnetic field lines. Once the electrons and ions detach, the ions are seen to continue along a rectilinear trajectory, uninfluenced by the magnetic field[106]. This means that an ECR thruster's divergence efficiency is solely dependent on the divergence angle of the magnetic field at the point at which the ions detach. Therefore, if the ions detach at a distance greater than 300 mm downstream, the divergence efficiency should be unaffected by the change in magnetic field divergence produced by adding the iron ring. The exception to this lies within the thruster chamber, where a reduction in magnetic field divergence leads to a reduction in plasma wall losses that could affect the divergence efficiency.

A study on ion detachment using a directional Faraday cup by R. Pioch[106] found that at a radius of 300 mm from the ring magnet, ions closer than $\sim 20^\circ$ from the central axis are still attached, while ions at greater angles have already detached at some point upstream. Notably, the thruster used in this study has a divergence efficiency of up to 80 %[36], meaning the results may not be comparable. It does however show that a significant portion of the ion plume is still attached to magnetic field lines 300 mm downstream of the ring magnet.

In conclusion, given that a significant portion of the ion plume is still attached to magnetic field lines 300 mm downstream of the ring magnet, and the magnetic field divergence is unchanged by the iron ring at this distance, the change in magnetic field divergence due to the addition of the iron ring should have a negligible effect on the divergence efficiency. The increase to the thruster performance that is observed when the iron ring is added can then be mostly attributed to the reduction in magnetic field strength gradient at the resonance region and the resulting increase in power delivered to the electrons.

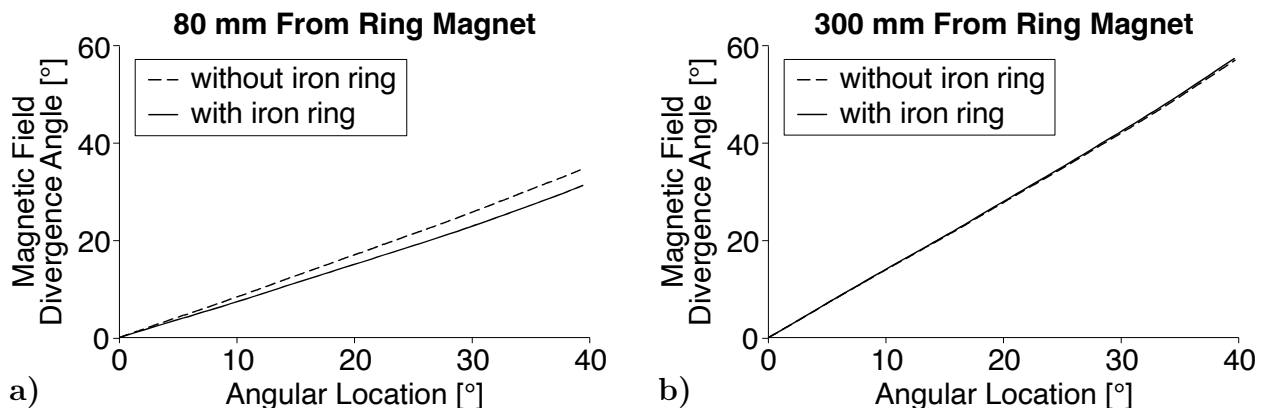


Figure 8.5: Magnetic field divergence angle as a function of angular location, at a radius of: a) 80 mm from the ring magnet; b) 300 mm from the ring magnet. Modelled using FEMM[93].

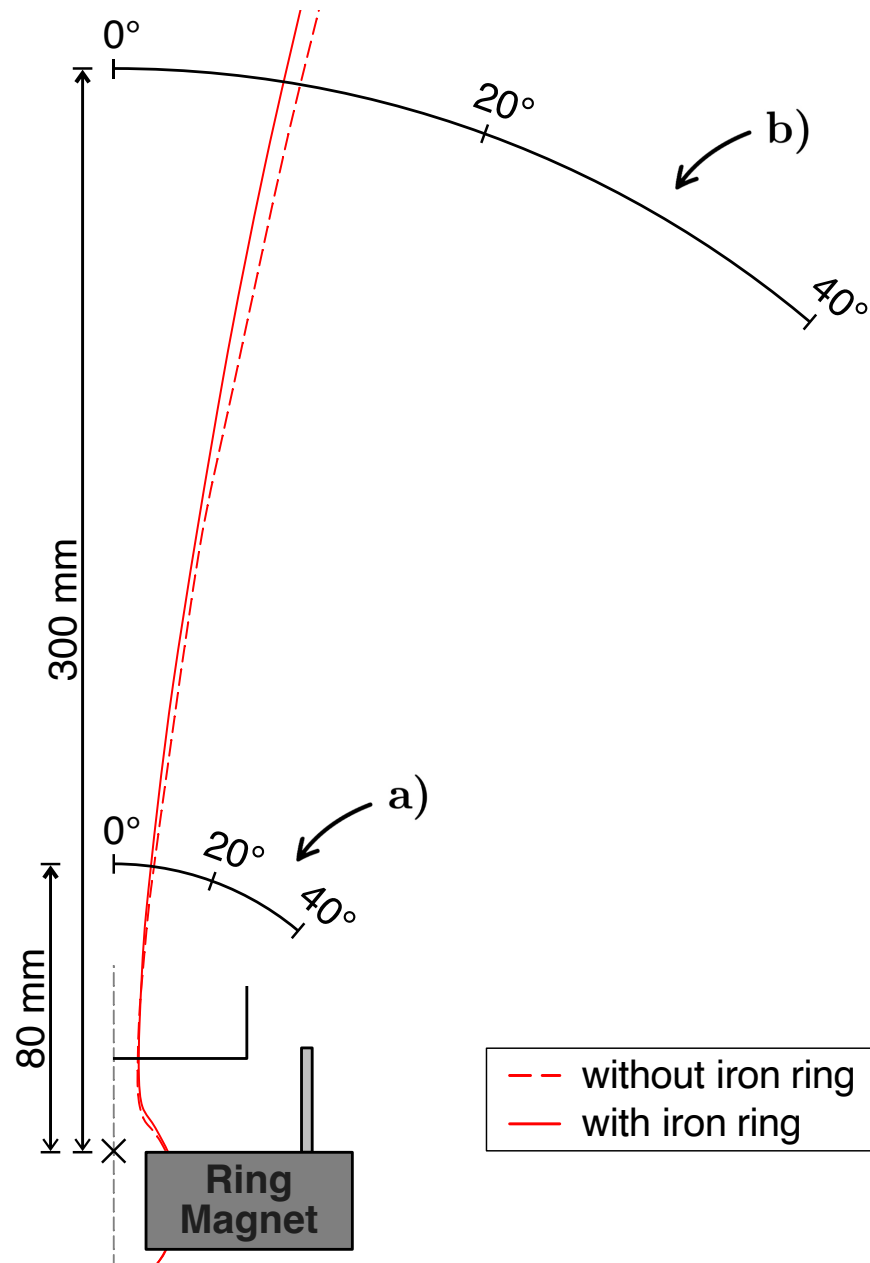


Figure 8.6: Diagram of the large ECR thruster, to show where measurements were taken for the plots in figure 8.5. The magnetic field lines that pass through the resonance region at a radius of 7 mm are shown in red. Modelled using FEMM[93].

8.2 Resonance Region Location Effects

Thrust Measurements

The addition of the iron ring has the effect of pulling the resonance region back towards the ring magnet, see figure 8.3. As the thruster's movement is limited, this results in the resonance region now only being able to be swept between 0 mm and 12 mm displacement from the backplate. Thruster power and reverse power at the microwave generator are plotted in figure 8.7.

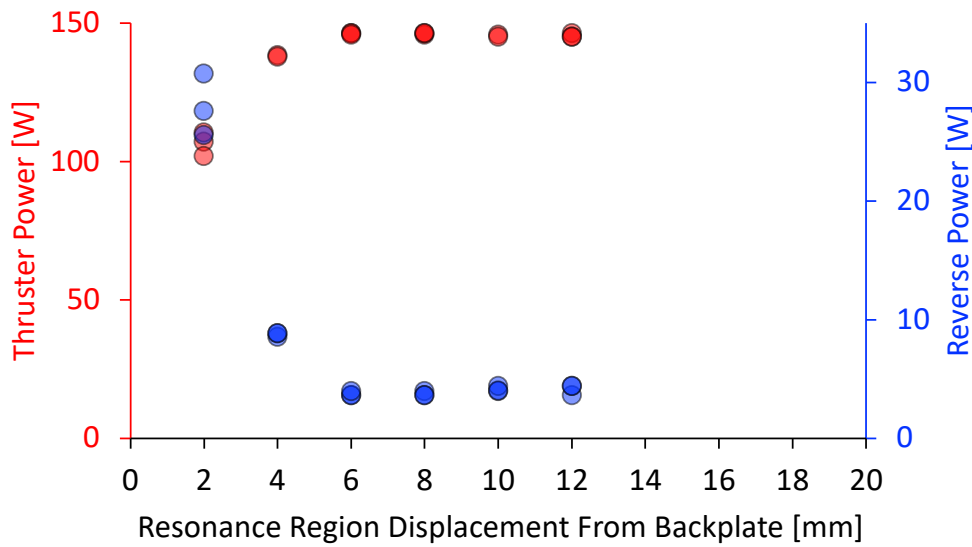


Figure 8.7: Thruster power and reverse microwave power measured at the generator as a function of the displacement of the resonance region from the backplate for the large ECR thruster with iron ring. 240 W forward microwave power at the generator, 0.39 mg/s xenon mass flow rate. Three measurements taken for each displacement, standard errors from 0.23 W to 2.48 W and 0.14 W to 1.51 W respectively.

As can be seen from figure 8.7, the thruster power is maximised for resonance region displacements from the backplate above 6 mm. The thrust and specific impulse are then plotted in figure 8.8. This shows that the decrease in thrust for displacements below 8 mm is also present when the iron ring is added. The thruster efficiency is also compared in figure 8.8. For resonance region displacements of 4 mm and above, the addition of the iron ring can be clearly seen to result in an increase to thruster performance. This is despite the slight reduction in thruster power due to an increase in reverse power, see figures 7.4 and 8.7. Ultimately a 10 mm resonance region displacement from the backplate was chosen for the following tests due to its high thruster performance both without and with the iron ring. All the following tests are conducted at this displacement.

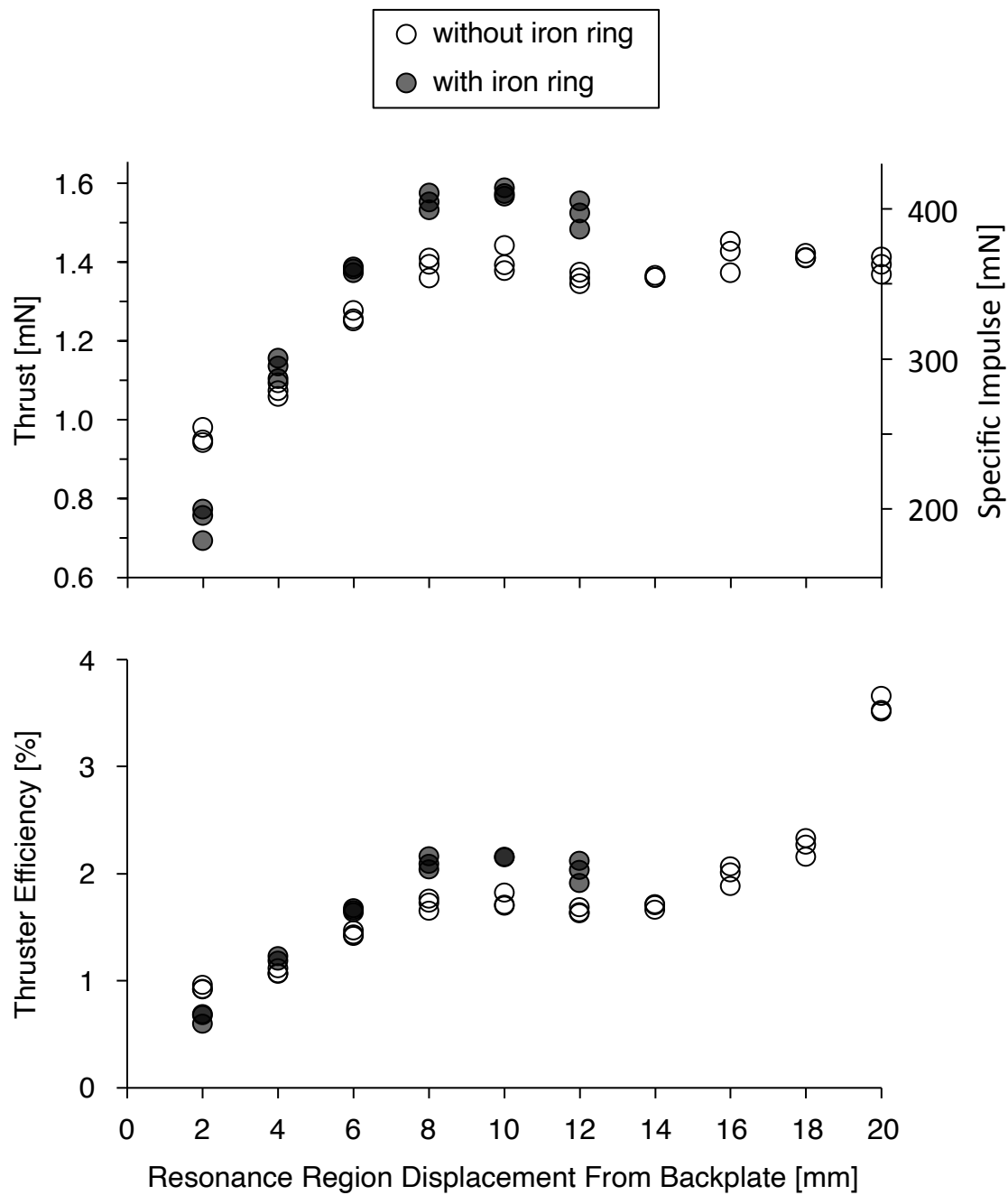


Figure 8.8: Thrust, specific impulse and thruster efficiency as a function of the displacement of the resonance region from the backplate both without and with the iron ring. Thruster powers can be found from figures 7.4 and 8.7 respectively. Large ECR thruster, 0.39 mg/s xenon mass flow rate. Three measurements taken for each test condition, standard errors from 0.006 mN to 0.024 mN.

Ion Beam Measurements

A Faraday probe was used to map out the ion beam profile of the large ECR thruster both without and with the iron ring at five different resonance region displacements from the backplate, see figure 8.9.

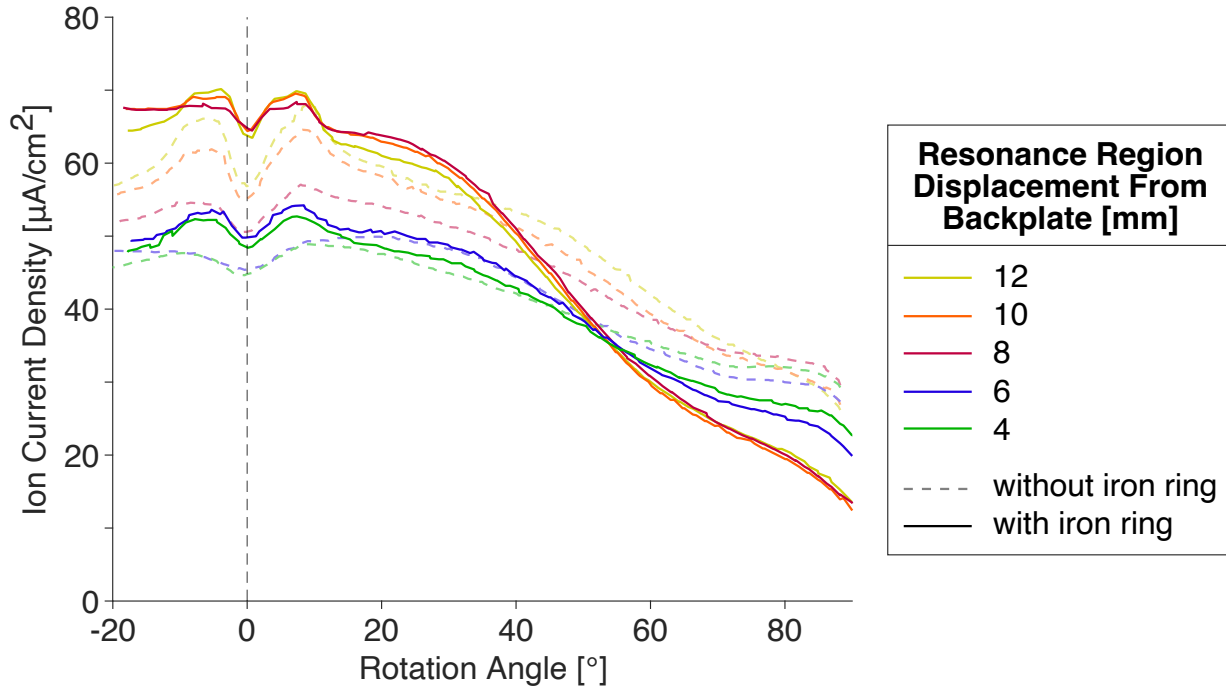


Figure 8.9: Ion current density as a function of rotation angle of the probe at five different resonance region displacements from the backplate for the large ECR thruster both without and with the iron ring. Thruster powers can be found from figures 7.4 and 8.7 respectively, 0.39 mg/s xenon mass flow rate.

The divergence of the ion beam without the iron ring is found to be $56^\circ \pm 1^\circ$ for all displacements of the resonance region from the backplate. Adding the iron ring is found to decrease the ion beam divergence to 51° for displacements 8 mm, 10 mm and 12 mm. This increases the divergence efficiency from 31 % to 40 %. However, the ion beam divergence is seen to return to $56^\circ \pm 1^\circ$ for displacements below 8 mm. Numerically integrating the curves of ion current density in figure 8.9 allows for the calculation of ion beam current, which is plotted as a function of resonance region displacement from the backplate in figure 8.10.

The ion beam current for the thruster without the iron ring can be seen to vary with the displacement of the resonance region from the backplate, see figure 8.10. Adding the iron ring however, can be seen to keep the ion beam current largely constant. This indicates that the larger resonance region configuration is less sensitive to its position in the thrust chamber. This makes sense, as the larger resonance region covers a larger fraction of the thrust chamber, especially around the antenna and chamber walls, see figure 8.3.

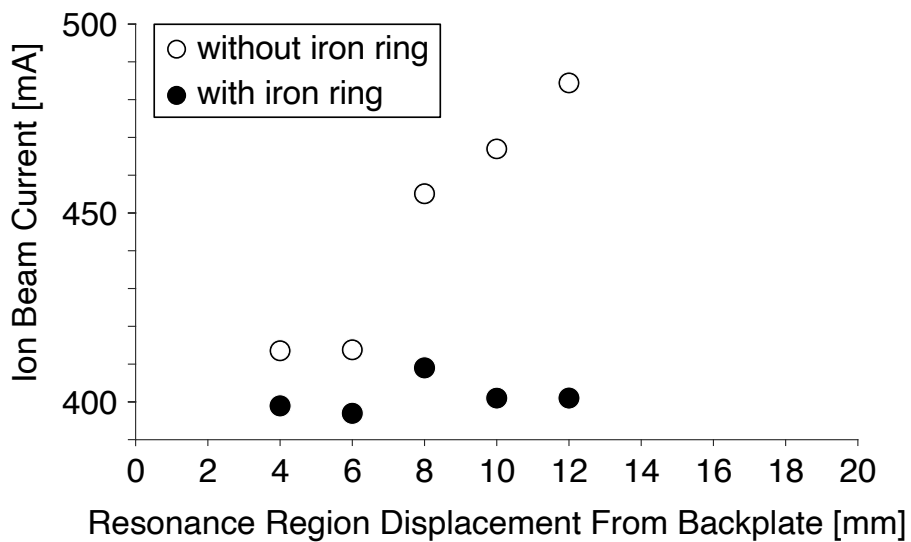


Figure 8.10: Ion beam current as a function of displacement of the resonance region from the backplate for the large ECR thruster both without and with the iron ring. Thruster powers can be found from figures 7.4 and 8.7 respectively, 0.39 mg/s xenon mass flow rate.

Electron Measurements

Langmuir probe measurements of electron temperature, taken 100 mm downstream of the thruster, are shown in figure 8.11. Adding the iron ring can be seen to increase electron temperatures for resonance region displacements from the backplate under 4 mm. For all other displacements, there is no statistically significant change to the electron temperature at this location.

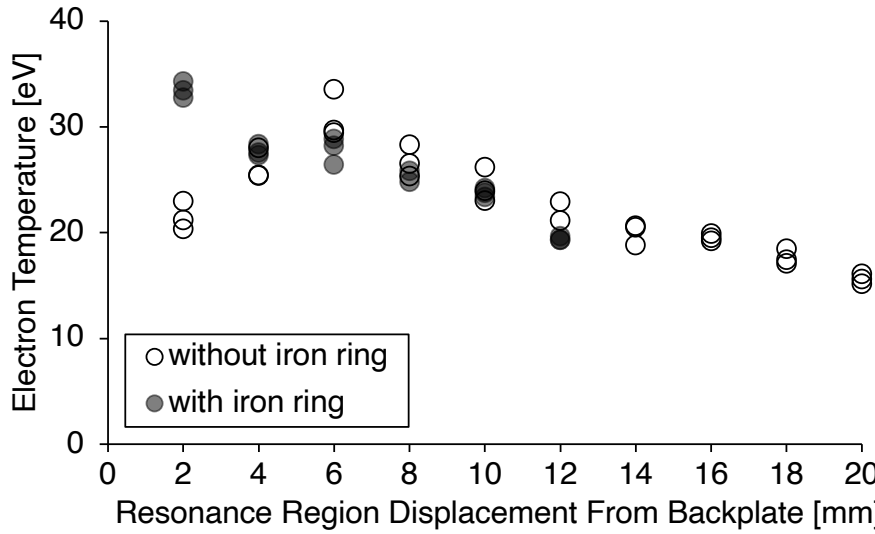


Figure 8.11: Electron temperature as a function of displacement of the resonance region from the backplate for the large ECR thruster both without and with the iron ring. Thruster powers can be found from figures 7.4 and 8.7 respectively, 0.39 mg/s xenon mass flow rate. Three readings taken for each test condition, standard errors from 0.1 eV to 1.6 eV.

Langmuir probe measurements of the plasma potential, taken 100 mm downstream of the thruster, are shown in figure 8.12. These also show no statistically significant change when the iron ring is added, except for a dip in plasma potential for resonance region displacements from the backplate between 6 mm and 10 mm.

The floating potential of the thruster is also plotted in figure 8.13. Adding the iron ring can be seen to increase the thruster potential for all displacements, with a jump up in potential seen for displacements of 8 mm and greater. This jump is also seen for measurements of ion beam current in figure 8.10, only it occurs for the thruster without the iron ring. This indicates that the plasma undergoes some sort of mode change when moving from 6 mm to 8 mm displacement. Without the iron ring this mode change results in an increase to the ion beam current, but when the iron ring is added the ion beam current stays constant and the mode change instead results in an increase to the floating potential of the thruster, which could indicate a stronger ambipolar electric field. This mode change is an interesting effect that results from changing the displacement of the resonance region from the backplate, and future work should aim to improve our understanding of it.

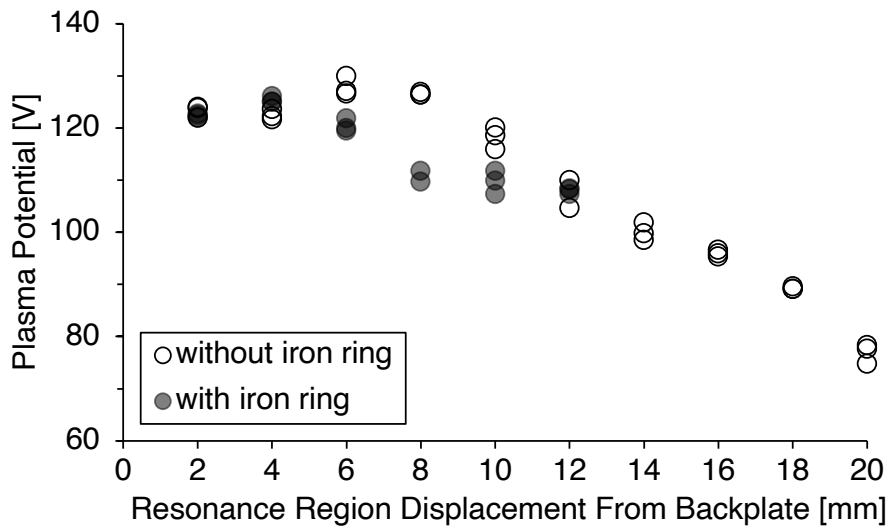


Figure 8.12: Plasma potential as a function of displacement of the resonance region from the backplate for the large ECR thruster both without and with the iron ring. Thruster powers can be found from figures 7.4 and 8.7 respectively, 0.39 mg/s xenon mass flow rate. Three readings taken for each test condition, standard errors from 0.2 V to 1.3 V.

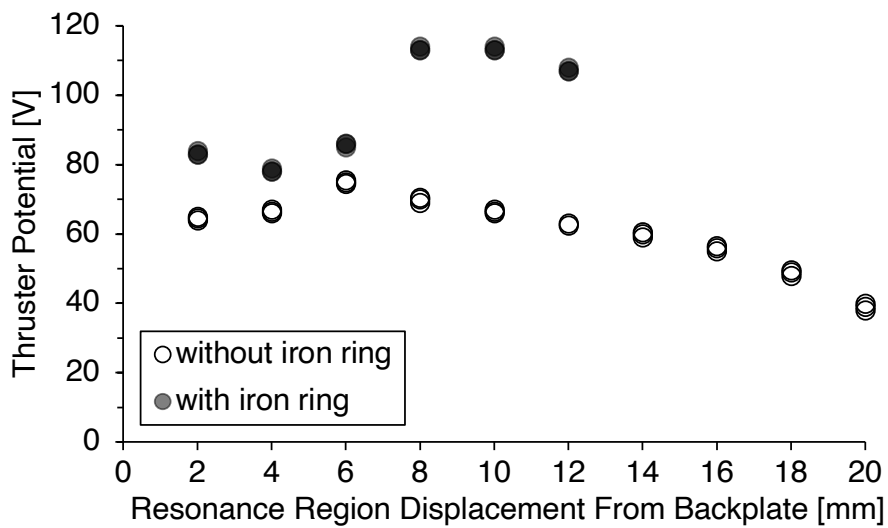


Figure 8.13: Thruster floating potential as a function of displacement of the resonance region from the backplate for the large ECR thruster both without and with the iron ring. Thruster powers can be found from figures 7.4 and 8.7 respectively, 0.39 mg/s xenon mass flow rate. Three readings taken for each test condition, standard errors from 0.4 V to 0.6 V.

RPA Measurements

A RPA was used to measure the energy of ions in the thruster's plume with a fixed resonance region displacement from the backplate of 10 mm, see figure 8.14. A significant reduction in the intensity of the second peak can be seen when the iron ring is added. Faraday probe measurements have shown that adding the iron ring results in a reduction in ion beam divergence from 56° to 51° at this resonance region location, see figure 8.9. As the RPA is located 20° off-axis from the thruster, it is possible that the divergence of the high energy ion beam decreases such that it no longer intersects the RPA.

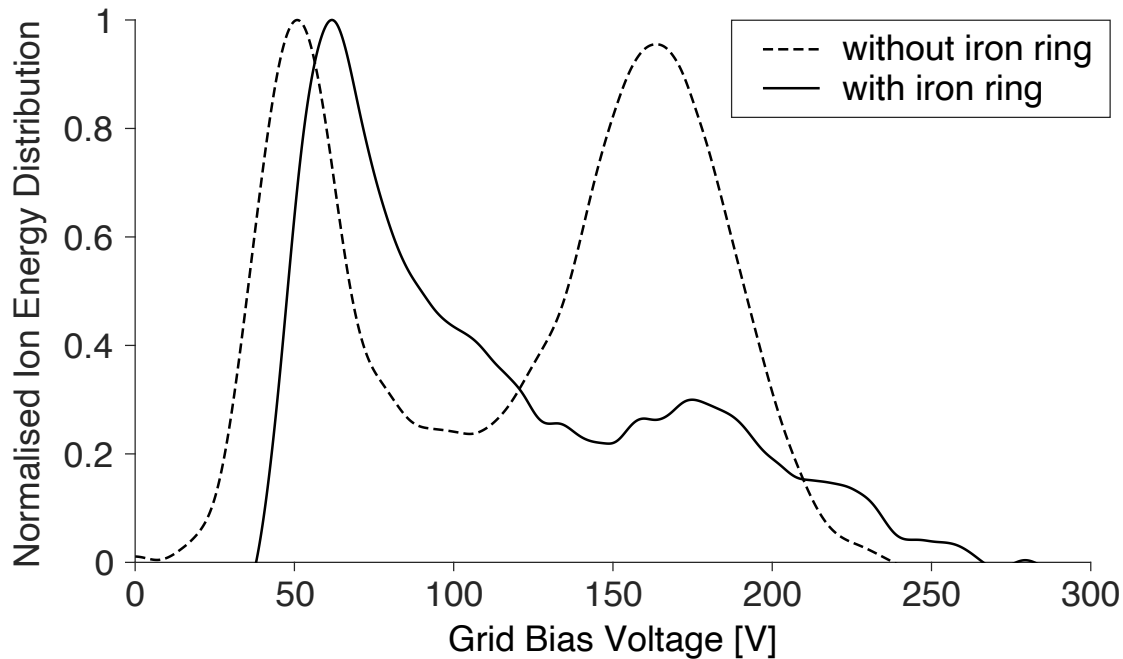


Figure 8.14: Normalised ion energy distribution for the large ECR thruster both without and with the iron ring. 10 mm displacement of the resonance region from the backplate, 144 W thruster power, 0.39 mg/s xenon mass flow rate.

Unfortunately, this discrepancy between the ion energy distributions of the thruster with and without the iron ring, prevents a fair comparison of RPA measurements between the two. The solution to this would be to move the RPA more inline with the thruster. However, in section 3.6 it was seen that this would require electron repelling grid potentials in excess of current laboratory equipment limitations. If the RPA was moved inline with the thruster, the resulting ion energy distribution of the thruster with the iron ring would likely resemble that without the iron ring, just shifted right by ~ 10 V.

8.3 Mass Flow Rate Effects

A resonance region displacement from the thruster backplate of 10 mm is used for all tests in section 8.3, both without and with the iron ring.

Thrust Measurements

A significant increase to the thruster performance is observed when the iron ring is added to the large ECR thruster for all mass flow rates tested, see figures 8.15 and 8.16. Adding the iron ring also allows for the thruster to be run at a lower xenon mass flow rate of 0.34 mg/s. The significant increase in specific impulse and thrust efficiency that is seen at this lower mass flow rate indicates that thruster performance could be improved if lower mass flow rates were able to be sustained. The plasma extinguishes at lower mass flow rates, likely because of insufficient neutral propellant density within the thrust chamber. Increasing neutral propellant density could be achieved by either decreasing the diameter of the chamber, or increasing its length. Alternatively, a nozzle could be added to the exit of the thrust chamber like was done by S. Peterschmitt[36], the results of which have yet to be disclosed.

When the iron ring is added, for 0.39 mg/s xenon mass flow rate and 145 W thruster power, thrust is seen to increase 15 % from 1.45 mN to 1.67 mN, specific impulse is seen to increase 15 % from 377 s to 432 s and thruster efficiency is seen to increase 32 % from 1.9 % to 2.5 %. This is found to be caused mostly by the increase in divergence efficiency from 31 % to 38 %, as seen from figure 8.18. An increase to the ion energy could also contribute to the observed performance increase, however a comparison of ion energy distributions is not possible with the current experimental setup.

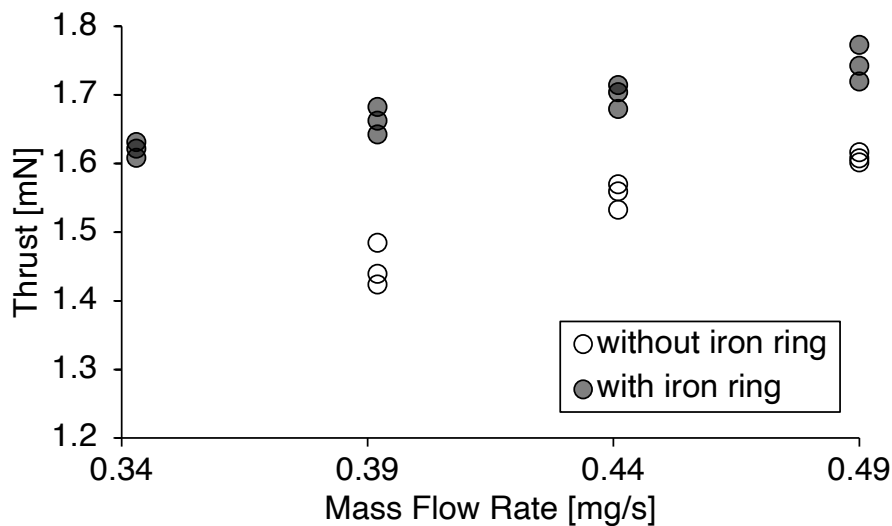


Figure 8.15: Thrust as a function of mass flow rate for the large ECR thruster both without and with the iron ring. 145 W thruster power. Three readings taken for each test condition, standard errors from 0.004 mN to 0.019 mN.

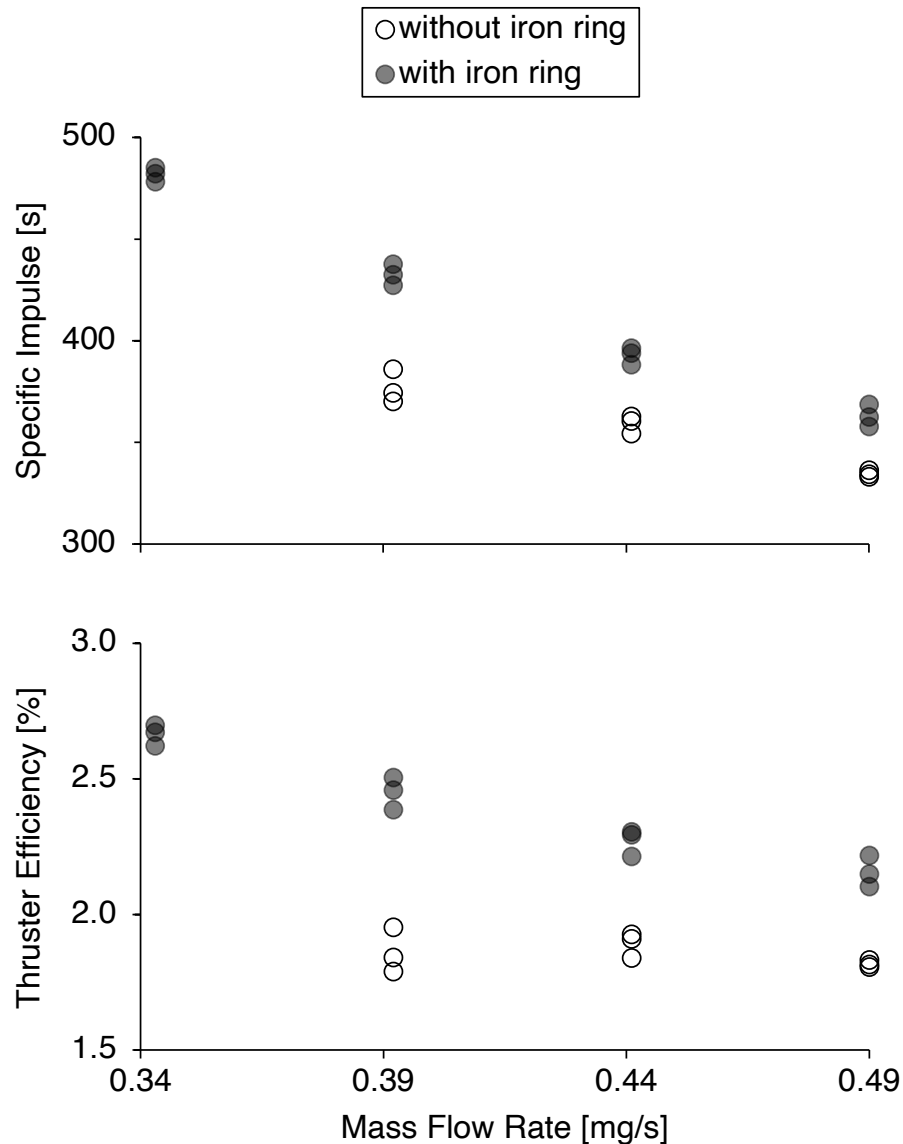


Figure 8.16: Specific impulse and thruster efficiency as a function of mass flow rate for the large ECR thruster both without and with the iron ring. 145 W thruster power. Three readings taken for each test condition, standard errors from 1 s to 3 s and 0.01 % to 0.05 % respectively.

The floating potential of the thruster is plotted in figure 8.17 both with and without the iron ring. The significant increase to thruster floating potential when the iron ring is added indicates a stronger ambipolar electric field. The amount by which thruster floating potential increases is seen to lessen at higher mass flow rates, however it remains significant.

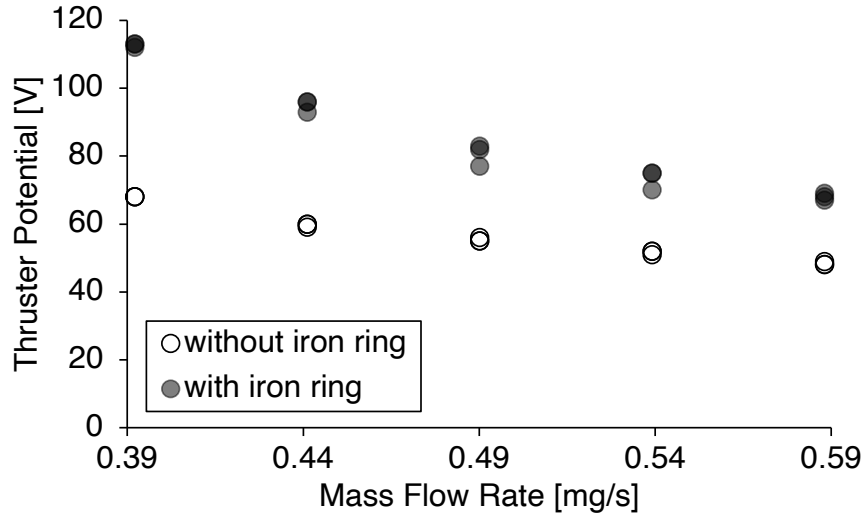


Figure 8.17: Thruster floating potential as a function of mass flow rate for the large ECR thruster both without and with the iron ring. 145 W thruster power. Three readings taken for each test condition, standard errors from 0.33 V to 1.53 V.

Ion Beam Measurements

A Faraday probe was used to map out the ion beam profile of the thruster at varying mass flow rates, see figure 8.18. A xenon mass flow rate of 0.34 mg/s without the iron ring was unable to be sustained indefinitely, but was able to be sustained long enough to obtain a Faraday probe measurement. Adding the iron ring is found to decrease the far field divergence of the beam from $56^\circ \pm 1^\circ$ to $52^\circ \pm 1^\circ$. This equals an increase to divergence efficiency from 31 % to 38 %. Ion beam current is found to decrease by $15\% \pm 2\%$ when the iron ring is added. As can be seen from figure 8.18, there is a negligible change to divergence angle with respect to mass flow rate.

For a xenon mass flow rate of 0.39 mg/s, adding the iron ring has been found to increase thrust and specific impulse by 15 %, while thruster efficiency increases by 32 %, see figures 8.15 to 8.16. Using equations 1.9 to 1.8, the increase of divergence efficiency from 31 % to 38 % results in an increase to thrust and specific impulse of 11 % and an increase to thruster efficiency of 23 %. The observed performance increase when the iron ring is added can then be largely attributed to this increase in divergence efficiency.

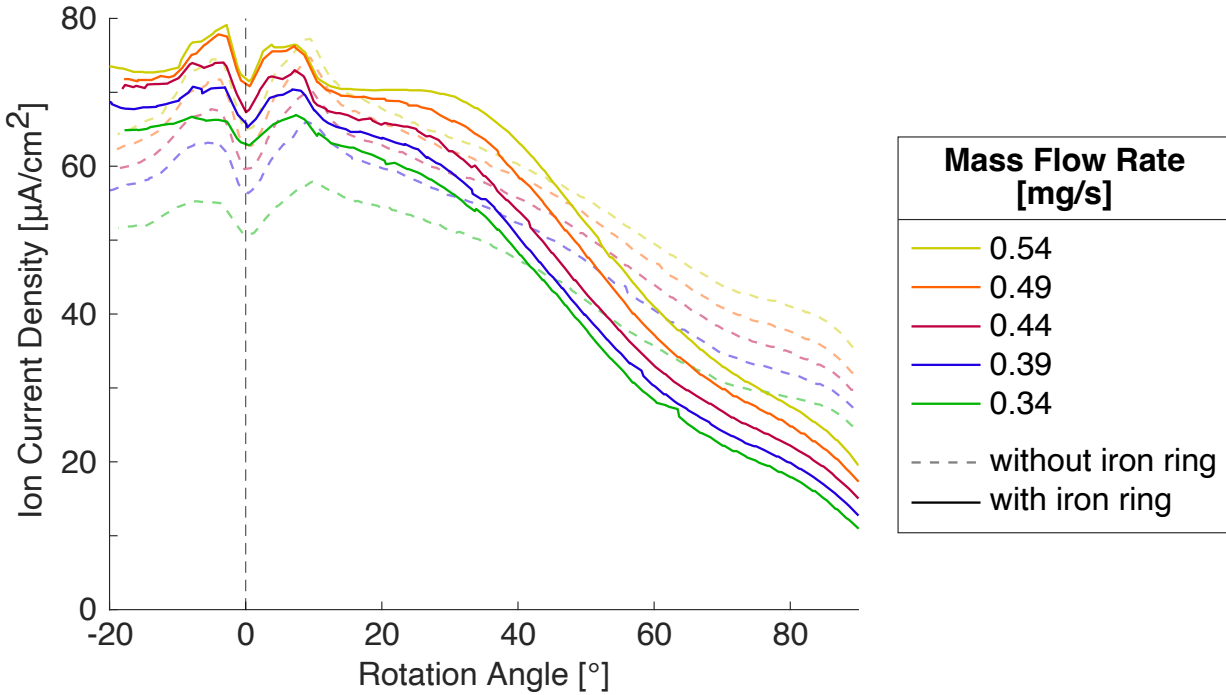


Figure 8.18: Ion current density as a function of rotation angle of the probe at five different xenon mass flow rates, for the large ECR thruster both without and with the iron ring. 143 W thruster power.

RPA Measurements

An RPA was used to measure the energy of ions in the thruster's plume. As discussed in section 8.2, the RPA measurements cannot be used to compare changes to the ion energy distribution due to the addition of the iron ring. However, RPA measurements can be used to evaluate the effect of a changing mass flow rate to the ion energy distribution. Figure 8.19 shows an increase to the energy of the ions in the plume as mass flow rate is decreased for the thruster without the iron ring. This is expected, as the power per unit mass of propellant is increasing. With the iron ring added, a similar increase to the energy of the ions in the plume is observed, see figure 8.20.

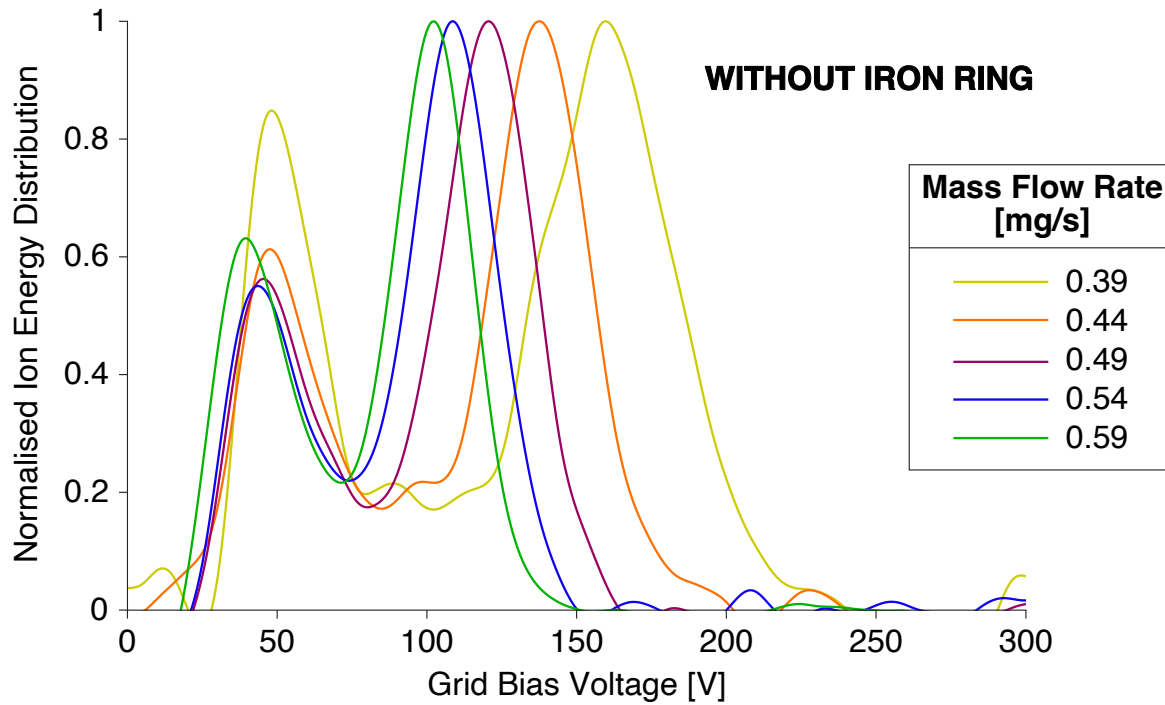


Figure 8.19: Normalised ion energy distribution for the large ECR thruster without the iron ring, at varying xenon mass flow rates. 146 W thruster power.

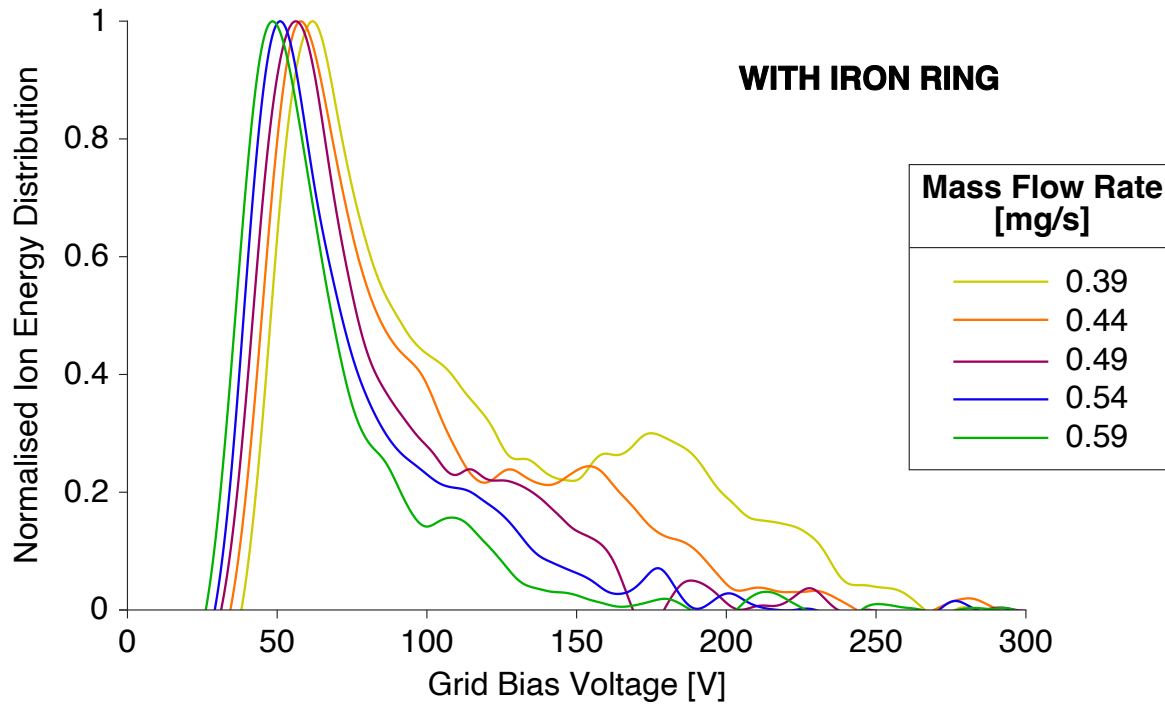


Figure 8.20: Normalised ion energy distribution for the large ECR thruster with the iron ring, at varying xenon mass flow rates. 144 W thruster power.

8.4 Thruster Power Effects

A resonance region displacement from the thruster backplate of 10 mm is used for all tests in section 8.4, both without and with the iron ring.

Thrust Measurements

Direct thrust measurements are taken at a range of thruster powers for the large ECR thruster both without and with the iron ring, see figure 8.21. Adding the iron ring can be seen to produce an increase in thrust at all power levels. From the plot of thruster efficiency in figure 8.22 it appears that the iron ring's increase to thruster performance is greater at lower thruster powers.

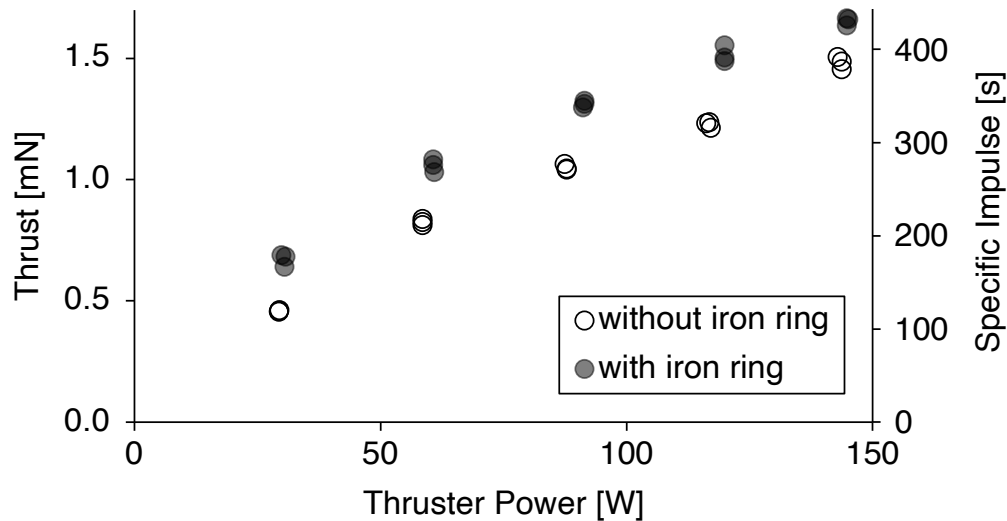


Figure 8.21: Thrust and specific impulse as a function of thruster power for the large ECR thruster both without and with the iron ring. 0.39 mg/s xenon mass flow rate. Three readings taken for each test condition, standard errors from 0.002 mN to 0.015 mN.

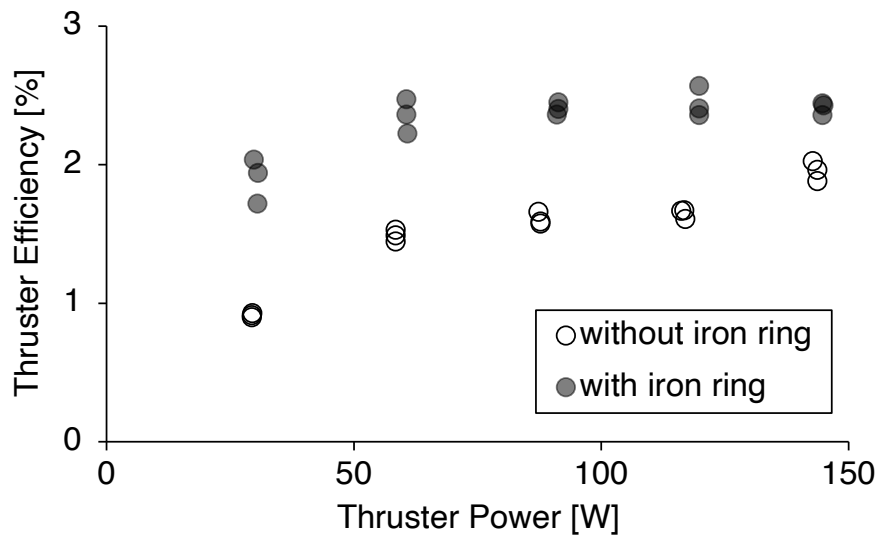


Figure 8.22: Thruster efficiency as a function of thruster power for the large ECR thruster both without and with the iron ring. 0.39 mg/s xenon mass flow rate. Three readings taken for each test condition, standard errors from 0.01 % to 0.07 %.

Thruster floating potential is plotted in figure 8.23 and shows a significant increase when the iron ring is added, indicating at a stronger ambipolar electric field. This increase to thruster floating potential is seen to increase for higher thruster powers.

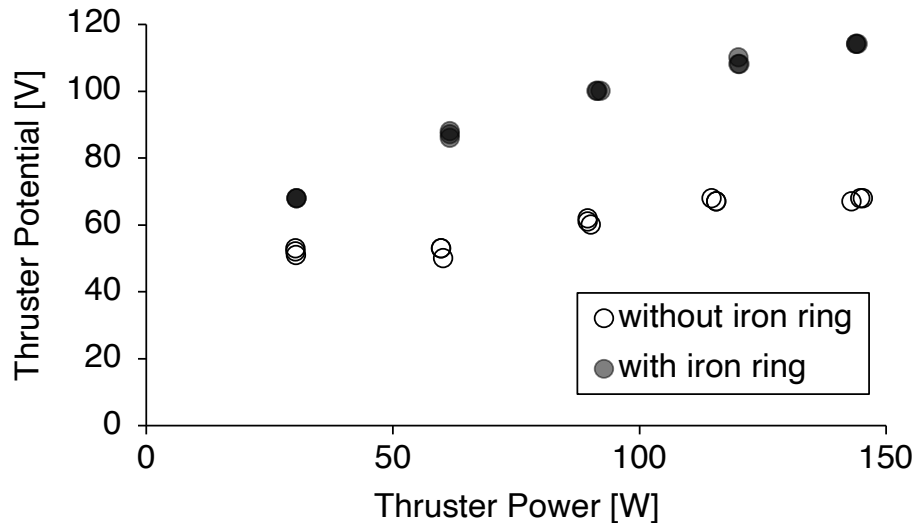


Figure 8.23: Thruster floating potential as a function of thruster power for the large ECR thruster both without and with the iron ring. 0.39 mg/s xenon mass flow rate. Three readings taken for each test condition, standard errors from 0.33 V to 0.67 V.

Ion Beam Measurements

Measurements of ion current density as a function of the rotation angle of the Faraday probe for different thruster powers are shown in figure 8.24. At 143 W thruster power, adding the iron ring is seen to decrease the far field divergence angle from 55° to 51°. This equals an increase to divergence efficiency from 33 % to 40 %. However, for powers below 91 W this change is less significant, with the addition of the iron ring only decreasing the far field divergence angle from 56 % to 54 %. This equals an increase to divergence efficiency from 31 % to 35 %.

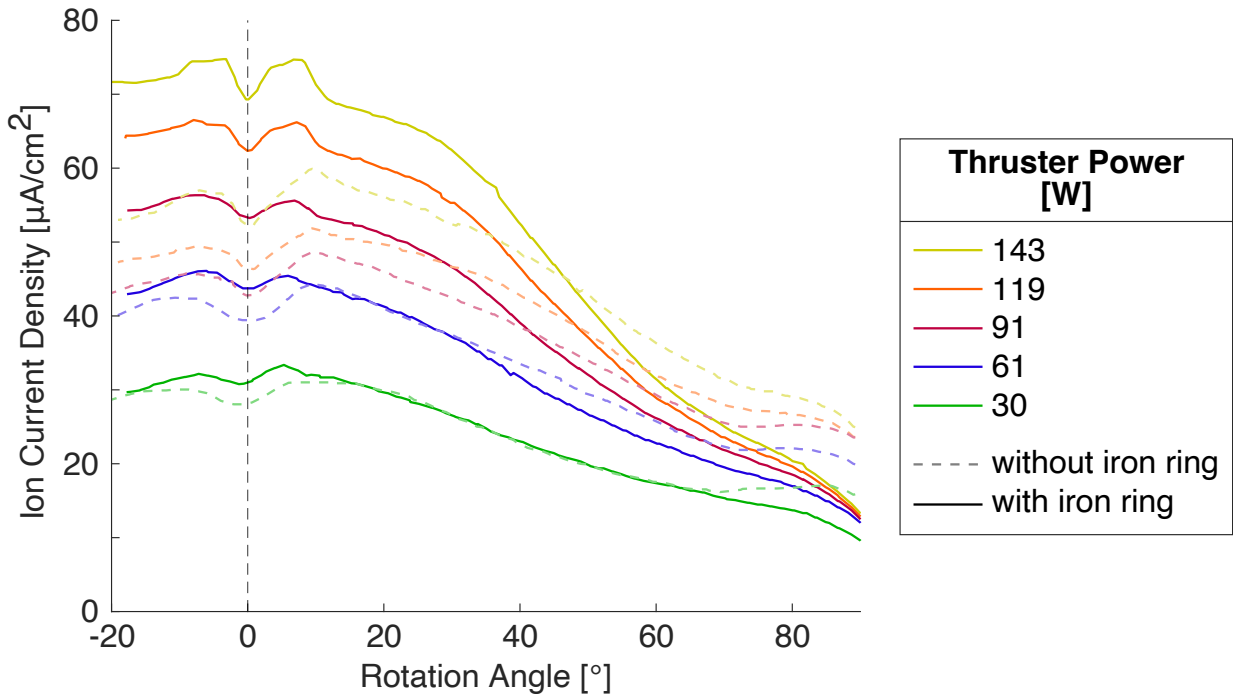


Figure 8.24: Ion current density as a function of rotation angle of the probe at five different thruster powers, for the large ECR thruster both without and with the iron ring. 0.39 mg/s xenon mass flow rate.

The presence of dual peaks in the ion current density profile of waveguide ECR magnetic nozzle thrusters has been investigated by M.R. Inchingolo, et al.[107]. This study found that greater power coupling near the thruster walls, where the injector holes are located and propellant density is greatest, could result in a hollow plume structure that would produce dual peaks in the ion current density distribution. This could be the reason for the presence of dual peaks in the ion current density distributions shown in figure 8.24. Although the dip in ion current density at 0° could also be produced by a central column of high energy electrons that are not sufficiently repelled by the 300 V probe bias.

Electron Measurements

The Electron Energy Distribution Function (EEDF) was found from Langmuir probe measurements using the method outlined in section 3.4[73], see figure 8.25. The EEDF can be seen to comprise two gaussian distributions, one centered at ~ 20 eV, and a second with a much larger variance that acts to extend the tail of the EEDF to higher electron temperatures. As power is increased, the intensity of the first peak increases, and the variance of the second gaussian distribution increases. Therefore, increasing thruster power can be said to increase the number of electrons at the ~ 20 eV peak, but also populates the tail of the EEDF at higher temperatures. Studies of other ECR magnetic nozzle thrusters have found evidence that the energy of electrons in the plume can reach up to 300 eV[107]. Numerical studies suggest these suprothermal electrons could produce a CFDL in the plume[108][109], however a CFDL has yet to be observed in ECR magnetic nozzle thrusters.

For thruster powers under 91 W, adding the iron ring appears to decrease the height of the peak in the EEDF, indicating a reduction in the number density of electrons at this Langmuir probe location. However, at 62 W the thruster without the iron ring appears to hit a limit on the number of electrons that can be heated to ~ 20 eV. The addition of the iron ring allows for a larger number of electrons to be heated. This implies that decreasing the magnetic field strength gradient at resonance increases the power that is able to be delivered to the propellant. This makes a shallow magnetic field strength gradient at resonance essential for the scaling up of ECR magnetic nozzle thrusters.

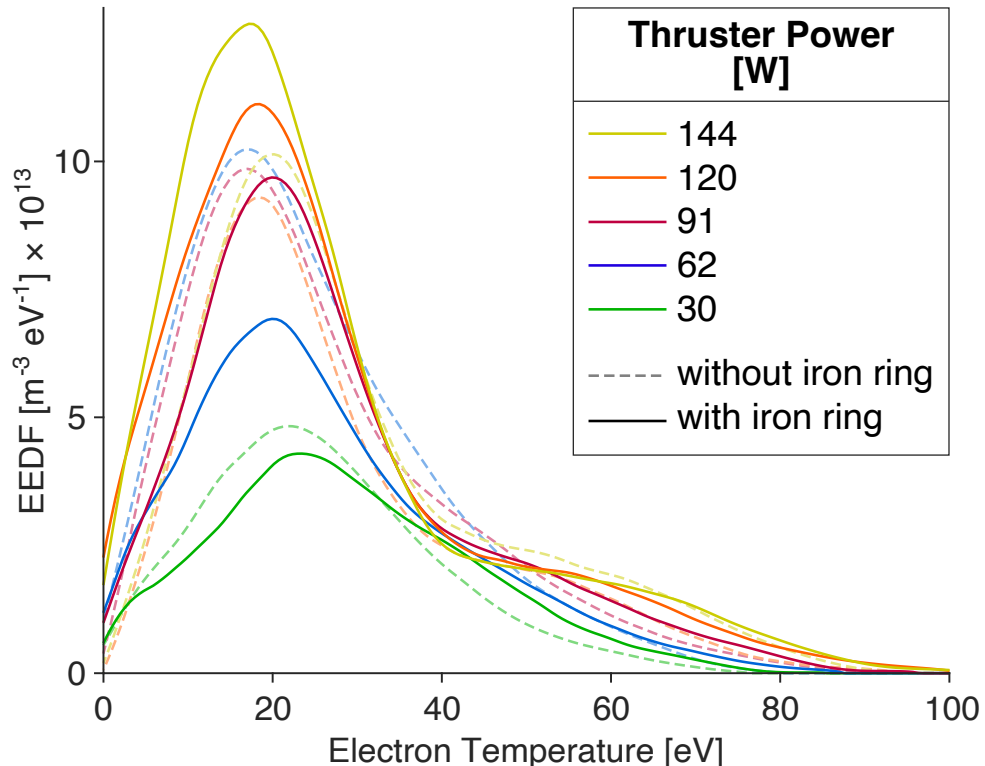


Figure 8.25: The effect of thruster power on the Electron Energy Distribution Function (EEDF) for the large ECR thruster both with and without the iron ring. Langmuir probe 150 mm downstream, along the thruster's central axis. 0.39 mg/s xenon mass flow rate.

8.5 Background Pressure Effects

A resonance region displacement from the thruster backplate of 10 mm is used for all tests in section 8.5, both without and with the iron ring. A controlled flow rate of xenon was fed into the vacuum chamber at a point above and behind the thruster, see figure 3.3. This allowed for the pressure within the vacuum chamber to be increased, so as to study the effects of background pressure on the large ECR thruster both without and with the iron ring. The effect of background pressure on ECR thruster performance is significant and is detailed in section 2.6.

Thrust Measurements

Direct thrust measurements are taken at a range of background pressures for the large ECR thruster both without and with the iron ring, see figure 8.26. Adding the iron ring can be seen to increase thrust for all background pressures. Thruster efficiency is also seen to increase, see figure 8.27. At higher background pressures, there is a higher density of neutral particles in the plume. This increases the fraction of electrons that collide with the neutrals, decreasing the net temperature of the electrons and the strength of the ambipolar electric field. The ions, subject to a weaker electric field, experience a decreased acceleration, reducing their final speed, thereby reducing thruster performance.[26]

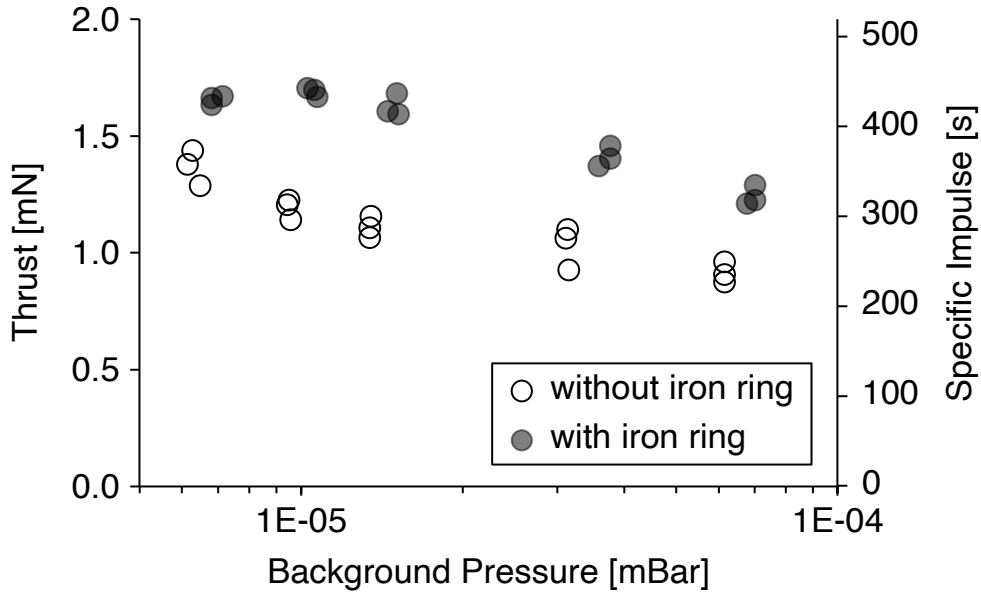


Figure 8.26: Thrust and specific impulse as a function of background pressure for the large ECR thruster both without and with the iron ring. 145 W thruster power, 0.39 mg/s xenon mass flow rate. Three readings taken for each test condition, standard errors from 0.011 mN to 0.044 mN.

A clear decrease to the performance of the large ECR thruster is observed as the background pressure is increased, both without and with the iron ring. On average, thrust is seen to decrease 29 % when the background pressure is increased from 6.6×10^{-6} mBar to 6.5×10^{-5} mBar. This is greater than the 26 % thrust decrease seen for the small ECR

thruster in section 5.5 for a similar rise in background pressure. This indicates that increasing the diameter of the thrust chamber could make ECR thrusters more sensitive to changes in background pressure. A similar study at ONERA also looked at the effect of background pressure on two different sizes of ECR thruster[7]. This study also found that the effect of background pressure on thruster performance differed between the two differently sized thrusters, however the cause of this has yet to be determined.

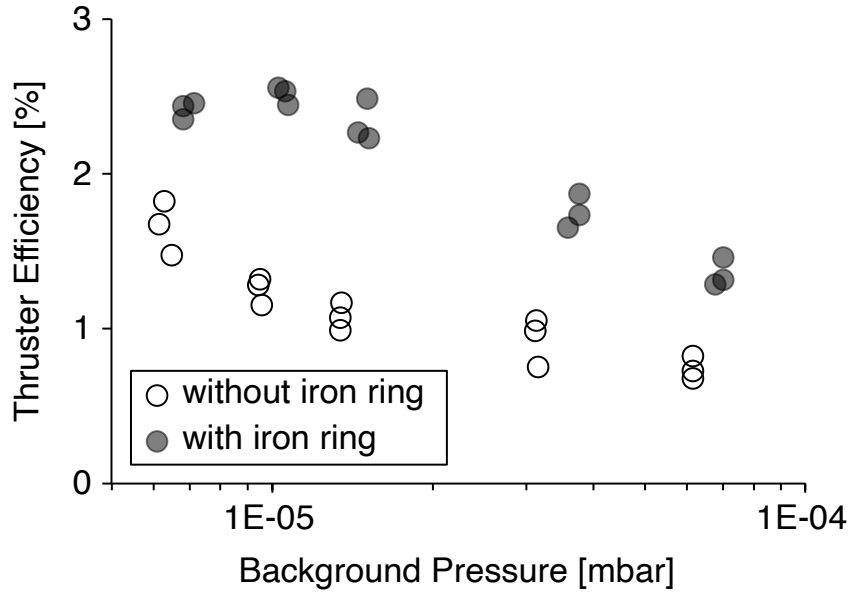


Figure 8.27: Thruster efficiency as a function of background pressure for the large ECR thruster both without and with the iron ring. 145 W thruster power, 0.39 mg/s xenon mass flow rate. Three readings taken for each test condition, standard errors from 0.04 % to 0.10 %.

Ion Beam Measurements

Faraday probe measurements of the ion current density for different background pressures are shown in figure 8.28. Numerically integrating these curves allows for the calculation of ion beam current and far field beam divergence angle, see figure's 8.29 and 8.30. Here it can be seen that the addition of the iron ring does not increase the ion beam current. Instead it works to redistribute the ions to a lower divergence angle, such that their momentum is more efficiently converted into thrust. From figure 8.30, it can be seen that this effect becomes more pronounced at lower pressures.

From figure 8.28 it can be seen that increasing background pressure broadens the ion current density profile, increasing the divergence of the beam. The increase of ion current density at high rotation angles is a well known phenomenon that also occurs to HETs and is found to be due to the generation of ions from charge exchange collisions in the plume[100]. These low energy ions move in random directions and so are collected by the Faraday probe at large rotation angles, artificially increasing the ion beam current.

The reduction of thrust at higher background pressures is due to a reduction in thruster efficiency. This is thought to be caused in two different ways. First, the beam becomes more divergent, see figure 8.30, resulting in a decrease to the thrusters beam divergence

efficiency. Second, the energy of the ions in the plume is decreased, this is shown via RPA measurements in figures 8.34 and 8.35 and results in a decrease to the thrusters electrical efficiency.

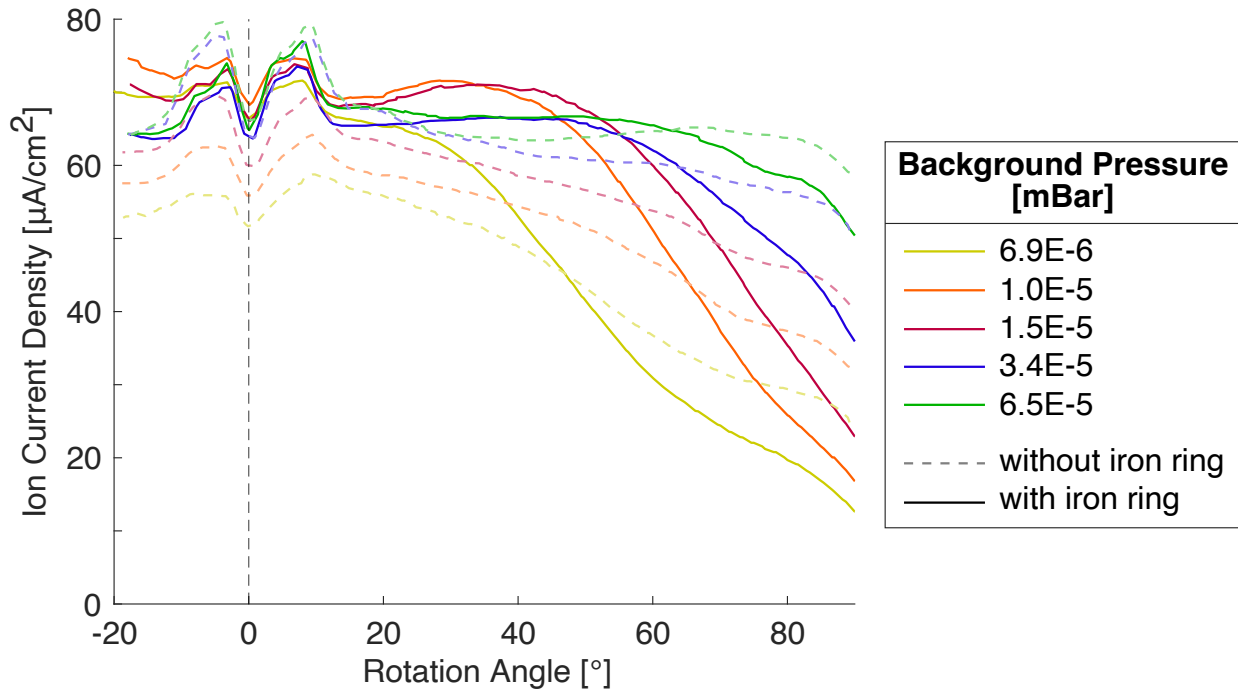


Figure 8.28: Ion current density as a function of rotation angle of the probe at five different background pressures, for the large ECR thruster both without and with the iron ring. 145 W thruster power, 0.39 mg/s xenon mass flow rate.

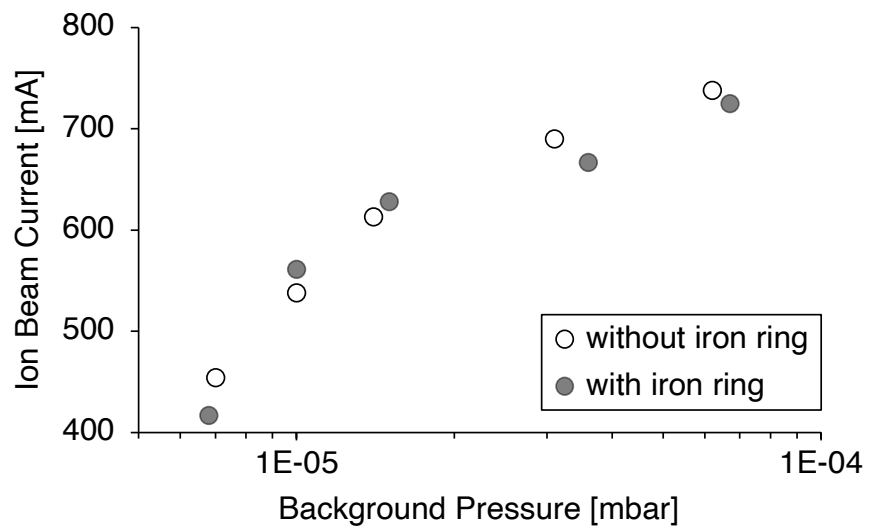


Figure 8.29: Ion beam current as a function of background pressure, for the large ECR thruster both without and with the iron ring. 145 W thruster power, 0.39 mg/s xenon mass flow rate.

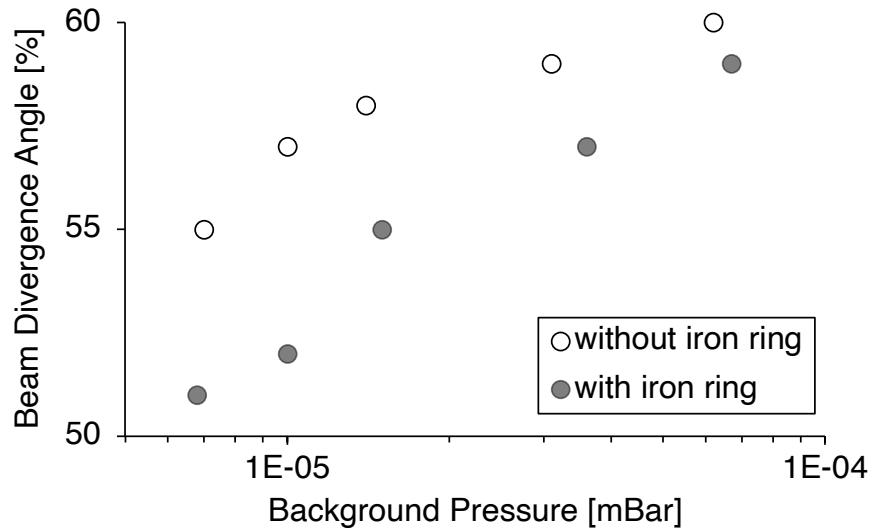


Figure 8.30: Far field beam divergence angle as a function of background pressure, for the large ECR thruster both without and with the iron ring. 145 W thruster power, 0.39 mg/s xenon mass flow rate.

Electron Measurements

Langmuir probe measurements of electron temperature and plasma potential, taken 100 mm downstream of the thruster, are shown in figures 8.31 and 8.32. Measurements at different background pressures were only taken without the iron ring. However, the thruster floating potential was measured at different background pressures both without and with the iron ring, see figure 8.33. The addition of the iron ring can be seen to increase thruster floating potential by a larger fraction at lower background pressures.

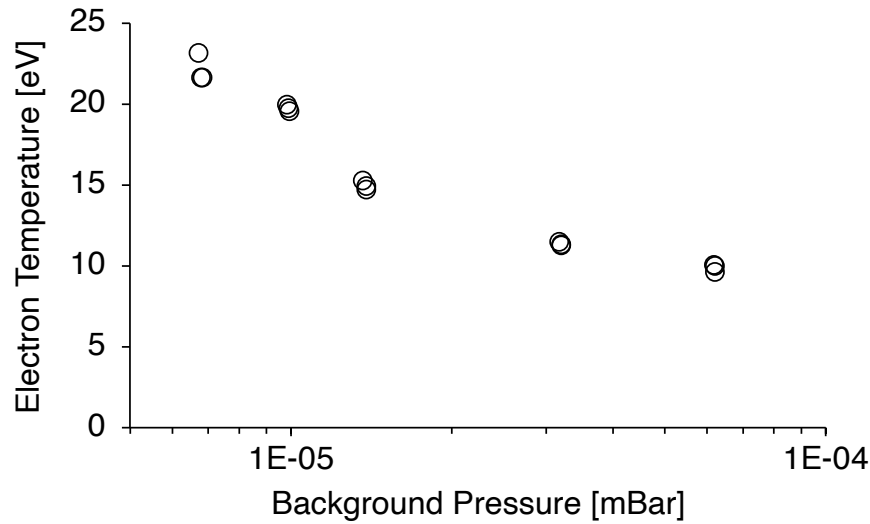


Figure 8.31: Electron temperature as a function of background pressure for the large ECR thruster without the iron ring. 145 W thruster power, 0.39 mg/s xenon mass flow rate. Three readings taken for each test condition, standard errors from 0.07 eV to 0.51 eV.

Electron temperature, plasma potential and thruster potential all increase as background pressure decreases. This is thought to be due to the higher neutral density at higher background pressures, increasing the fraction of electrons that collide with the neutral particles. This reduces the net energy of the electrons, leading to a reduction in the strength of the ambipolar electric field.[26]

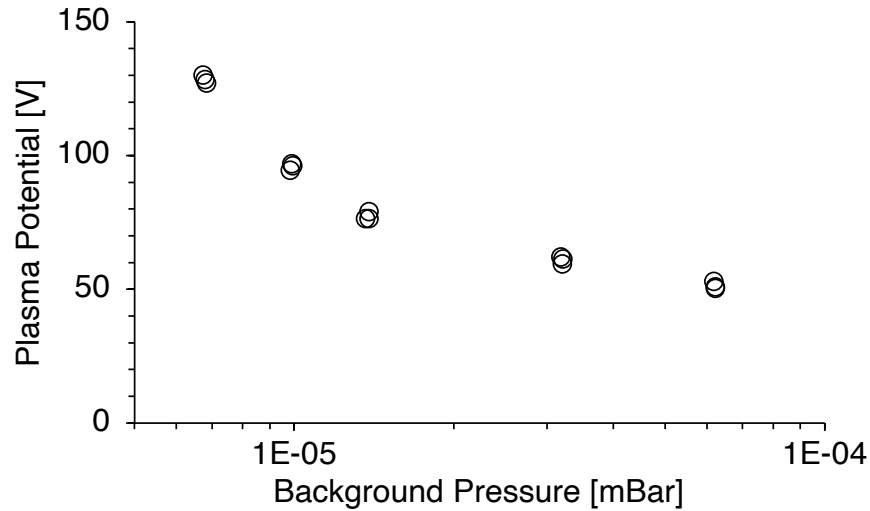


Figure 8.32: Plasma potential as a function of background pressure for the large ECR thruster without the iron ring. 145 W thruster power, 0.39 mg/s xenon mass flow rate. Three readings taken for each test condition, standard errors from 0.71 V to 0.88 V.

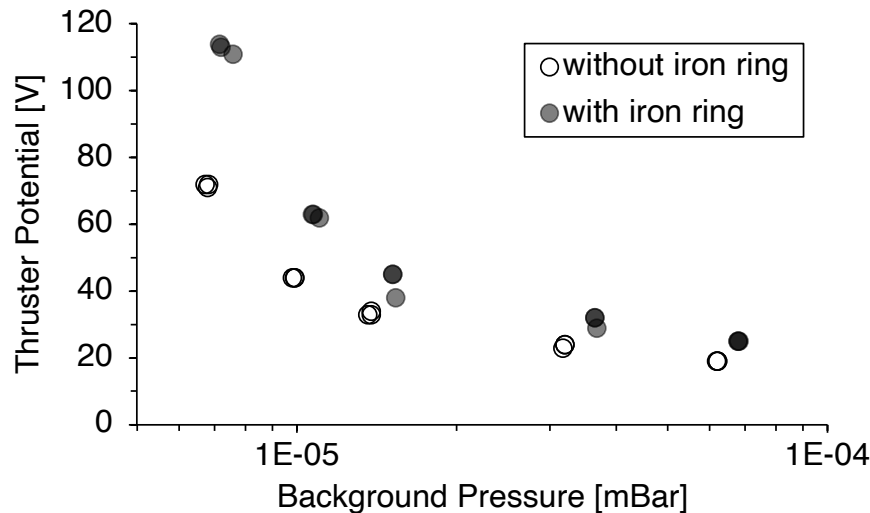


Figure 8.33: Thruster floating potential as a function of background pressure for the large ECR thruster both without and with the iron ring. 145 W thruster power, 0.39 mg/s xenon mass flow rate. Three readings taken for each test condition, standard errors from 0.33 V to 2.33 V.

RPA Measurements

A RPA was used to measure the energy of ions in the thruster's plume. As discussed in section 8.2, the RPA measurements cannot be used to compare changes to the ion energy distribution due to the addition of the iron ring. However, RPA measurements can be used to evaluate the effect of a changing background pressure on the ion energy distribution. Decreasing background pressure is shown to increase the energy of ions in the plume both without and with the iron ring, see figures 8.34 and 8.35. With the iron ring, this increase in ion energy is only apparent at pressures below $\sim 1 \times 10^{-5}$ mBar.

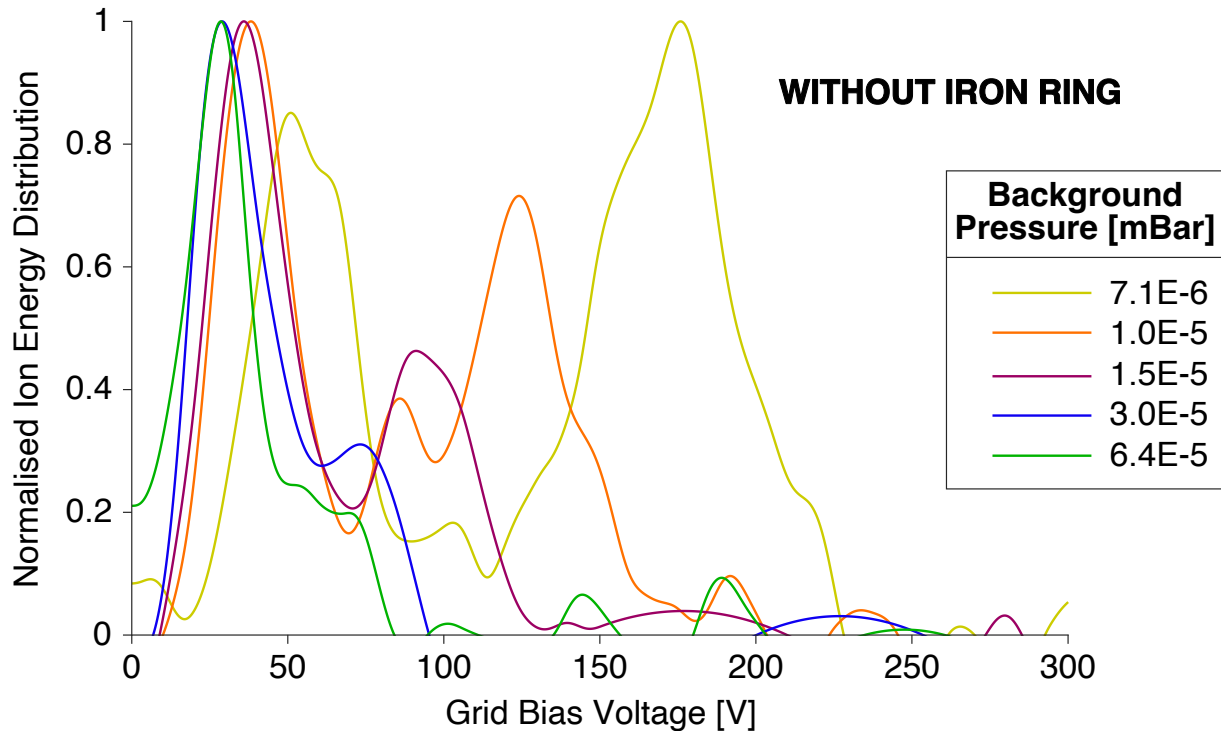


Figure 8.34: Normalised ion energy distribution for the large ECR thruster without the iron ring, at varying background pressures. 144 W thruster power, 0.39 mg/s xenon mass flow rate.

As can be seen from figure 8.34, the large thruster without the iron ring produces two distinct peaks in ion energy. As the background pressure is decreased, the second peak can be seen to move rightwards, this shows that the energy of these ions is increasing. The same increase to the energy of the ions in the second peak is also seen in figure 8.35 for the large ECR thruster with the iron ring, however the second peak is only observed for background pressures below 1.1×10^{-5} mBar. Plots 8.34 and 8.35 show clear evidence that higher background pressures work to decrease the average energy of ions in the plume. This is likely the primary cause for the decrease in thrust seen at higher background pressures. The reduction in the energy of the ions in the beam is likely due to the reduction in electron energies leading to a reduction in the strength of the ambipolar electric field, as indicated by figures 8.31 to 8.33.

The grid bias voltage of the first peak in the ion energy distribution multiplied by 0.64 is a crude approximation for the local plasma potential at the RPA, see section 3.6. This local

plasma potential is plotted as a function of background pressure in figure 8.36. Similar trends are seen in the plots of plasma potential and thruster floating potential in figures 8.32 and 8.33. This is further evidence that the ion energy distribution can be used to approximate the local plasma potential, allowing for the calculation of ion energy using equation 3.19.

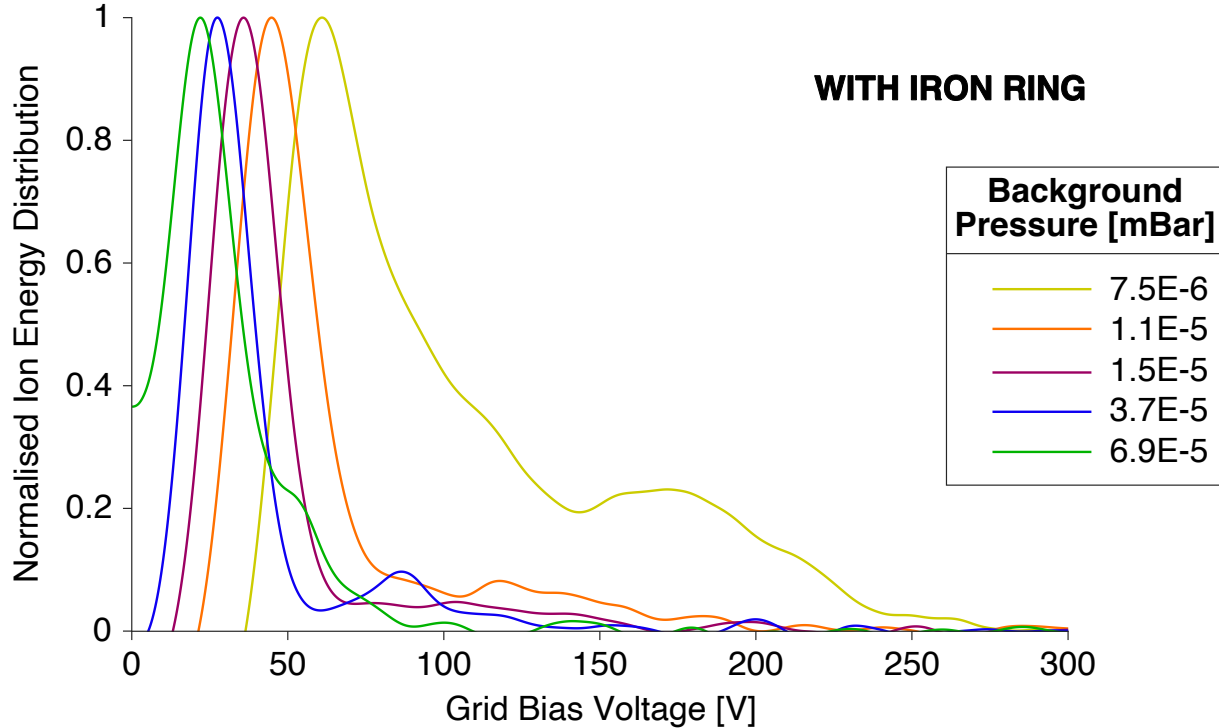


Figure 8.35: Normalised ion energy distribution for the large ECR thruster with iron ring, at varying background pressures. 144 W thruster power, 0.39 mg/s xenon mass flow rate.

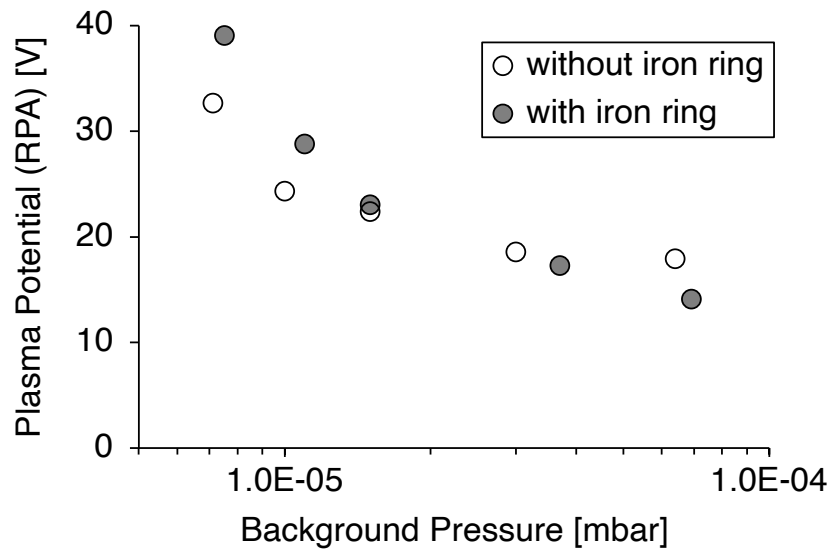


Figure 8.36: Plasma potential at the RPA as a function of background pressure. Approximated using the technique outlined in section 3.6. Large ECR thruster both without and with the iron ring, 144 W thruster power, 0.39 mg/s xenon mass flow rate.

Summary of Background Pressure Effects

Higher background pressures increase the performance of HETs due to the entrainment of neutral particles artificially increasing the propellant mass flow rate[110]. However, the performance of ECR thrusters is seen to decrease at higher background pressures. This relationship has been investigated in prior studies[7][26], see section 2.6, but has yet to be fully understood. Increasing the background pressure from $\sim 6 \times 10^{-6}$ to $\sim 6 \times 10^{-5}$ is seen to decrease thrust by 26 % for the small ECR thruster, and 29 % for the large ECR thruster. This indicates that increasing the diameter of the thrust chamber could increase the dependence of thruster performance on the background pressure.

Ion beam current is seen to increase as the background pressure is increased. This is a well known phenomenon that also occurs to HETs and is thought to be due to the generation of ions from charge exchange collisions in the plume[100]. However, unlike HETs, ECR thrusters experience a decreased thrust at these higher background pressures and ion beam currents. This has been observed to be due to a decrease to the beam divergence efficiency as well as the velocity of the ions. Beam divergence efficiency decreases by an average of 29 % when background pressure is increased from 6.9×10^{-6} to 6.5×10^{-5} , see figure 8.30. However, the reduced velocity of the ions is thought to be the predominant mechanism by which the thruster performance is decreased[26].

The greater density of neutral particles at higher background pressures cause more electrons to collide with neutral particles in the plume[26]. This can be seen to reduce the net energy of the electrons in the plume, see figure 8.31. This can then be seen to reduce the strength of the ambipolar electric field, as indicated by figures 8.32 and 8.33. This has the effect of reducing the acceleration of the ions in the plume. This can be seen from the plots of the ion energy distribution in figures 8.34 and 8.35. This significant decrease to the energy of the ion beam results in the decreased thruster efficiency that is observed at higher background pressures. This theorised sequence of events is explained in the form of a flowchart in figure 8.37.

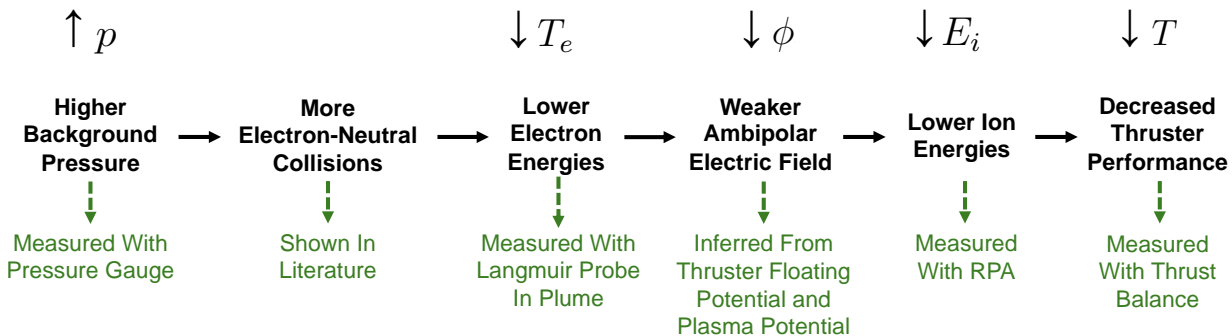


Figure 8.37: Flowchart showing the theorised sequence of events and the variables that are increased/decreased as a result. The method with which each variable was measured is shown in green.

8.6 Alternative Propellants (Krypton & Argon)

A resonance region displacement from the thruster backplate of 10 mm is used for all tests in section 8.6, both without and with the iron ring.

Thrust Measurements

The xenon propellant can be switched to lighter and cheaper alternatives like krypton and argon, see table 8.2. As these propellants have a lower atomic mass and a higher first ionisation energy, more energy is required to ionise a unit mass of the propellant. In HETs this results in a decrease to the thruster efficiency[111].

Table 8.2: Atomic mass, first ionisation energy and first ionisation cross section[112] (assuming electron temperatures of 20 eV) for xenon, krypton and argon.

	Xenon	Krypton	Argon
Atomic Mass [u]	131	84	40
First Ionisation Energy [kJ/mol]	1170	1351	1521
First Ionisation Cross Section [$\times 10^{-22} \text{ m}^2$]	207	107	41

Specific impulse can be seen to be directly proportional to the inverse of the square-root of the ion mass[111], see equation 8.1, where I_{sp} is the specific impulse in s, g_0 is the standard acceleration of gravity in ms^{-2} , q is the ion charge in C, m_i is the ions mass in kg and ϕ_a is the ion acceleration voltage in V. This means that the switch from xenon to krypton should increase specific impulse by 25 %, and switching to argon should increase specific impulse by 81 %.

$$I_{sp} = \frac{1}{g_0} \sqrt{2 \frac{q}{m_i} \phi_a} \quad (8.1)$$

The ratio of thrust to power can be seen to be directly proportional to the inverse of the specific impulse and therefore is directly proportional to the square-root of the ion mass[113], see equation 8.2, where T is the thrust in N, P_T is the thruster power in W and η_t is the thruster efficiency. This means that for a fixed thruster power, the switch from xenon to krypton should decrease thrust by 20 %, and switching to argon should decrease thrust by 45 %. Note that this decrease will be larger in reality due to the additional decrease to thruster efficiency, η_t , caused by the increased energy required to ionise a unit mass of the propellant.

$$\frac{T}{P_T} = \frac{2\eta_t}{g_0 I_{sp}} \quad (8.2)$$

The large ECR thruster was run with xenon, krypton and argon propellants at a range of mass flow rates. Direct thrust measurements are taken both without and with the iron ring, see figure 8.38. For each test condition, the minimum mass flow rate that the thruster could run at was found.

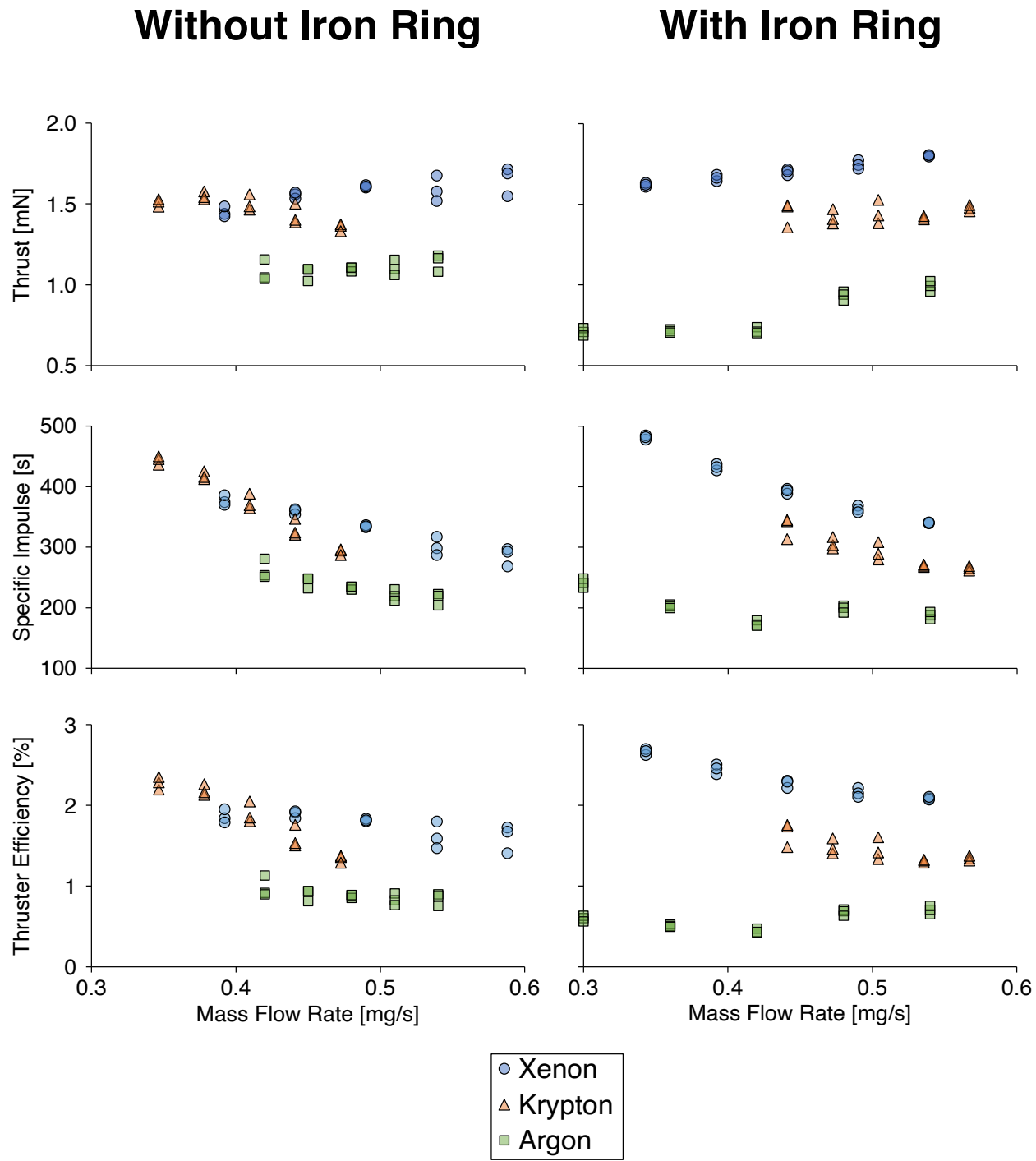


Figure 8.38: Thrust, specific impulse and thruster efficiency as a function of mass flow rate for the large ECR thruster both without and with the iron ring operating with xenon, krypton and argon. 144 W thruster power. Three readings taken for each test condition, standard errors from 0.004 mN to 0.046 mN.

Switching to a lighter propellant was expected to decrease thrust, increase specific impulse and decrease thruster efficiency. Looking first at the thruster without the iron ring, switching to krypton at a mass flow rate of 0.4 mg/s appears to have a negligible effect on thrust, specific impulse or thruster efficiency. This is in disagreement with the relations found from equations 8.1 and 8.2. Furthermore, a plasma is able to be sustained at a lower mass flow rate when krypton is used, allowing for increased thruster performance. Its comparable performance at a significantly lower cost makes krypton a promising propellant option. Switching to argon was expected to significantly increase specific impulse, however specific impulse was instead decreased. This is likely because the cryopanel wasn't cold enough to condense argon, resulting in significantly elevated background pressures, see table 3.2.

A similar study by A.J. Sheppard et al.[76] found that specific impulse decreases when lighter propellants are used, despite an increase in ion velocity. This reduction in specific impulse for lighter propellants was found to be due to a decrease in the mass utilisation efficiency. It was determined that the mass utilisation efficiency is proportional to the ratio of thruster chamber length to the ionisation mean free path. The lighter propellants have a lower mass (and thereby a higher thermal velocity), higher ionisation energy and smaller ionisation cross section, see table 8.2. These all work to increase the ionisation mean free path of the lighter propellants, thereby decreasing mass utilisation efficiency and specific impulse. Increasing the length of the thruster's chamber would better confine the propellant within the thruster, increasing mass utilisation efficiency and thruster performance.

Adding the iron ring produces the expected increase to thruster performance for xenon and decreases the minimum mass flow rate. However, it is seen to significantly increase the minimum mass flow rate for krypton. A significant increase in thruster floating potential is observed for krypton when the iron ring is added, see figure 8.39. The reason for this increase in thruster floating potential not resulting in a corresponding increase to thruster performance is likely due to the lack of confinement of neutral particles to the thrusters chamber. Therefore, lengthening the thruster's chamber is expected to significantly improve the performance of the thruster with krypton, both without and with the iron ring.

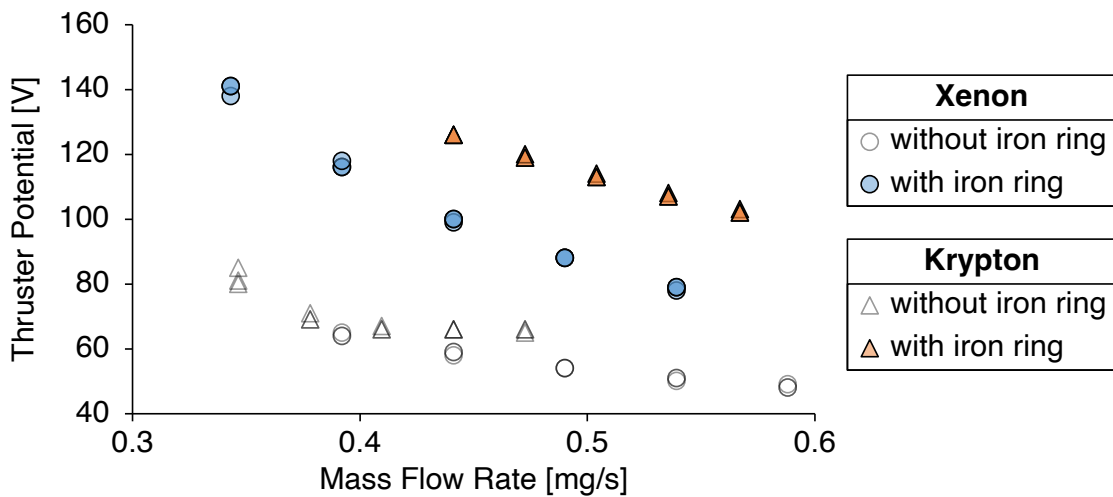


Figure 8.39: Thruster floating potential as a function of mass flow rate for the large ECR thruster both without and with the iron ring for xenon and krypton. 144 W thruster power. Three readings taken for each test condition, standard errors from 0.33 V to 1.00 V.

Ion Beam Measurements

Faraday probe measurements of the ion current density for both xenon and krypton are shown in figure 8.40. The addition of the iron ring can be seen to decrease the far field divergence angle from 55° to 52° for both propellants. This results in the beam divergence efficiency increasing from 33 % to 38 %. For xenon, this increase in divergence efficiency is accompanied by an increase to the peak ion current density, whereas for krypton the peak ion current density remains largely the same. This means that while the axial ion beam current decreases by 4 % for xenon, it decreases by 9 % for krypton.

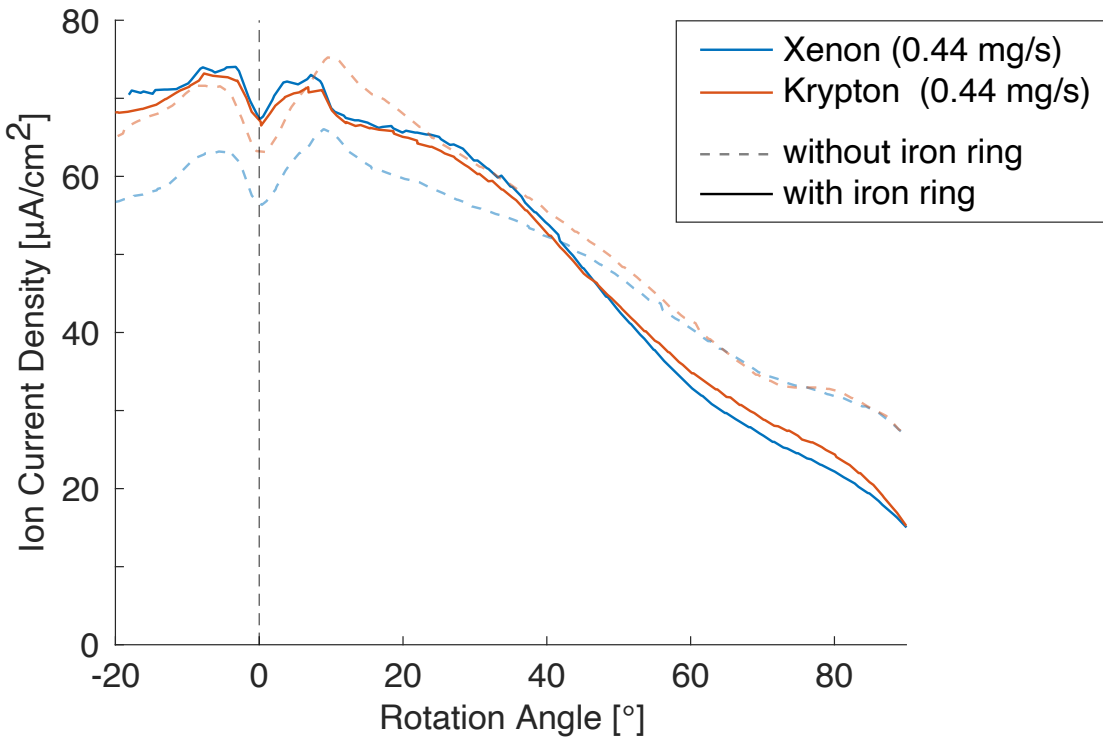


Figure 8.40: Ion current density as a function of rotation angle of the probe for the large ECR thruster both without and with the iron ring using xenon and krypton propellant. 144 W thruster power, 0.44 mg/s propellant mass flow rate.

Numerically integrating the curves of ion current density in figure 8.40 allows for the calculation of the ion beam current. As there are 56 % more krypton particles for a given mass flow rate than xenon particles, the ion beam current for krypton should be significantly higher than that for xenon. However, the ion beam current for krypton is only 5 % higher than that for xenon. This indicates that there is a significant reduction in mass utilisation efficiency when switching to a lighter propellant[76]. Increasing the length of the thrusters chamber would increase the residence time of krypton within the chamber, increasing mass utilisation efficiency and boosting thruster performance. Adding the iron ring is seen to decrease ion beam current by 11 % for xenon and 14 % for krypton.

RPA Measurements

An RPA was used to measure the energy of ions in the large ECR thruster's plume with the iron ring attached. Switching from xenon to krypton propellant, a clear increase in ion energy is observed. The high energy tail appears to end at ~ 200 V for xenon, but is extended to ~ 300 V when krypton is used. This would usually result in an increase to specific impulse, however Faraday probe measurements have indicated that there is also a significant decrease in mass utilisation efficiency when switching to krypton. This then results in a decrease to the specific impulse.

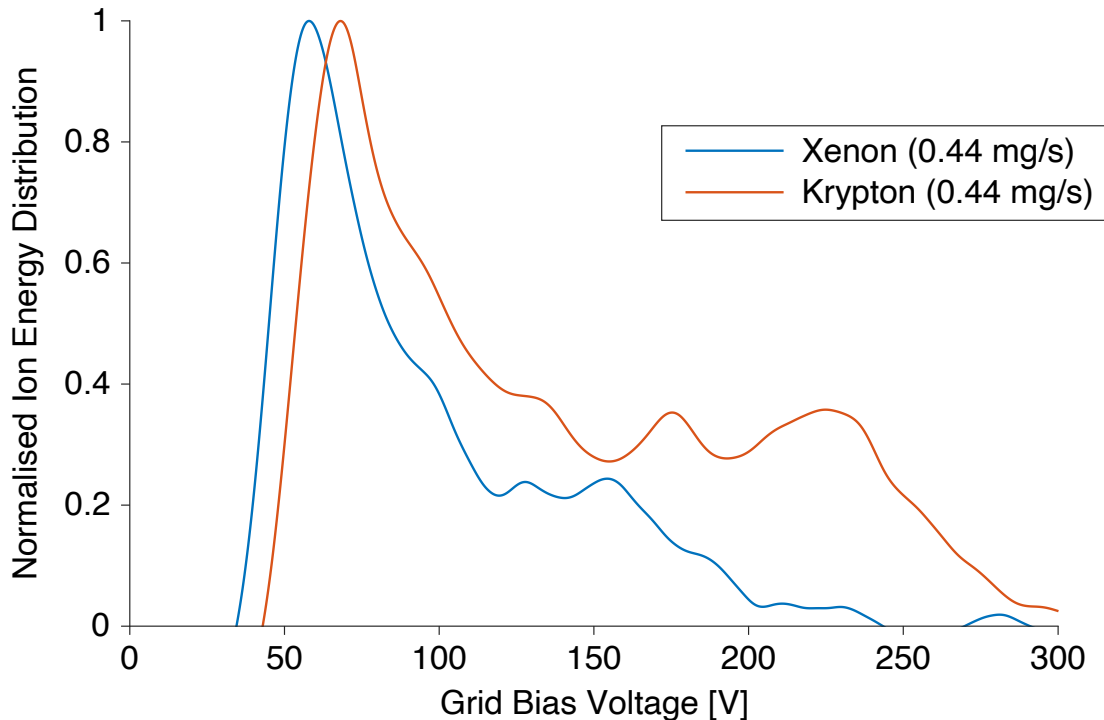


Figure 8.41: Normalised ion energy distribution for the large ECR thruster with the iron ring, using both xenon and krypton propellants. 144 W thruster power, 0.44 mg/s xenon mass flow rate.

Summary of Alternative Propellants

It has been shown that for ECR thrusters, krypton propellant can provide comparable performance to xenon for a fraction of the cost. A significant decrease to the mass utilisation efficiency is seen when switching to lighter propellants due to their longer ionisation mean free path. Therefore, lengthening the thrusters chamber should increase the mass utilisation efficiency for lighter propellants[76]. This could result in krypton outperforming xenon in ECR magnetic nozzle thrusters. A telescopic thruster chamber, like that used by E. Rosati Azevedo et al.[27], would be an ideal test setup to determine the chamber length that produces the highest thruster performance for each propellant.

8.7 Plasma Plume Map

The Langmuir probe is mounted on a rotational and translational stage. This allows for a map of the plasma plume to be created. Measurements were taken at the points shown in figure 8.42. A resonance region displacement from the thruster backplate of 10 mm is used for all tests in section 8.7, both without and with the iron ring.

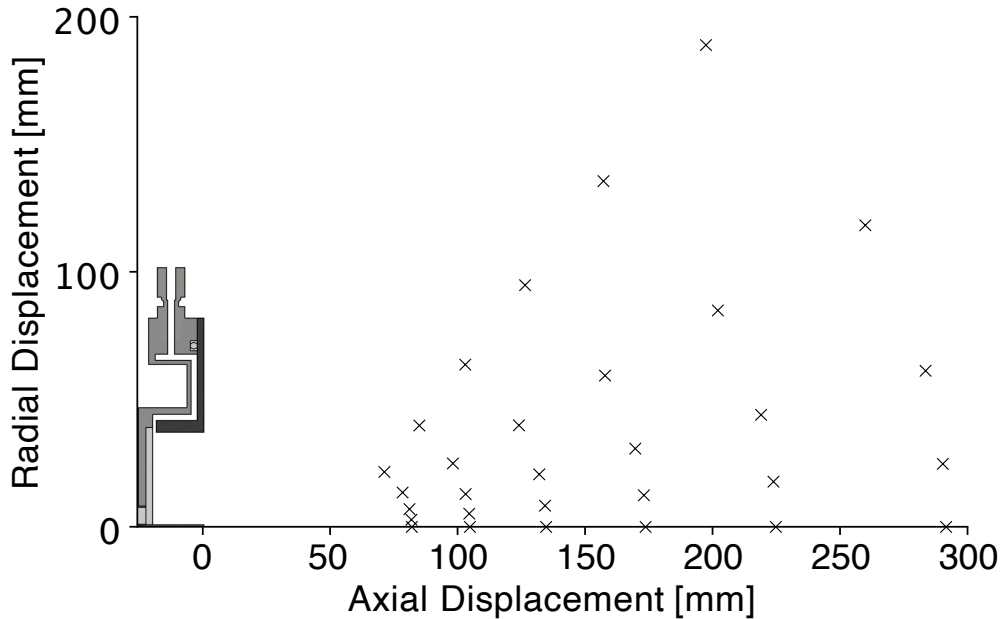


Figure 8.42: Points at which Langmuir probe measurements were taken to create the maps of plasma potential and electric field strength in figures 8.43 and 8.44. Radial displacement relative to the large ECR thruster's central axis, axial displacement relative to the thrust chamber's exit.

Figure 8.43 shows a map of the plasma potential for the large ECR thruster both without and with the iron ring. The gradual decrease in plasma potential as axial displacement is increased agrees with other experimental studies in literature[10][114][60]. By spatially differentiating the plasma potential, the electric field strength can be plotted, see figure 8.44, allowing for the visualisation of the ambipolar electric field that acts to accelerate the ions. Adding the iron ring can be seen to decrease the gradient of the plasma potential in the plume, decreasing the electric field strength. This is unexpected, as the iron ring is seen to increase thruster performance and thruster floating potential, indicating the presence of a stronger ambipolar electric field. It is likely then, that adding the iron ring compresses the ambipolar electric field, moving the higher electric field strengths upstream where the plume was not mapped. Ion acceleration has been found to be greatest at distances less than 50 mm from the thruster[60]. Therefore an accurate map of the ambipolar electric field should include this region of high acceleration near the thruster. This is difficult to achieve with a Langmuir probe, as it was observed to perturb the plasma when moved closer to the thruster. Mapping the plume via non-intrusive techniques would allow for an expanded map of the ambipolar electric field[60].

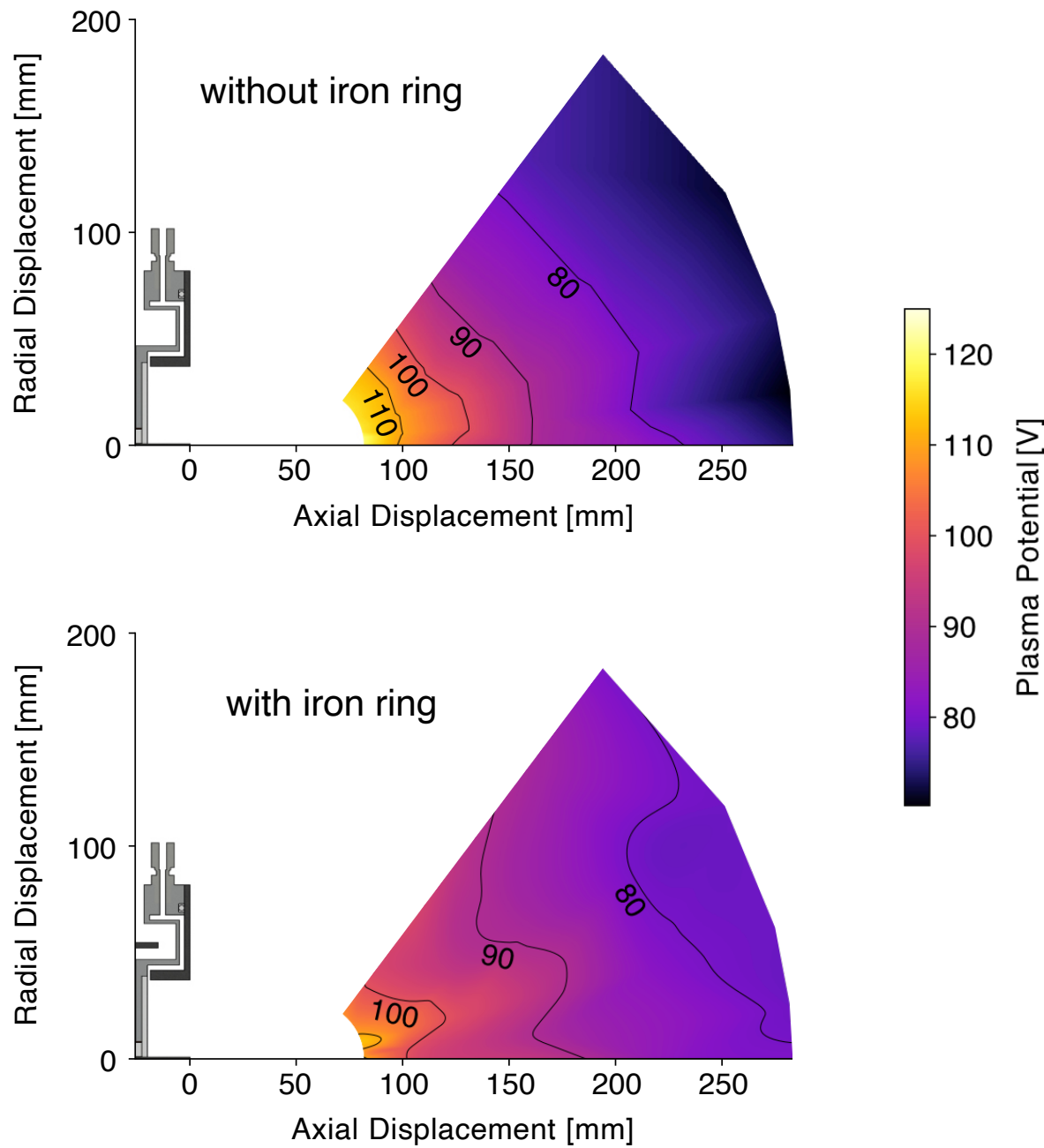


Figure 8.43: Plasma potential map for the large ECR thruster both without and with the iron ring. Radial displacement relative to the thruster's central axis, axial displacement relative to the thrust chambers exit. 90 W thruster power, 0.39 mg/s xenon mass flow rate.

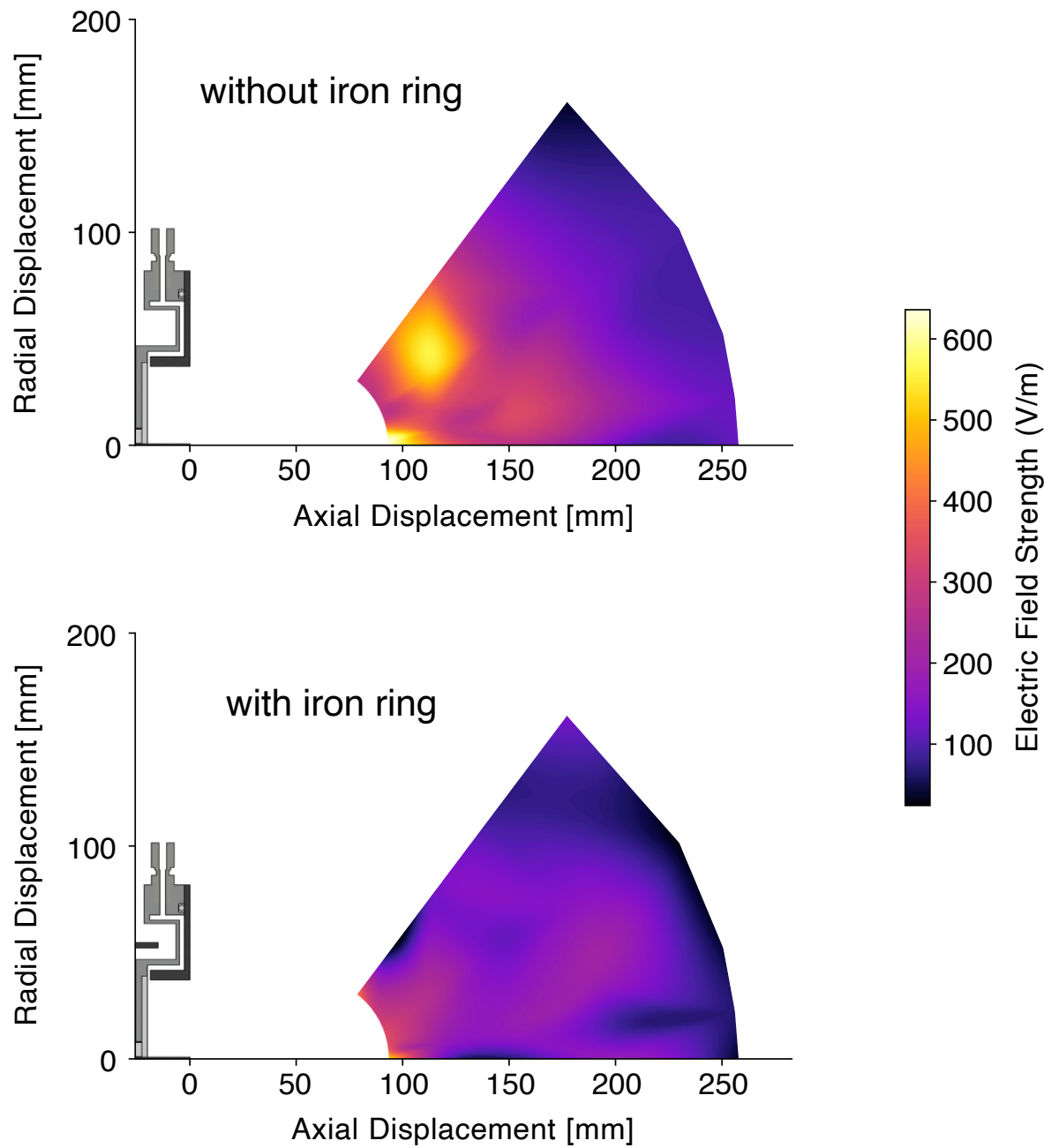


Figure 8.44: Electric field strength map for the large ECR thruster both without and with the iron ring. Radial displacement relative to the thruster's central axis, axial displacement relative to the thrust chambers exit. 90 W thruster power, 0.39 mg/s xenon mass flow rate.

8.8 Conclusion

It has been found experimentally that ECR magnetic nozzle thruster performance is increased when a ferromagnetic ring is added downstream of the thruster's magnet. This ferromagnetic ring acts to reduce the magnetic field strength gradient at resonance, increasing the thickness of the resonance region as well as the amount of energy that electrons absorb while passing through. Langmuir probe measurements have shown that this can result in an increase to the number of high energy electrons in the plume. This is seen to increase the thruster's floating potential, which could translate into increased ion acceleration. While this is thought to produce an increase to the energy of the ions, measurements of ion energy were unable to be compared due to the limitations of the RPA. However, an increase to the beam divergence efficiency was measured with a Faraday probe. This results in an increase in thrust and specific impulse of 15 %, while thrust efficiency increases by 32 %.

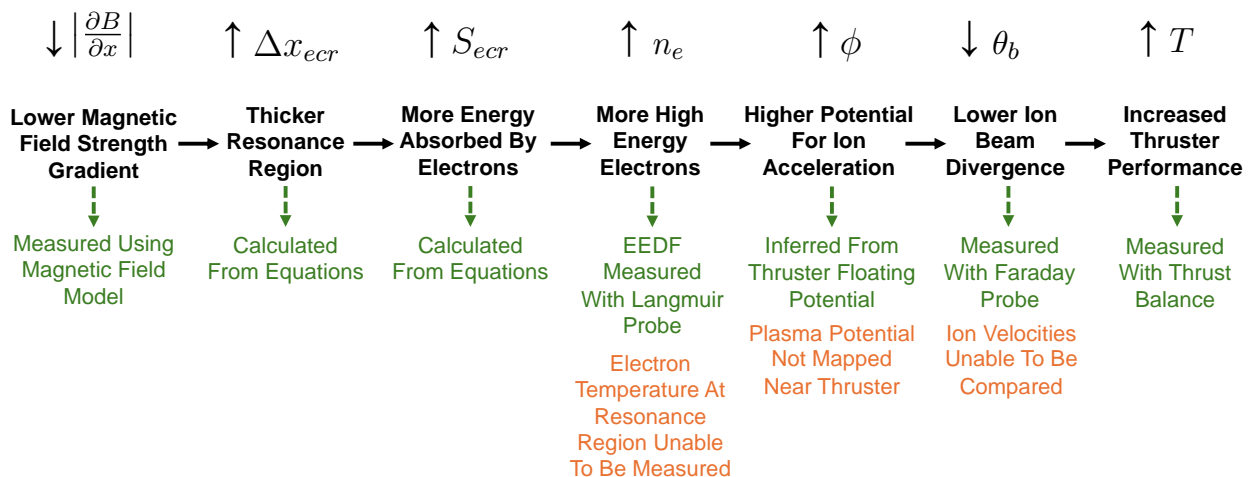


Figure 8.45: Flowchart showing the theorised sequence of events and the variables that are increased/decreased as a result. The method with which each variable was measured is shown in green. It is thought that decreasing the magnetic field strength gradient at resonance also results in increased electron temperatures in the resonance region and higher ion energies, however these were unable to be measured with the current experimental setup.

Achieving this reduction in the magnetic field strength gradient at resonance passively, by using a ferromagnetic ring, allows for higher thruster efficiencies than doing it actively with an electromagnet. In summary, decreasing the magnetic field strength gradient at resonance has been proven to significantly increase thruster performance.

9 EFFECTS OF ADDING A SECOND MICROWAVE FREQUENCY

ECR magnetic nozzle thrusters typically use microwave power at a single frequency to efficiently transfer energy into a plasma via ECR heating. The use of microwave power evenly split between two signals of different frequency has already been investigated by B. Wachs[61] and was found to not significantly improve thruster performance. However, the frequency difference between the two signals was never less than 50 MHz.

The study in this section also uses dual microwave signals with the aim of determining their effect on thruster performance. The frequency difference between the two signals has been found to have a significant effect on both thrust and thruster floating potential. Notably, this dependence is strongest at frequency differences less than 100 kHz. At thruster powers of 64 W and above, the use of dual microwave signals is found to increase thrust by up to 13 %. Thrust is found to peak when the frequency difference between the two signals is between 30 kHz and 60 kHz. This suggests that the performance increase may be the result of an interaction between the intermodulation-generated signal and the azimuthal magnetosonic wave.

This section on adding a second microwave frequency is split into four parts:

9.1	Microwave Generator Design	176
9.2	Frequency Difference Effects	179
9.3	Discussion	182
9.4	Conclusion	184

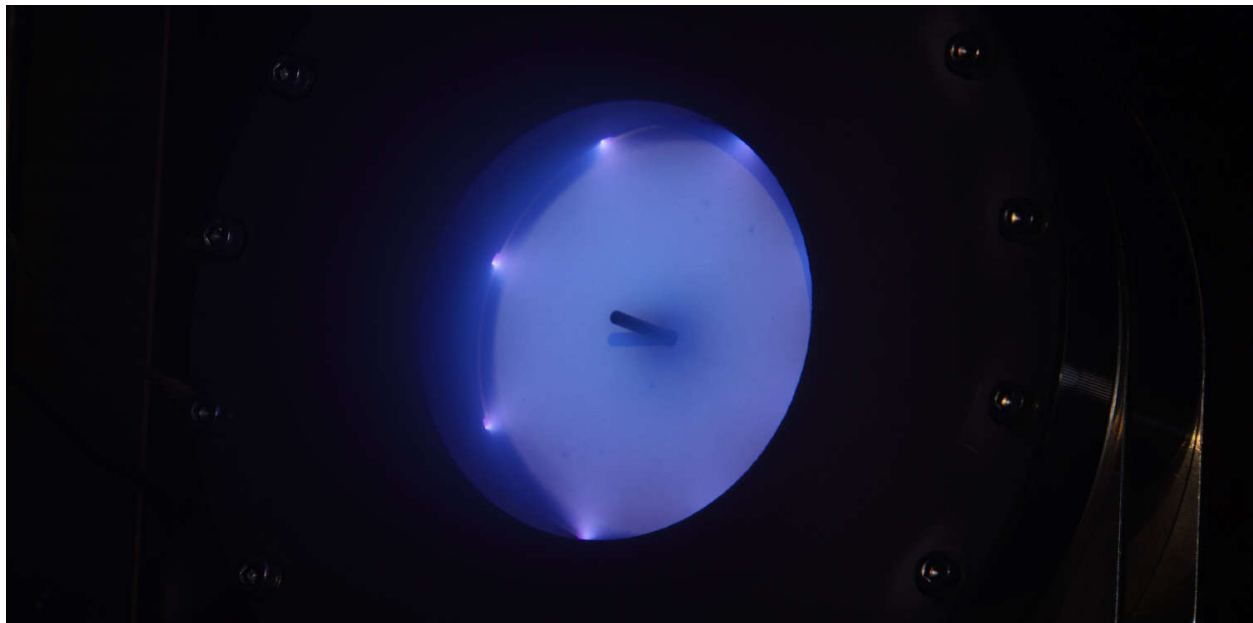


Figure 9.1: Photo of the large ECR thruster operating at 129 W thruster power and 0.39 mg/s xenon mass flow rate. There was no visual difference observed when switching between using single and dual microwave frequencies.

9.1 Microwave Generator Design

Work in this section was done in collaboration with S. Lane. S. Lane is responsible for the development of the generator and its code.

This section describes the design of a Software Defined Radio (SDR) driven microwave generator that is used to power the large ECR thruster. This new microwave generator was designed to study the effects of spectral broadening on the thruster performance. By increasing the bandwidth of the microwave signal, the power spectral density is decreased, as power is spread over a larger range of frequencies. The aim of the study was to find the power spectral density at which thruster performance was greatest. However, limitations of the ADALAM-PLUTO SDR prevented the use of large bandwidth signals, so the study pivoted to investigating dual frequencies. The aim of this was to generate dual resonance regions or a thicker resonance region that could increase thruster performance.

A microwave signal is generated using an ADALAM-PLUTO SDR. This signal either has all power concentrated at one frequency, or power is evenly split between two frequencies. The signal is then fed into a pre-amplifier before being fed into a ZHL-2425-250X+ amplifier, see figure 9.2. This allows for the amplification of frequencies between 2.4 GHz and 2.5 GHz at powers up to 300 W. The amplifier also measures forward and reverse powers that are read using an Arduino. The values of these forward and reverse powers are calibrated using an Anritsu MA24105A power meter. The microwave generator is connected to the large ECR thruster, as shown in figure 9.3.

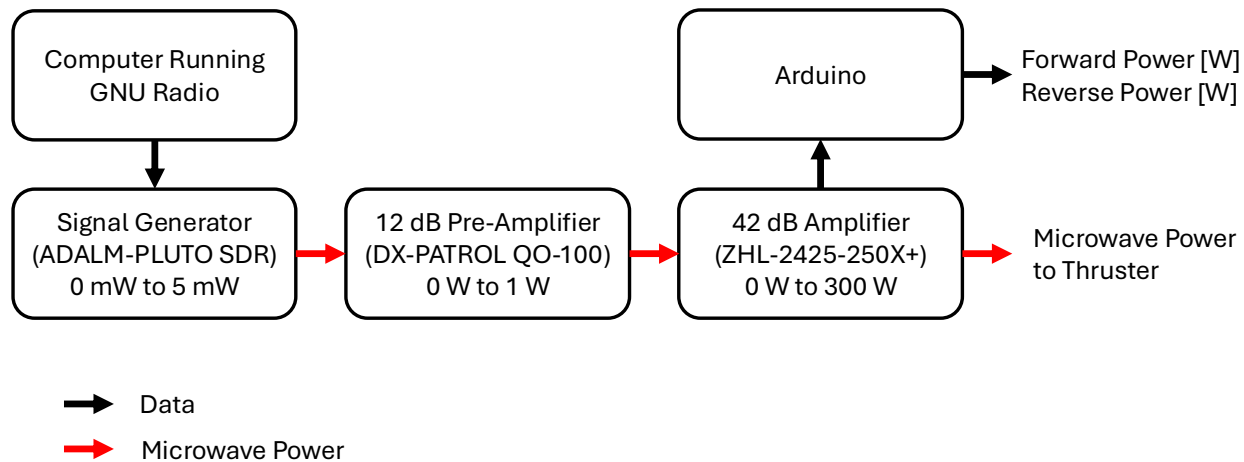


Figure 9.2: Diagram showing the individual components of the new SDR driven microwave generator in black boxes.

The generation of the microwave signal using an ADALAM-PLUTO SDR allows for a high degree of flexibility. Although not shown here, more than two microwave frequencies were able to be generated that could sustain a plasma in the thruster. This microwave generator could also allow for the spectral broadening of the microwave signal. This would show if for a constant power, ECR heating is more efficient for broader signals (with low power spectral density) or narrower signals (with higher power spectral density).

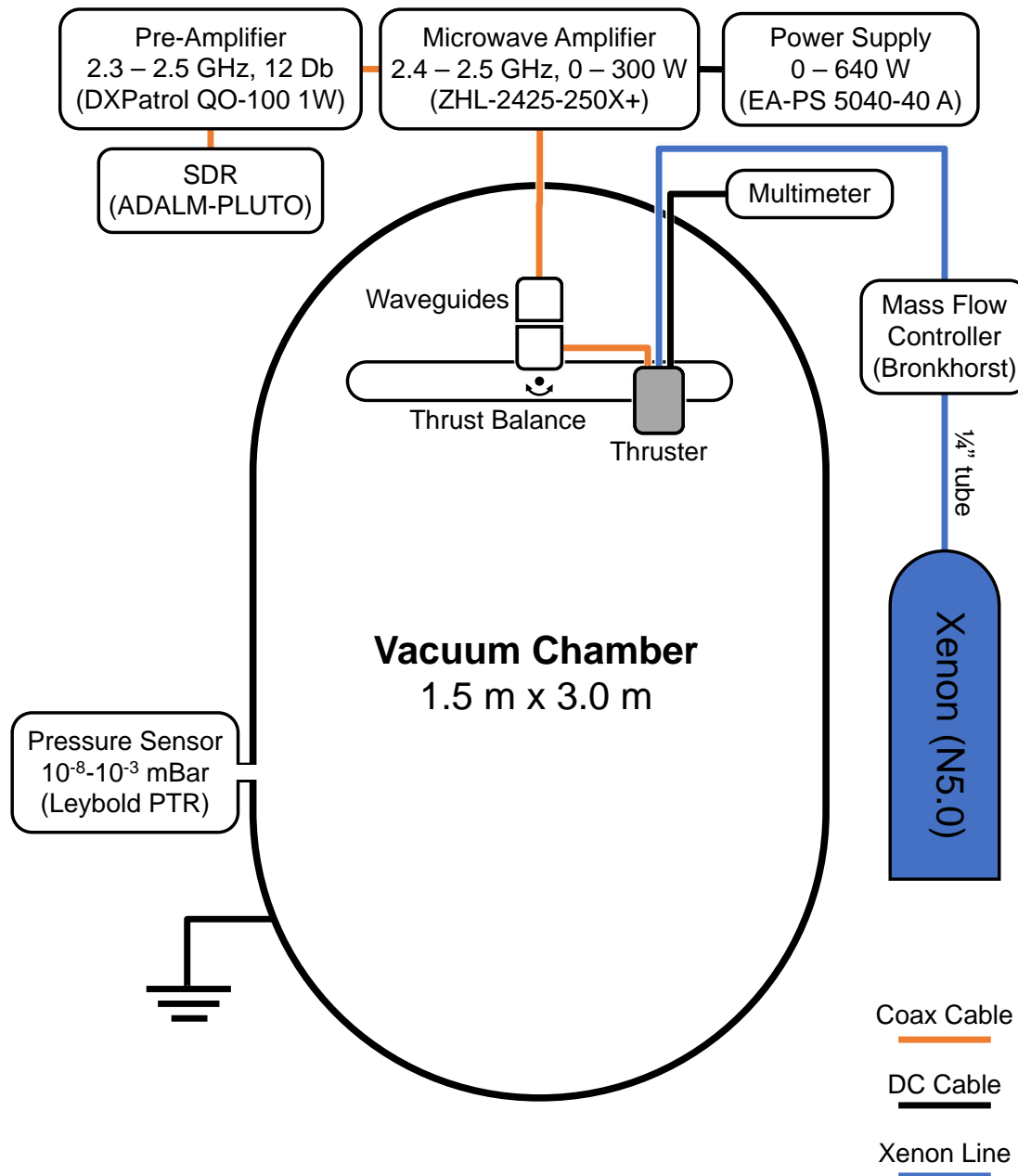


Figure 9.3: Diagram of the experimental setup for the tests in chapter 9.

Microwave Generator Validation

It is necessary to ensure that this new microwave generator performs similarly to the older microwave generator that was used in chapters 4 to 8. To evaluate this, thrust is plotted as a function of thruster power in figure 9.4. An offset can be seen between the two generators, which is likely due to inaccuracies in the measurement of forward and reverse power. This is thought to have a negligible effect on the results presented in the following sections.

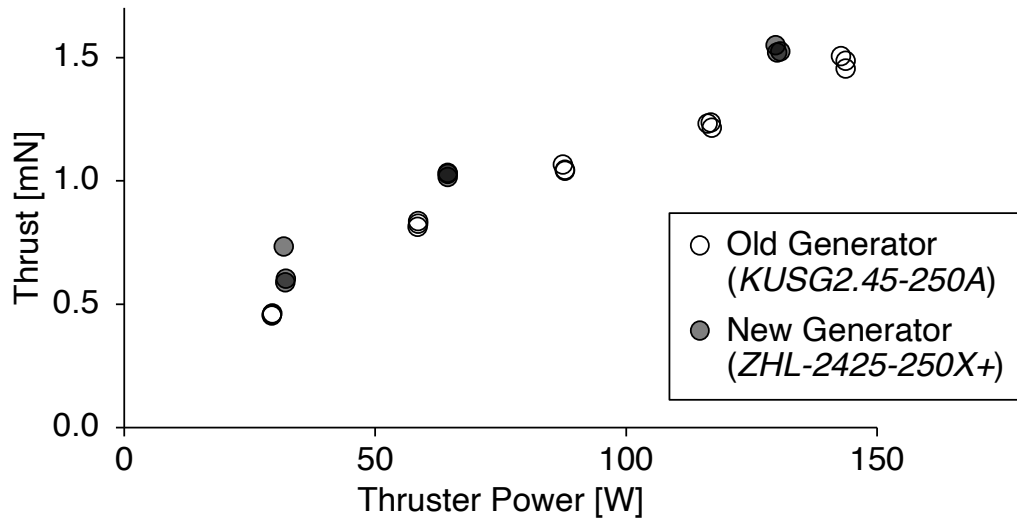


Figure 9.4: Thrust as a function of thruster power for the large ECR thruster without the iron ring. Comparing the older generator against the newer generator. 0.39 mg/s xenon mass flow rate. Three readings taken for each test condition, standard errors from 0.002 mN to 0.046 mN.

A more important check for the purpose of this study is whether thruster power remains constant as the frequency difference between the two signals is changed. This is evaluated at three different power levels in figure 9.5. The three power levels have average thruster powers of 32 W, 64 W and 129 W. Thruster power can be seen to vary by 2.5 W, 2.4 W and 2.0 W respectively as the frequency difference of the two signals is swept. These power deviations are thought to have a negligible effect on the results presented in the following sections.

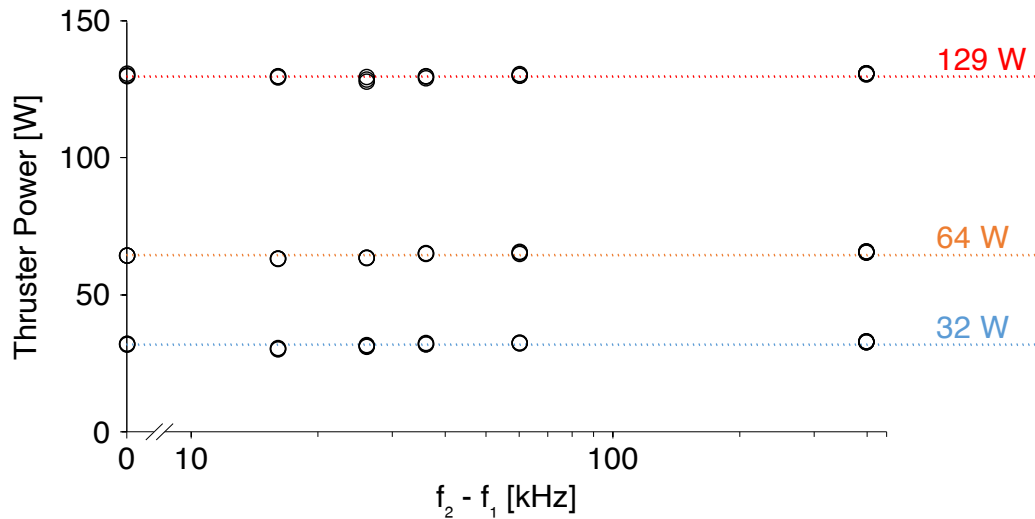


Figure 9.5: Thruster power as a function of the frequency difference of the two microwave signals at three power levels. Large ECR thruster, 0.39 mg/s xenon mass flow rate, $f_1 = 2.435$ GHz. Three readings taken for each test condition, standard errors from 0.07 W to 0.48 W.

9.2 Frequency Difference Effects

Thruster Floating Potential Measurements

Studies in literature have shown that adding a second microwave frequency can reduce the plasma instabilities of an ECR generated plasma in a magnetic mirror trap[115]. The addition of a second microwave frequency in an ECR thruster has also been investigated, but has shown no improvement to thruster performance[61]. In both of these studies, the frequency difference between the two microwave signals was never less than 50 MHz. The aim of this chapter is therefore to determine if adding a second microwave frequency can improve thruster performance if the frequency difference of the two signals lies below 50 MHz.

While direct thrust measurements are the most reliable measurement of thruster performance, the floating potential was recorded first as it requires far less time to measure. The large ECR thruster without the iron ring was used, with microwave power equally split between the two signals. The first signal has a frequency, f_1 , equal to 2.435 GHz. The second signal has a variable frequency, f_2 , that is between 14 kHz and 440 kHz higher than f_1 . Limitations of the ADALAM-PLUTO SDR prevented frequency differences between f_1 and f_2 lower than 14 kHz. Figure 9.6 shows how the thruster floating potential varies as the difference between f_1 and f_2 increases. The floating potential of the thruster when all power is delivered through f_1 is shown on the left of figure 9.6.

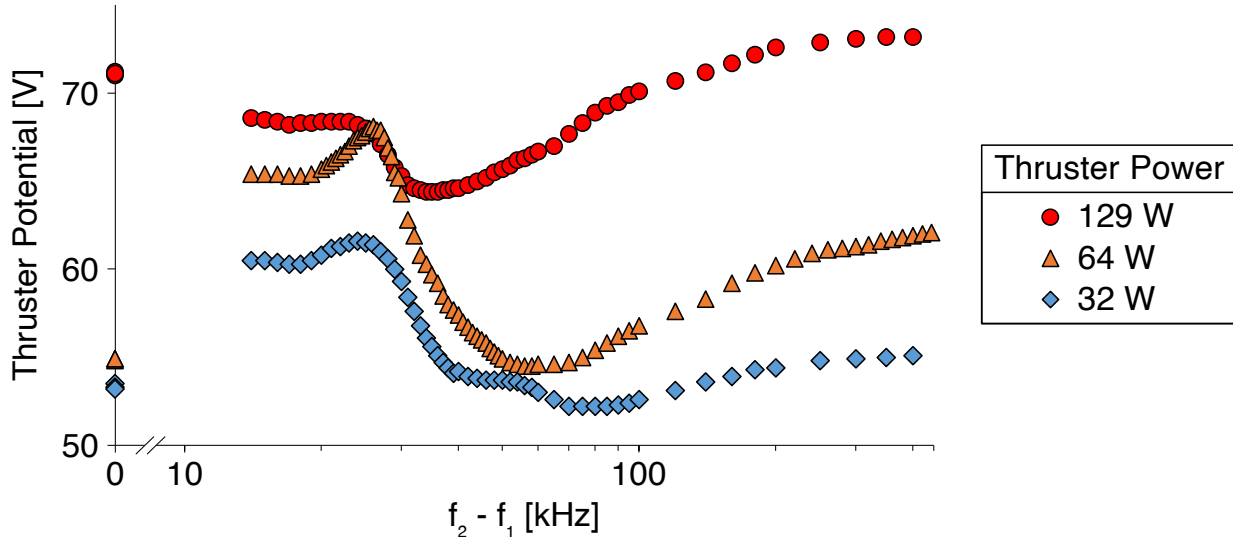


Figure 9.6: Thruster floating potential as a function of the frequency difference of the two microwave signals at three different thruster powers. Large ECR thruster without the iron ring, 0.39 mg/s xenon mass flow rate, $f_1 = 2.435$ GHz.

The thruster floating potential is seen to vary significantly as the frequency difference of the two signals is increased. This change to the thruster floating potential could affect ion acceleration and thus alter the thruster's performance. To verify that these trends are due to the difference in the frequency of the two signals, and not their individual values, the same measurements were taken with f_1 equal to 2.450 GHz. The same thruster floating potentials were measured as when f_1 was equal to 2.435 GHz. This confirms that the thruster floating

potential profiles seen in figure 9.6 are caused by the frequency difference between f_1 and f_2 , not their individual values. Testing at more values of f_1 would help to validate this.

Thrust Measurements

To determine the relationship between the frequency difference of the two microwave signals and the thruster performance, direct thrust measurements were taken. Figure 9.7 shows the relationship between thrust and the frequency difference of the microwave signals for a thruster power of 64 W. The thrust that is measured when all power is delivered at f_1 is shown on the left of figure 9.7. The use of dual microwave frequencies can be seen to result in a thrust increase when $f_2 - f_1$ is greater than 36 kHz. The thrust is seen to peak when $f_2 - f_1 = 60$ kHz, resulting in a 13 % thrust increase over the single frequency case.

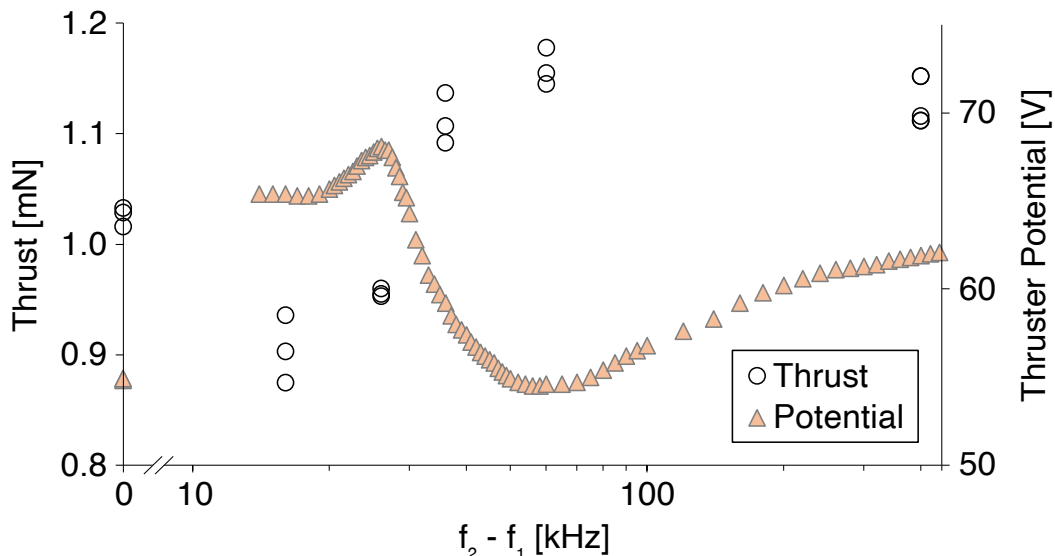


Figure 9.7: Thrust and thruster floating potential as a function of the frequency difference of the two microwave signals for the large ECR thruster without the iron ring. 64 W thruster power, 0.39 mg/s xenon mass flow rate, $f_1 = 2.435$ GHz. Three thrust readings taken at each frequency difference, standard errors from 0.002 mN to 0.018 mN.

The same measurements were taken for thruster powers of 129 W and 32 W, these are plotted in figure 9.8. At 129 W thruster power, the use of dual microwave frequencies can be seen to increase thrust when $f_2 - f_1$ is less than 60 kHz. A maximum thrust increase of 11 % is measured when $f_2 - f_1$ is between 20 kHz and 40 kHz. At 32 W thruster power, no statistically significant increase in thrust is observed. Noticeably, for thruster powers of 129 W and 64 W, the maximum thrust appears to occur at the frequency difference at which the thruster's floating potential is the lowest.

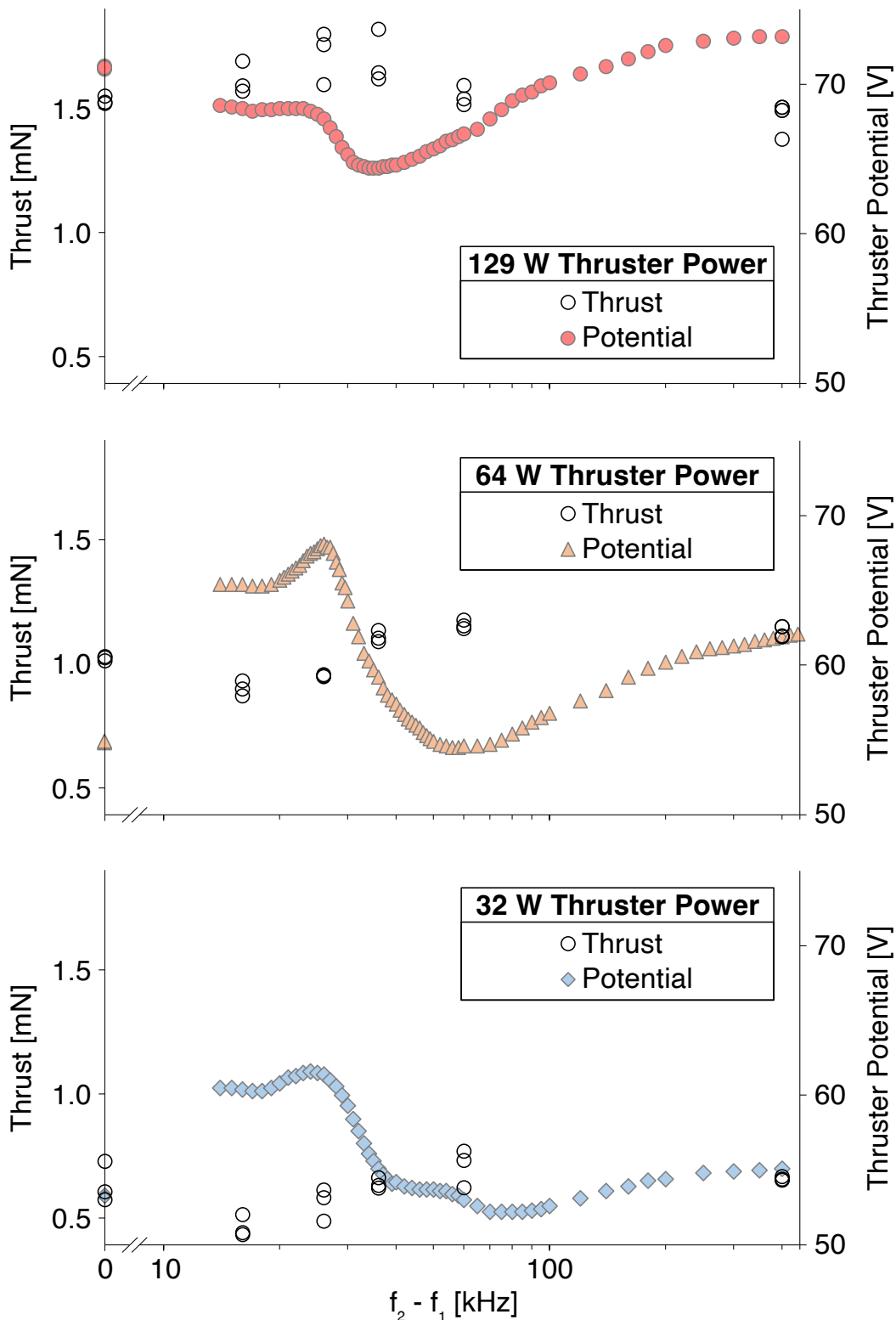


Figure 9.8: Thrust and thruster floating potential as a function of the frequency difference of the two microwave signals for the large ECR thruster without the iron ring at thruster powers of 129 W, 64 W and 32 W. 0.39 mg/s xenon mass flow rate, $f_1 = 2.435$ GHz. Three thrust readings taken for each test condition, standard errors from 0.002 mN to 0.061 mN.

9.3 Discussion

From figure 9.8, the thrust is found to peak when the frequency difference between the two signals is between 30 kHz and 60 kHz. To identify why this frequency difference leads to an increase in thrust, oscillations within the plasma are investigated.

Plasma Oscillations

A study of ECR thruster plasma oscillations by D. Maddaloni et al.[116] found two low frequency oscillations. The frequency of these oscillations was seen to be dependent on both the mass flow rate and power of the ECR thruster, see figure 9.9. The first oscillation can be seen to occur between 5 kHz and 12 kHz, with the second oscillation occurring between 25 kHz and 70 kHz.

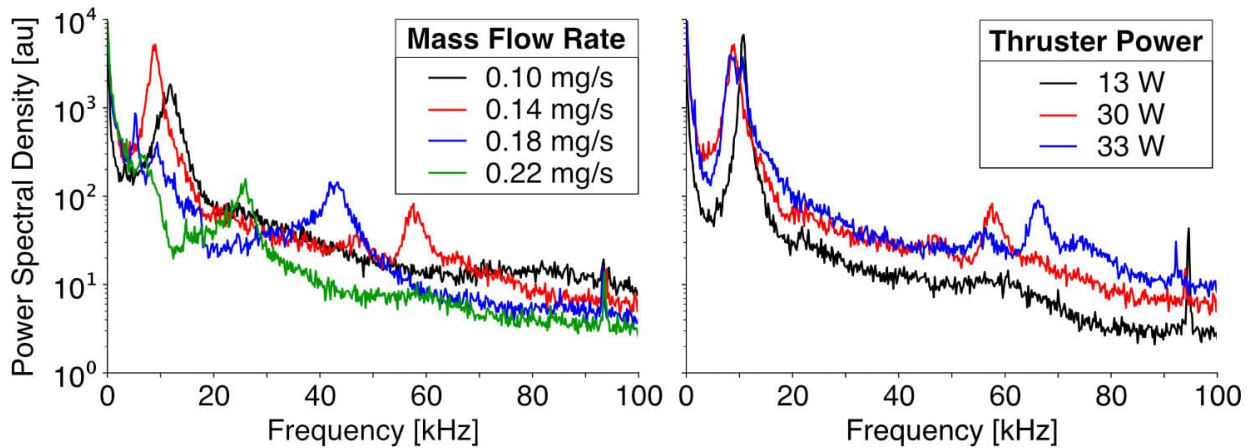


Figure 9.9: Power spectral density plot of the floating potential of a Langmuir probe in the plume of the smaller ONERA ECR thruster. Varying xenon mass flow rate at 30 W thruster power (left). Varying thruster power at 0.14 mg/s xenon mass flow rate (right). Arbitrary units used for the y-axis. Reproduced from D. Maddaloni et al.[116].

(i) Breathing Mode Oscillation (5 kHz - 12 kHz)

Neutral propellant is injected into the thruster's chamber and ionised, increasing ion and electron density, these charged particles are then accelerated out of the thruster, reducing ion and electron density. This oscillation in plasma density is known as the breathing mode and typically occurs between 1 kHz and 50 kHz[116]. As the oscillation that occurs between 5 kHz and 12 kHz in figure 9.9 was found to be due to oscillations in electron density within the thrusters chamber, this would suggest that it is the result of a breathing mode oscillation.[116][117]

(ii) Azimuthal Magnetosonic Wave (25 kHz - 70 kHz)

As the ions are unmagnetised, they do not follow magnetic field lines. Therefore, when the magnetic field lines diverge, the ions do not follow, resulting in an inward cross-field ion current towards the central axis. This creates a radial electric field that acts to attract the electrons inward towards the central axis. This radial electric field

propagates in the azimuthal direction and is known as an azimuthal magnetosonic wave. Azimuthal magnetosonic waves typically have a frequency in the range of 40 kHz to 50 kHz[118], they are therefore thought to be responsible for the oscillation observed in figure 9.9 that occurs between 25 kHz and 70 kHz[116].

Intermodulation-Generated Signal

The thrust in figure 9.8 is found to peak when the frequency difference between the two microwave signals is between 30 kHz and 60 kHz. As the dual microwave signals are two sine waves in a nonlinear system, they undergo intermodulation, generating a signal with a frequency equal to the frequency difference of the two microwave signals, see figure 9.10. The thrust is therefore found to peak when the intermodulation-generated signal has a frequency between 30 kHz and 60 kHz.

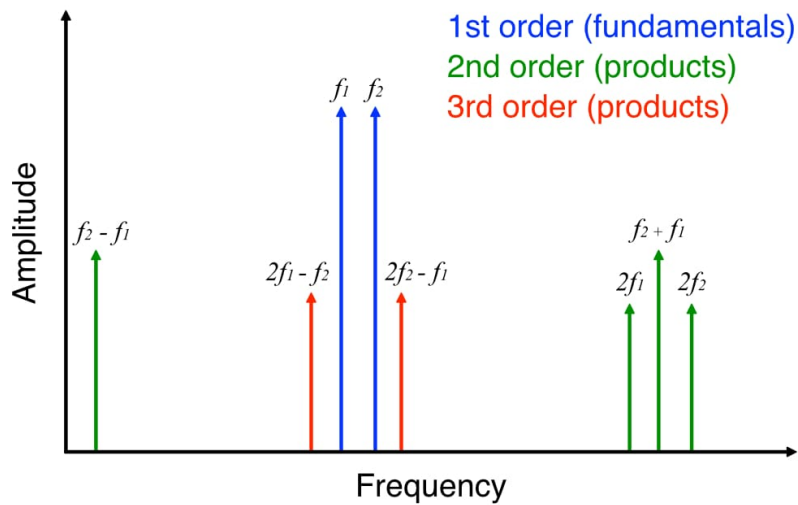


Figure 9.10: The harmonics and intermodulation products of the two microwave signals. Reproduced from [119].

The frequency of an ECR thruster's magnetosonic wave was found to lie between 25 kHz and 70 kHz[116]. As thrust is seen to peak when the frequency of the intermodulation-generated signal lies within this range, it is possible that this increase to thruster performance is due to the interaction of the intermodulation-generated signal with the magnetosonic wave. A resonant interaction could act to efficiently transfer energy from the intermodulation-generated signal into the magnetosonic wave. As the magnetosonic wave has been found to drive inward electron flux towards the central axis[118], increasing its energy could increase inward electron flux, reducing beam divergence and increasing the thruster performance. Faraday probe measurements of beam divergence could be used to verify this. As the magnetosonic wave comprises a radial electric field, increasing its energy could indirectly affect the ambipolar electric field. This would explain why the thruster floating potential is seen to have a minimum at the same frequency difference as performance is seen to peak, see figure 9.8. This interaction between the intermodulation-generated signal and the magnetosonic wave is the current theory as to how dual microwave frequencies increase the thruster performance. However, further work is required to verify this theory.

9.4 Conclusion

The large ECR thruster has been run in two modes, one with all microwave power at a single frequency, and a second with microwave power evenly split between two frequencies. It is found that for thruster powers above 64 W, using dual frequencies can result in an increase to thrust of up to 13 %. This effect is determined to be due to the frequency difference of the two signals, irrespective of their individual frequencies. The thrust is found to peak when the frequency difference of the two signals is between 30 kHz and 60 kHz. This low frequency difference explains why these results were not seen in previous studies, as frequency differences below 50 MHz have never before been tested with an ECR magnetic nozzle thruster[61].

Although the mechanism behind this thrust increase is unknown, a theory is proposed. The two microwave signals create an intermodulation-generated signal with a frequency equal to their frequency difference. The peak in thrust appears to occur when the frequency of this intermodulation-generated signal is the same as the frequency at which the magnetosonic wave is thought to propagate. This could result in a resonant transfer of energy into the magnetosonic wave, increasing the inward electron flux towards the central axis. This would increase the divergence efficiency and improve the thruster performance.

10 CONCLUSIONS

ECR magnetic nozzle thrusters are a promising technology due to their electrodeless nature allowing for reduced erosion rates and therefore long lifetimes. Their simple design makes them relatively low cost, however their generally low performance prevents them from becoming commercially viable. This thesis has developed two different novel techniques that have been found to enhance the performance of ECR magnetic nozzle thrusters, these are summarised in the following sections:

10.1	Decreasing Magnetic Field Strength Gradient at Resonance	186
10.2	Dual Microwave Frequencies	188

The effect of resonance region location and adding a magnetic mirror trap were also investigated and are summarised in the following sections:

10.3	Resonance Region Location	189
10.4	Magnetic Mirror Trap	190

Future work is then outlined in the final section:

10.5	Future Work: Other Ideas	191
-------------	------------------------------------	-----

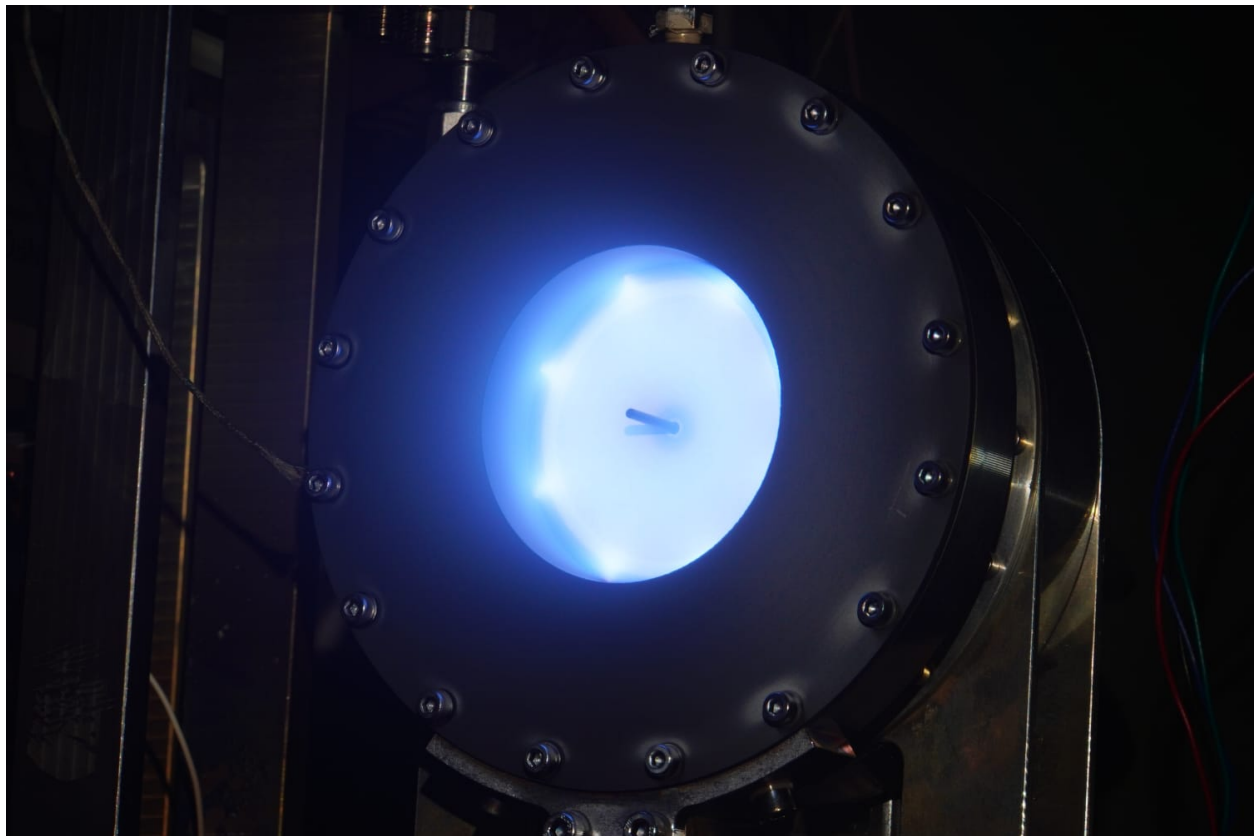


Figure 10.1: Photo of the large ECR thruster operating at 145 W thruster power and 0.39 mg/s xenon mass flow rate.

10.1 Decreasing Magnetic Field Strength Gradient at Resonance

The effect of the gradient of the magnetic field at resonance was the primary focus of this thesis and was investigated experimentally using two different ECR thrusters. An analytical review of ECR heating in section 2.2 found that a lower magnetic field strength gradient at resonance results in a thicker resonance region and more energy transferred to the electrons passing through. This should then result in an increase to thruster performance.

The first test campaign used a small ECR thruster, this had an electromagnetic coil at the thruster's exit that could change the magnetic field strength gradient at resonance. An axisymmetric magnetic field model was used to determine the thickness of the resonance region, which was found to be highly correlated with measurements of thrust and ion beam current. As thrust and ion beam current peak at the same coil current as resonance region thickness, it is highly unlikely that the increase in performance was caused by something other than the magnetic field strength gradient at resonance. It was found that minimising the magnetic field strength gradient at resonance increased thrust and specific impulse by 60 %, with thruster efficiency presenting a relative percentage increase of 16 %. This increase to thruster efficiency would have been 174 % if not for the power used by the electromagnet. This drove the design of a new large ECR thruster, that could decrease its magnetic field strength gradient at resonance passively.

The second test campaign used the new large ECR thruster. An iron ring could be added to the thruster to decrease the magnetic field strength gradient at resonance. Adding the iron ring was found to increase thrust and specific impulse by 15 %, while thrust efficiency increased by 32 %. This showed that decreasing the magnetic field strength gradient at resonance passively, using an iron ring, allows for a higher increase to thruster efficiency than by doing it actively with an electromagnet.

The current theory as to the sequence of events which leads to this increase in thruster performance is shown in figure 10.2. While measurements of electron temperature and density appear to verify this, electron temperature at the resonance region needs to be measured to conclude that a decrease in magnetic field strength gradient at resonance results in hotter electrons. While the ambipolar electric field was mapped, it needs to be mapped much closer to the thruster to conclude that the hotter electrons result in a stronger net ambipolar electric field. Lastly, ion velocities need to be mapped to verify that the stronger ambipolar electric field results in higher net ion velocities. To summarise, while it has been determined that reducing the magnetic field strength gradient at resonance results in increased thruster performance, the full sequence of events need to be experimentally measured to fully characterise this relationship.

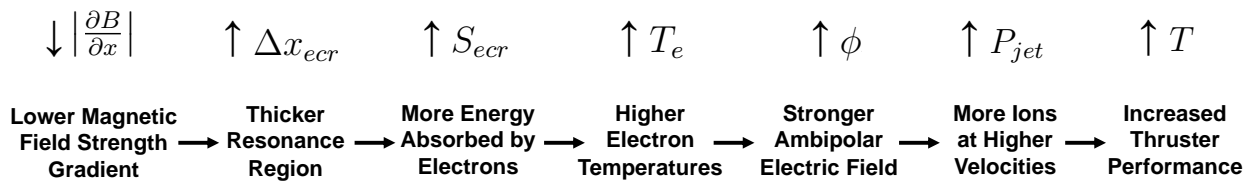


Figure 10.2: Flowchart showing the theorised sequence of events that relates a decrease in magnetic field strength gradient at resonance to an increase in thruster performance.

Further Work - *Decreasing Magnetic Field Strength Gradient at Resonance*

Results suggest that the performance of the large ECR thruster could be significantly improved if lower propellant mass flow rates were able to be used without the plasma extinguishing. This could be achieved by increasing the neutral propellant density within the chamber. Future work should then modify the geometry of the large ECR thruster with the aim of increasing the neutral propellant density. This could be achieved by adding an extension or nozzle to the thruster's exit, similar to that done by S. Peterschmitt[36]. Further work should also aim to better define the resonance region's thickness across the radius of the thruster. This would increase the accuracy of the magnetic model.

As electron temperature has been shown to have a significant effect on thruster performance, efforts should be concentrated on improving its measurement. Measurements of electron temperature in the resonance region, before the electrons have had the chance to cool down[120], would be more representative of the thruster's operation. Similarly, mapping the ambipolar electric field closer to the thruster, where ion acceleration has been found to be greatest[60], would allow for a better understanding of the ambipolar electric field. These measurements were attempted using a static Langmuir probe, but the electrode melted and it was also observed to perturb the plasma. Therefore, nonintrusive measurement techniques such as laser-induced fluorescence could be used to measure ion acceleration and thereby map the electric field near the thruster[60][121].

More accurate measurements of ion velocity are required to determine the mechanism by which decreasing the magnetic field strength gradient at resonance improves thruster performance. Redesigning the RPA to enable it to map the plume at different rotation angles would significantly help this understanding. A Wein filter was initially used in an attempt to measure the velocity and charge of the ions. However, when placed downstream of the thruster, the thruster performance dropped significantly. This is thought to be due to the Wein filters large ferrous plates that warp the magnetic nozzle. This could funnel the electrons towards its grounded chassis, acting like an electron sink that significantly reduces the strength of the ambipolar electric field.

Sputter erosion of the thruster's chamber walls was observed, see appendix C, and the antenna's diameter was also observed to decrease from 2.5 mm to 2.3 mm over the duration of the test campaign, see appendix D. Antenna erosion is thought to be the limiting factor for ECR thruster lifetime and so the effect of thickening the resonance region on antenna erosion should be the subject of further studies. A study by S. Peterschmitt[36] has determined the lifetime of their small ECR thruster to be over 1000 hours.

The minimum magnetic field strength gradient at resonance that was achieved in this thesis was 0.69 T/m. Lower magnetic field strength gradients should be investigated to find the magnetic field strength gradient and corresponding resonance region thickness that allows for the highest thruster performance.

10.2 Dual Microwave Frequencies

A new microwave generator was developed that uses a Software Defined Radio (SDR) to generate microwave signals that are subsequently amplified before being fed into the thruster. This allowed for the microwave power to be evenly split between two microwave frequencies. It was found that there was a high dependancy of the floating potential of the thruster on the frequency difference of the two signals when their frequency difference was below 100 kHz. This was found to be dependent on the frequency difference of the two signals and not their individual frequencies. Direct thrust measurements had a similar dependancy, and it was found that for the same thruster power the use of dual microwave frequencies can increase thrust by up to 13 %.

The dual microwave signals create an intermodulation-generated signal with a frequency equal to the frequency difference of the dual microwave signals. Thrust is seen to peak when the frequency of the intermodulation-generated signal is between 30 kHz and 60 kHz. Similarly, thruster floating potential is found to have a minimum when the frequency of the intermodulation-generated signal is between 30 kHz and 70 kHz. The magnetosonic wave of an ECR thruster is thought to propagate at a frequency of between 25 kHz and 70 kHz[116]. It is therefore theorised that the intermodulation-generated signal could be resonantly transferring energy into the magnetosonic wave, resulting in the observed performance increase. Further work is required to verify this theory and determine its effects on wider thruster operation.

Further Work - *Dual Microwave Frequencies*

It is of primary importance that this performance increase is replicated using a different microwave generator. This would help verify that the effects seen here are not due to how the amplifiers or SDR behave when dual frequencies are generated at low frequency differences.

The working theory behind the increase in thrust is resonant energy transfer between the intermodulation-generated signal and the azimuthal magnetosonic wave. The frequency of both the intermodulation-generated signal and the azimuthal magnetosonic wave should be measured to verify that they overlap and energy transfer can occur. As the magnetosonic wave is thought to increase inward electron flux towards the central axis, transferring energy to the magnetosonic wave could increase this inward electron flux. This would result in a decrease to electron divergence, which could be verified by mapping the plume with a Langmuir probe.

The original aim of this study was to evaluate the effects of spectral broadening on the thruster performance. However this was unable to be investigated so should be looked at in future work. The SDR driven microwave generator can also be used to study the effects of introducing a third microwave frequency and modulating the main signal with various sub-signals.

10.3 Resonance Region Location

The generally accepted understanding in the field is that the resonance region should be located near the rear of the thruster's chamber to maximise performance[16]. To test this, the thrusters chamber was mounted on a linear rail, so as to allow it to be displaced from its annular magnet.



Figure 10.3: Photos of the large ECR thruster with the resonance region at the front of the thruster's chamber (left), middle (middle) and rear (right). The resonance region can be seen as a faint band of light on the inner wall of the thruster's chamber.

Direct thrust measurements show that thrust is decreased when the resonance region is located within the rear 6 mm of the thruster's 20 mm chamber. This is found to be partly due to a reduction in ion beam current, which could be caused by a decreased ionisation rate or an increase in ion losses to the thrust chamber's wall. This apparent contradiction with prior studies could be due to the larger diameter of the ECR thruster used.

Further Work - *Resonance Region Location*

It is common practise to position the resonance region of ECR thrusters at the back of the thrust chamber, near the backplate. This is largely based on research by F. Cannat et al.[57] that has shown that a small ECR thruster's performance is increased when the resonance region is nearer the backplate. This new study has shown that scaling up an ECR thruster results in a change to the position of the resonance region that produces the highest thruster performance. Further work should therefore be conducted to determine the relationship between the diameter of the thrust chamber and the position of the resonance region that produces the highest thruster performance.

10.4 Magnetic Mirror Trap

By adding a second ring magnet to the throat of the small ECR thruster, a region of high magnetic field strength was generated at the thruster's exit. This acted as a magnetic mirror, reflecting escaping electrons back into the chamber where they could gain further energy. The aim was therefore to prove that a magnetic mirror could be used to increase the electron temperature in ECR thrusters, however electron temperature measured in the plume was seen to decrease by 21 %. Adding the second ring magnet had the unintended effect of increasing the magnetic field strength gradient at resonance, resulting in less energy being transferred to electrons passing through. This is thought to be the cause of the reduction in electron temperature.

Adding the second ring magnet was also seen to decrease ion beam current, likely due to increased plasma losses to the wall. The thrust was observed to decrease by 29 % and the thruster efficiency reduced from 7.3 % to 3.6 %. However, with the second ring magnet installed, thrust efficiency and electron temperature are seen to increase as xenon mass flow rate is decreased. This indicates that for a miniaturised, low mass flow rate ECR thruster, adding a magnetic mirror trap could increase thruster performance.

Without the magnetic mirror, the thruster required a xenon mass flow rate of 0.7 mg/s to ignite a plasma within the thruster. Confining the electrons to the thruster's chamber with a magnetic mirror increases the electron density, thereby increasing the rate of ionisation within the chamber. Therefore a secondary aim of adding the magnetic mirror trap was to reduce the propellant mass flow rate required for ignition. With the second ring magnet installed, the xenon mass flow rate required to ignite the thruster reduced to 0.1 mg/s. This indicates that the magnetic mirror does confine electrons to the chamber and could be used to aid ECR thruster ignition for thrusters that are unable to achieve high neutral propellant densities.

Further Work - *Magnetic Mirror Trap*

While adding a magnetic mirror trap failed to increase thruster performance, it did decrease the mass flow rate required to ignite the thruster. This is an indication that the magnetic mirror is working to confine electrons to the chamber. A future implementation of a magnetic mirror trap on an ECR magnetic nozzle thruster should aim to do so without increasing the magnetic field strength gradient at resonance so as to not reduce electron temperatures. A future implementation should also aim to not decrease the ion beam current. This could be done by not having the magnetic field lines intercept the thruster walls, or by adding a magnetic mirror at the walls to reflect incident electrons and reduce plasma wall losses. The magnetic mirror trap could also be moved downstream of the thicker resonance region. This would expose the trapped electrons to the thicker resonance region, increasing the energy they gain before escaping the magnetic mirror trap.

10.5 Future Work: Other Ideas

Further Decreasing Magnetic Field Strength Gradient

This section outlines the process that was used to optimise the thruster's magnetic circuit for a low magnetic field strength gradient at resonance. Figure 10.4.a) shows a magnetic field model of the large ECR thruster with only its ring magnet. The magnetic field strength at which resonance occurs is shown in red. Magnetic field strengths greater than this are shown in purple, and magnetic field strengths lower are shown in blue. The resonance region can be seen to be stretched between regions of low magnetic field strength, this is shown using a blue arrow. With just the ring magnet, the resonance region is only stretched in one location. The iron ring is added in figure 10.4.b), which can be seen to cause the resonance region to be stretched in two places, increasing its net thickness. Figure 10.4.c) then shows a new ferromagnetic geometry that causes the resonance region to be stretched in three places, further increasing its thickness. This method of optimising for a thick resonance region can be used to find magnetic circuits with the lowest magnetic field strength gradient at resonance. Further work could therefore concentrate on investigating these alternative geometries to find the geometry that provides the greatest thruster performance.

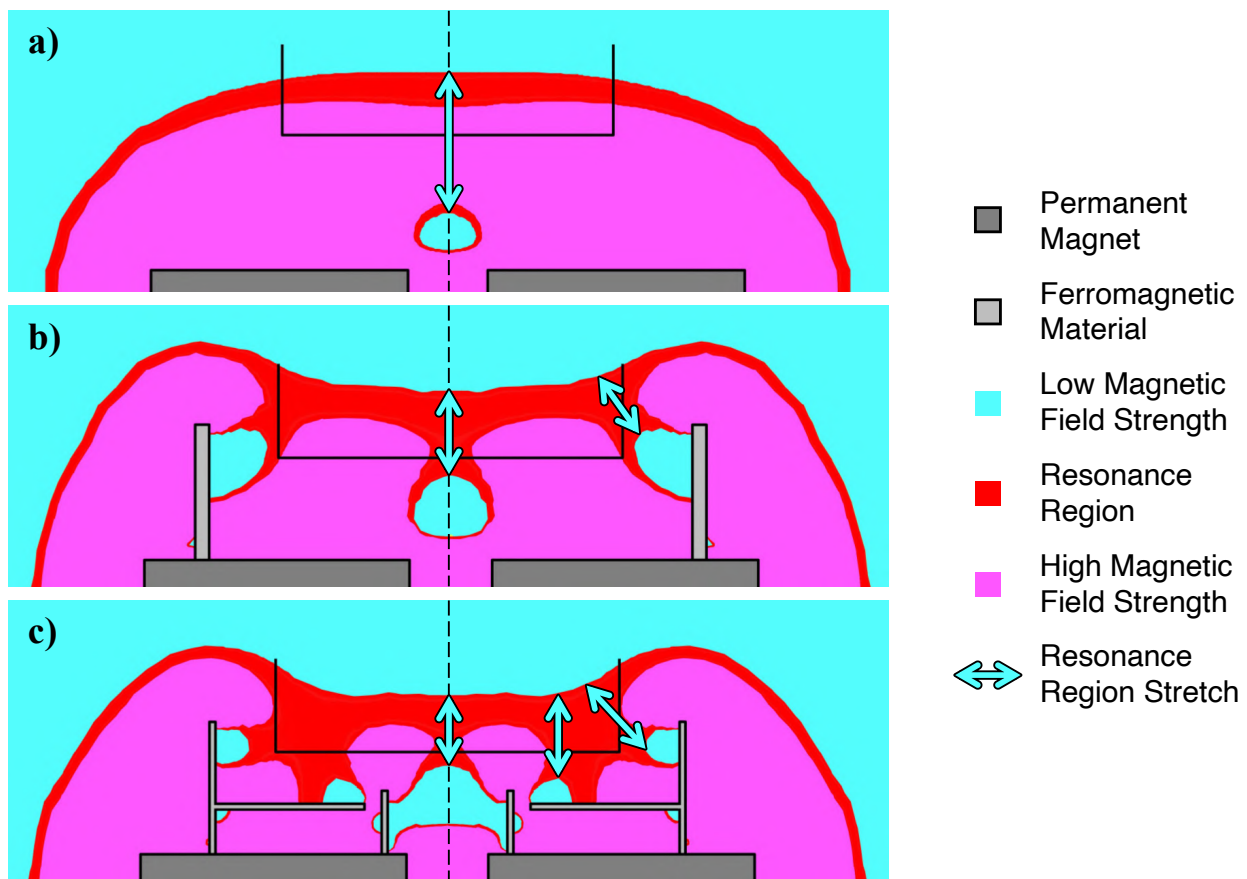


Figure 10.4: Three different levels of magnetic thickening of the resonance region. With the resonance region stretched at: a) a single point, b) two points and c) three points. Modelled using FEMM[93].

Prevention of Back-streaming Plasma

Testing by S. Peterschmitt[36] found erosion marks on the back of the ONERA ECR thruster. These were thought to be caused by a small fraction of plasma that was not separating from the magnetic field lines and was impinging on the back of the thruster. The addition of a dielectric plate around the exit of the thruster interrupted this flow resulting in a 40 % increase in thruster floating potential and a 20 % increase in trust.

A dielectric plate was therefore added to the small ECR thruster. However, no increase to thruster performance was observed and so it was removed, see section 4.5. After the test campaign of the large ECR thruster had concluded, brown erosion marks were found on the rear of the thruster, see figure 10.5. These marks appear to be due to plasma that is attached to the magnetic field lines of the thruster. This conclusion is based on the fact that erosion is concentrated at the location at which magnetic field strength is greatest, and that the outline of the rectangular aluminium block in-front of it can be clearly seen, indicating that the plasma approaches the surface perpendicular to it. The addition of a dielectric plate around the exit of the thruster could therefore interrupt this flow and increase thruster performance.

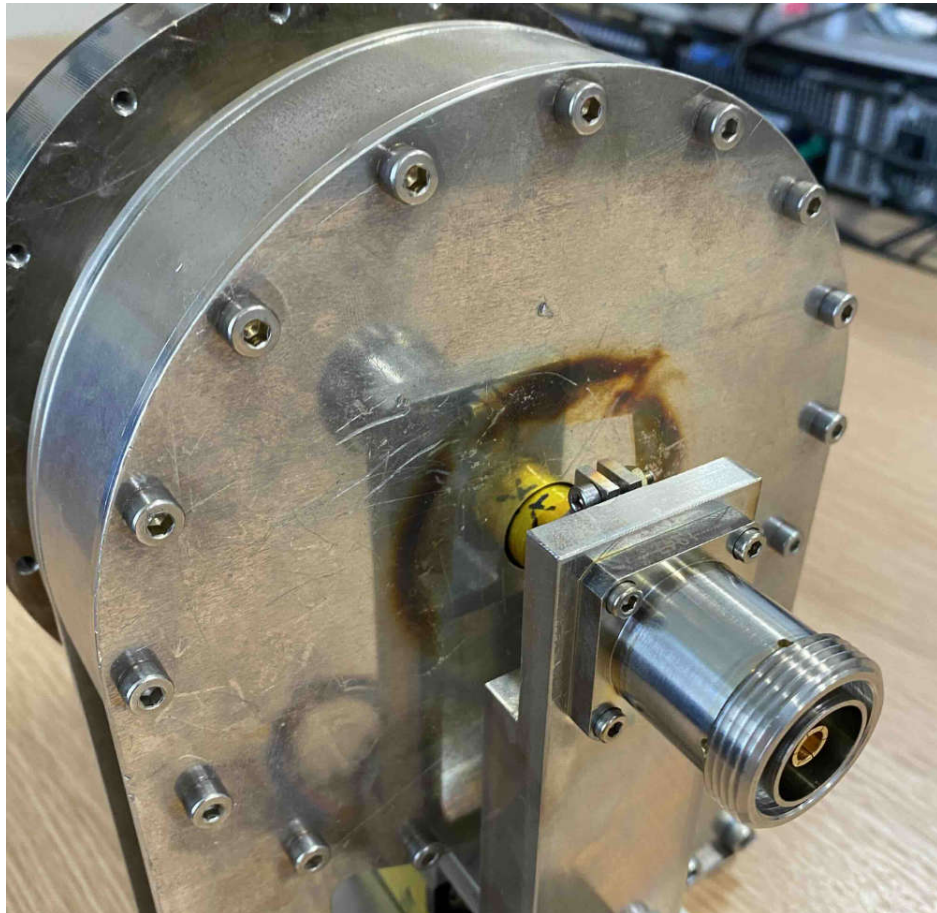


Figure 10.5: Erosion marks on the rear of the thruster are evidence that a fraction of the plasma does not separate from magnetic field lines and impinges on the rear of the thruster.

APPENDIX

A List of Thrusters with a Nominal Thrust between 0.1 and 10.0 mN

Table A.1: List of thrusters with a nominal thrust between 0.1 and 10.0 mN. Including Field-Emission Electric Propulsion (FEEP), Hall Effect Thrusters (HET), Gridded Ion Thrusters (GIT) and Electron Cyclotron Resonance (ECR) thrusters. Performance values obtained from ENPULSION GmbH.[20][21][22] and I.S. Vavilov[23].

Thruster	Company	Type	Thrust [mN]	Specific Impulse [s]	Power [W]
NANO	Enpulsion	FEEP	0.4	4200	40
NANO IR3	Enpulsion	FEEP	0.5	2400	50
MICRO R3	Enpulsion	FEEP	1.0	2000	105
SPT-35	OKB Fakel	HET	10.0	1200	200
SPT-25	OKB Fakel	HET	7.0	900	100
CHT	Princeton University	HET	6.0	1650	185
HT-100	Alta S.p.A	HET	10.0	1000	235
TCHT-4	Osaka Institute of Tech	HET	3.5	1200	240
Micro-Hall	Stanford University	HET	1.6	850	40
RIT μ X	ArianeGroup	GIT	0.5	3000	48
RIT 10	ArianeGroup	GIT	5.0	1900	145
BIT 1	Busek Co. Inc.	GIT	0.2	1600	28
BIT 3	Busek Co. Inc.	GIT	1.2	2100	75
μ 10	JAXA	GIT	10.0	3000	400
MIPS-EM	University of Tokyo	GIT	0.3	1200	39
I-COUPS	University of Tokyo	GIT	0.4	1000	38
Small ECR	ONERA	ECR	1.5	1580	36
Large ECR	ONERA	ECR	5.6	2310	209

B Test Diagram for Small ECR Thruster

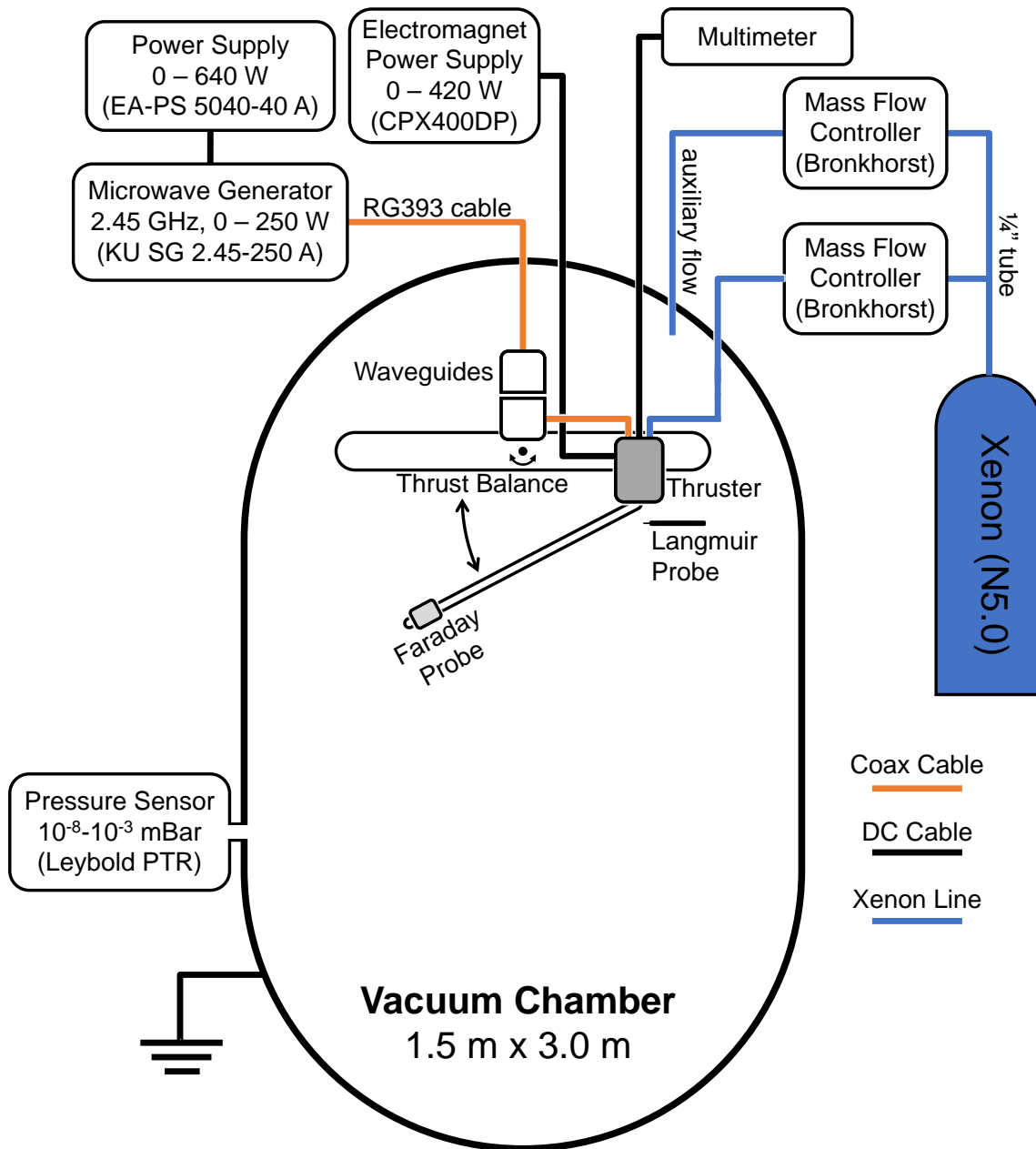


Figure B.1: Diagram of the test configuration and equipment for the small ECR thruster.

C Sputter Deposition on Backplate



Figure C.1: Photo of the large ECR thruster after testing, showing dark patches on the dielectric backplate between the injector holes. These were found to be conductive and so are thought to be carbon deposited via sputter erosion of thruster's graphite chamber wall.

D Antenna Erosion

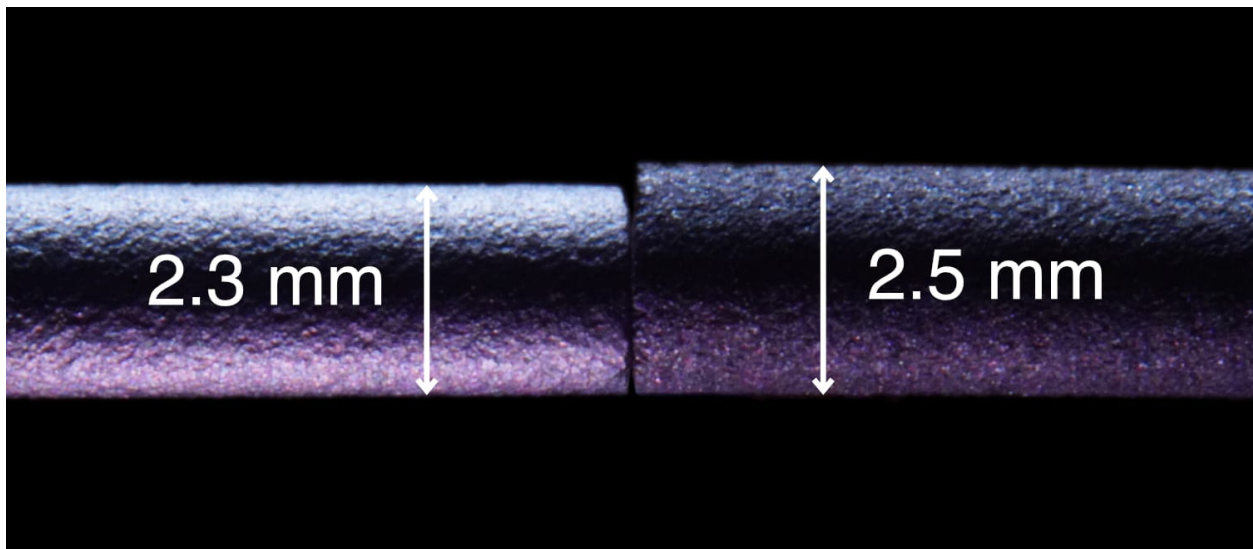


Figure D.1: Photo of the eroded antenna that was used with the large ECR thruster (left) and a new antenna (right). The eroded antenna's diameter at its tip reduced from 2.5 mm to 2.3 mm over the course of the test campaign.

References

- [1] Office of Management and Budget, Executive Office of the President, Budget of the U.S. Government (2024).
URL https://www.whitehouse.gov/wp-content/uploads/2023/03/budget_fy2024.pdf
- [2] U. Carion, I made a delta-v subway map of the Solar System, 29 June 2014.
URL <https://imgur.com/gallery/AAGJvD1>
- [3] T. Pultarova, E. Howell, Starlink satellites: Facts, tracking and impact on astronomy, <https://www.space.com/spacex-starlink-satellites.html>, [Published 01-Jul-2024].
- [4] D. Connell, B. R. Zamora, A Powerhouse in Deep Space: Gateway's Power and Propulsion Element, <https://www.nasa.gov/missions/artemis/gateway/a-powerhouse-in-deep-space-gateways-power-and-propulsion-element/>, [Published 15-Dec-2022].
- [5] W. R. Kerslanke, L. R. Ignaczak, Development and flight history of sert ii spacecraft, in: 28th Joint Propulsion Conference and Exhibit, 1992.
URL <https://ntrs.nasa.gov/citations/19920019740>
- [6] Y. Choi, Modeling an anode layer hall thruster and its plume, Ph.D. thesis, University of Michigan (2008).
URL <https://hdl.handle.net/2027.42/60648>
- [7] V. Désangles, et al., Ecra thruster advances, 30w and 200w prototypes latest performances, Journal of Electric Propulsion (2023). doi:10.1007/s44205-023-00046-x.
- [8] D. M. Goebel, I. Katz, Fundamentals of Electric Propulsion: Ion and Hall Thrusters, John Wiley & Sons, Inc, 2008. doi:10.1002/9780470436448.
- [9] K. J. Chung, Transmission Line Theory, High-voltage Pulsed Power Engineering, Lecture, seoul National University, (2018).
URL https://ocw.snu.ac.kr/sites/default/files/NOTE/Lecture_03_Transmissionlinetheory.pdf
- [10] S. Correyero, J. Jarrige, D. Packan, E. Ahedo, Plasma beam characterization along the magnetic nozzle of an ecr thruster, Plasma Sources Science and Technology 28 (9) (2019) 095004. doi:10.1088/1361-6595/ab38e1.
- [11] D. B. Miller, G. W. Bethke, G. F. Crimi, Investigation of plasma accelerator (cyclotron resonance propulsion system) final report, Tech. rep., NASA (1965).
URL <https://ntrs.nasa.gov/citations/19660008731>
- [12] M. Nagatomo, Plasma acceleration by microwave discharge in magnetic field gradient, Proceedings Sixth Int. Symp. Sp. Technol. Science. (1965).
- [13] J. C. Sercel, An experimental and theoretical study of the ecr plasma engine, Ph.D. thesis, California Institute of Technology (1993). doi:10.7907/PDWR-J354.
- [14] J. C. Sercel, Electron-cyclotron-resonance (ecr) plasma acceleration, AIAA-87 -1407 (1987). doi:10.2514/6.1987-1407.
- [15] T. Vialis, Developpement d'un propulseur plasma a resonance cyclotron electronique pour les satellites, Ph.D. thesis, Sorbonne Universite (2018).
URL <https://theses.hal.science/tel-02076358/>
- [16] F. Cannat, Caractérisation et modélisation d'un propulseur plasma à résonance cyclotronique des électrons, Ph.D. thesis, Ecole Polytechnique ParisTech (2015).
URL <https://pastel.hal.science/tel-01271986v2>

- [17] F. Boni, et al., Investigation of facility effects on the performance of an electron cyclotron resonance magnetic nozzle thruster, in: 38th International Electric Propulsion Conference, 2024.
 URL <https://hal.science/hal-04646781>
- [18] H. Hayashi, et al., Experimental demonstration of microwave discharge ion engine with 10,000 sec isp, Transactions of the Japan Society for Aeronautical and Space Sciences, Aerospace Technology Japan 7 (2009). doi:10.2322/tstj.7.Tb_1.
- [19] Periodic Reporting for period 2 - MINOTOR (MagnetIc NOzzle thruster with elecTron cyclOtron Resonance), <https://cordis.europa.eu/project/id/730028/reporting>, [Online; accessed 19-Oct-2022].
- [20] ENPULSION GmbH, ENPULSION NANO, doc.No: ENP2019-086, Iss/Rev.: B.1.
- [21] ENPULSION GmbH, ENPULSION NANO IR3, doc.No: ENP2020-078, Iss/Rev.: B.1.
- [22] ENPULSION GmbH, ENPULSION MICRO R3, doc.No: ENP2018-002, Iss/Rev.: I.1.
- [23] I. S. Vavilov, et al., Review of electric thrusters with low consumption power for corrective propulsion system of small space vehicles, Journal of Physics: Conference Series 1546 (1) (2020) 012071. doi: 10.1088/1742-6596/1546/1/012071.
- [24] B. N. Wachs, Optimization and characterization of facility effects for a low-power electron cyclotron resonance magnetic nozzle thruster, Ph.D. thesis, University of Michigan (2022). doi:10.7302/5985.
- [25] J. Little, E. Choueiri, Plasma detachment and momentum transfer in magnetic nozzles, in: 47th AIAA/ASME/SAE/ASEE Joint Propulsion Conference & Exhibit, 2011. doi:10.2514/6.2011-6001.
- [26] B. Wachs, B. Jorns, Background pressure effects on ion dynamics in a low-power magnetic nozzle thruster, Plasma Sources Science and Technology 29 (4) (2020) 045002. doi:10.1088/1361-6595/ab74b6.
- [27] R. Azevedo, et al., Xjet: Design upgrade and preliminary characterization for an electrodeless ecr thruster, in: Space Propulsion Conference 2020/21, 2021.
 URL <https://www.researchgate.net/publication/350688685>
- [28] S. S. Baldinucci, et al., Impact of facility electrical boundary conditions on the performance of an electron cyclotron resonance magnetic nozzle thruster, in: 37th International Electric Propulsion Conference, 2022.
 URL <https://pepl.engin.umich.edu/pdf/IEPC-2022-Baldinucci.pdf>
- [29] F. F. Chen, Introduction to Plasma Physics and Controlled Fusion, Springer New York, NY, 1984. doi:10.1007/978-3-319-22309-4.
- [30] SpaceX, Starship Flight IFT-4 Livestream, <https://www.spacex.com/vehicles/starship/>, [06-Jun-2024].
- [31] I. Dodin, Plasma Waves and Instabilities, Lecture notes (under development), <http://www.princeton.edu/~idodin/ast553/main.pdf>, [Last modified: December 27, 2023].
- [32] I. Funaki, et al., 20 mn-class microwave discharge ion thruster, 27th International Electric Propulsion Conference (2001).
 URL <https://www.academia.edu/6923926/>
- [33] J. Musil, F. Zacek, Penetration of a strong electromagnetic wave in an inhomogeneous plasma generated by ecr using a magnetic beach, Plasma Physics 13 (6) (1971) 471. doi:10.1088/0032-1028/13/6/003.
- [34] S. Reeve, et al., Development update of the x-ept microwave gridded ion thruster for the impulse propulsion architecture, in: 7th Space Propulsion Conference Proceedings, 2021.
- [35] A. J. Thomas, Design and optimization of an electron cyclotron resonance thruster, Master's thesis, Western Michigan University (2022).
 URL https://scholarworks.wmich.edu/masters_theses/5326

- [36] S. Peterschmitt, Development of a stable and efficient electron cyclotron resonance thruster with magnetic nozzle, Ph.D. thesis, Institut Polytechnique de Paris (2022).
URL <https://theses.hal.science/tel-04368923>
- [37] R. Geller, Electron Cyclotron Resonance Ion Sources and ECR Plasmas (1st ed.), Routledge, 1996. doi:10.1201/9780203758663.
- [38] J. Musil, F. Zacek, Linear transformation of waves in a magnetoactive plasma generated by a strong microwave signal, *Plasma Physics* 12 (1) (1970) 17. doi:10.1088/0032-1028/12/1/002.
- [39] M. C. Williamson, A. J. Lichtenberg, M. A. Lieberman, Self-consistent electron cyclotron resonance absorption in a plasma with varying parameters, *Journal of Applied Physics* (1992). doi:10.1063/1.352244.
- [40] H. Wheeler, A helical antenna for circular polarization, *Proceedings of the IRE* 35 (12) (1947) 1484–1488. doi:10.1109/JRPROC.1947.234573.
- [41] M. A. Lieberman, A. J. Lichtenberg, Principles of Plasma Discharges and Materials Processing, John Wiley & Sons, Inc., 2005. doi:10.1002/0471724254.
- [42] G. D. Alton, J. Dellwo, R. F. Welton, D. N. Smithe, Computational studies for an advanced design ecr ion source, in: 16th Particle Accelerator Conference and International Conference on High-Energy Accelerators, 1996.
URL <https://inspirehep.net/literature/410209>
- [43] T. A. Grotjohn, Modeling the electron heating in a compact electron cyclotron resonance ion source, *Review of Scientific Instruments* 67 (3) (1996) 921–923. doi:10.1063/1.1146772.
- [44] H. Koivisto, The effect of microwave frequency and grad b on the energy of electrons in an electron cyclotron resonance ion source, *Review of Scientific Instruments* 70 (7) (1999) 2979–2983. doi:10.1063/1.1149857.
- [45] J. Porto, P. Q. Elias, A. Ciardi, Anisotropic electron heating in an electron cyclotron resonance thruster with magnetic nozzle, *Physics of Plasmas* 30 (2) (2023) 023506. doi:10.1063/5.0124834.
- [46] W. Demtröder, Laser Spectroscopy, Vol. 1, Springer Berlin, Heidelberg, 2008. doi:10.1007/978-3-540-73418-5.
- [47] X. Sun, Nonthermal processes of fast outflows from astrophysical objects, Ph.D. thesis, Ruperto-Carola-University (2017).
URL <https://api.semanticscholar.org/CorpusID:125718217>
- [48] F. Kiefer, K. Keil, K. Holste, P. J. Klar, R. Thüringer, Analysis of the radiated emission of an ecr thruster with magnetic nozzle in terms of its emc, *Journal of Electric Propulsion* 3 (8) (2024).
- [49] T. Lafleur, F. Cannat, J. Jarrige, P. Q. Elias, D. Packan, Electron dynamics and ion acceleration in expanding-plasma thrusters, *Plasma Sources Science and Technology* 24 (6) (2015) 065013. doi:10.1088/0963-0252/24/6/065013.
- [50] H. G. Kosmahl, D. B. Miller, G. W. Bethke, Plasma acceleration with microwaves near cyclotron resonance, *Journal of Applied Physics* (1966). doi:10.1063/1.1709188.
- [51] D. Packan, et al., Minotor h2020 project for ecr thruster development, Tech. rep., EPIC Workshop 2017 (2017).
URL <http://www.minotor-project.eu/overview/ecra-technology-3>
- [52] S. Correyero, et al., Characterization of diamagnetism inside an ECR thruster with a diamagnetic loop, *Physics of Plasmas* 26 (5) (2019) 053511. doi:10.1063/1.5093980.
- [53] F. Ebersohn, et al., Magnetic nozzle plasma plume: Review of crucial physical phenomena, in: 48th AIAA/ASME/SAE/ASEE Joint Propulsion Conference & Exhibit, 2012. doi:10.2514/6.2012-4274.
- [54] E. Ahedo, M. Merino, On plasma detachment in propulsive magnetic nozzles, *Physics of Plasmas* 18 (5) (2011) 053504. doi:10.1063/1.3589268.

- [55] P. Schmit, N. Fisch, Magnetic detachment and plume control in escaping magnetized plasma, *Journal of Plasma Physics* 75 (2009) 359 – 371. doi:10.1017/S0022377808007666.
- [56] A. V. Arefiev, B. N. Breizman, Magnetohydrodynamic scenario of plasma detachment in a magnetic nozzle, *Physics of Plasmas* 12 (4) (2005) 043504. doi:10.1063/1.1875632.
- [57] F. Cannat, J. Jarrige, P. Elias, D. Packan, Experimental investigation of magnetic gradient influence in a coaxial ecr plasma thruster, in: *Space Propulsion 2014*, 2014.
URL <https://onera.hal.science/hal-01068649v1>
- [58] B. N. Wachs, B. A. Jorns, Technique for two-frequency optimization of an ecr magnetic nozzle thruster, in: *36th International Electric Propulsion Conference*, 2019.
URL <https://api.semanticscholar.org/CorpusID:203690562>
- [59] S. Peterschmitt, D. Packan, Impact of the microwave coupling structure on an electron-cyclotron resonance thruster, *Journal of Propulsion and Power* 37 (6) (2021) 806–815. doi:10.2514/1.B38156.
- [60] J. Jarrige, S. C. Plaza, P.-Q. Elias, D. Packan, Investigation on the ion velocity distribution in the magnetic nozzle of an ecr plasma thruster using lif measurements, in: *35th International Electric Propulsion Conference*, 2017.
URL <https://core.ac.uk/download/pdf/288500211.pdf>
- [61] B. Wachs, B. Jorns, Optimization of an ecr thruster using two frequency and pulsed waveforms, in: *AIAA Propulsion and Energy 2021 Forum*, 2021. doi:10.2514/6.2021-3382.
- [62] A. Hermann, et al., Fundamentals of Vacuum Technology, Leybold Vacuum GmbH.
URL https://www.leyboldproducts.com/media/pdf/87/a8/be/FVT_Fundamentals_of_Vacuum_Technology_EN58774555441f3.pdf
- [63] A. Ferreira, L. Lobo, The sublimation of argon, krypton, and xenon, *J. Chem. Thermodynamics* (2008). doi:10.1016/j.jct.2008.07.023.
- [64] R. R. Hofer, P. Y. Peterson, A. D. Gallimore, Characterizing vacuum facility backpressure effects on the performance of a hall thruster, in: *27th International Electric Propulsion Conference*, 2001.
URL <https://api.semanticscholar.org/CorpusID:16004423>
- [65] J. W. Dankanich, et al., Recommended practice for pressure measurement and calculation of effective pumping speed in electric propulsion testing, *Journal of Propulsion and Power* (2017). doi:10.2514/1.B35478.
- [66] R. Holanda, Sensitivity of hot-cathode ionization vacuum gages in several gases, Tech. rep., NASA TN D-681 (1972).
URL <https://ntrs.nasa.gov/citations/19720020804>
- [67] A. Cofer, et al., Film-evaporation mems tunable array for low-mass smallsat propulsion: Design improvements and thrust characterization, in: *51st AIAA/SAE/ASEE Joint Propulsion Conference*, 2015. doi:10.2514/6.2015-3993.
- [68] Ionization Vacuum Gauge Gas Correction Factors, <https://www.mks.com/n/gas-correction-factors>, [Online; accessed 17-Jan-2023].
- [69] R. A. Kishek, et al., Multipactor discharge on metals and dielectrics: Historical review and recent theories, *Physics of Plasmas* 5 (5) (1998) 2120–2126. doi:10.1063/1.872883.
- [70] S. Masillo, J. Stubbing, K. Swar, D. Staab, A. Garbayo, A. Lucca Fabris, Validation of a torsional balance for thrust measurements of hall effect and microwave-based space propulsion systems, *Review of Scientific Instruments* 93 (11) (2022) 114501. doi:10.1063/5.0117584.
- [71] F. F. Chen, Langmuir probe diagnostics, in: *Mini-Course on Plasma Diagnostics*, IEEE-ICOPS meeting, Jeju, Korea, 2003.
URL <https://www.seas.ucla.edu/~ffchen/Publs/Chen210R.pdf>

- [72] M. Tisaev, Enabling air-breathing electric propulsion for vleo: Computational analysis of orbital envelope and experimental development of microwave plasma cathode, Ph.D. thesis, University of Surrey (2024). doi:10.15126/thesis.901023.
- [73] R. B. Lobbia, B. E. Beal, Recommended practice for use of langmuir probes in electric propulsion testing, *Journal of Propulsion and Power* 33 (3) (2017) 566–581. doi:10.2514/1.B35531.
- [74] S. Masillo, Experimental characterisation of a novel hall-type plasma thruster for small satellite applications, Ph.D. thesis, University of Surrey (2023). doi:10.15126/thesis.900682.
- [75] D. L. Brown, et al., Recommended practice for use of faraday probes in electric propulsion testing, *Journal of Propulsion and Power* 33 (3) (2017) 582–613. doi:10.2514/1.B35696.
- [76] A. J. Sheppard, J. M. Little, Performance analysis of an electron cyclotron resonance thruster with various propellants, *Journal of Propulsion and Power* 38 (6) (2022) 998–1008. doi:10.2514/1.B38698.
- [77] H. Kim, Y. Lim, W. Choe, J. Seon, Effect of multiply charged ions on the performance and beam characteristics in annular and cylindrical type hall thruster plasmas, *Applied Physics Letters* 105 (10 2014). doi:10.1063/1.4897948.
- [78] S. Mazouffre, et al., Characterization of miniature hall thruster plume in the 50-200 w power range, in: 8th European Conference for Aeronautics and Space Sciences (EUCASS), 2019. doi:10.13009/EUCASS2019-214.
- [79] A. Snyder, et al., Single-string integration test measurements of the next ion engine plume, 40th Joint Propulsion Conference and Exhibit (2005). doi:10.2514/6.2004-3790.
- [80] F. Cannat, et al., Optimization of a coaxial electron cyclotron resonance plasma thruster with an analytical model, *Physics of Plasmas* 22 (5) (2015) 053503. doi:10.1063/1.4920966.
- [81] M. J. Baird, et al., Hall thruster plume measurements of time resolved ion energy, in: 36th International Electric Propulsion Conference, Vienna, Austria, 2019.
URL <https://electricrocket.org/2019/516.pdf>
- [82] C. Bohm, J. Perrin, Retarding-field analyzer for measurements of ion energy distributions and secondary electron emission coefficients in low-pressure radio frequency discharges, *Review of Scientific Instruments* (1993). doi:10.1063/1.1144398.
- [83] B. S. Sommers, et al., Preliminary characterization of ion energy spectra acquired from high current hollow cathodes, in: 33rd International Electric Propulsion Conference, 2013.
URL <https://api.semanticscholar.org/CorpusID:99728615>
- [84] J. Jarrige, et al., Performance comparison of an ecr plasma thruster using argon and xenon as propellant gas, in: 33rd International Electric Propulsion Conference, 2013.
URL <https://api.semanticscholar.org/CorpusID:54051607>
- [85] K. Takahashi, Helicon-type radiofrequency plasma thrusters and magnetic plasma nozzles, *Reviews of Modern Plasma Physics* (2019). doi:10.1007/s41614-019-0024-2.
- [86] M. Merino, Analysis of magnetic nozzles for space plasma thrusters, Ph.D. thesis, Universidad Politecnica de Madrid (2013).
URL <https://api.semanticscholar.org/CorpusID:127963097>
- [87] T. Lafleur, Helicon plasma thruster discharge model, *Physics of Plasmas* (2014). doi:10.1063/1.4871727.
- [88] A. Caldarelli, Radio-frequency plasma expansion in different magnetic nozzle configurations, Ph.D. thesis, The University of Auckland (2024). doi:10.13140/RG.2.2.30024.53766.
- [89] A. Bennet, C. Charles, R. Boswell, Separating the location of geometric and magnetic expansions in low-pressure expanding plasmas, *Plasma Sources Science and Technology* 27 (7) (2018) 075003. doi:10.1088/1361-6595/aacd6d.

- [90] G. D. Conway, A. J. Perry, R. W. Boswell, Evolution of ion and electron energy distributions in pulsed helicon plasma discharges, *Plasma Sources Science and Technology* (1998). doi:10.1088/0963-0252/7/3/012.
- [91] M. R. Vasquez, et al., Ion energy distribution measurements of low-energy ion beams extracted from a hot cathode dc ion source, in: *The Science and Engineering Review of Doshisha University*, Vol. 51, 2011.
URL <https://api.semanticscholar.org/CorpusID:21697117>
- [92] K. Takahashi, et al., Axial momentum lost to a lateral wall of a helicon plasma source, *Physical Review Letters* (2015). doi:10.1103/PhysRevLett.114.195001.
- [93] D. Meeker, Finite Element Method Magnetics, Version 4.2, <https://www.femm.info>, [28-Feb-2018 Build].
- [94] J. Kraus, The helical antenna, *Proceedings of the IRE* 37 (3) (1949) 263–272. doi:10.1109/JRPROC.1949.231279.
- [95] C. Morlaas, B. Souny, A. Chabory, Helical-ring antenna for hemispherical radiation in circular polarization, *IEEE Transactions on Antennas and Propagation* 63 (11) (2015) 4693–4701. doi:10.1109/TAP.2015.2479640.
- [96] M. Ahmed, et al., A novel diamond-based plasma neutraliser, in: *37th International Electric Propulsion Conference*, 2022.
URL <https://openresearch.surrey.ac.uk/esploro/outputs/99687266202346>
- [97] A. Shih, et al., Secondary electron emission from diamond surfaces, *Journal of Applied Physics* 82 (4) (1997) 1860–1867. doi:10.1063/1.365990.
- [98] R. M. A. Vaz, Studies of the secondary electron emission from diamond films, Ph.D. thesis, University of Bristol (2013).
URL www.chm.bris.ac.uk/pt/diamond/raquelthesis/Raquel-Vaz-PhD-thesis.pdf
- [99] H. Bruining, *Physics and Applications of Secondary Electron Emission*, Pergamon Press Ltd., 1954. doi:10.1016/C2013-0-01633-7.
- [100] M. L. R. Walker, A. L. Victor, R. R. Hofer, A. D. Gallimore, Effect of backpressure on ion current density measurements in hall thruster plumes, *Journal of Propulsion and Power* 21 (3) (2005) 408–415. doi:10.2514/1.7713.
- [101] M. Walker, R. Hofer, A. Gallimore, The effects of nude faraday probe design and vacuum facility backpressure on the measured ion current density profile of hall thruster plumes, in: *38th AIAA/ASME/SAE/ASEE Joint Propulsion Conference*, 2002. doi:10.2514/6.2002-4253.
- [102] B. Wachs, B. Jorns, Effect of background pressure on ion dynamics in an electron cyclotron resonance thruster, in: *2018 Joint Propulsion Conference Joint Propulsion Conference*, 2018. doi:10.2514/6.2018-4585.
- [103] R. Stenzel, Mirror reflection of a stronger electron beam in a magnetic field which converges to the right, <https://www.physics.ucla.edu/plasma-exp/beam/BeamLoopyMirror.html>, [25-Jan-2000].
- [104] P. P. Uroine, R. Hinrichs, *Magnetic Field Strength: Force on a Moving Charge in a Magnetic Field*, Technische Universität Dresden, 2012.
URL https://phys.libretexts.org/Courses/Skyline/Survey_of_Physics/09:_Magnetism
- [105] A. Peeters, Physics of fusion power, lecture 5: particle motion, University of Warwick (2009).
URL <https://warwick.ac.uk/fac/sci/physics/research/cfsa/people/pastmembers/peeters/teaching/lecture5.pdf>
- [106] R. Pioch, V. Desangles, Influence of the operating conditions of an ecr thruster on the ion detachment from the magnetic nozzle, in: *38th International Electric Propulsion Conference*, 2024.
URL <https://hal.science/hal-04647918>

- [107] M. R. Inchingolo, et al., Thrust measurements of a waveguide electron cyclotron resonance thruster, *Journal of Applied Physics* 135 (9) (2024) 093304. doi:10.1063/5.0186778.
- [108] E. Ahedo, M. Martínez Sánchez, Theory of a stationary current-free double layer in a collisionless plasma, *Phys. Rev. Lett.* 103 (2009) 135002. doi:10.1103/PhysRevLett.103.135002.
- [109] M. Merino, E. Ahedo, Two-dimensional quasi-double-layers in two-electron-temperature, current-free plasmas, *Physics of Plasmas* 20 (2) (2013) 023502. doi:10.1063/1.4789900.
- [110] A. Piragino, et al., Background pressure effects on the performance of a 20 kw magnetically shielded hall thruster operating in various configurations, *Aerospace* 8 (3) (2021). doi:10.3390/aerospace8030069.
- [111] M. Nakles, W. Hargus, J. Delgado, R. Corey, A performance comparison of xenon and krypton propellant on an spt-100 hall thruster, in: 32nd International Electric Propulsion Conference, 2011.
URL <https://api.semanticscholar.org/CorpusID:38032972>
- [112] E. Krishnakumar, S. K. Srivastava, Ionisation cross sections of rare-gas atoms by electron impact, *Journal of Physics B: Atomic, Molecular and Optical Physics* 21 (6) (1988) 1055. doi:10.1088/0953-4075/21/6/014.
- [113] K. Takahashi, Y. Takao, A. Ando, Increased thrust-to-power ratio of a stepped-diameter helicon plasma thruster with krypton propellant, *Journal of Propulsion and Power* 36 (6) (2020) 961–965. doi:10.2514/1.B37940.
- [114] M. R. Inchingolo, M. Merino, J. Navarro-Cavallé, Plume characterization of a waveguide ecr thruster, *Journal of Applied Physics* 133 (11) (2023) 113304. doi:10.1063/5.0138780.
- [115] E. Naselli, et al., Impact of two-close-frequency heating on ecr ion source plasma radio emission and stability, *Plasma Sources Science and Technology* 28 (8) (2019) 085021. doi:10.1088/1361-6595/ab32f9.
- [116] D. Maddaloni, et al., Experimental characterization of oscillations in the magnetic nozzle of an electron cyclotron resonance thruster, in: 38th International Electric Propulsion Conference, 2024.
URL <https://hal.science/hal-04646669>
- [117] S. Hepner, The influence of instabilities on the electron dynamics of a magnetic nozzle, Ph.D. thesis, University of Michigan (2022). doi:10.7302/4630.
- [118] K. Takahashi, C. Charles, R. W. Boswell, Wave-driven electron inward transport in a magnetic nozzle, *Scientific Reports* (2022). doi:10.1038/s41598-022-24202-9.
- [119] everything RF, What is Intermodulation Distortion?, <https://www.everythingrf.com/community/what-is-intermodulation-distortion>, [07-Apr-2020].
- [120] J. Y. Kim, et al., Kinetic electron cooling in magnetic nozzles: experiments and modeling, *Plasma Sources Science and Technology* 32 (7) (2023) 073001. doi:10.1088/1361-6595/acd71c.
- [121] I. Romadanov, et al., On limitations of laser-induced fluorescence diagnostics for xenon ion velocity distribution function measurements in hall thrusters, *Physics of Plasmas* 25 (3) (2018) 033501. doi:10.1063/1.5020749.